



OMV Australia



Cultus Timor Sea Ltd
(ACN 064 126 138)

Level 29, 44 St George's Tce
Perth WA 6000
Australia

Tel: (61 8) 9223 5000
Fax: (61 8) 9223 5004

**AUSTRALIA
GIPPSLAND BASIN
VIC/RL5**

BALEEN-2

**WELL COMPLETION REPORT
BASIC GEOTECHNICAL DATA**

**-VOLUME 1B-
Appendices 14-16, Enclosures**

Prepared by: Alex Warris

CONFIDENTIAL

907961 002



OMV Australia

Cultus Timor Sea Ltd
(ACN 064 126 138)

Level 29, 44 St George's Tce
Perth WA 6000
Australia

Tel: (61 8) 9223 5000
Fax: (61 8) 9223 5004

**AUSTRALIA
GIPPSLAND BASIN
VIC/RL5**

BALEEN-2

**WELL COMPLETION REPORT
BASIC GEOTECHNICAL DATA**

**-VOLUME 1B-
Appendices 14-16, Enclosures**

Prepared by: Alex Warris

CONFIDENTIAL



OMV Australia

Cultus Timor Sea Ltd
(ACN 064 126 138)Level 29, 44 St George's Tce
Perth WA 6000
AustraliaTel: (61 8) 9223 5000
Fax: (61 8) 9223 5004

AUSTRALIA
GIPPSLAND BASIN
VIC/RL5

BALEEN-2

WELL COMPLETION REPORT BASIC GEOTECHNICAL DATA

-VOLUME 1B-
Appendices 14-16, Enclosures

Prepared by: Alex Warris

Approved by:


Exploration Manager

July, 2000

CONFIDENTIAL

Copy No. 5.....

BALEEN-2

BASIC DATA REPORT

-Volume 1A-

TABLE OF CONTENTS

I.	LIST OF FIGURES.....	ii
II.	LIST OF TABLES.....	ii
III.	LIST OF APPENDICES	ii
V.	DISTRIBUTION LIST	iv
1	WELL SUMMARY	
1.1	WELL SUMMARY CARD – BALEEN-2.....	1
1.2	SUMMARY	2
1.3	CASING.....	3
1.4	STRATIGRAPHY.....	3
1.5	CONVENTIONAL CORES	4
1.6	SIDEWALL CORES.....	4
1.7	CUTTINGS	5
1.8	MDT SUMMARY	5
1.9	DST SUMMARY	5
2	GEOLOGY	
2.1	GEOLOGICAL SUMMARY.....	6
3	HYDROCARBON SHOWS	
3.1	OIL FLUORESCENCE SHOWS.....	8
3.2	GAS SHOWS	8
4	WIRELINE AND MUD LOGS	
4.1	WIRELINE LOGS	10
4.2	MUD LOGS	10
4.3	VELOCITY SURVEY	11
5	SAMPLE ANALYSES	
5.1	OIL ANALYSES.....	12
5.2	GAS ANALYSIS	12
5.3	MUD ANALYSES	12
5.4	WATER ANALYSES.....	12
5.5	FILTRATE ANALYSIS	12

I. LIST OF FIGURES

FIGURE 1	RL5 Location Map
FIGURE 2	Well Location Map
FIGURE 3	Abandonment Schematic

II. LIST OF TABLES

TABLE 1	Casing Summary.....	3
TABLE 2	Coring Summary	4
TABLE 3	Cuttings Summary.....	5
TABLE 4	Summary of Drilling Gas	8
TABLE 5	Drilling Gas Peaks.....	9
TABLE 6	Wireline Logging Summary	10
TABLE 7	Mud Data.....	10
TABLE 8	Fluid Sample Collection Summary	13

III. LIST OF APPENDICES

APPENDIX 1	Daily Geological Reports - Cultus
APPENDIX 2	Core Chip Description Report - Cultus
APPENDIX 3	Cuttings Description Report - Cultus
APPENDIX 4	Coring Report - Security DBS
APPENDIX 5	5 Metre Core Photography - ACS Laboratories
APPENDIX 6	Wireline Logging Report / Operations Summary - Cultus
APPENDIX 7	MDT Summary Report - Cultus
APPENDIX 8	Mud Logging Daily Reports - Geoservices
APPENDIX 9	Final Mud logging Report - Geoservices
APPENDIX 10	Palynological Report – Basic Data - Biostrata
APPENDIX 11	VSP / Geogram Report - Schlumberger
APPENDIX 12	Routine Core Analysis Report - ACS Laboratories
APPENDIX 13	Fluids Analysis Report - ACS Laboratories

I. LIST OF FIGURES

FIGURE 1	RL5 Location Map
FIGURE 2	Well Location Map
FIGURE 3	Abandonment Schematic

II. LIST OF TABLES

TABLE 1	Casing Summary.....	3
TABLE 2	Coring Summary.....	4
TABLE 3	Casing Summary.....	5
TABLE 4	Summary of Drilling Gas.....	8
TABLE 5	Drilling Gas Peaks.....	9
TABLE 6	Wireline Logging Summary.....	10
TABLE 7	Mud Data.....	10
TABLE 8	Fluid Sample Collection Summary.....	13

III. LIST OF APPENDICES

APPENDIX 1	Daily Geological Reports - Cultus
APPENDIX 2	Core Chip Description Report - Cultus
APPENDIX 3	Cuttings Description Report - Cultus
APPENDIX 4	Coring Report - Security DBS
APPENDIX 5	5 Metre Core Photography - ACS Laboratories
APPENDIX 6	Wireline Logging Report / Operations Summary - Cultus
APPENDIX 7	MDT Summary Report - Cultus
APPENDIX 8	Mud Logging Daily Reports - Geoservices
APPENDIX 9	Final Mud logging Report - Geoservices
APPENDIX 10	Palynological Report – Basic Data - Biostrata
APPENDIX 11	VSP / Geogram Report - Schlumberger
APPENDIX 12	Routine Core Analysis Report - ACS Laboratories
APPENDIX 13	Fluids Analysis Report - ACS Laboratories

-Volume 1B-

III. LIST OF APPENDICES

- APPENDIX 14 Petrology and Reservoir Quality Report - ACS Laboratories
APPENDIX 15 Core Lithological Description and Sedimentological Interpretation
Report - ACS Laboratories
APPENDIX 16 Single and Multiple Failure Triaxial Tests on Baleen-2 Sands Report
- CSIRO

IV. LIST OF ENCLOSURES

ENCLOSURE 1 Merged Composite Playback (1:200 scale) – Cultus

(From Geoservices Final Report)

- ENCLOSURE 2 Formation Evaluation Log
ENCLOSURE 3 Drilling Data Log
ENCLOSURE 4 Pressure Log

(From Schlumberger VSP / Geogram Report)

- ENCLOSURE 5 Plot 1 – Z Median Stack
ENCLOSURE 6 Plot 2 – Downgoing Wavefield after VELF
Plot 3 – Upgoing Wavefield after VELF
Plot 4 – Downgoing Wavefield after WSF
Plot 5 – Upgoing Wavefield after WSF
ENCLOSURE 7 Plot 6 – Composite Display- normal polarity 20cm/sec
ENCLOSURE 8 Plot 7 – Composite Display- reversed polarity 20cm/sec
ENCLOSURE 9 Plot 8 – Drift Corrected Sonic
ENCLOSURE 10 Plot 9 – Velocity Crossplot

V. DISTRIBUTION LIST

1. OMV Australia Pty Ltd Library, Perth
2. OMV Australia Pty Ltd Exploration Department, Perth
3. OMV, Vienna
- 4,5. VicDNRE, Melbourne (2 copies)
- 6,7. AGSO, Canberra (2 copies)

907961 009

APPENDICES

BALEEN-2

APPENDICES

14 - 16

907961 011

APPENDIX 14

BALEEN-2

PETROLOGY AND RESERVIOR QUALITY REPORT

-ACS LABORATORIES-

907961 013



10 April, 2000

OMV Australia Pty Ltd
Level 29, St Martins Tower
44 St Georges Tce
PERTH WA 6000

Attention: Mark Adamson

FINAL REPORT: 0425-01

CLIENT REFERENCE: Contract No. OSA-1999-008
RFS Basin No. 1

MATERIAL: 12 core sample off-cuts

LOCALITY: Baleen-2

WORK REQUIRED: Petrology and Reservoir Quality

Please direct technical enquiries regarding this work to the signatory below under whose supervision the work was carried out.

A handwritten signature in black ink, appearing to read 'Peter N Crozier', written over a horizontal line.

PETER N CROZIER
Operations Manager

ACS Laboratories Pty Ltd shall not be liable or responsible for any loss, cost, damages or expenses incurred by the client, or any other person or company, resulting from any information or interpretation given in this report. In no case shall ACS Laboratories Pty Ltd be responsible for consequential damages including, but not limited to, lost profits, damages for failure to meet deadlines and lost production arising from this report.

907361 014



PETROLOGY and RESERVOIR QUALITY

of

BALEEN-2

for

OMV AUSTRALIA PTY LTD

by

ACS LABORATORIES PTY LTD

907961 015

PETROLOGY and RESERVOIR QUALITY

of

BALEEN-2 CORE SAMPLES

A final report prepared for

OMV AUSTRALIA PTY LTD

by

JULIAN C. BAKER Ph.D.

April 2000

CONTENTS

	Page
EXECUTIVE SUMMARY	1
1. INTRODUCTION	2
2. ANALYTICAL PROGRAM	
2.1 Thin-Section Analysis	2
2.2 X-Ray Diffraction Analysis	2
2.3 Scanning Electron Microscopy	2
3. TEXTURE	3
4. THIN-SECTION COMPOSITION	3
5. X-RAY DIFFRACTION ANALYSES	7
6. DIAGENESIS	9
7. RESERVOIR QUALITY	
7.1 General	10
7.2 Individual Samples	15
8. SUMMARY AND CONCLUSIONS	18
 TABLES	
TABLE 1 ANALYSES PERFORMED	3
TABLE 2 THIN-SECTION ANALYSES	5
TABLE 3 QFR COMPOSITIONS	6
TABLE 4 BULK XRD ANALYSES	8
TABLE 5 CLAY MINERALOGY	8
TABLE 6 RESERVOIR QUALITY SUMMARY	17

C O N T E N T S cont.

	Page
FIGURES	
FIGURE 1 QFR COMPOSITIONS	6
FIGURE 2 POROSITY/PERMEABILITY CROSS-PLOT	11
FIGURE 3 CLAY + GLAU + MICA + OPAQUES + SIDERITE/PERM. CROSS-PLOT	12
FIGURE 4 VISIBLE POROSITY/PERMEABILITY CROSS-PLOT	13
FIGURE 5 CLAY + GLAU. + MICA + OPAQUES + SID./VIS. POR. CROSS-PLOT	14

APPENDICES

- 1. X-RAY DIFFRACTOGRAMS**
- 2. EDS SPECTRUM FOR EARLY SIDERITE CEMENT IN 52**
- 3. PHOTOMICROGRAPHS**

EXECUTIVE SUMMARY

A petrological study was carried out on twelve plug offcuts from Baleen-2 between 750.41m and 777.80m. Analytical techniques used were thin-section analysis, bulk rock/clay fraction X-ray diffraction analysis and scanning electron microscopy.

Samples are variably argillaceous, well sorted, very fine grained subarkoses in which framework grains include minor K-feldspar, mica and glauconite. Detrital clay forms dispersed and patchy matrix and is also locally concentrated into small, irregular patches, fine wisps and very thin laminae, the distribution of which has locally been influenced by bioturbation. Detrital clay minerals are almost entirely illite and kaolinite. Glauconite is a low expandability illite/smectite that has formed by alteration of biotite and faecal pellets. Non-glauconitic authigenic clay is minor kaolinite that has formed by alteration of micaceous grains and by recrystallisation of detrital clay. Differences in clay mineralogy between samples relate to fluctuations in glauconite abundance, with illite/smectite only being detected in samples with elevated glauconite content.

Excluding 52 and 70, which are from two tight sideritic zones, samples have been little affected by diagenesis. Besides glauconite and kaolinite formation, the only diagenetic effects in these samples are minor pyrite and siderite precipitation, localised compaction of glauconite and micaceous grains, and incipient feldspar dissolution. The samples are generally poorly compacted and virtually uncemented, and are consequently highly friable.

Siderite in 52 and 70 forms a widespread finely/medium-crystalline cement that fills intergranular pores and replaces detrital clay and glauconite. The siderite is enriched in calcium and magnesium, which is consistent with siderite precipitation from a marine porewater. The siderite encapsulates framboidal pyrite and uncompacted glauconite grains, indicating that it formed after pyrite and before compaction, probably within a shallow methanogenic or methane oxidation zone.

Excluding 52 and 70, visible macroporosity ranges from 1.5% to 18.7% and is mainly restricted to localised areas that contain little or no detrital clay. All macroporosity is primary and intergranular. Macroporosity is mainly reduced by the presence of detrital clay and compacted glauconite. Accordingly, reservoir quality is almost totally dependent on detrital clay and glauconite content, implying that most permeability variation is attributable to original compositional differences.

1. INTRODUCTION

Five zones have been identified between 750m and 779m in Baleen-2 based on log and core analysis data. Two samples from each of the five zones were petrologically analysed. An additional two sideritic samples from 765.59m and 771.60m were examined specifically to provide information on the timing of siderite cementation. A sample list, analyses performed and core analyses are given in Table 1.

2. ANALYTICAL PROGRAM

2.1 Thin-Section Analysis

Thin-sections were cut in kerosene and impregnated with blue dyed epoxy resin to assist in porosity recognition. Mineral composition and visible porosity were determined by a count of 400 points in each thin-section, and mean grain size and sorting were estimated in thin-section with the aid of an eyepiece graticule. Photomicrographs were taken to illustrate features such as clay distribution, composition and porosity.

2.2 X-Ray Diffraction Analysis

Qualitative, bulk rock X-ray diffraction (XRD) analysis was carried out on all samples using a finely ground whole rock powder sample. Qualitative XRD analysis was carried out on the fine fraction of all samples in order to precisely determine clay mineralogy. The fine fraction was separated from each sample by disaggregation and settling in distilled water and was air dried on glass discs to produce oriented specimens for XRD analysis. Samples were analysed in air dried condition and also following treatment with ethylene glycol.

2.3 Scanning Electron Microscopy

Scanning electron microscopy (SEM) was carried out on all samples to provide information on the nature and distribution of clays, siderite cement and intergranular porosity. An energy dispersive spectrometer (EDS) attached to the SEM provided qualitative elemental data on some of the authigenic minerals.

TABLE 1. ANALYSES PERFORMED

Sample #	Depth (m)	Zone	PETROLOGICAL ANALYSES					CORE ANALYSES	
			MA	XRD bulk	XRD fine	SEM	PM	Porosity (amb) (%)	Permeability (air) (mD)
S5	750.41	1	x	x	x	x	x	33.1	131
S6	751.42	1	x	x	x	x	x	33.5	127
S9	754.41	2	x	x	x	x	x	36.7	467
S12	757.42	2	x	x	x	x	x	36.1	337
52	765.59	-	x	x	x	x	x	14.4	0.05
S21	768.79	3	x	x	x	x	x	31.3	33
S22	770.05	3	x	x	x	x	x	-	-
70	771.60	4	x	x	x	x	x	11.7	0.13
S24	771.81	4	x	x	x	x	x	32.8	82
S26	773.79	4	x	x	x	x	x	35.6	119
S28	775.82	5	x	x	x	x	x	36.1	396
S30	777.80	5	x	x	x	x	x	35.6	563

MA = modal analysis XRD = X-ray diffraction analysis SEM = scanning electron microscopy
PM = photomicroscopy

3. TEXTURE

Estimated grain size and sorting are given in Table 2. Samples are variably argillaceous, well sorted, very fine grained sandstones with a mean clastic grain size ranging from 0.07mm to 0.10mm. Glauconite is significantly coarser than coexisting clastic grains, having a mean grain size of 0.25mm and a maximum grain length of 0.90mm. Detrital clay forms a patchy and, in the more argillaceous samples (e.g., S5, S21, S22), widely dispersed matrix and is also locally concentrated into small, irregular patches, fine wisps and very thin laminae, the distribution of which has locally been influenced by bioturbation. Scattered sandy burrow fills are included in S5, S6, S9 and S28, and there are common sideritic clay-lined/filled burrows in 70. Despite the presence of the clay matrix, the sands are mainly grain supported, with clay being absent in some areas and with much matrix tending to be only thinly dispersed. Samples 52 and 70 are extensively cemented by siderite. Quartz grains are mainly angular to subrounded.

4. THIN-SECTION COMPOSITION

Thin-section composition is given in Table 2, QFR ratios are given in Table 3 and plotted in Figure 1, and annotated photomicrographs are presented in Appendix 2. The two strongly siderite-cemented sandstones (52, 70) are not included in the following description, and are instead described separately at the end of this section.

Samples are subarkoses with a mean QFR ratio of 87:12:1, and have a framework grain assemblage consisting mainly of quartz and minor feldspar, mica and glauconite.

Quartz content ranges from 34.3% to 46.8%, averages 42.8%, and exceeds 41.0% in all samples except S22, which has a relatively low quartz content on account of being highly argillaceous. Nearly all quartz is monocrystalline, which is partly a reflection of the very fine grain size.

Feldspar ranges from 5.3% to 7.2%, averages 6.1%, and is entirely K-feldspar (orthoclase, microcline) that is mainly fresh or slightly altered and locally corroded.

Mica varies from 1.8% to 5.8%, averages 3.2%, and consists of biotite and subordinate muscovite that are commonly partly altered to kaolinite and, in the case of biotite, to glauconite. Some mica grains are compactionally deformed and split along cleavage planes, and there are also mica grains in which contaminant halite has precipitated along cleavage planes.

Glauconite occurs in all samples, but only exceeds 1.8% in four sands (S9, S24, S26, S28), where it ranges from 6.8% to 10.3%. Glauconite occurs mainly as very fine to coarse sand-sized, mica-like grains that have formed by glauconitisation of biotite flakes, and there are also fine to medium sand-sized glauconite peloids. Glauconite grains are commonly compactionally deformed between adjacent rigid grains, particularly in the four glauconite-rich sands.

Other framework grains include very minor to rare chert, micaceous metamorphic rock fragments, argillaceous/glauconitic sedimentary rock fragments (intraclasts), fine organic fragments, phosphatic fossil fragments, and accessory heavy minerals (tourmaline, zircon, monazite, leucoxene). Rare monazite grains are rimmed by radiogenically-immobilised bitumen (Plate 10, Fig. 1).

The framework grain assemblage is indicative of a mainly granitic provenance.

Detrital clay content varies from 15.8% to 44.3%, and is highest in the zone 3 sands (S21, S22) and lowest in the zone 5 sands (S28, S30). Detrital clay forms patchy and widely dispersed matrix, and is also concentrated into small, irregular patches, fine wisps and very thin laminae. Sharp boundaries commonly separate highly argillaceous areas from clean areas (e.g., Plate 2, Fig. 1; Plate 11, Fig. 1).

Authigenic clay does not exceed 3.9%, averages 2.1%, and consists mainly of kaolinite that has formed by partial to complete alteration of micaceous grains and by recrystallisation of detrital clay.

Opaque content ranges up to 7.5% and varies according to clay content. Opaques are mainly fine organic fragments and finely dispersed/densely concentrated framboidal pyrite that is associated with detrital clay, organic fragments and altered biotite. Rare opaque leucoxene grains occur where detrital Fe-Ti oxides have altered.

Zone 4 sands (S24, S26) contain 3-4% carbonate, all of which is siderite that forms finely disseminated and localised concentrations of 10-20 μ m rhombic/granular crystals that replace detrital clay matrix. Sample S9 contains 0.3% finely-crystalline siderite, and the other samples lack carbonate.

Visible porosity ranges from 1.5% to 18.7% and varies mainly according to total content of clay, glauconite and, of much lesser importance, mica, opaques and siderite (see Fig. 5). Lowest visible porosity occurs in the highly argillaceous zone 3 sands

TABLE 2. THIN-SECTION ANALYSES

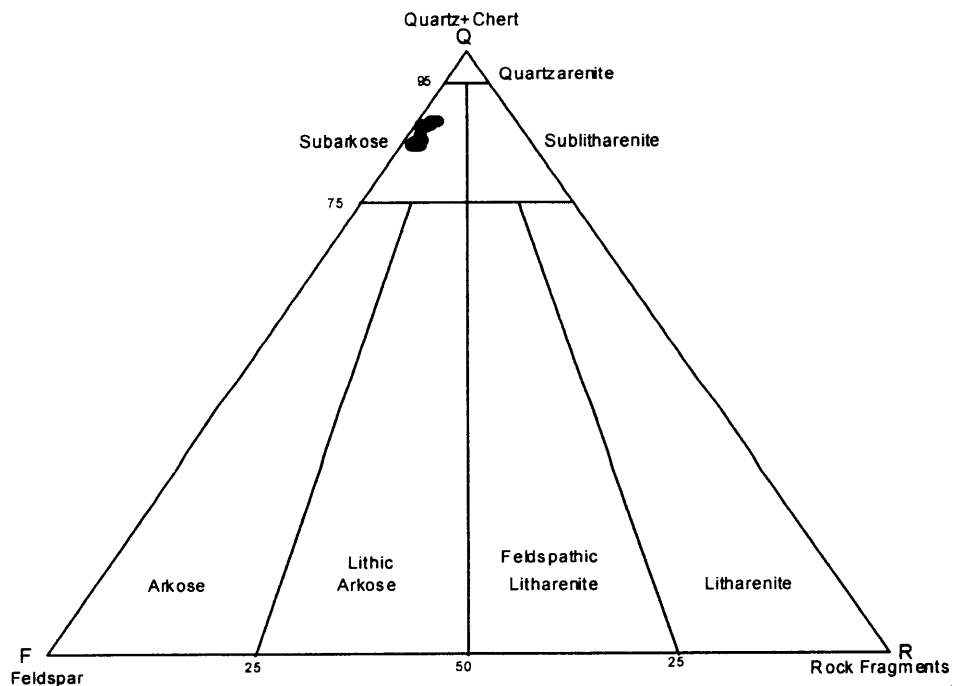
Sample #	Depth (m)	COMPOSITION														TEXTURE		
		Qzm	Qzp	Cht	Kfe	Pla	IRF	MRF	SRF	Mca	HM	Opq	Sid	Glau	AC	DC	VP	MGS
S5	750.41	42.7	0.3	-	6.0	-	0.3	-	2.0	-	7.5	-	0.7	1.5	34.2	4.8	0.09	well
S6	751.42	41.0	0.3	-	5.3	-	-	3.3	0.3	0.3	5.5	-	1.5	33.5	7.8	0.10	well	
S9	754.41	45.0	-	-	6.8	-	0.7	2.3	0.3	0.3	2.5	0.3	9.5	19.5	11.6	0.09	well	
S12	757.42	46.8	-	-	5.8	-	0.5	2.3	-	-	3.1	-	1.0	30.9	8.3	0.10	well	
S2	765.59	28.0	-	0.3	3.1	-	0.3	-	0.3	0.3	1.1	50.5	11.3	3.7	0.8	0.10	well	
S21	768.79	41.1	0.3	-	6.5	-	-	0.3	3.0	0.5	7.3	-	1.0	36.0	2.0	0.07	well	
S22	770.05	34.3	-	-	5.5	-	0.5	-	3.3	0.3	8.0	-	0.3	44.3	1.5	0.07	well	
70	771.60	17.8	-	-	1.3	-	0.5	-	1.3	-	1.3	67.3	5.0	3.8	1.2	0.07	well	
S24	771.81	41.5	-	-	6.8	-	0.3	-	5.8	-	4.0	4.0	6.8	25.5	2.8	0.08	well	
S26	773.79	42.6	-	0.3	5.8	-	0.3	-	3.8	0.3	3.8	3.3	10.3	19.5	7.5	0.08	well	
S28	775.82	46.5	0.3	0.3	5.5	-	0.5	-	1.8	0.3	2.0	-	8.3	16.7	15.5	0.10	well	
S30	777.80	46.3	-	-	7.2	-	0.8	-	3.0	0.5	2.0	-	1.8	15.8	18.7	0.10	well	

Qzm = monocrystalline quartz Qzp = polycrystalline quartz Cht = chert Kfe = K-feldspar Pla = plagioclase IRF = igneous rock fragments MRF = metamorphic rock fragments SRF = sedimentary rock fragments Mca = mica HM = heavy minerals Opq = opaques Sid = siderite Glau = glauconite AC = authigenic clay DC = detrital clay VP = visible porosity MGS = estimated mean grain size (mm)

TABLE 3. QFR COMPOSITIONS

Sample #	Depth (m)	Q Quartz + chert	F Feldspar	R Rock fragments
S5	750.41	87.2	12.2	0.6
S6	751.42	88.6	11.4	0.0
S9	754.41	86.2	12.5	1.3
S12	757.42	88.8	10.3	0.9
52	765.59	89.3	9.8	0.9
S21	768.79	85.9	13.5	0.6
S22	770.05	85.2	13.6	1.2
70	771.60	89.4	9.0	1.5
S24	771.81	85.4	14.0	0.6
S26	773.79	88.4	11.0	0.6
S28	775.82	88.7	10.4	0.9
S30	777.80	85.2	13.3	1.5

FIGURE 1. QFR COMPOSITIONS



(S21, S22), whereas highest visible porosity occurs in the zone 5 sands (S28, S30), which contain the least detrital clay. All porosity is primary and intergranular.

The two highly sideritic samples (52, 70) are well sorted, very fine grained subarkoses ($Q_{90}F_9R_1$) with the same framework grain composition as the other sands. Like S9, S24, S26 and S28, they have an elevated (11.3%, 5.0%) glauconite content. Most of the glauconite has formed by alteration of fine to coarse sand-sized biotite flakes and retains the morphology of precursor biotite. Peloidal glauconite is rare. Glauconite grains that are tightly encapsulated by siderite cement are uncompacted. Opaques are mainly scattered fine pyrite crystals/framboids. Siderite forms a pervasive cement made up of intergrown, 0.02-0.20mm, anhedral/subhedral rhombic crystals that fill intergranular pores and replace detrital clay and glauconitised biotite. Sideritised detrital clay forms scattered patches in 52 and dispersed matrix in 70. Sideritised clay-filled and -lined burrows are common in 70. Ignoring obvious artificial porosity resulting from partial to complete plucking of glauconite grains during thin-sectioning, the two samples contain little (<1.3%) visible porosity mainly due to extensive pore filling by siderite and associated detrital clay.

5. X-RAY DIFFRACTION ANALYSES

Results of bulk rock and fine fraction XRD analyses are given in Tables 4 and 5, respectively. Bulk rock XRD analyses confirm that the sands have a consistent mineralogy, with all samples except 52 and 70 containing abundant quartz, major illite and kaolinite, minor K-feldspar, and minor to trace pyrite and contaminant halite. In 52 and 70, the amount of these components is reduced by the presence of abundant siderite. Bulk rock XRD analyses also indicate trace to minor illite/smectite in S9, S24, S26, S28, 52 and 70 and confirm that minor siderite is present in S9, S24 and S26.

Fine fraction XRD analyses show that the clay mineral suite is consistently dominated by illite and kaolinite and also includes minor or major illite/smectite in S9, S24, S26, S28, 52 and 70 and trace chlorite in S12, S21, S26, S28, 52 and 70. The illite/smectite is a low expandability variety containing between 80% and 90% illite interlayers. Highly smectitic clays are absent.

Detected illite would be accounted for by fine mica and detrital illitic clay, whereas detected kaolinite would be both detrital and authigenic. With illite/smectite only being detected in samples with an elevated glauconite content, the illite/smectite is most certainly accounted for by glauconite. Evidently, glauconite is insufficiently abundant in the other samples for detection by XRD.

TABLE 4. BULK XRD ANALYSES

Sample #	Depth (m)	Qtz	Kfe	Pla	K	I/M	I/S	Sm	Chl	Py	Sid	Ha
S5	750.41	A	m	-	M	M	-	-	-	m	-	m
S6	751.42	A	m	-	M	M	-	-	-	T	-	m
S9	754.41	A	m	-	M	M	m	-	-	T	T	m
S12	757.42	A	m	-	M	M	-	-	-	T	-	T
S2	765.59	A	m	-	m	m	m	-	-	m	A	-
S21	768.79	A	m	-	M	M	-	-	-	m	-	m
S22	770.05	A	m	-	M	M	-	-	-	m	-	m
70	771.60	M	m	-	m	M	T	-	-	T	A	-
S24	771.81	A	m	-	M	M	m	-	-	m	m	T
S26	773.79	A	m	-	M	M	m	-	-	m	m	T
S28	775.82	A	m	-	M	M	m	-	-	T	-	T
S30	777.80	A	m	-	M	M	-	-	-	T	-	T

Qtz = quartz Kfe = K-feldspar Pla = plagioclase K = kaolinite I/M = illite/mica I/S = illitic illite/smectite Sm = smectite Chl = chlorite Py = pyrite Sid = siderite Ha = halite
 Nominal scale: A = abundant (>40%), M = major (>10%), m = minor (1-10%), T = trace

TABLE 5. CLAY MINERALOGY

Sample #	Depth (m)	K	I	I/S	Sm	Chl
S5	750.41	A	A	-	-	-
S6	751.42	A	A	-	-	-
S9	754.41	A	A	m	-	-
S12	757.42	M	A	-	-	T
S2	765.59	M	A	M	-	T
S21	768.79	M	A	-	-	T
S22	770.05	M	A	-	-	-
70	771.60	M	A	m	-	T
S24	771.81	A	A	m	-	-
S26	773.79	A	A	m	-	T
S28	775.82	A	A	m	-	T
S30	777.80	A	A	-	-	-

K = kaolinite I = illite/mica I/S = illitic illite/smectite Sm = smectite Chl = chlorite
 A = (nominally >40%) M = major (>10%) m = minor (1-10%) T = trace

6. DIAGENESIS

The main diagenetic process to have affected the sands is glauconite formation, although there is the possibility that the glauconite is allochthonous (i.e., has been reworked) rather than autochthonous. Most glauconite has formed by alteration of biotite, and retains the morphology of precursor biotite grains (Plate 2, Fig. 1; Plate 6, Fig. 1; Plate 8, Fig. 1). Incompletely glauconitised biotite grains are common. Glauconite also occurs as microcrystalline peloids (Plate 2, Fig. 1; Plate 8, Fig. 1). Glauconite is most abundant in S9, S24, S26, S28, 52 and 70, which contain between 5.0% and 11.3% glauconite. In the other samples, glauconite does not exceed 1.8%. XRD analyses indicate that the glauconite is a low expandability illite/smectite containing 80-90% illite interlayers, which implies that the glauconite is an evolved variety containing around 7.5-8.0% K_2O . If the glauconite is autochthonous, its presence indicates that the sands probably accumulated in a normal marine shelf environment during a period of slow sediment accumulation.

The other product of mica alteration is kaolinite, which forms mica-like grains and scattered microcrystalline patches where biotite and muscovite have altered (Plate 1, Fig. 4). Authigenic kaolinite has also formed by recrystallisation of detrital clay matrix (Plate 2, Fig. 4; Plate 9, Fig. 4). In all sands, authigenic kaolinite is only a minor component of the total clay fraction.

Glauconite grains are commonly compactionally deformed between adjacent rigid grains, particularly in the four, non siderite-cemented, relatively glauconitic sands (S9, S24, S26, S28) (Plate 10, Fig. 1). Small patches of glauconitic pseudomatrix occur where groups of glauconite grains have compactionally deformed and dispersed. Mica grains and patches of authigenic kaolinite are also commonly compactionally deformed, and many micaceous grains (including glauconitised biotite) are split along cleavage planes (Plate 5, Figs. 3 & 4), which with at least some grains appears to be the result of halite precipitation between cleavage planes during core desiccation. Clean areas dominated by clastic grains are poorly compacted, with all clastic grains in these areas having only point grain contacts (e.g., Plate 3, Fig. 3; Plate 11, Fig. 3).

Samples 52 and 70, which are from sideritic zones visible in core, are extensively cemented by siderite that forms a mosaic of intergrown, anhedral and subhedral rhombic crystals that fill intergranular pores and replace detrital clay and, locally, glauconite. Most detrital clay in the two samples is replaced by siderite, although XRD indicates that significant amounts of detrital clay, which could not be distinguished from the siderite in thin-section, are associated with the siderite. EDS analyses reveal that in both samples, the siderite is an impure variety containing minor calcium and magnesium (Appendix 2), which is consistent with siderite precipitation from a marine porewater. Siderite encloses pyrite (Plate 8, Fig. 4) and uncompact glauconite grains (Plate 8, Fig. 1), indicating that the siderite formed after glauconite and pyrite and before compaction. Given that the siderite formed at shallow burial below the sulphate reduction zone (where pyrite would have formed), the siderite is probably the result of early methanogenesis or oxidation of early-formed, biogenic methane.

Other diagenetic processes include minor precipitation of fine framboidal pyrite within detrital clay, organic fragments and altered biotite (including glauconite), replacement of detrital clay by small amounts (<4.1%) of finely-crystalline siderite (S9, S24, S26) (Plate 9, Fig. 1), and incipient K-feldspar dissolution.

The highly friable character of the non siderite-cemented sands reflects the fact that these sands are generally poorly compacted and virtually uncemented.

7. RESERVOIR QUALITY

7.1 General

The following discussion excludes 52 and 70, which have anomalously low porosity and permeability (Table 1) on account of being extensively cemented by siderite.

Reservoir quality is quite variable, with permeability values for the sandstone samples ranging from 33mD to 563mD, despite measured porosity being consistently higher than 31% (Table 1). Figure 2, which includes core analyses for other samples from within the sampled interval, shows that there is a strong positive correlation between measured porosity and permeability and that the sampled section is highly porous, with porosity for all samples except one being between 30.2% and 38.3%. With permeability in the sampled section varying considerably (27mD-735mD) (ignoring the strongly siderite-cemented zones), despite consistently high porosity, porosity type (macroporosity versus microporosity) as well as porosity volume clearly exerts a strong control on reservoir quality. The one low porosity sample plotted in Figure 2, which was not petrologically analysed, is probably partly cemented by siderite.

Total clay content is a major control on reservoir quality, with visible intergranular macroporosity being most abundant in samples containing the least clay. However, a cross-plot of clay against permeability only produces a moderate ($R^2 = 0.502$) negative correlation, indicating that clay content is not the only controlling influence on reservoir quality.

The correlation is improved significantly ($R^2 = 0.849$) if glauconite, mica, opaques and siderite are included with clay (Fig. 3). This is to be expected given that opaques (mainly pyrite and fine organic fragments) and siderite, which are associated with detrital clay, occupy intergranular spaces and that glauconite and mica grains were susceptible to compactional deformation, particularly in S9, S24, S26, S28, where these grains were sufficiently common to take up much of the overburden load during burial.

Figure 4 shows that there is a strong positive correlation ($R^2 = 0.778$) between visible porosity and permeability. This correlation is predictable given that visible porosity (i.e. macroporosity) is conducive to permeability. Much of the scatter in Figure 4 would reflect the patchy distribution of the macroporosity.

Given that there is a negative correlation between clay, glauconite, mica, opaques and siderite content and permeability (Fig. 3) and a positive correlation between visible porosity and permeability (Fig. 4), there should be a negative correlation between

FIGURE 2. POROSITY/PERMEABILITY CROSS-PLOT

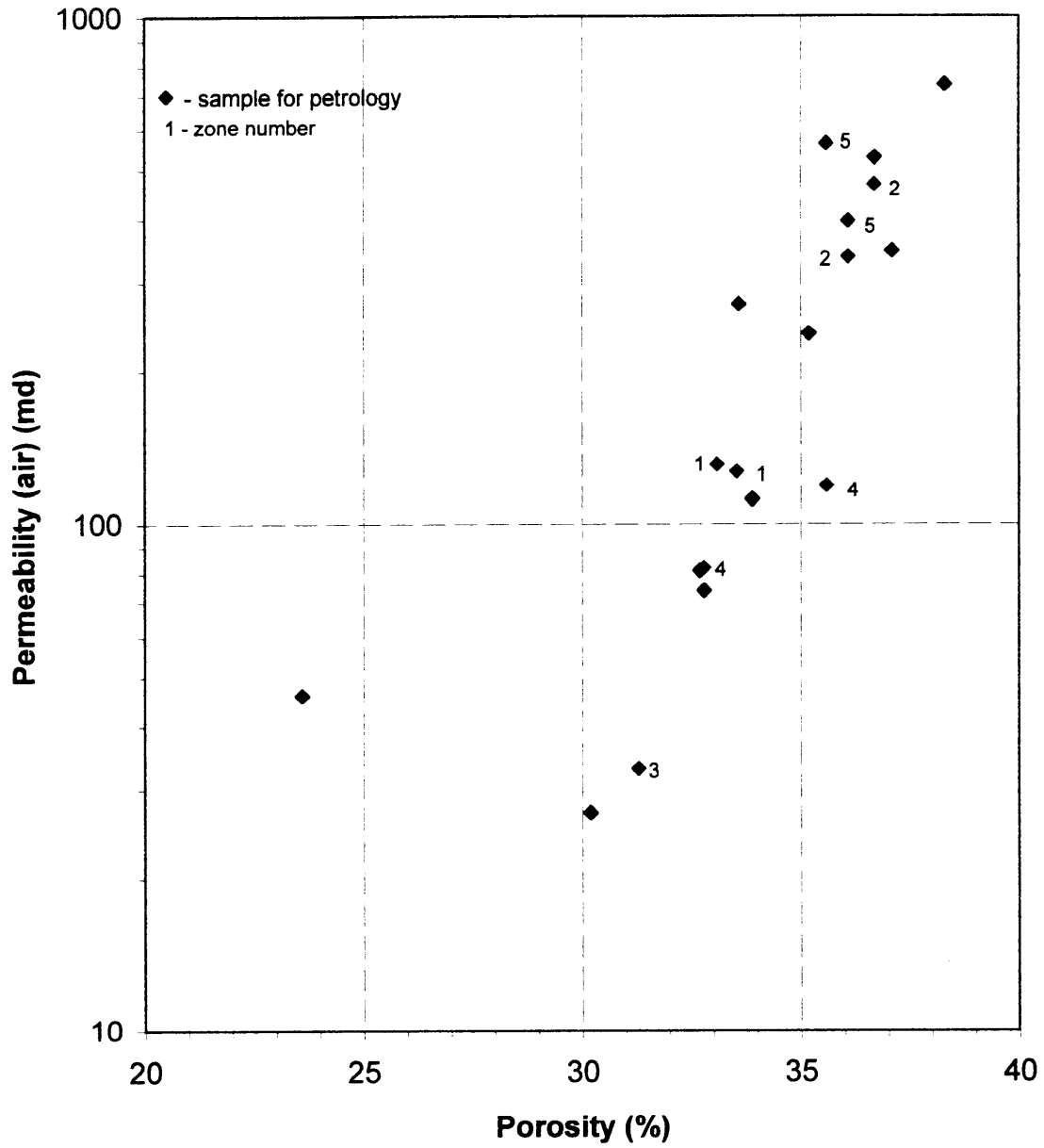
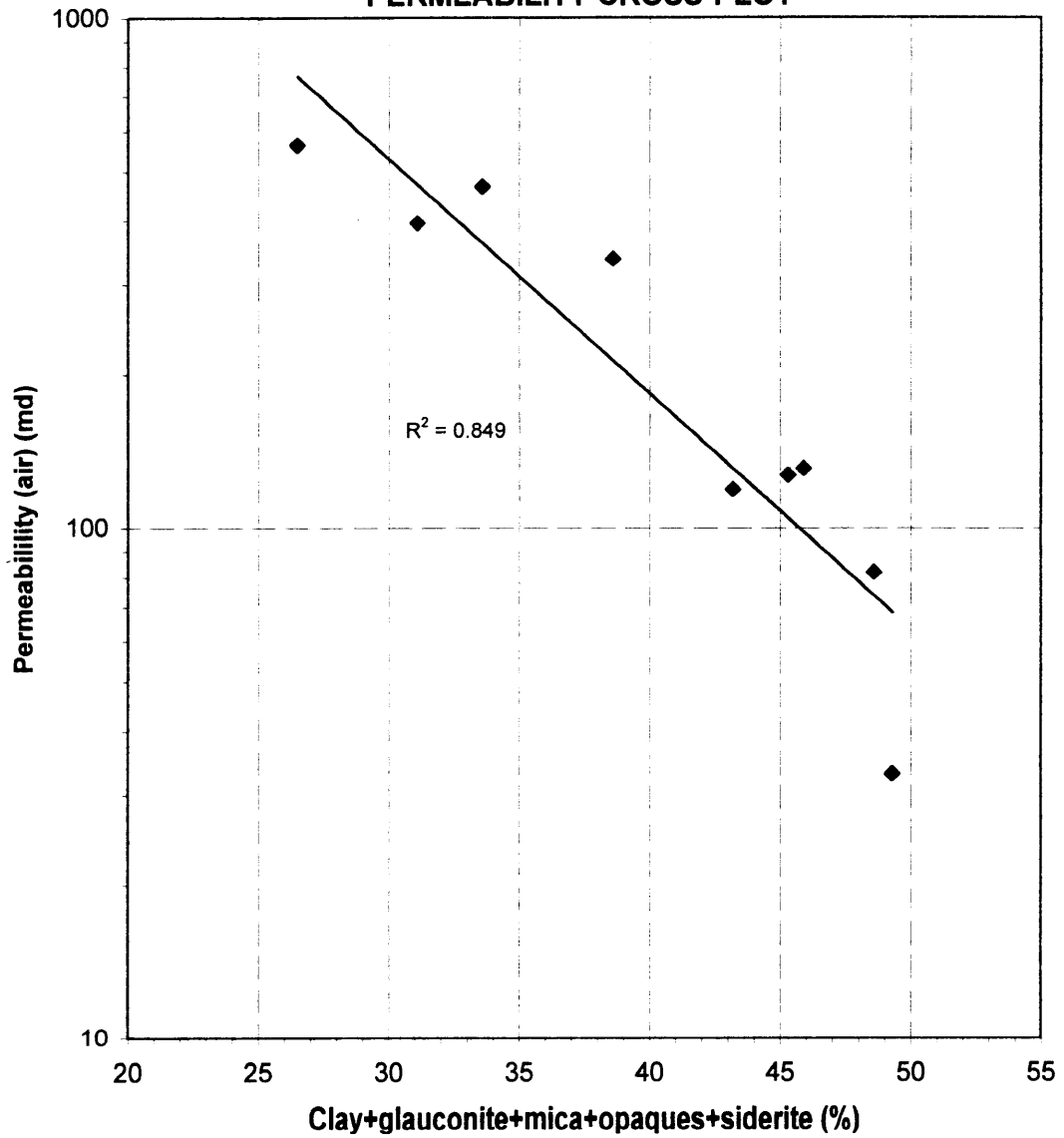


FIGURE 3.
**CLAY+GLAUCONITE+MICA+OPAQUES+SIDERITE/
 PERMEABILITY CROSS-PLOT**



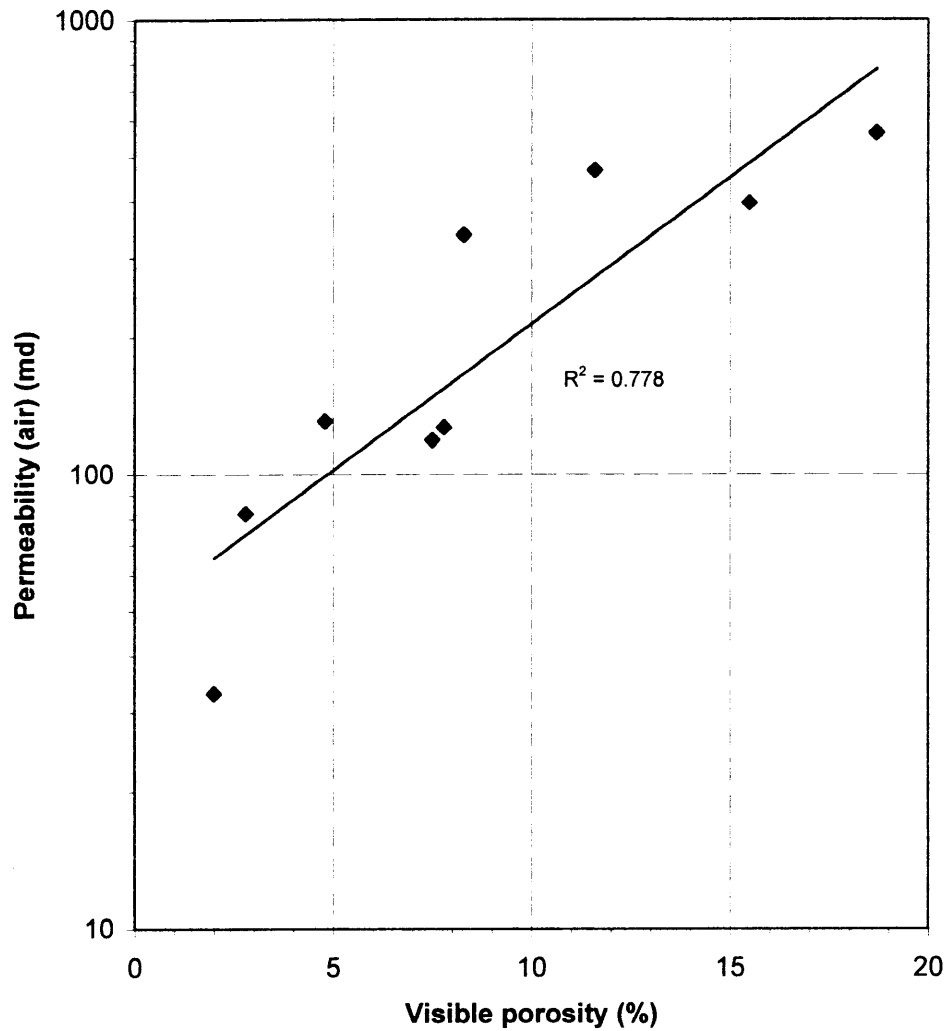
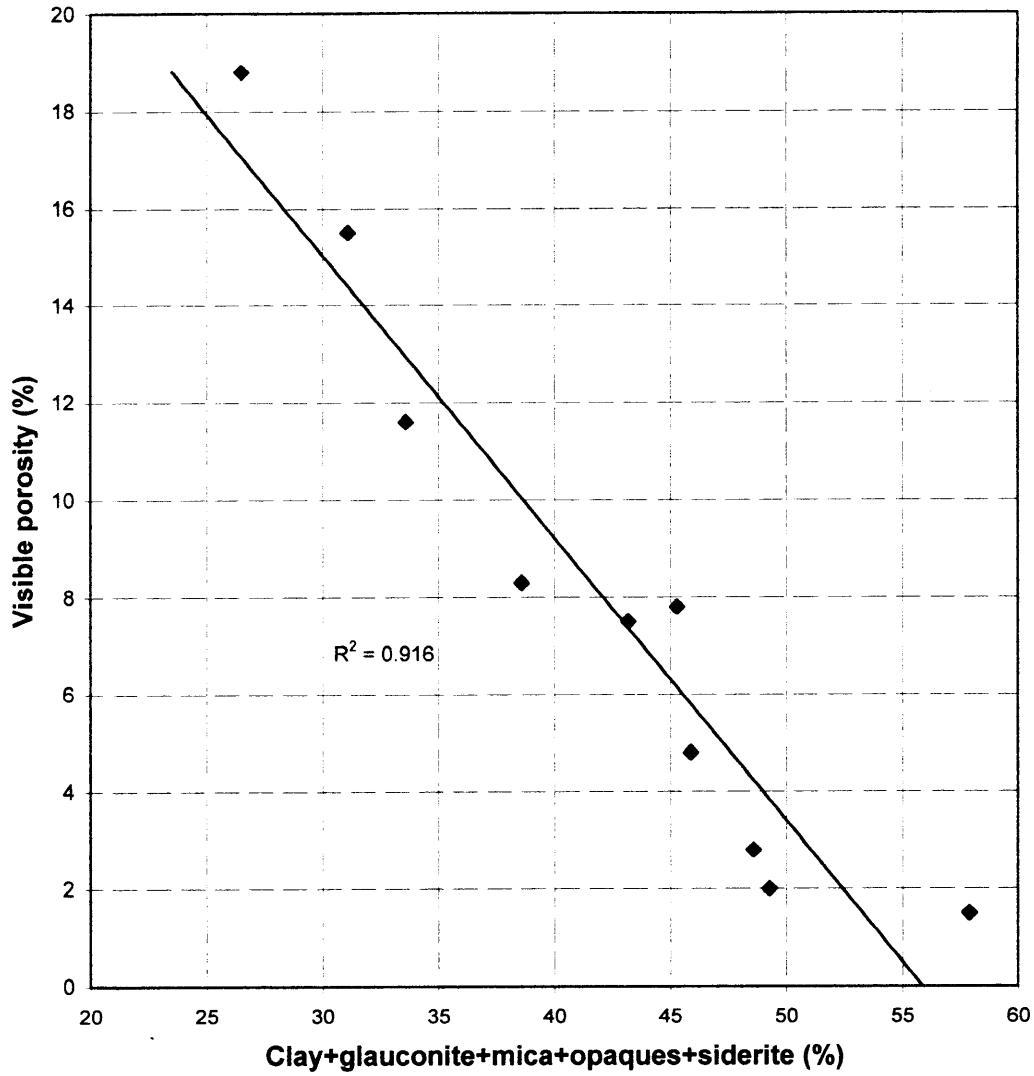
**FIGURE 4. VISIBLE POROSITY/PERMEABILITY
CROSS-PLOT**

FIGURE 5.
**CLAY+GLAUCONITE+MICA+OPAQUES+SIDERITE/
 VISIBLE POROSITY CROSS-PLOT**



clay, glauconite, mica, opaques and siderite content and visible porosity. Figure 5 confirms that there is such a correlation, showing that, by controlling visible porosity, clay + glauconite + mica + opaques + siderite controls permeability.

Grain size and sorting do not vary significantly between samples, and would therefore have little bearing on permeability variation within the sampled section.

The wide difference (16.8-30.0%) between visible thin-section macroporosity and helium injection porosity indicates that the sands are highly microporous. Given the abundance of detrital clay, the vast majority of microporosity would be associated with detrital clay. SEM analysis confirmed that abundant microporosity occurs within detrital clay, which is typically loosely packed within intergranular spaces (Plate 2, Fig. 4; Plate 6, Fig. 4). Microporosity is also associated with glauconite, authigenic kaolinite and etched feldspar.

Voids recognised as pore throats under the SEM (Plate 12, Fig. 1) are between 10µm and 20µm in length in areas where macropores and pore throats are not choked by detrital clay matrix.

In summary, permeability variations between each of the five zones mainly reflect differences in the amount of detrital clay, glauconite and, to a much lesser extent, mica, opaques and siderite, and are thus for the most part directly controlled by original sediment composition rather than by grain size/sorting variations or diagenesis.

7.2 Individual Samples

Zone 1 samples (S5, S6) contain only modest (4.8%, 7.8%) visible porosity due to the presence of widespread detrital clay matrix and associated opaques (pyrite and organics). Most macroporosity is confined to small, localised areas that contain little or no clay, where abundant primary intergranular porosity is preserved between loosely packed framework grains. Some of these clean areas are sandy burrow fills. With intervening areas being highly argillaceous, intergranular macropores have limited interconnection.

Sample S12 from near the base of **zone 2** is similar to the zone 1 sands in that it is highly argillaceous (>30% detrital clay) and contains only modest (8.3%) macroporosity. The other zone 2 sand (S9) is more like S26 (from zone 4; see below) in that it has an elevated (11.8%) content of glauconite + mica, contains less than 20% detrital clay, and is largely composed of loosely packed grains between which there has been only minor pore filling by compacted glauconite/mica. Some of the clean, macroporous areas in S9 are the result of bioturbation. The higher permeability of S9 compared with the zone 1 sands and the other zone 2 sand reflects its higher (11.6%) macroporosity content.

Zone 3 sands (S21, S22) contain the most detrital clay and are consequently the least macroporous of all the samples, with each of the two samples containing no more than 2.0% visible porosity, most of which is confined to small, localised areas that are largely free of clay. With surrounding areas being highly argillaceous and microporous, intergranular pores are poorly interconnected, as reflected by the low (33mD) permeability measured for S21. Permeability was not able to be measured for S22, but it is likely that this sample would be less permeable than S21 given its very high clay content.

Like the zone 3 sands, S24 from the upper part of **zone 4** contains only minor (2.8%) visible porosity, with most intergranular areas in the sand being filled by dispersed detrital clay matrix and associated finely-crystalline siderite. In addition, the sand has an elevated (12.6%) content of glauconite + mica, which, in the cleaner areas, have reduced porosity by undergoing compactional deformation, locally to form pseudomatrix. Macroporosity in S24 is mainly confined to localised areas and zones that are surrounded by microporous, argillaceous/sideritic sandstone, and is thus not conducive to high permeability.

The other zone 4 sample (S26) is similar to S24 in that it contains minor finely-crystalline siderite replacement and has an elevated (14.1%) content of glauconitic + mica, but differs by being less argillaceous and consequently more macroporous, containing 7.5% visible porosity. Much of the sand consists of loosely packed grains between which there has been only minor pore filling by patchy detrital clay and compacted glauconite/mica. Elsewhere, the sand is microporous due to extensive pore filling by dispersed detrital clay matrix and associated patchy siderite.

Zone 5 sands (S28, S30) are distinguished by their relatively low (15-17%) content of detrital clay and correspondingly high (15-19%) content of visible porosity. With the detrital clay being concentrated into patches rather than forming a dispersed matrix, both sands are largely clean and highly macroporous, despite additional porosity reduction having occurred in the clean parts of S28 by glauconite compaction. The sands have good permeability (396mD, 563mD), reflecting their relatively low clay and high macroporosity content.

Specific petrological characteristics that account for differences in reservoir quality between the five zones are summarised in Table 6.

TABLE 6. RESERVOIR QUALITY SUMMARY

Zone	Sample	Comments
1	S5 (131mD) S6 (127mD)	Only modest permeability due to extensive pore filling by detrital clay matrix and associated opaques. Macroporosity restricted to localised clean areas, including sandy burrow fills.
2	S9 (467mD) S12 (337mD)	Largely argillaceous sands, particularly S12, and there has been further porosity loss in S9 by glauconite/mica compaction. However, clean, macroporous areas are more common than in zone 1, and permeability is consequently much higher.
3	S21 (33mD) S22 -	Most argillaceous and consequently least macroporous and permeable of the five zones. Intergranular spaces mainly filled by widespread detrital clay matrix and associated opaques. Only very minor macroporosity, hence low permeability.
4	S24 (82mD) S26 (119mD)	Extensive pore filling by detrital clay and associated minor opaques/finely-crystalline siderite, and there has also been porosity reduction by glauconite/mica compaction. Macroporosity restricted to localised areas (which are more common in S26 than in S24), hence only low/moderate permeability.
5	S28 (396mD) S30 (563mD)	Only localised pore filling by patchy detrital clay and, in S28, compacted glauconite/mica. Throughout much of the sands, abundant primary intergranular porosity is preserved between loosely packed framework grains, hence high permeability.

8. SUMMARY AND CONCLUSIONS

- Twelve samples from between 750.41m and 777.80m in Baleen-2 are variably argillaceous, well sorted, very fine grained subarkoses in which framework grains include minor K-feldspar, mica and glauconite. The sample suite includes two highly sideritic samples (52, 70), results for which are summarised separately at the end of this section.
- The sands are derived mainly from granitic rocks.
- Samples contain between 15.8% and 44.3% detrital clay, which forms dispersed and patchy matrix and is also locally concentrated into small, irregular patches, fine wisps and very thin laminae, the distribution of which has locally been influenced by bioturbation. Detrital clay minerals are almost entirely illite and kaolinite.
- Non-glauconitic authigenic clay is less than 4% and consists of kaolinite that has formed by alteration of micaceous grains and by recrystallisation of detrital clay.
- Glauconite ranges from 6.8% to 10.3% in four samples (S9, S24, S26, S28), and does not exceed 1.8% in the other six samples. Most glauconite occurs as mica-like grains that are partly to completely glauconitised biotite flakes, and there is also peloidal glauconite. The glauconite is a low expandability illite/smectite containing 80-90% illite interlayers. If the glauconite is autochthonous, its presence may indicate that the sands accumulated in a normal marine shelf environment during a period of slow sediment accumulation.
- Other diagenetic effects besides glauconite and kaolinite formation include minor pyrite and siderite precipitation, localised compaction of glauconite and micaceous grains, and incipient feldspar dissolution. The sands are generally poorly compacted (particularly clean areas that are dominated by clastic grains) and virtually uncemented, and are consequently highly friable.
- Visible macroporosity ranges from 1.5% to 18.7% and occurs mainly in localised areas that contain little or no detrital clay. All macroporosity is primary and intergranular.
- Intergranular macroporosity is reduced by the presence of clay and, of much lesser importance, associated opaques (pyrite and fine organics) and siderite, and there has also been some intergranular porosity loss in the glauconitic sands by compactional deformation of glauconite and mica. Accordingly, there is a strong negative correlation between visible macroporosity and total content of clay, glauconite, mica, opaques and siderite.
- Reservoir quality is mainly dependent on detrital clay and glauconite content, implying that most permeability variation is attributable to original compositional differences.

- Samples 52 and 70, taken from two tight sideritic zones, are extensively cemented by finely/medium-crystalline siderite that fills intergranular pores and replaces detrital clay and glauconite. The siderite is enriched in calcium and magnesium, and encloses pyrite and uncompacted glauconite grains, suggesting that the siderite precipitated at shallow burial, probably in a methanogenic or methane oxidation zone, in the presence of marine porewater.

APPENDIX 1
X-RAY DIFFRACTOGRAMS

Key to abbreviations:

C - chlorite

H – halite (contaminant)

I - illite/mica

I/S - illitic illite/smectite

K - kaolinite

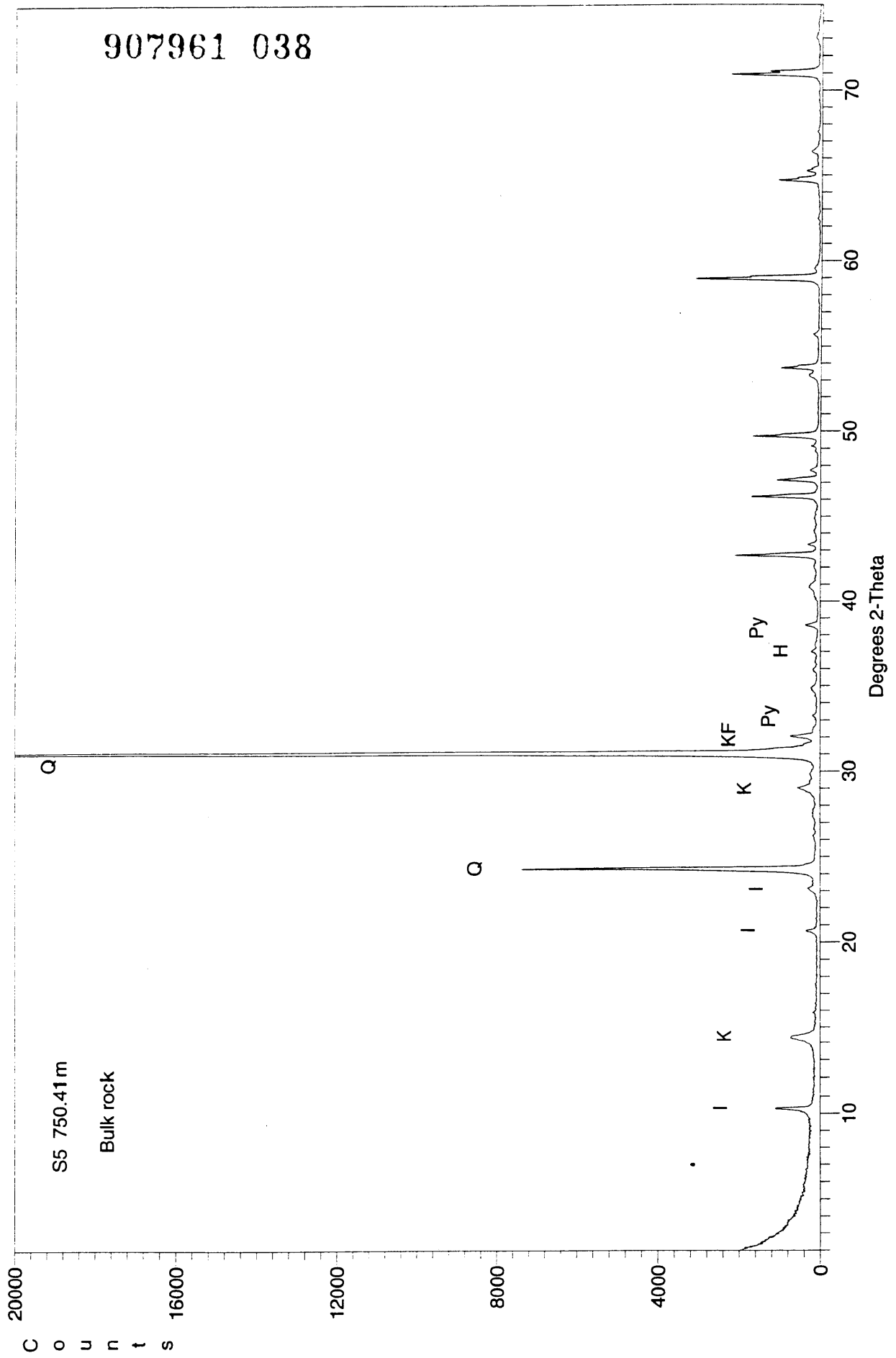
KF - K-feldspar

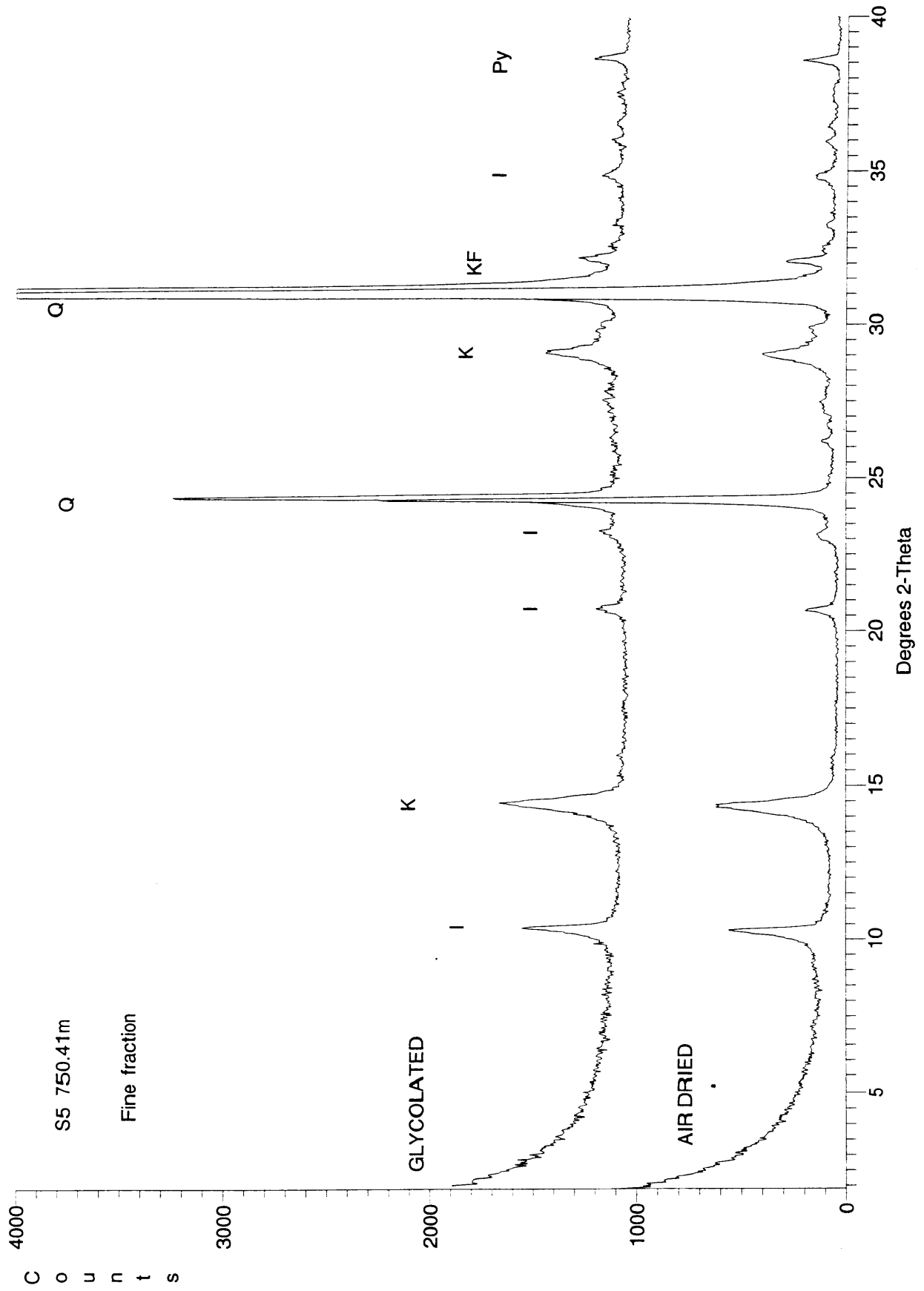
Py - pyrite

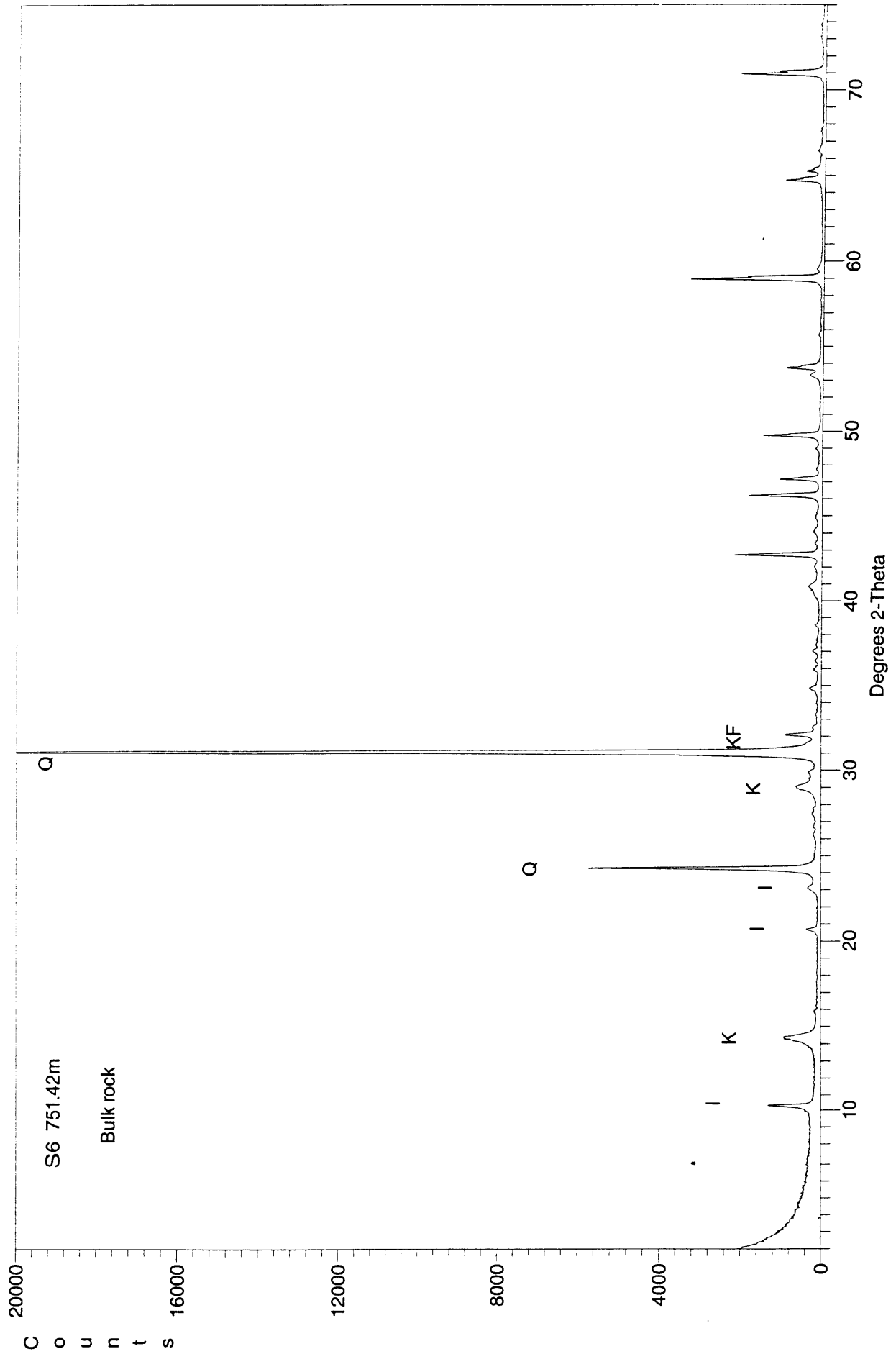
Q - quartz

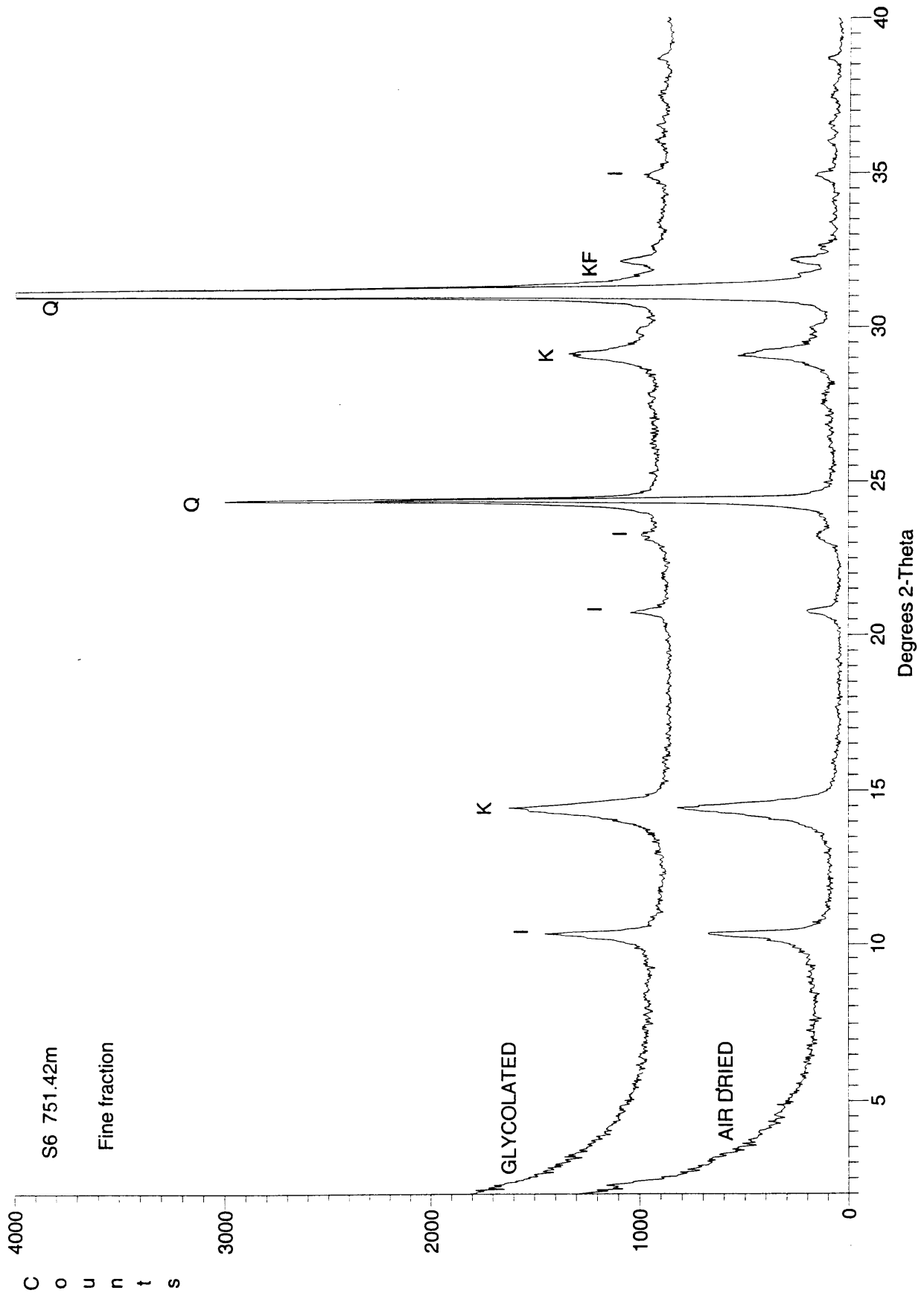
S – siderite

907961 038



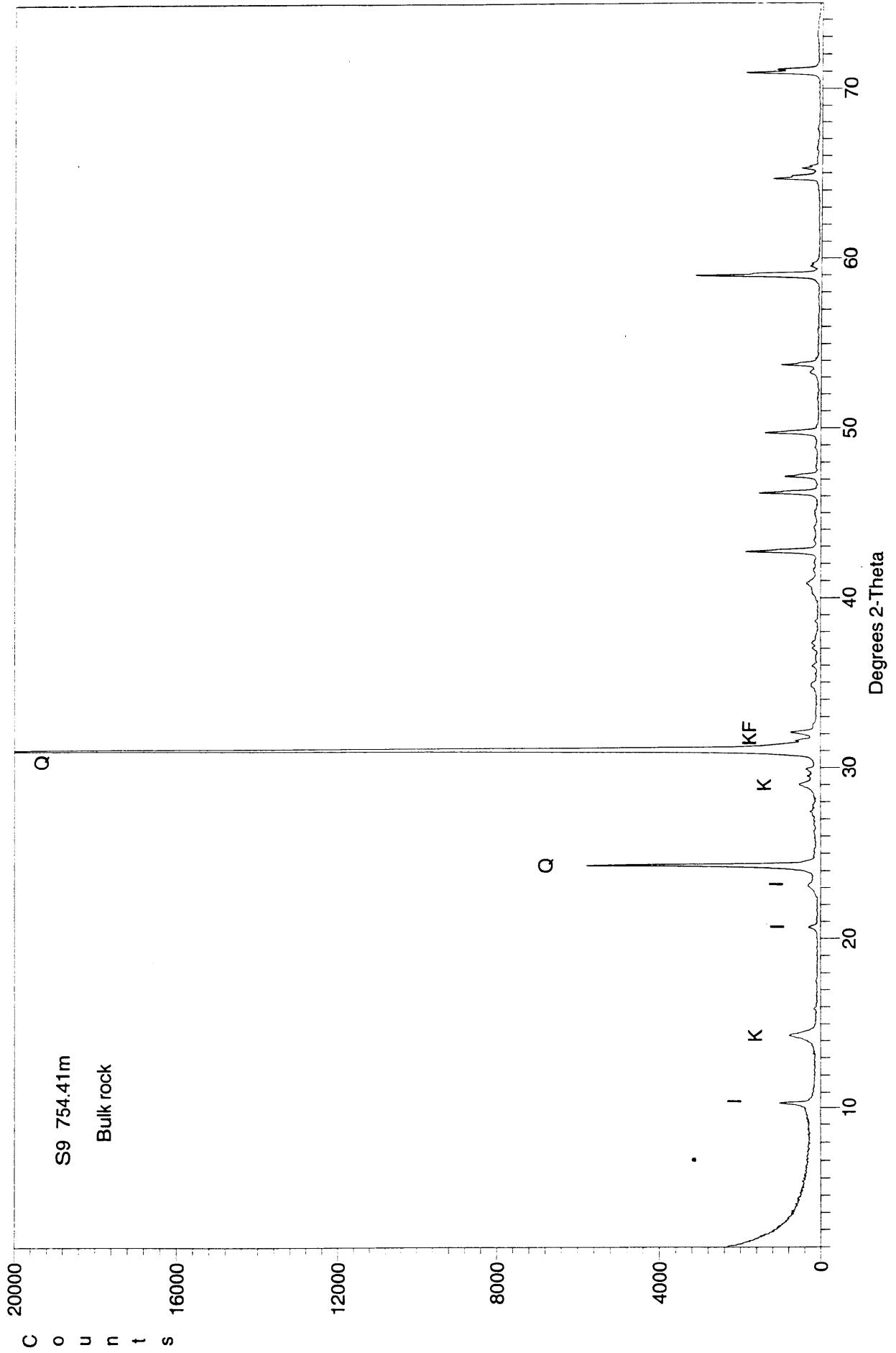


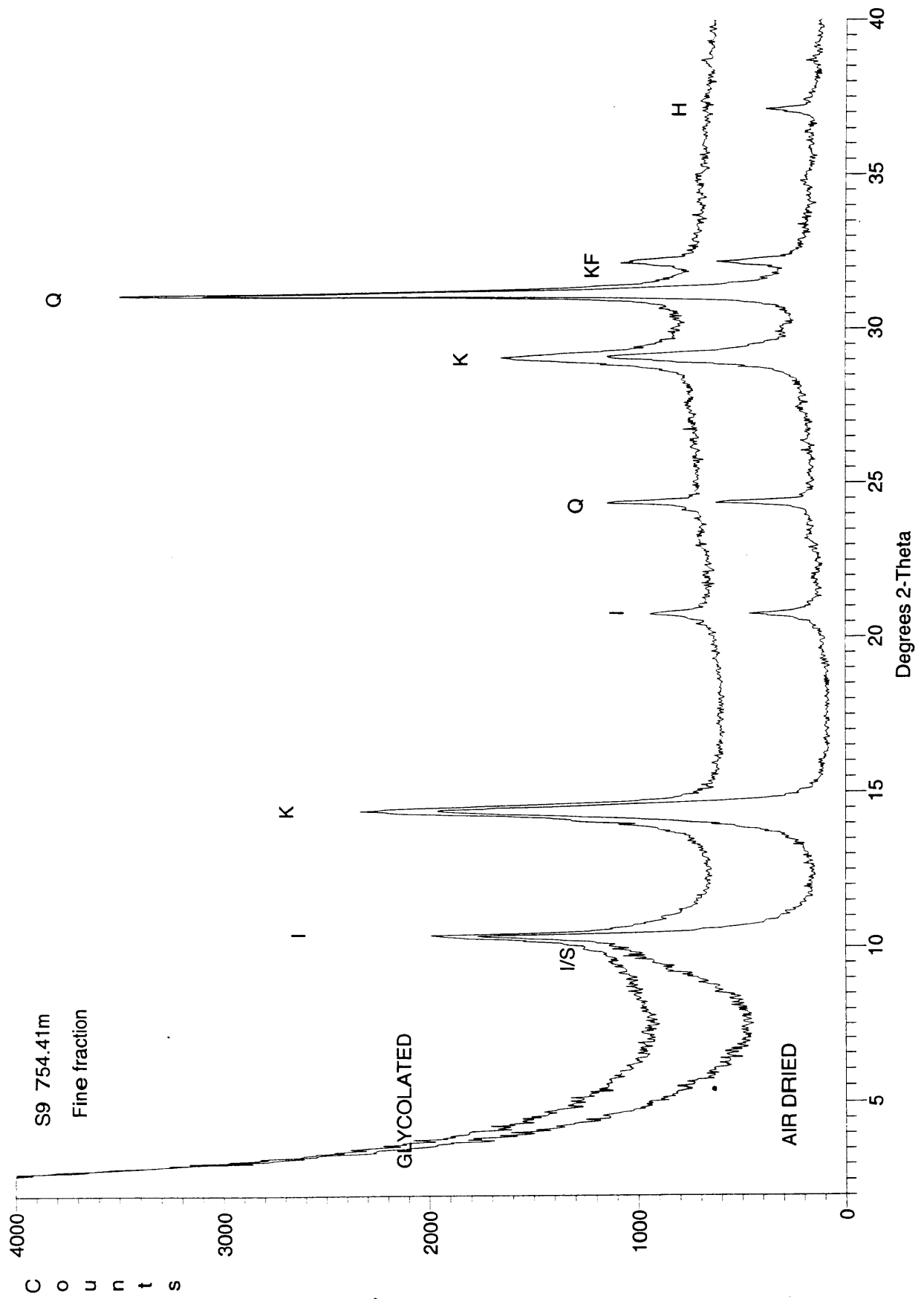


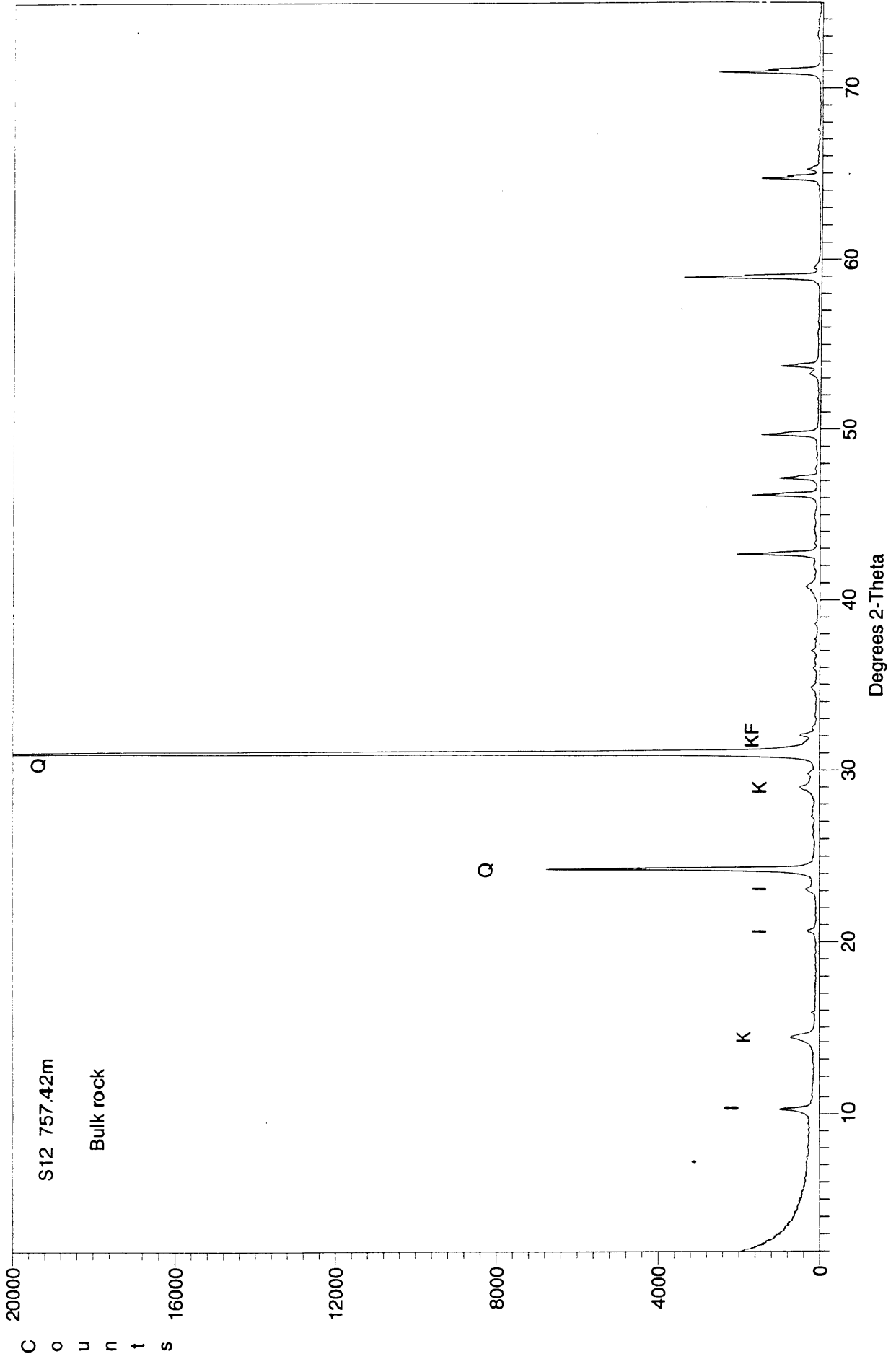


S6 751.42m
Fine fraction

C
o
u
n
t
s





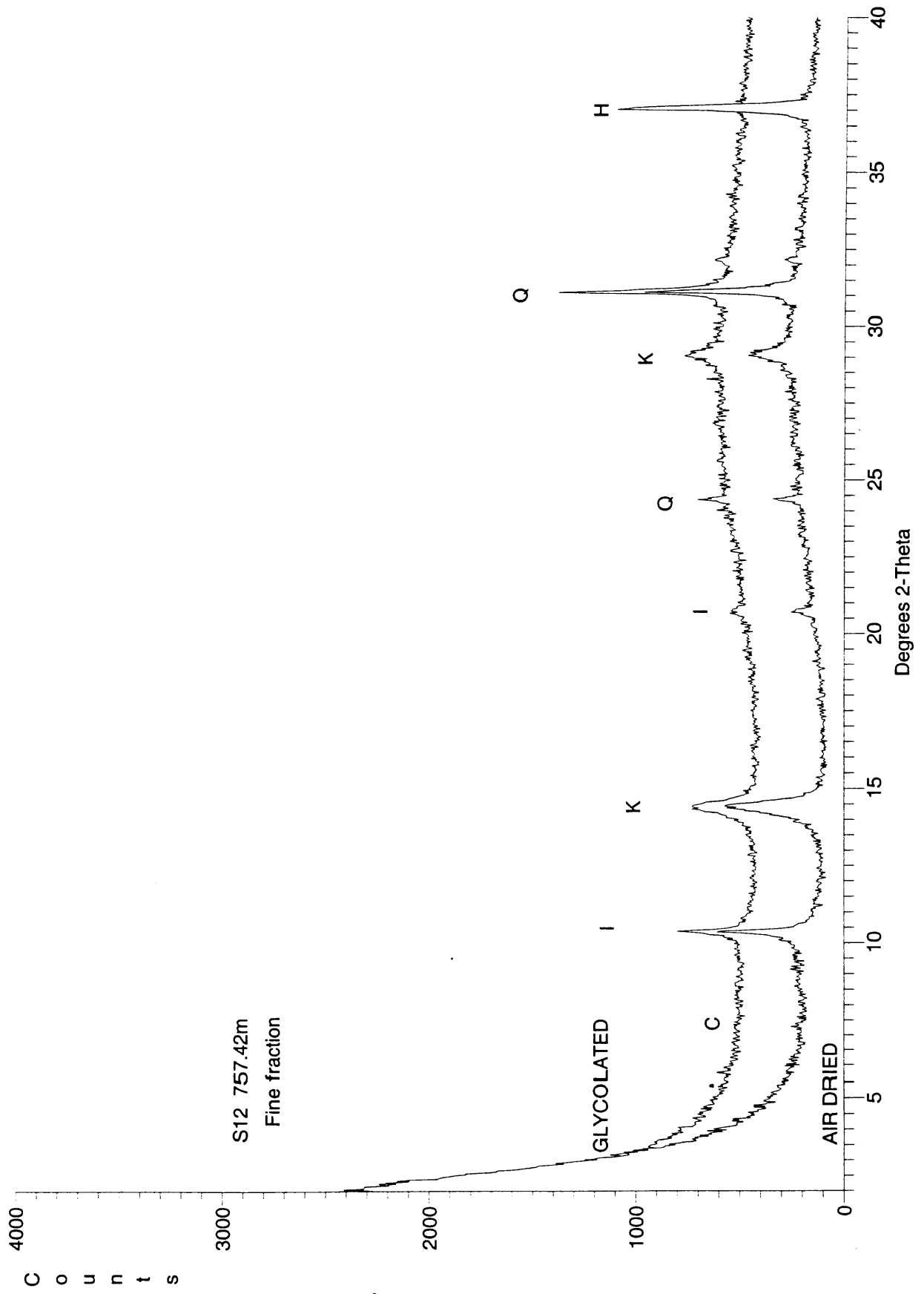


S12 757.42m

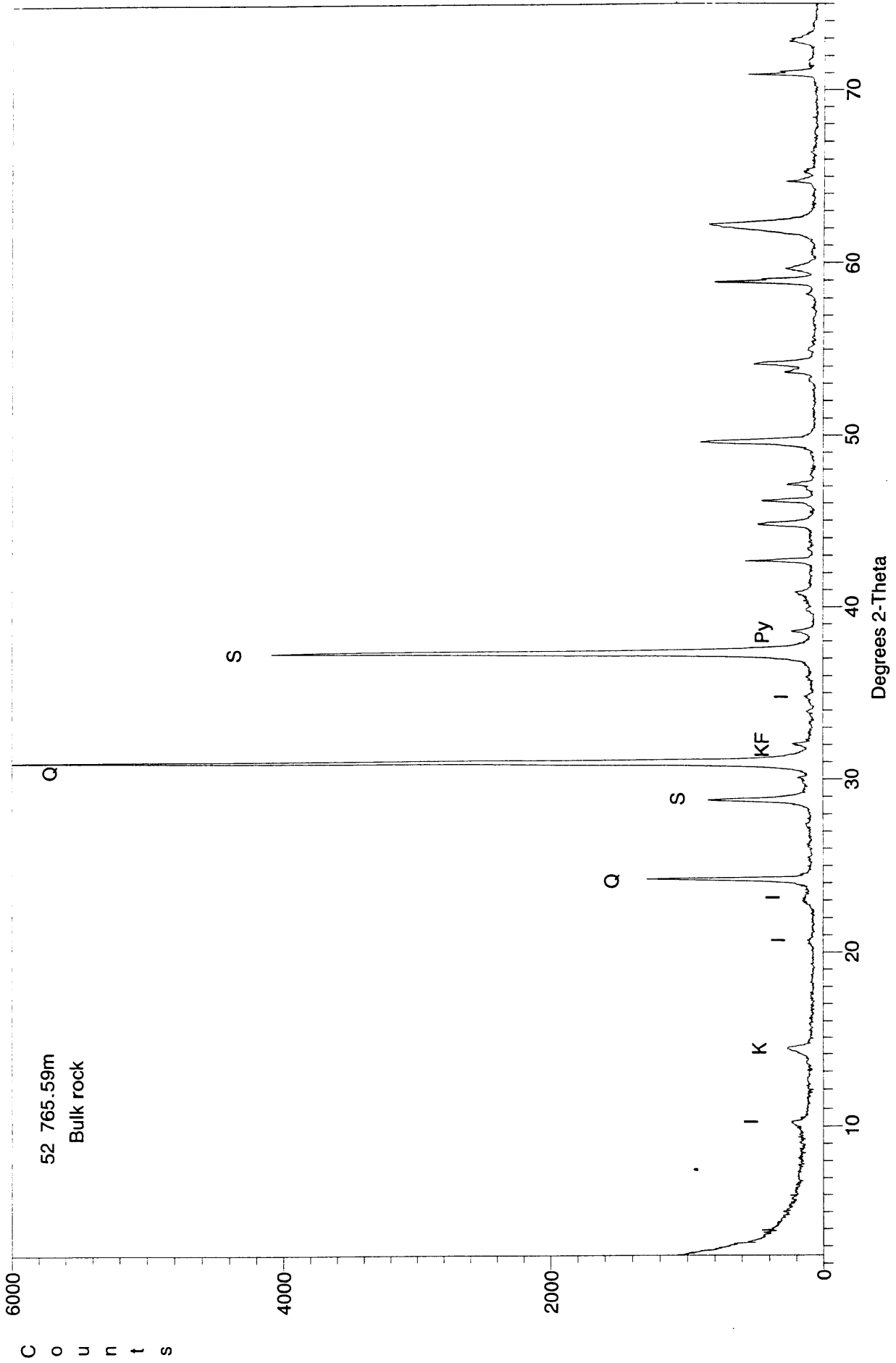
Bulk rock

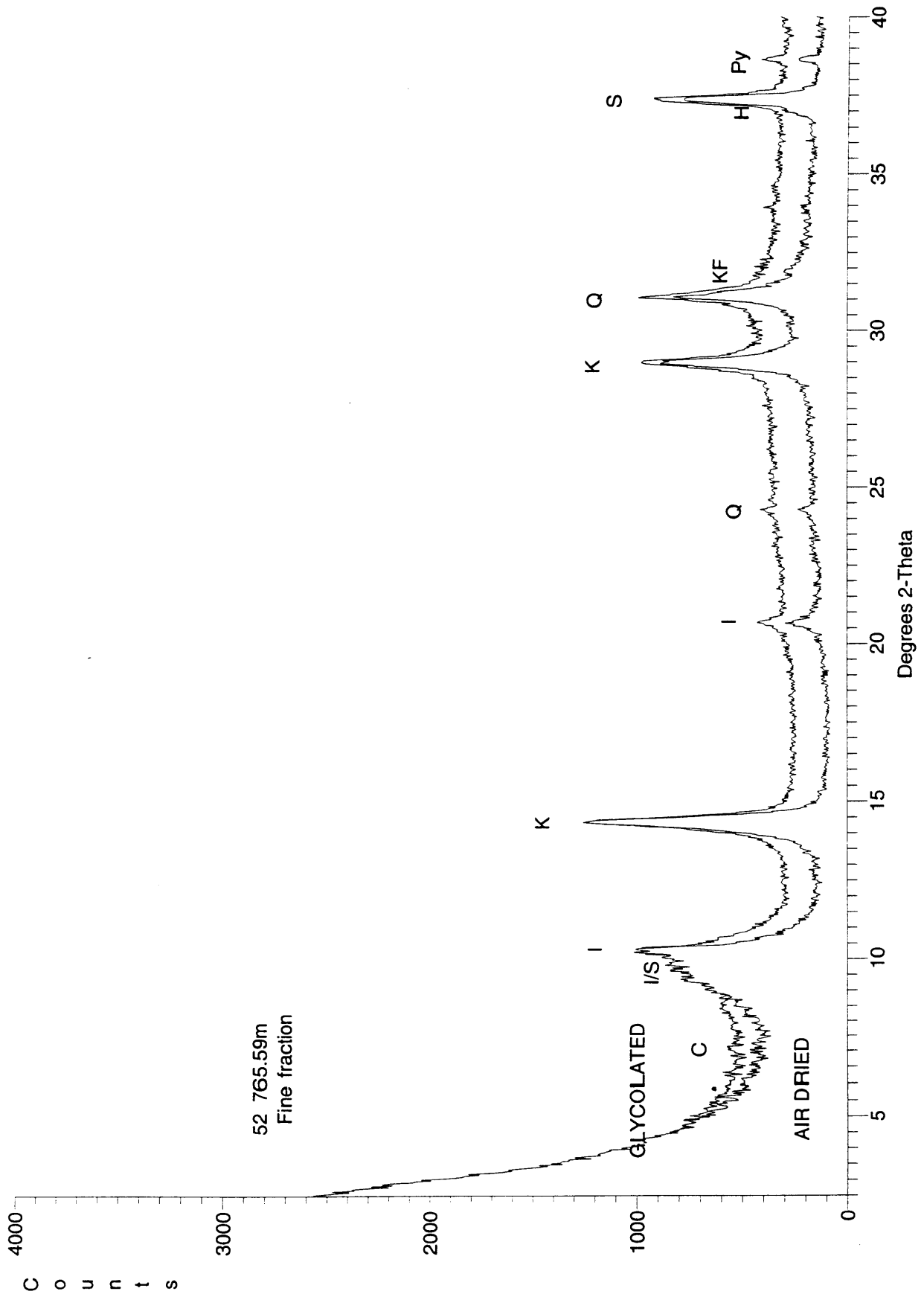
C
o
u
n
t
s

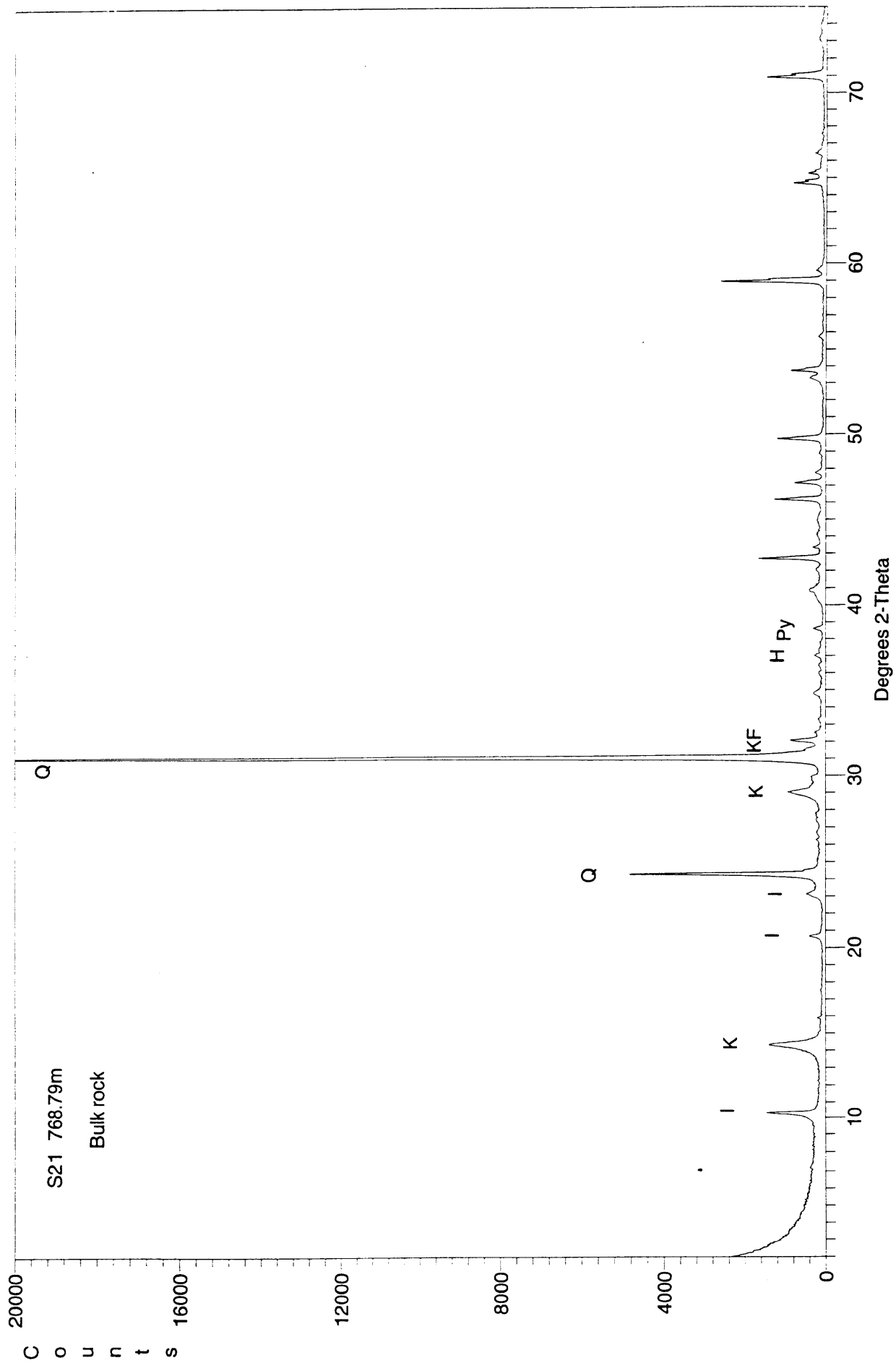
Degrees 2-Theta

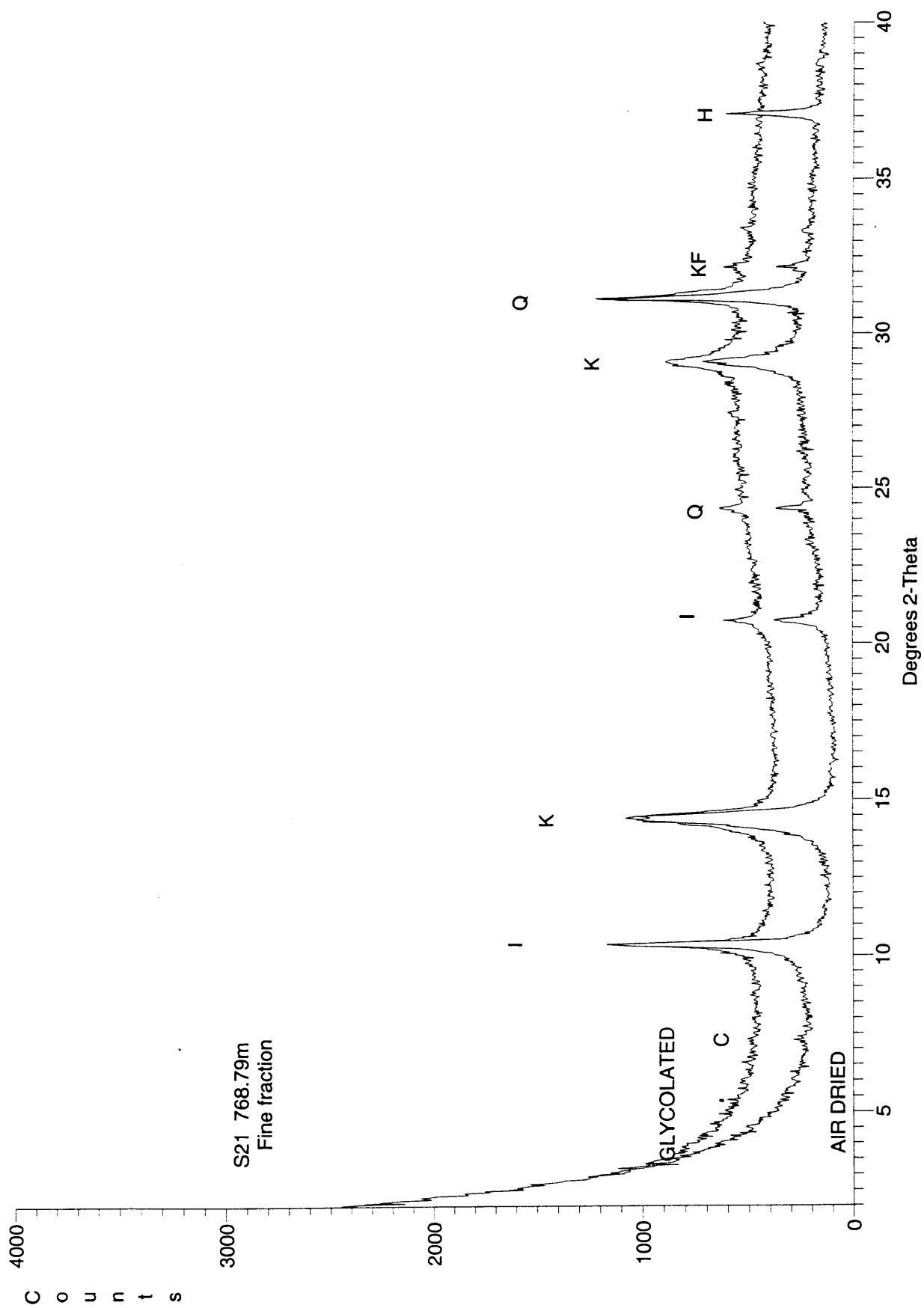


S12 757.42m
Fine fraction





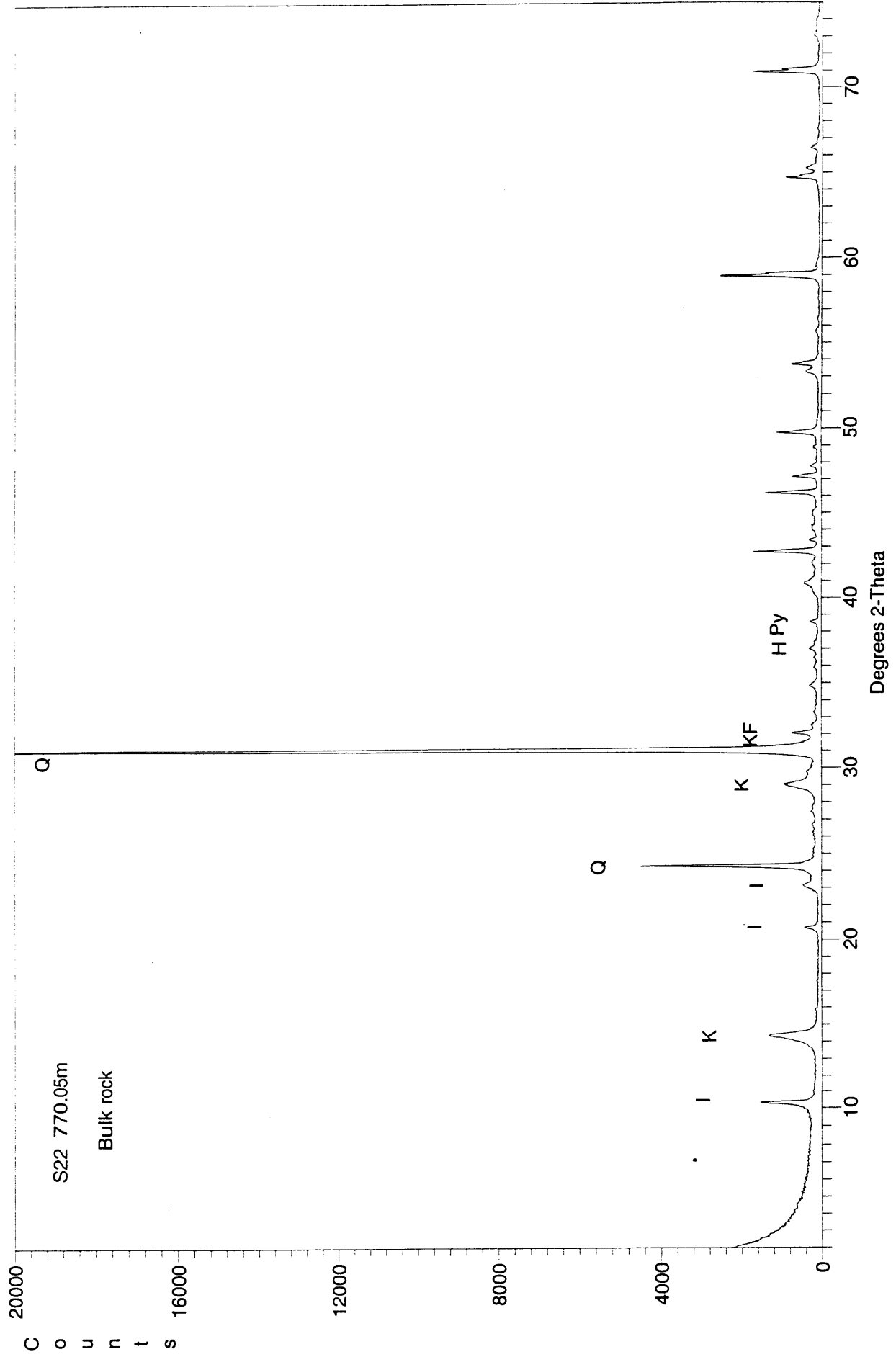




S21 768.79m
Fine fraction

GLYCOLATED

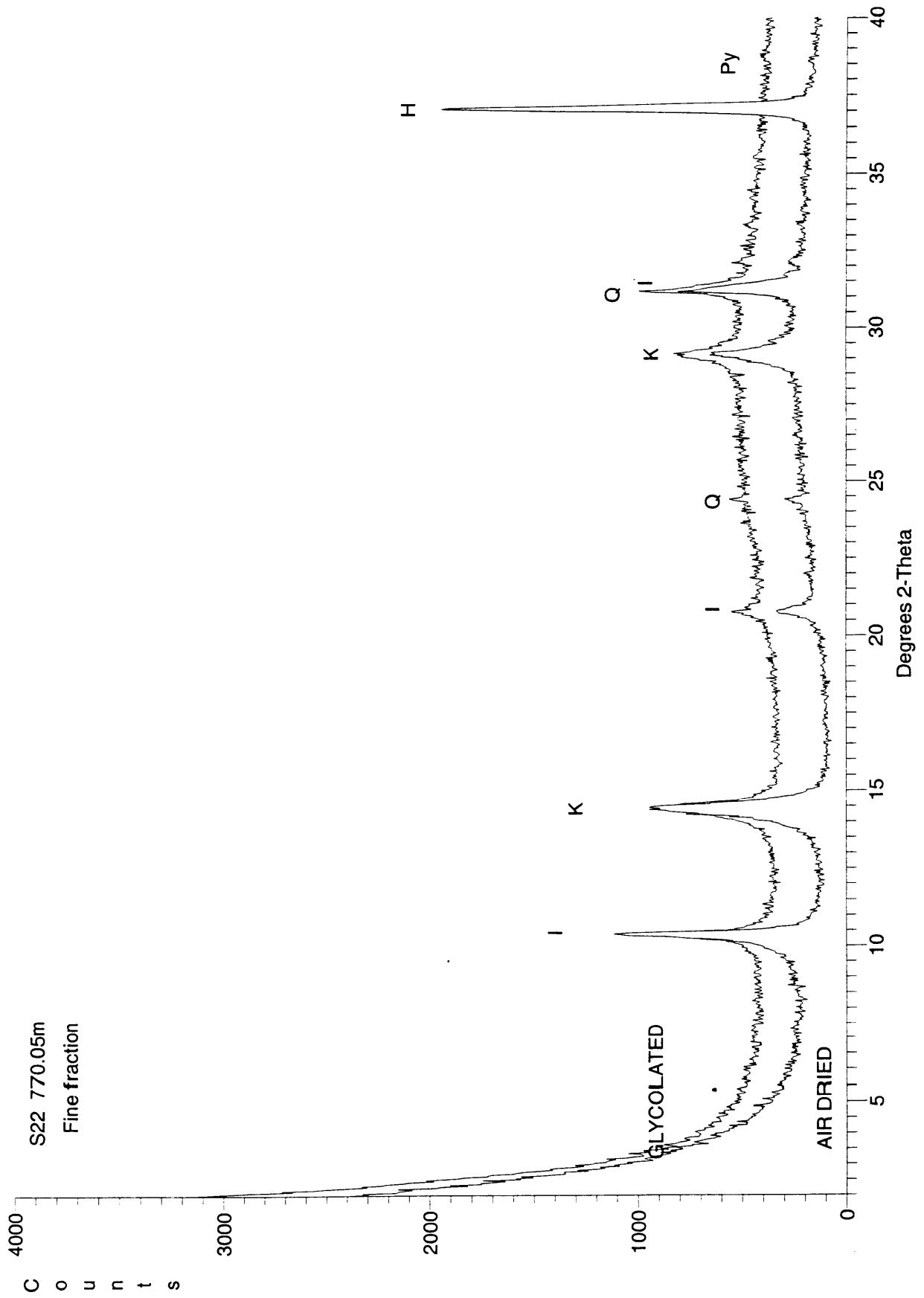
AIR DRIED

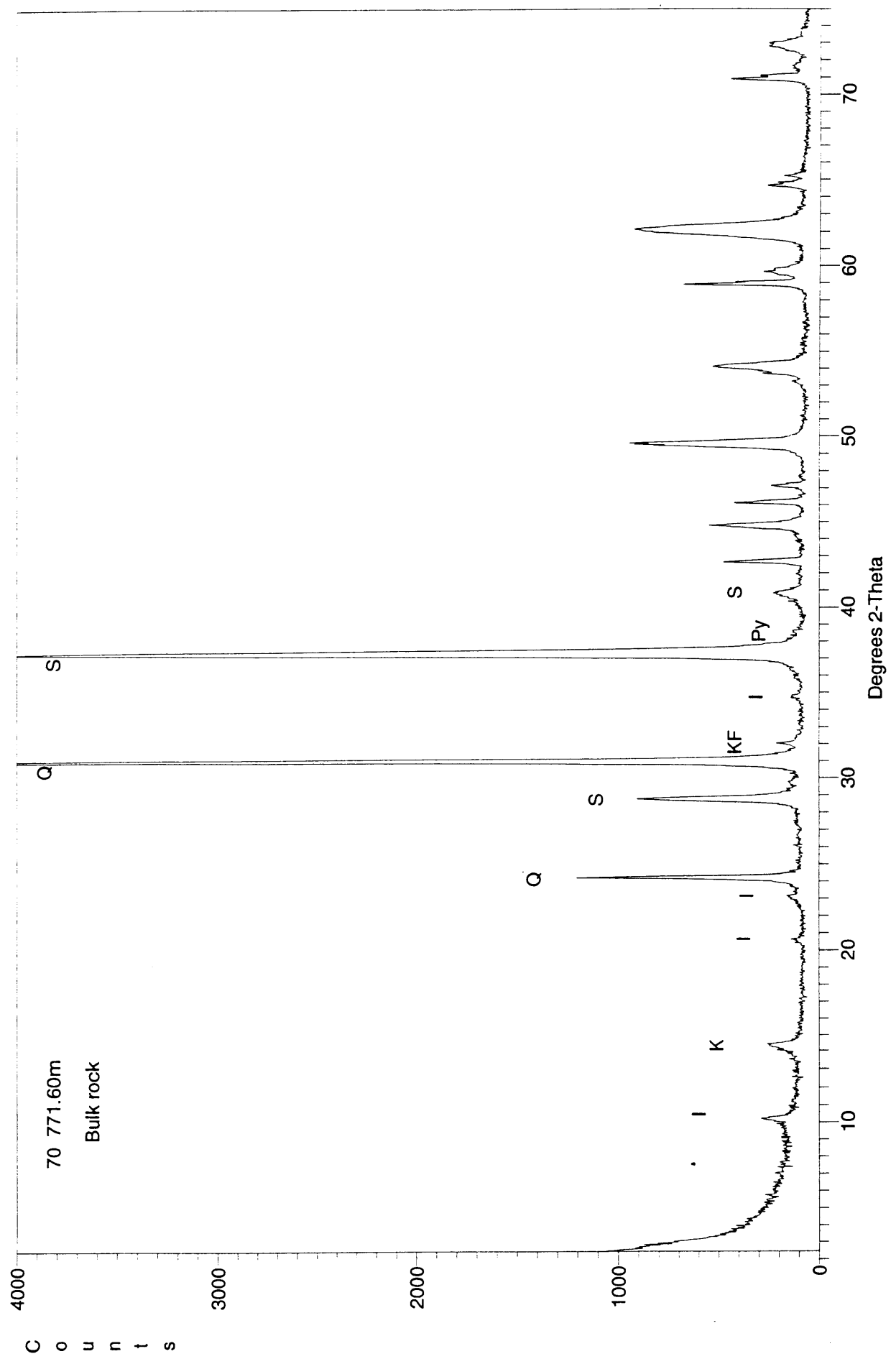


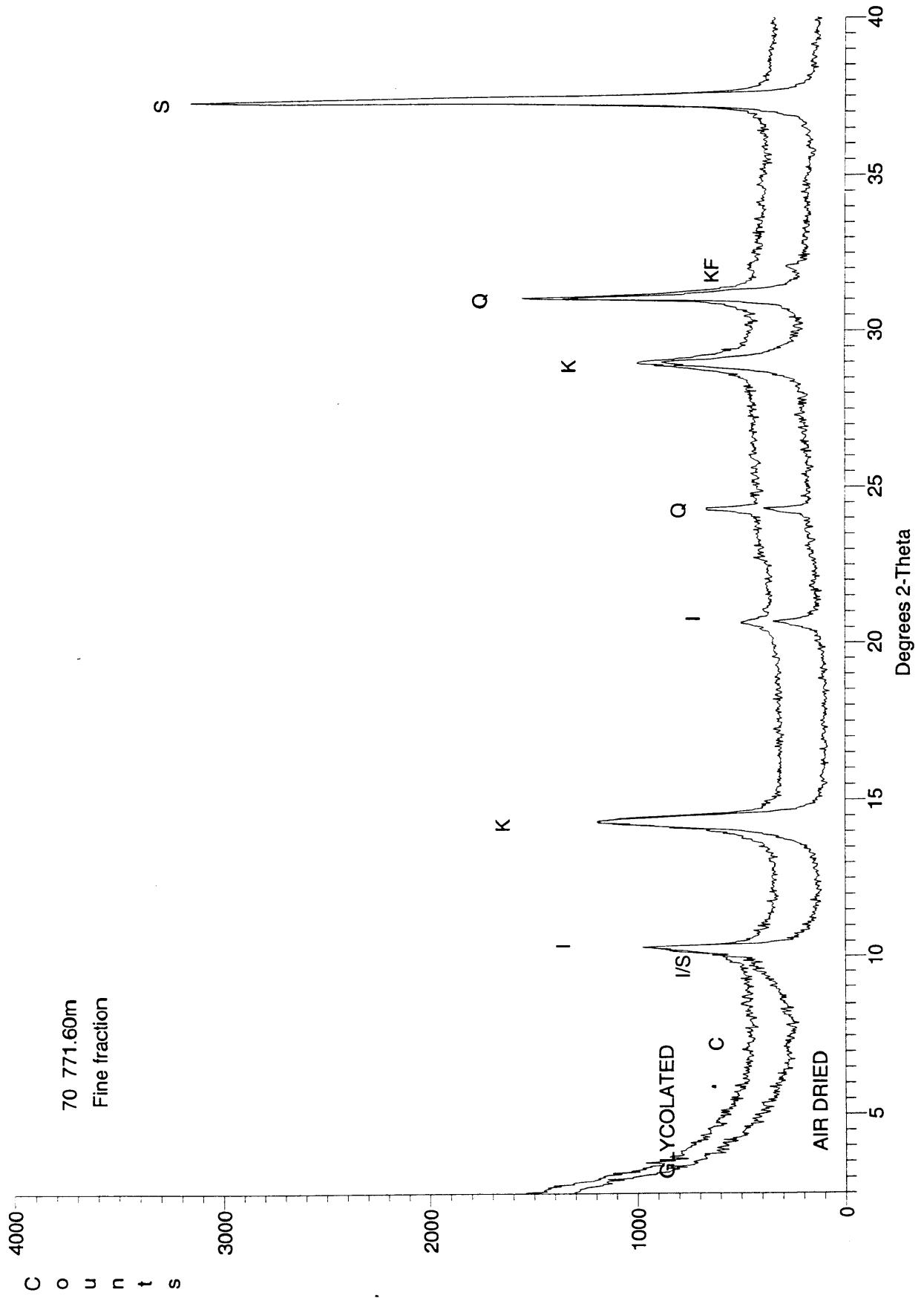
S22 770.05m
Bulk rock

C
o
u
n
t
s

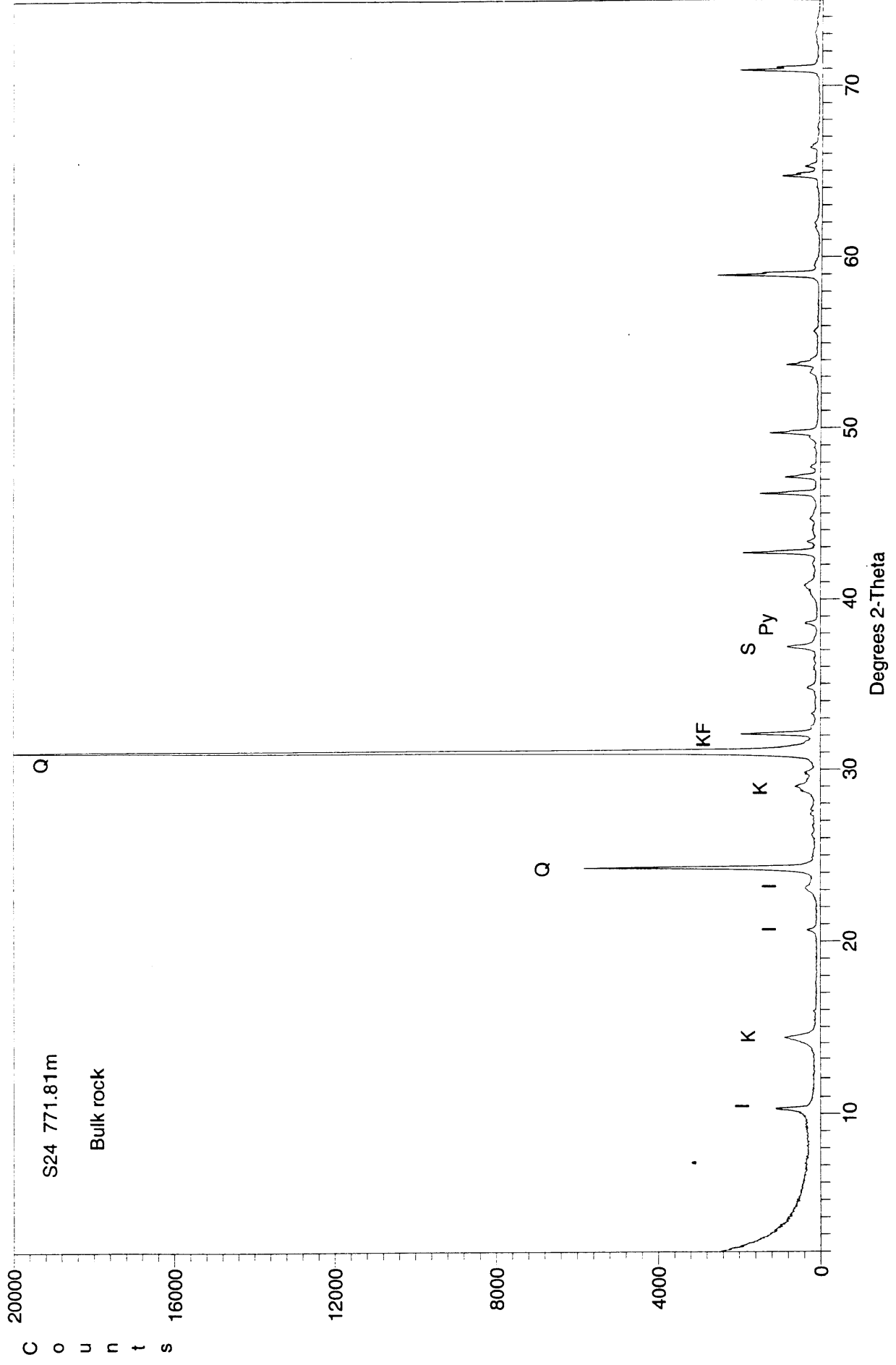
Degrees 2-Theta

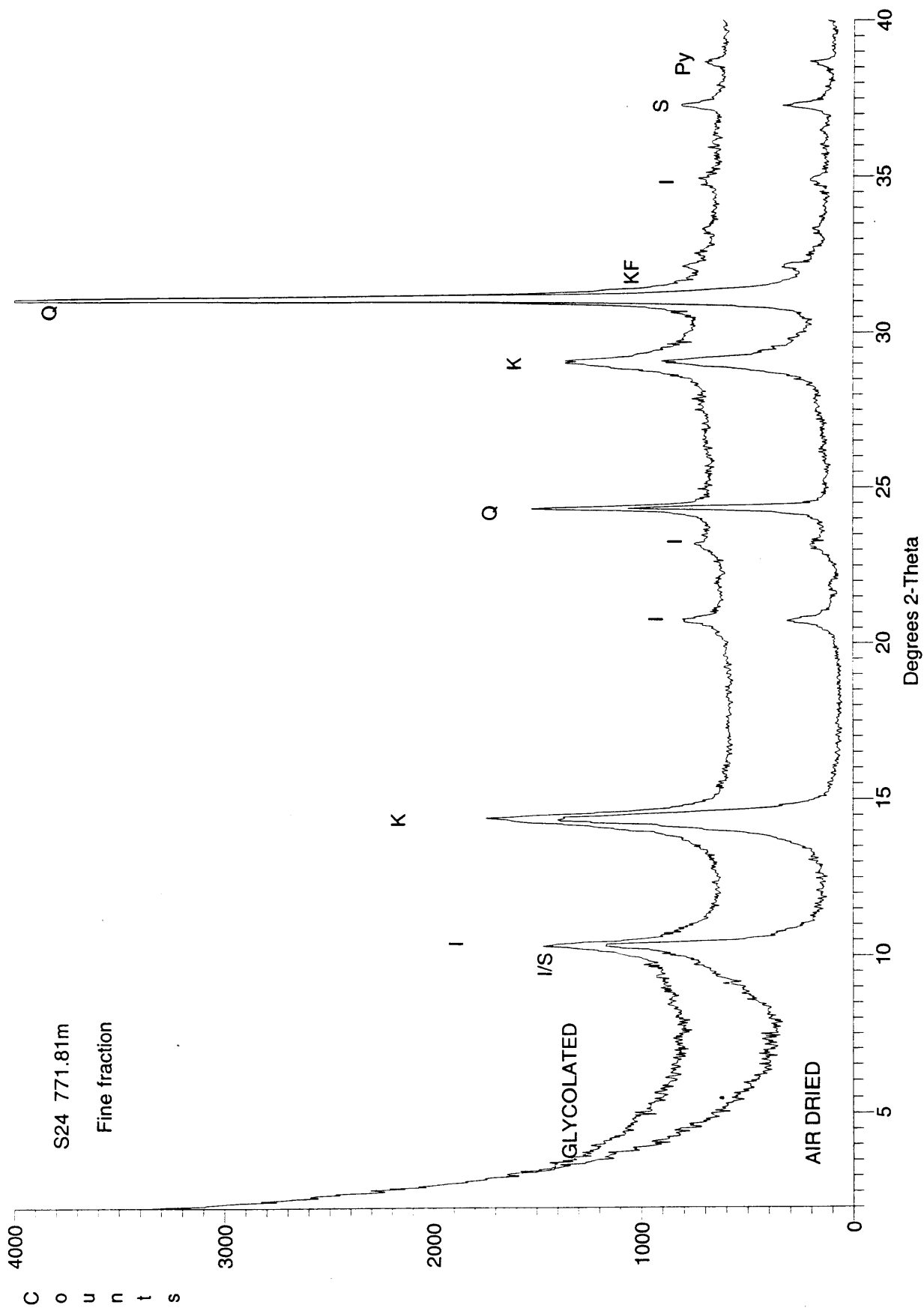






70 771.60m
Fine fraction





S24 771.81m

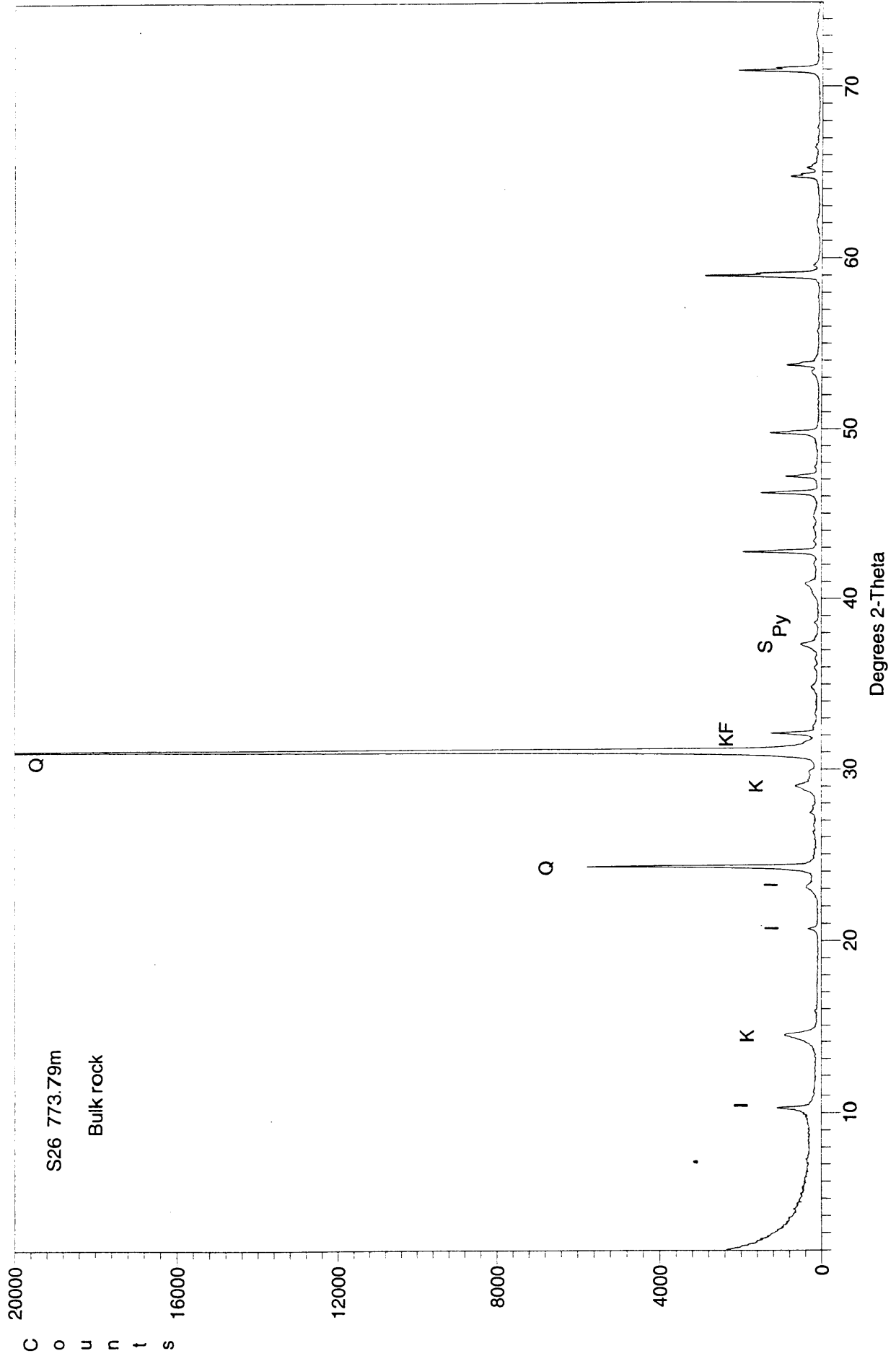
Fine fraction

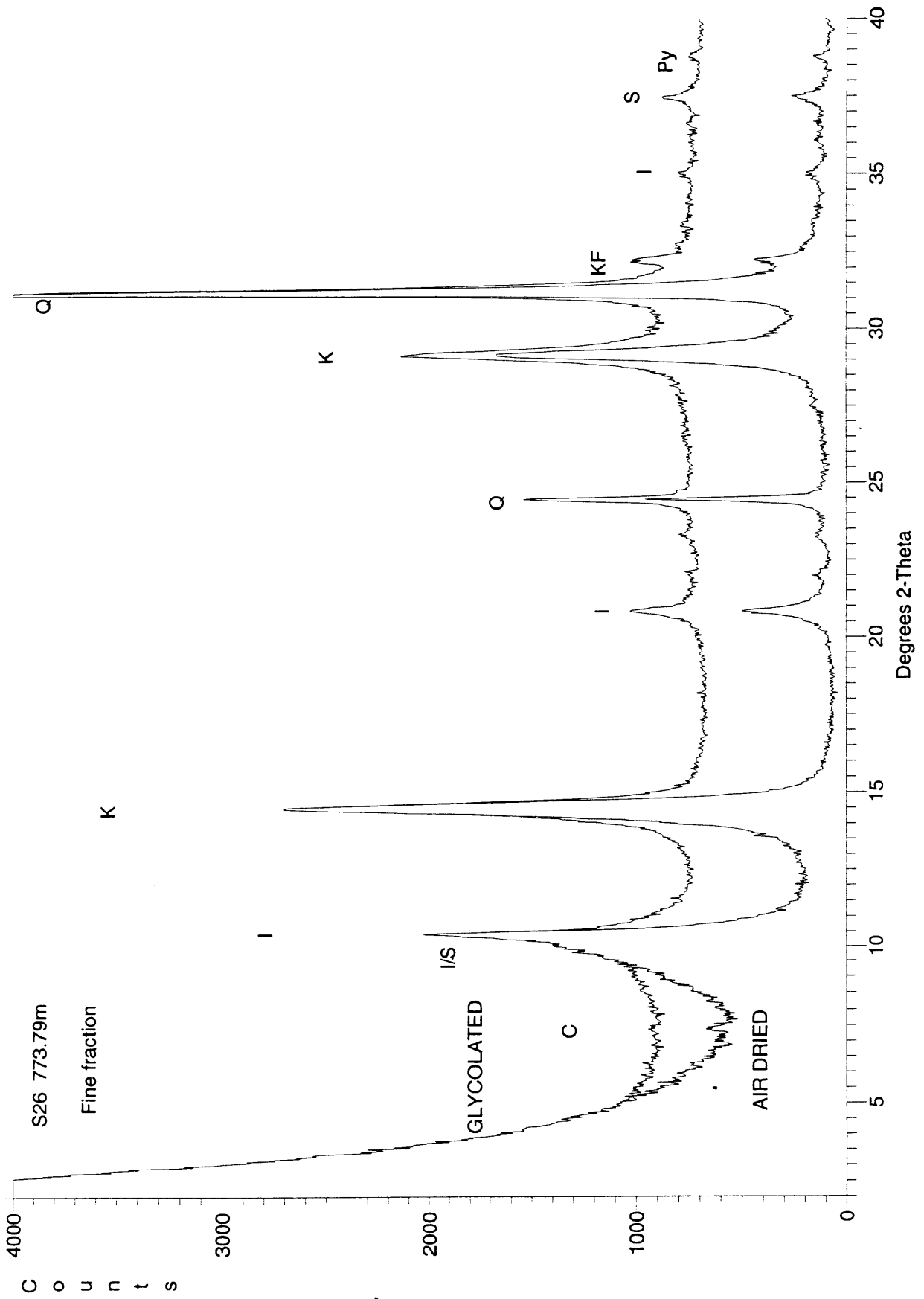
C
o
u
n
t
s

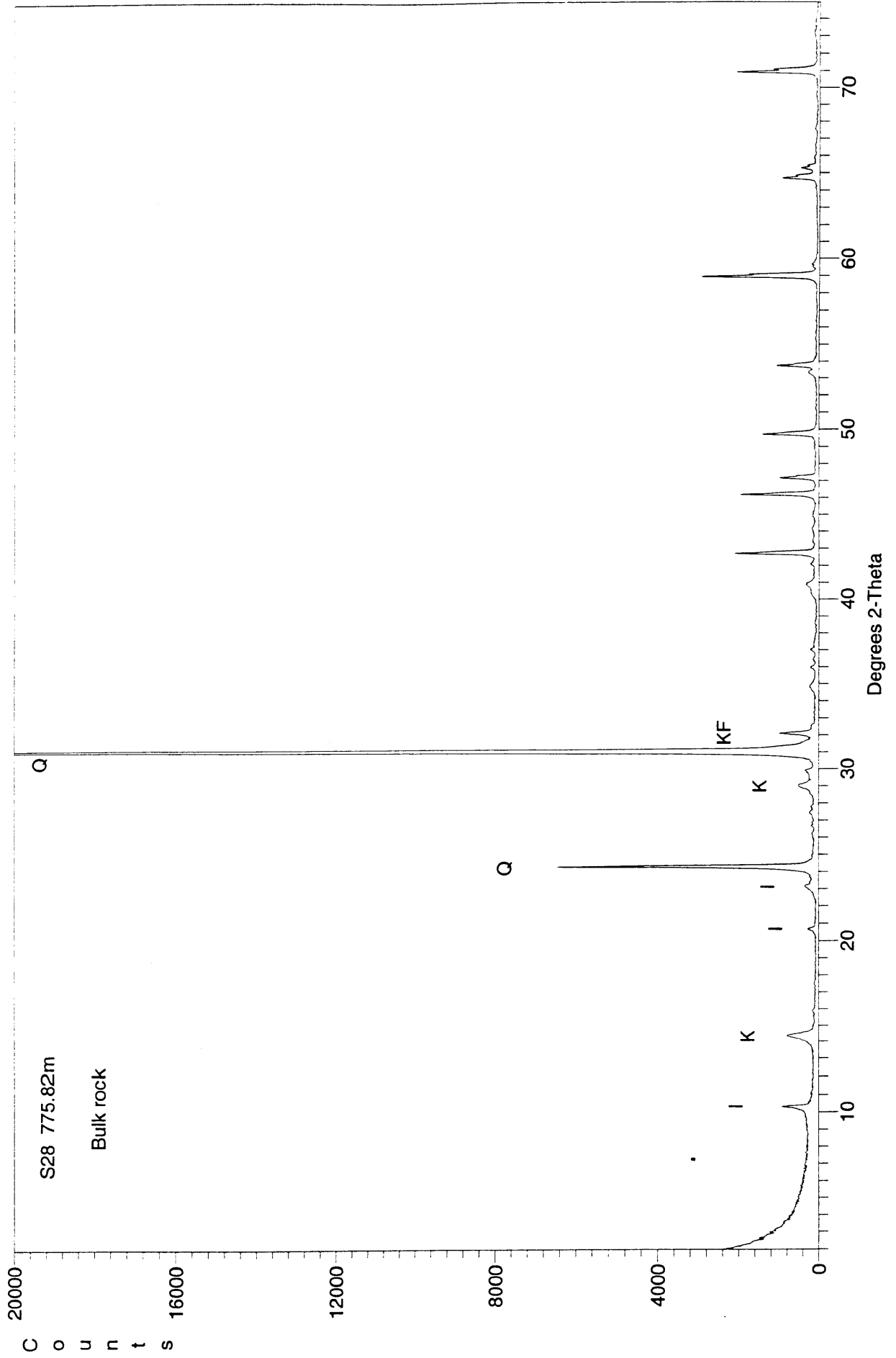
GLYCOLATED

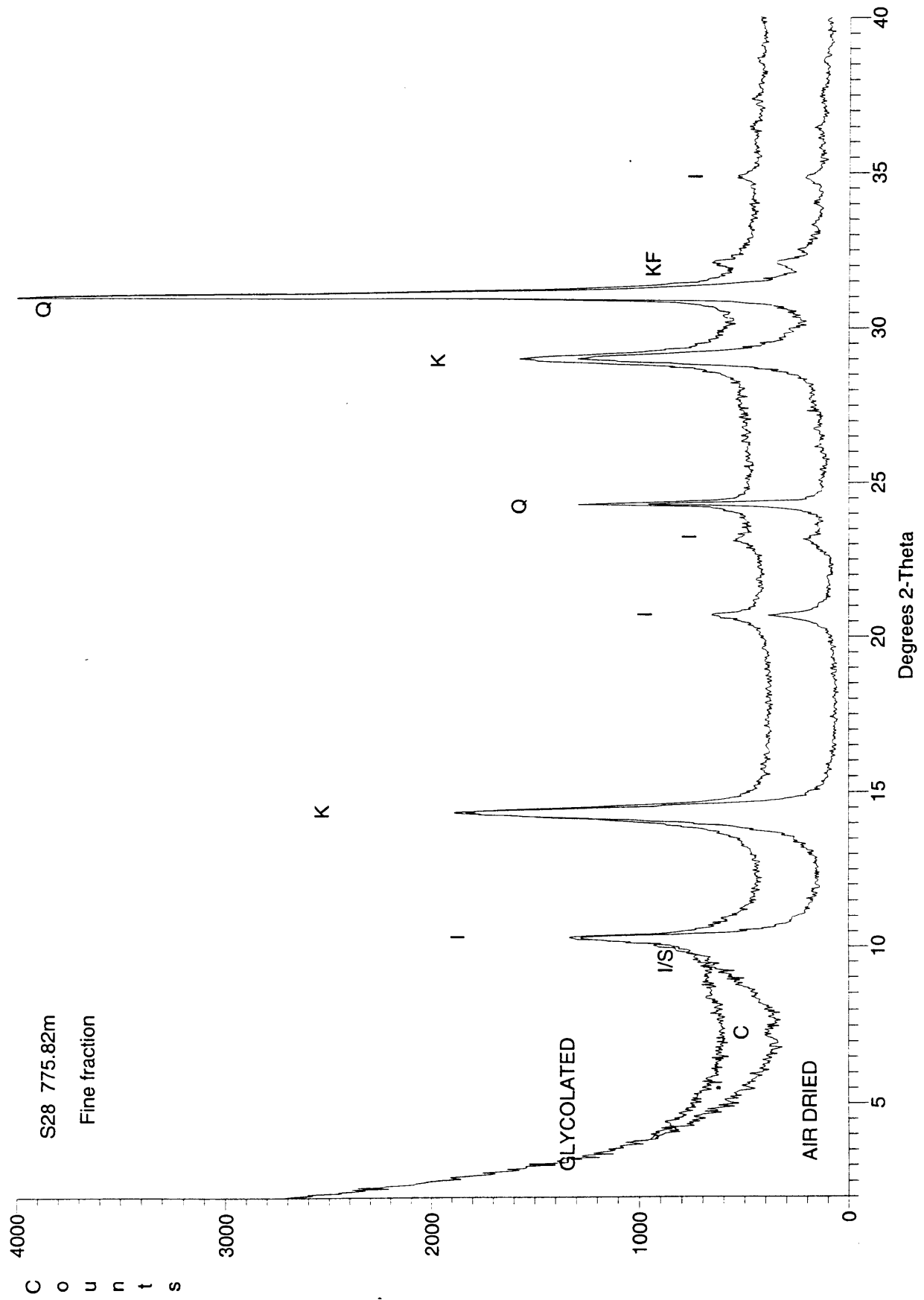
AIR DRIED

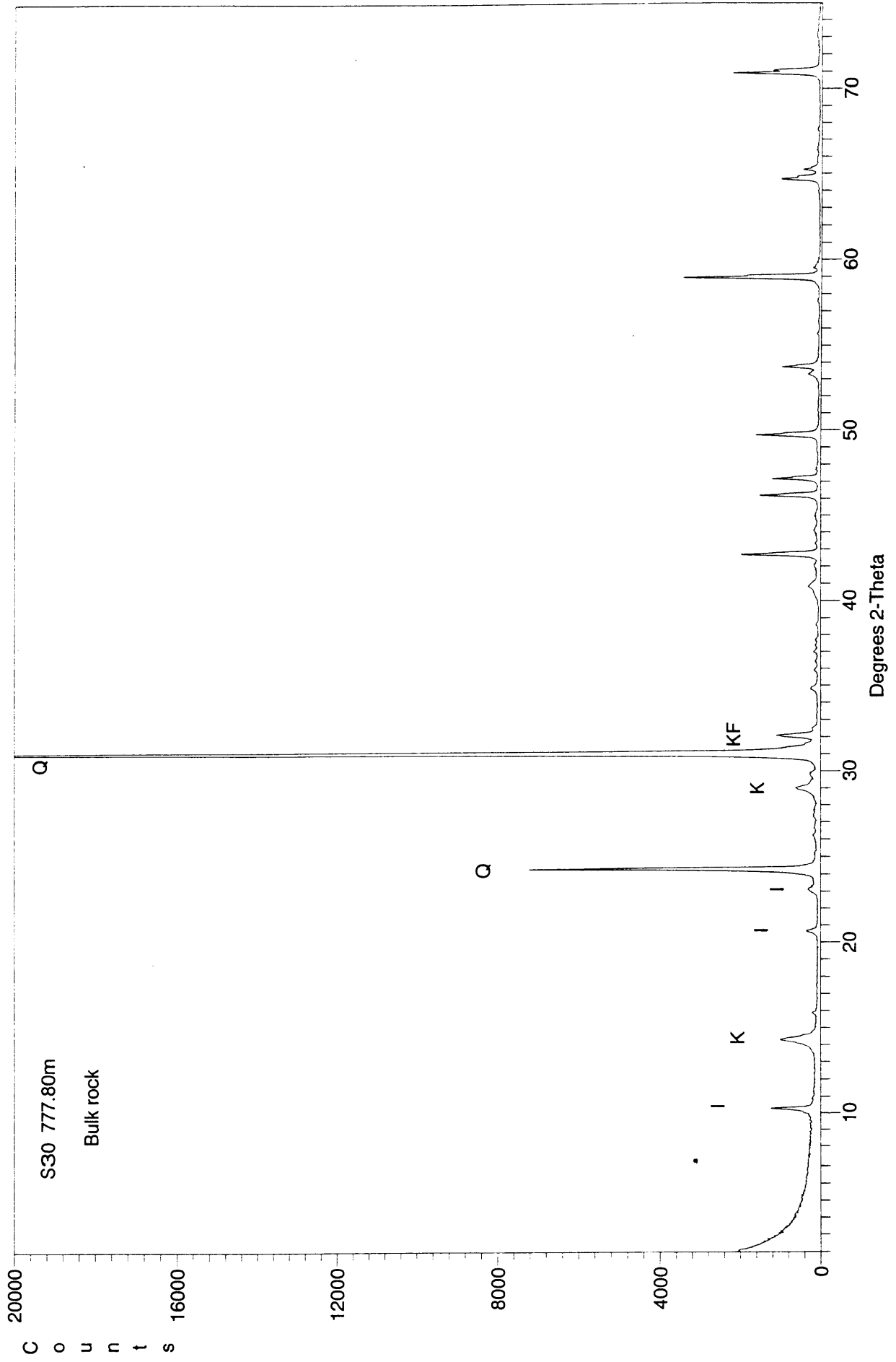
Degrees 2-Theta

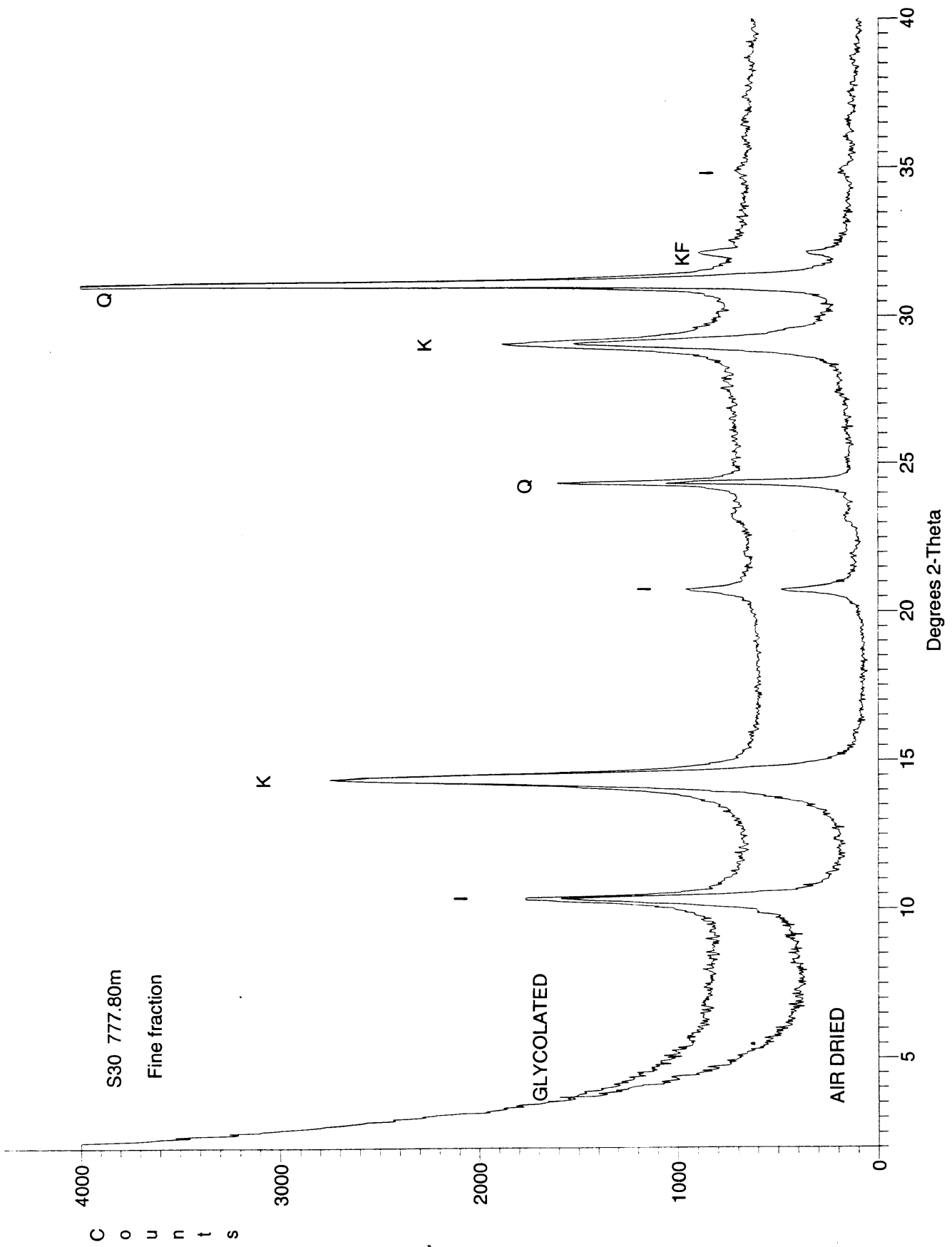










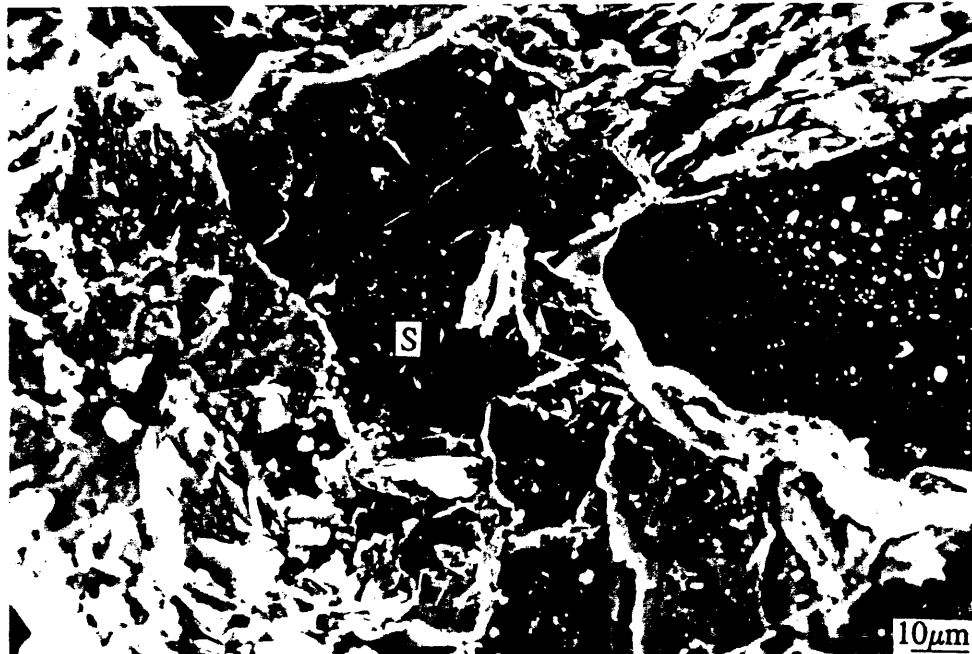
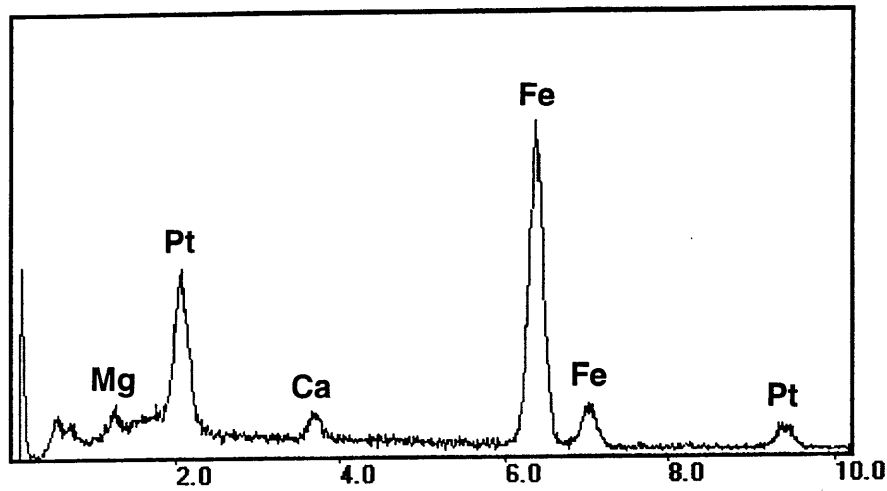


APPENDIX 2

**EDS SPECTRUM FOR EARLY
SIDERITE CEMENT IN 52**

EDS SPECTRUM FOR EARLY SIDERITE CEMENT IN 52

EDS spectrum reveals that the siderite contains minor calcium and magnesium, which is consistent with siderite precipitation from a connate marine porewater. Pt is from conductive coating. Accompanying SEM micrograph shows the analysed siderite cement (S).



APPENDIX 3

PHOTOMICROGRAPHS

PLATE 1**S5 750.41m Zone 1****FIGURE 1** Plane polarised light**FIGURE 2** Crossed polarisers

Porosity in this very fine grained sandstone has been significantly reduced by pore filling by detrital clay matrix (C). Within a localised area that contains only minor clay (upper half of micrograph), abundant primary intergranular porosity (PP) is preserved between poorly compacted grains of quartz, K-feldspar (KF) and altered biotite (B).

FIGURE 3

This SEM micrograph shows an argillaceous area (centre-right), where intergranular spaces are filled by detrital clay matrix (C). Outside of the argillaceous area, good primary intergranular porosity (PP) is preserved between poorly compacted framework grains. Mica (M) is a common framework grain constituent.

FIGURE 4

In a clean part of the sandstone, primary intergranular pores (PP) are preserved between loosely packed framework grains, and a compacted micaceous grain has altered to finely-crystalline kaolinite (K). Most authigenic clay is kaolinite that has formed by alteration of micaceous grains and recrystallisation of detrital clay.

PLATE 1

907961 066

FIGURE 1

FIGURE 2

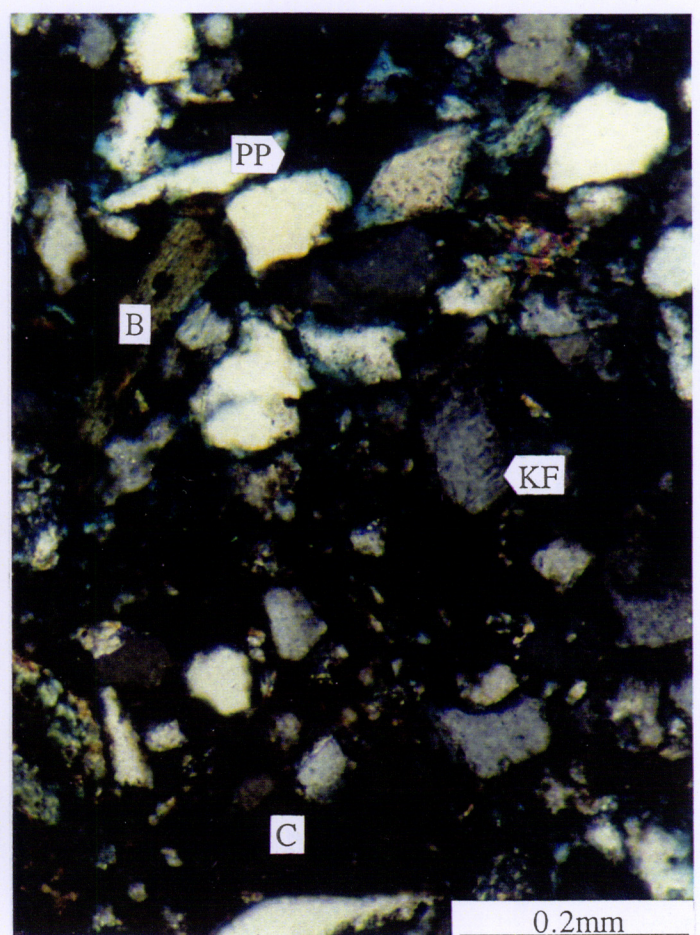
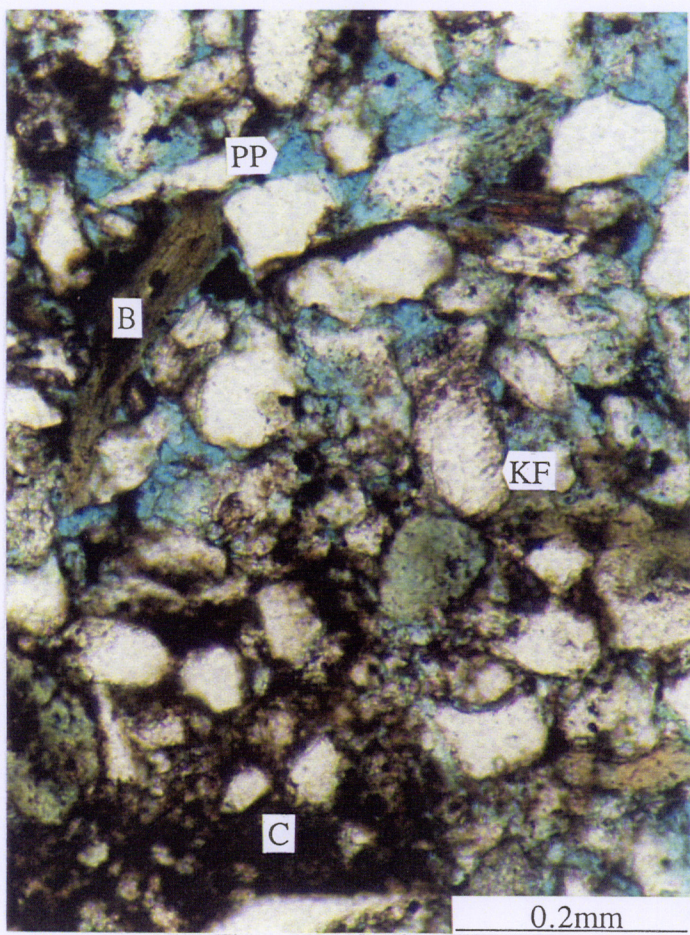


FIGURE 3

FIGURE 4

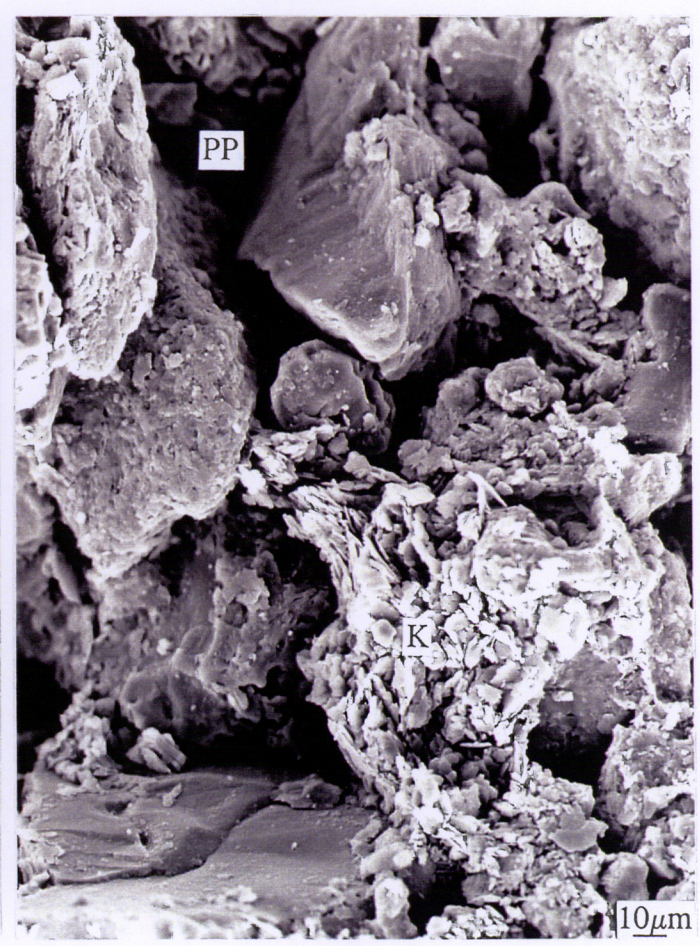
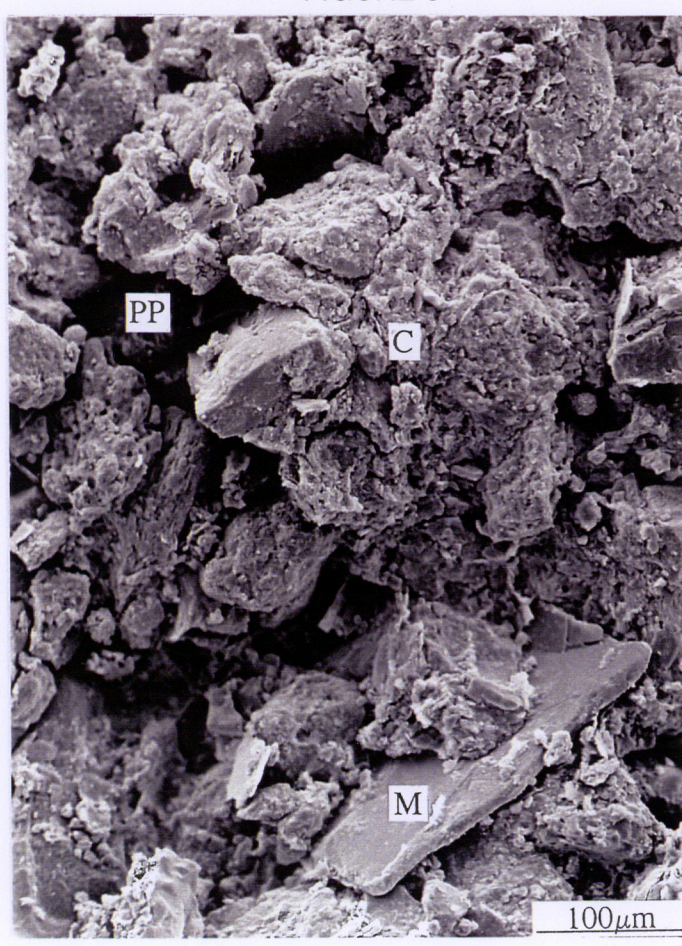


PLATE 2**S6 751.42m Zone 1****FIGURE 1** Plane polarised light**FIGURE 2** Crossed polarisers

Contact between argillaceous sandstone (lower half of micrograph), where all intergranular areas are filled by detrital clay (C), and a patch of clean, poorly compacted, macroporous (P) sandstone. Most of the sample is argillaceous. Grains include peloidal glauconite (G) and glauconitised biotite (arrow).

FIGURE 3

Only scattered intergranular pores (P) remain in a sandstone that contains abundant detrital clay matrix (C).

FIGURE 4

Detail of kaolinitic/illitic detrital clay matrix (C) that chokes intergranular pores (P). The clay is highly microporous (MP) and appears to have recrystallised to kaolinite (K) in some places.

FIGURE 1

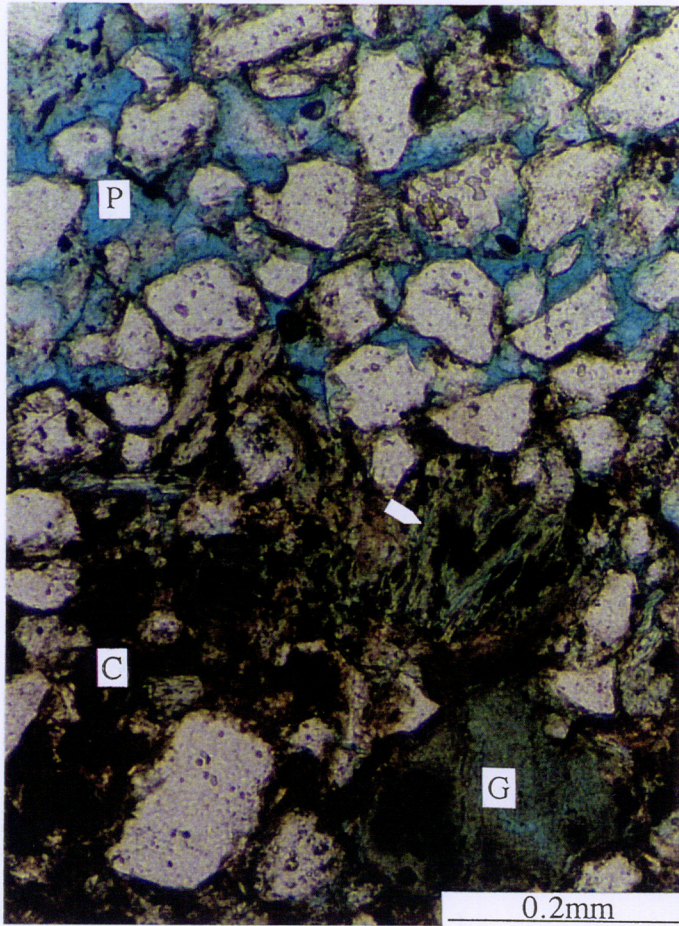


FIGURE 2

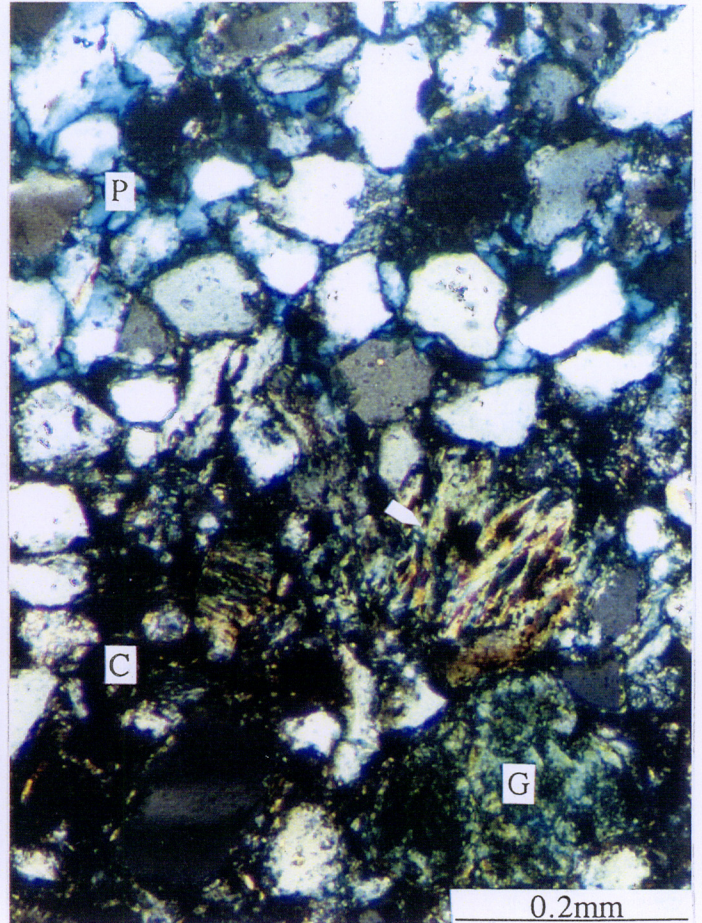


FIGURE 3

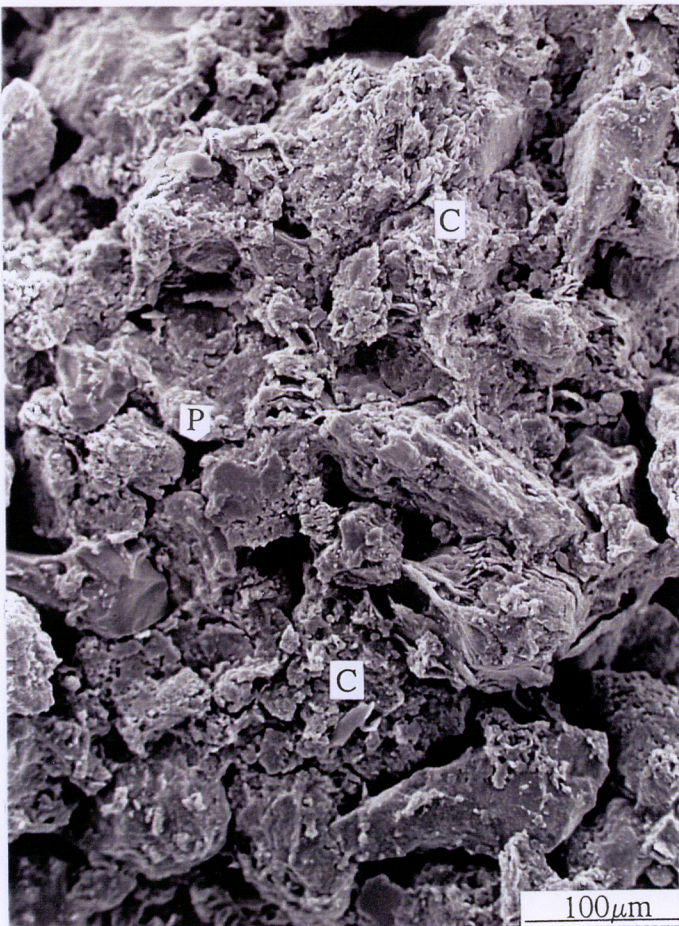


FIGURE 4

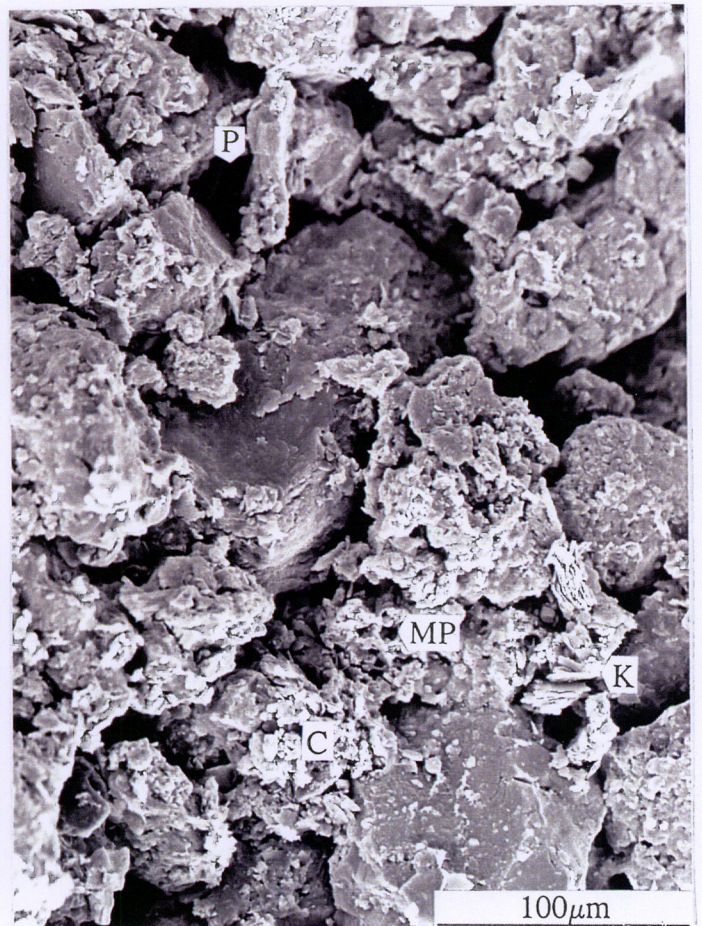


PLATE 3**S9 754.41m Zone 2****FIGURE 1** Plane polarised light**FIGURE 2** Crossed polarisers

Very fine grained sandstone consisting of loosely packed grains of quartz, K-feldspar (KF), peloidal glauconite (G) and altered biotite (B), between which abundant primary intergranular porosity (PP) is preserved.

FIGURES 3 & 4

Abundant clean, primary intergranular porosity (PP) is preserved between poorly compacted, uncemented grains of quartz, K-feldspar, glauconite and mica (M). Much of the sample is clean and highly macroporous.

PLATE 3

907961 070

FIGURE 1

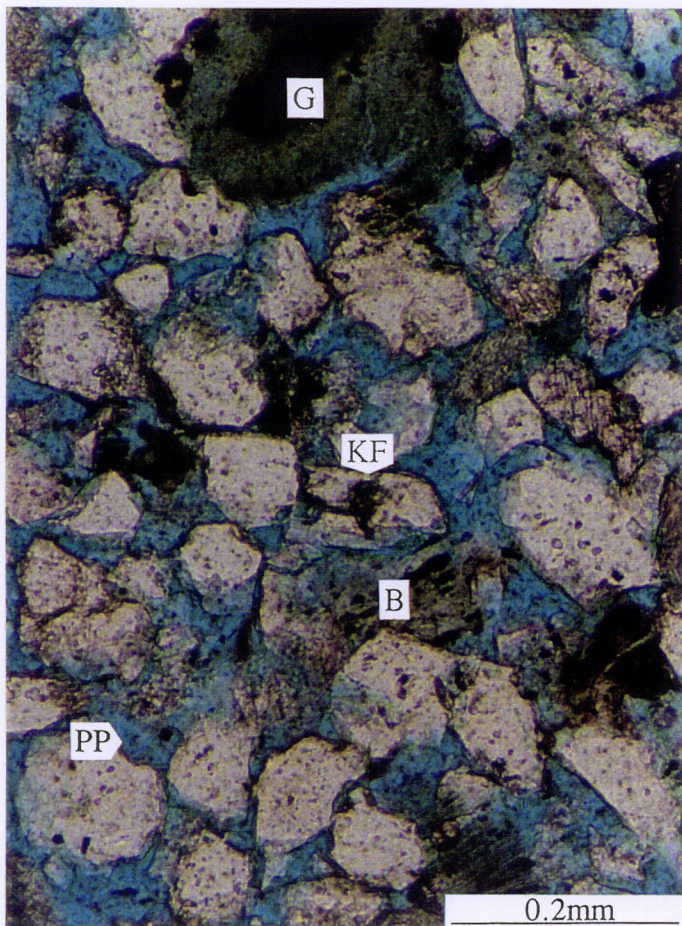


FIGURE 2

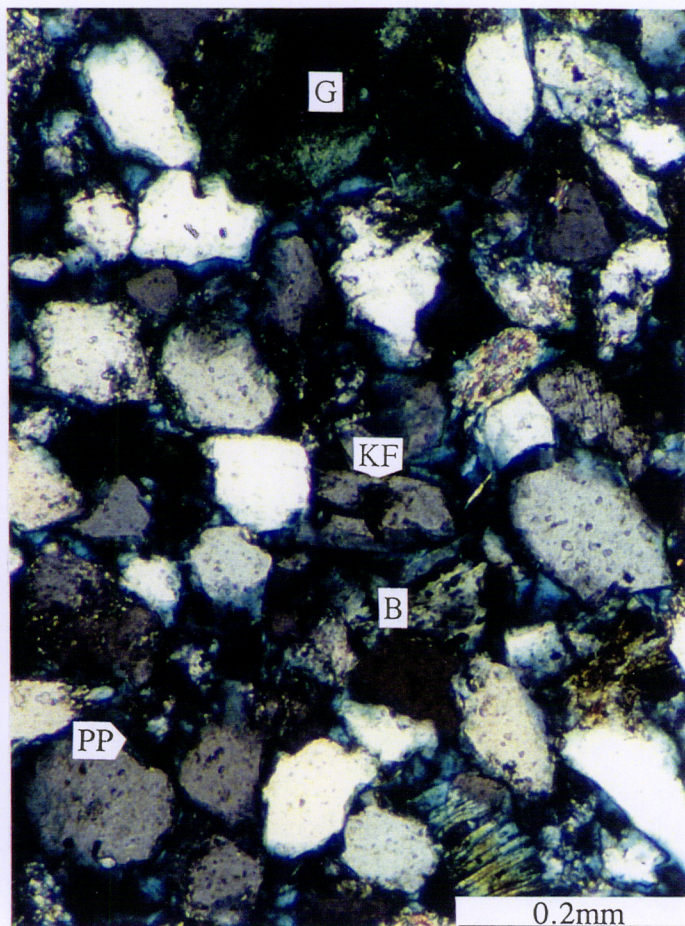


FIGURE 3

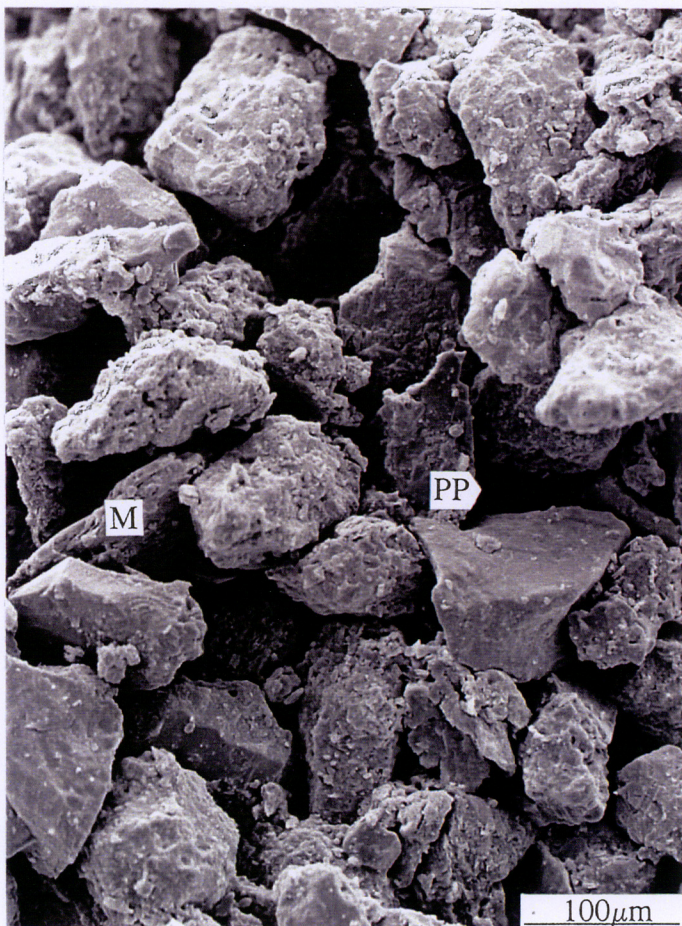


FIGURE 4

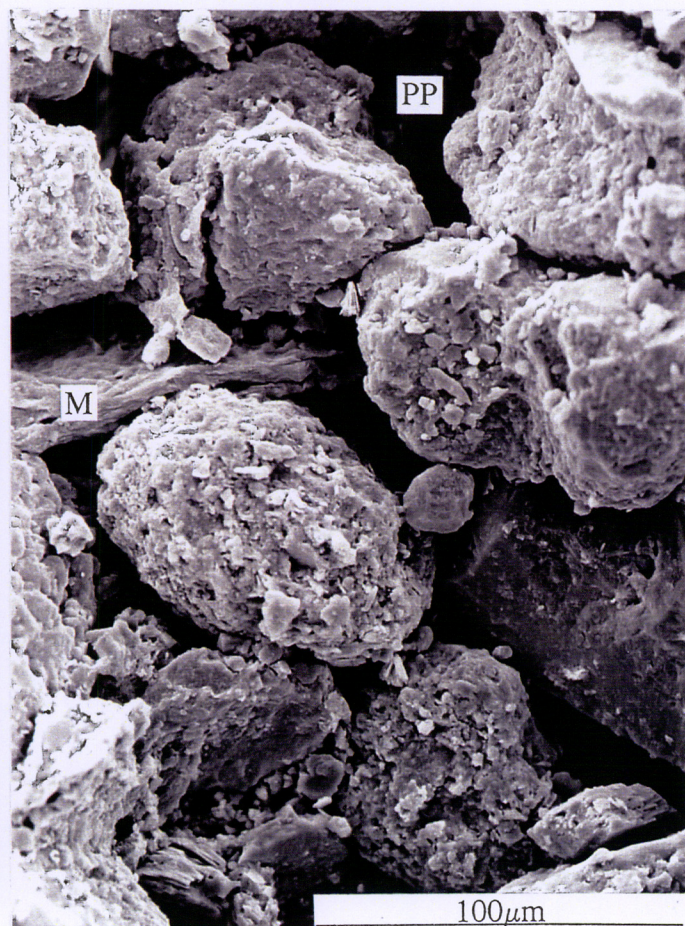


PLATE 4**S12 757.42m Zone 2****FIGURE 1** Plane polarised light**FIGURE 2** Crossed polarisers

Good primary intergranular porosity (PP) is preserved in an area that contains little detrital clay (upper half of micrograph). Elsewhere, porosity has been reduced by pore filling by detrital clay (C) and associated fine pyrite (Py). Variably altered biotite (B) is a common framework grain constituent.

FIGURE 3

Porosity has been reduced in this sandstone by pore filling by patchy detrital clay matrix (C). Areas lacking clay are highly macroporous (P).

FIGURE 4

Abundant primary intergranular porosity (PP) is preserved between poorly compacted quartz and K-feldspar (KF) grains. Rigid framework grains only ever have point grain contacts, indicating that there was no grain contact dissolution (pressure solution) during burial.

PLATE 4

907961 072

FIGURE 1

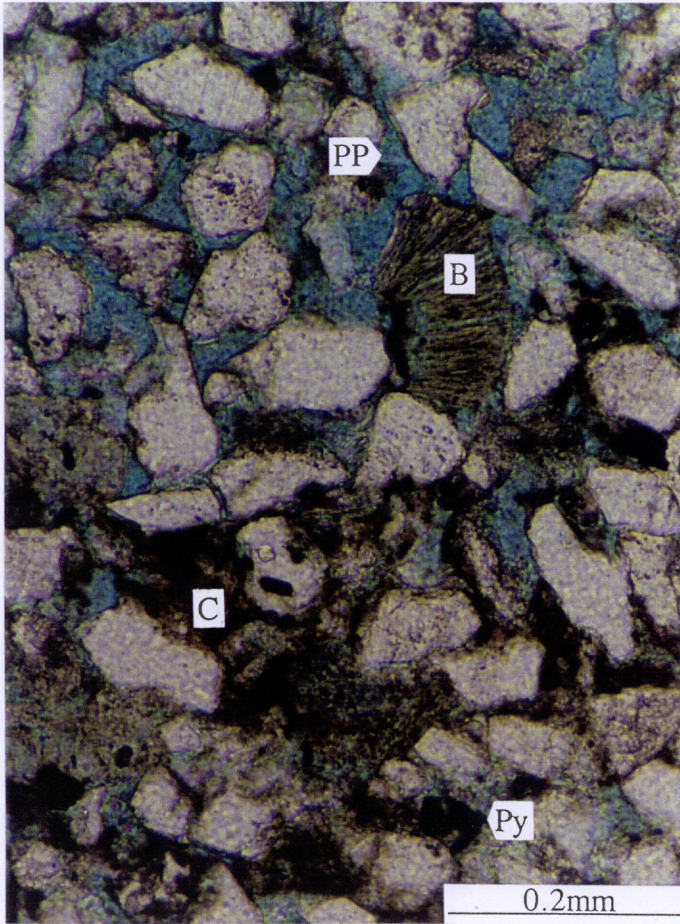


FIGURE 2

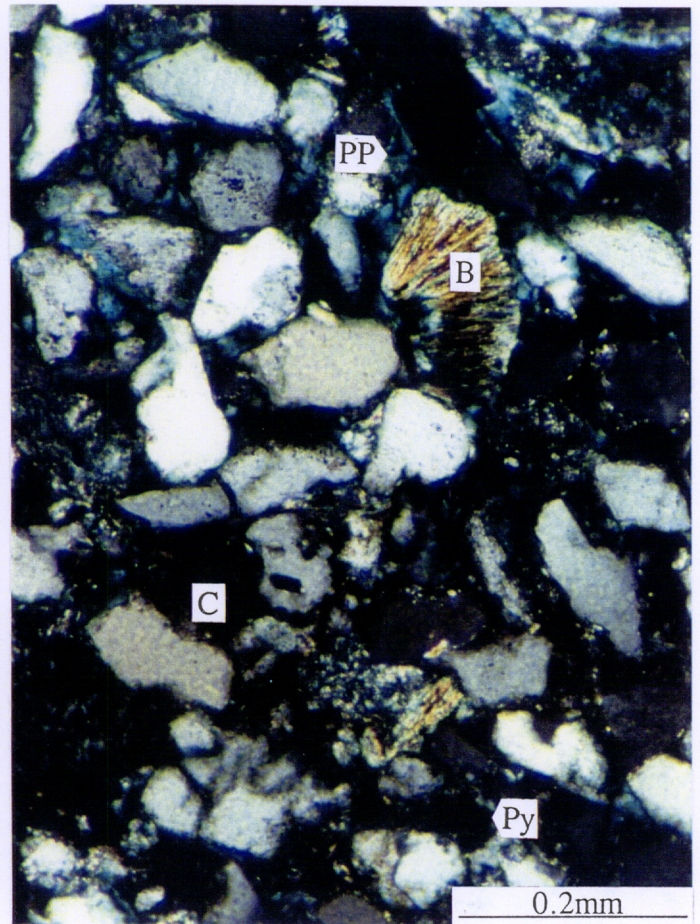


FIGURE 3



FIGURE 4

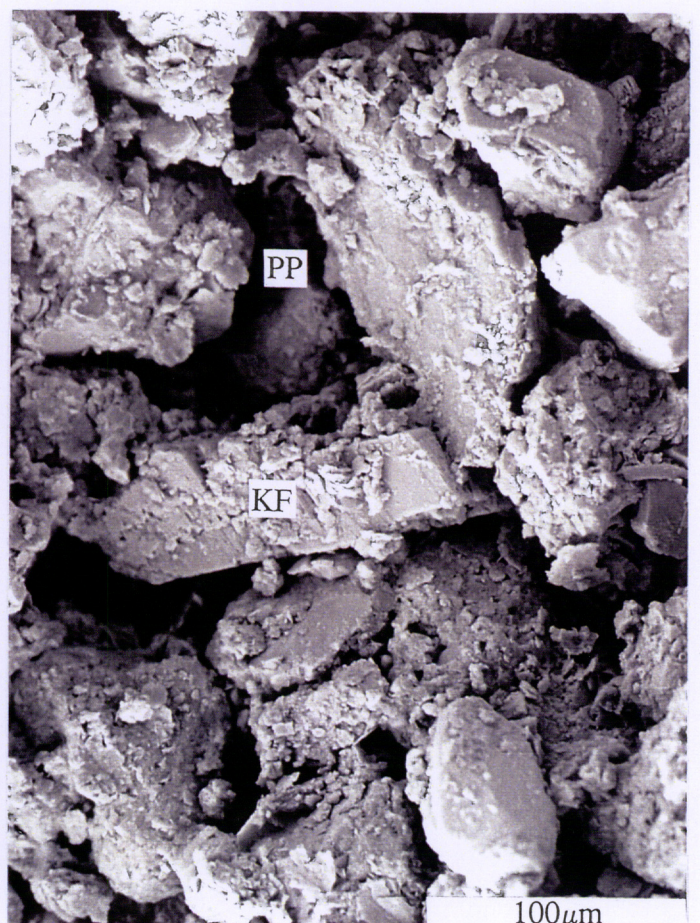


PLATE 552 765.59m**FIGURE 1** Plane polarised light**FIGURE 2** Crossed polarisers

Early diagenetic siderite (S) occupies all intergranular spaces and partly replaces a glauconitised biotite grain (G). The sand has negligible permeability due to the presence of widespread siderite cement.

FIGURES 3 & 4

Representative areas in which all intergranular spaces are filled by siderite cement (S). Minor porosity (P) that is associated with split grains of glauconitised biotite (G) may be the result of grain shrinkage during core desiccation. A higher magnification SEM micrograph of siderite cement in the sample is included in Appendix 2.

PLATE 5

907961 074

FIGURE 1

FIGURE 2

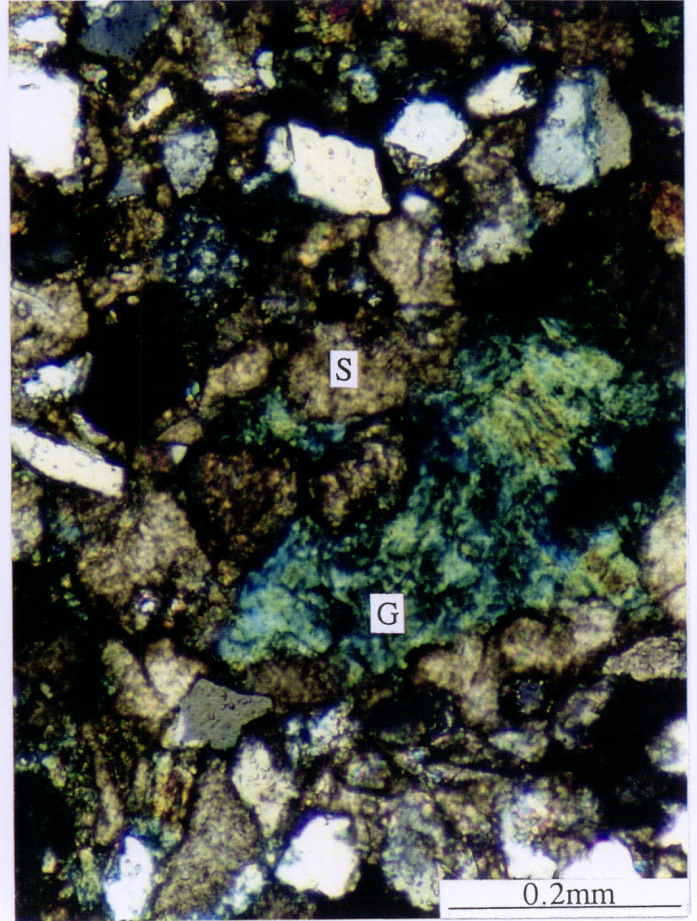
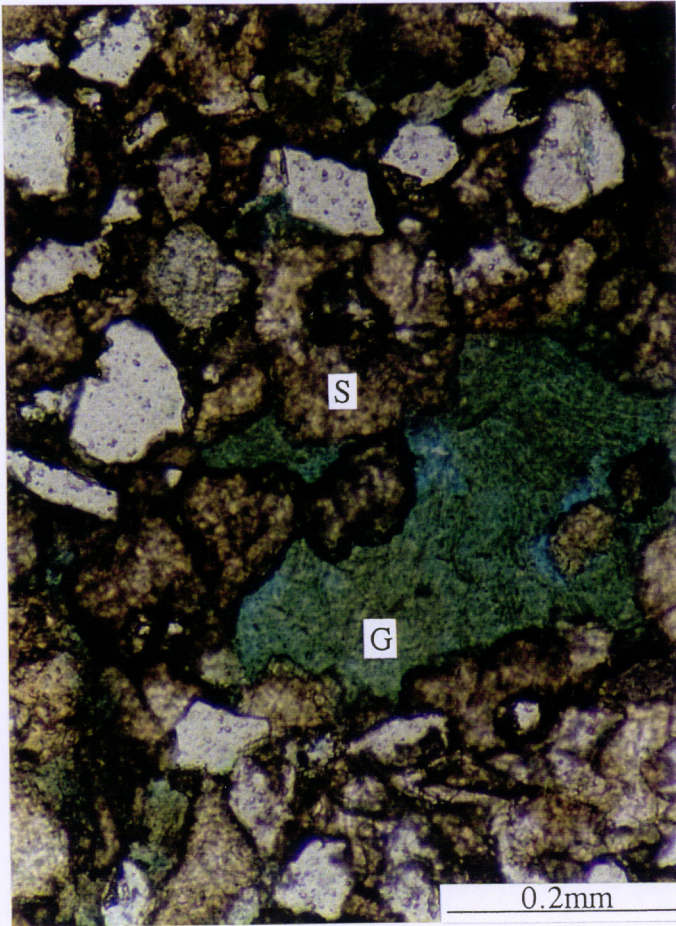


FIGURE 3

FIGURE 4

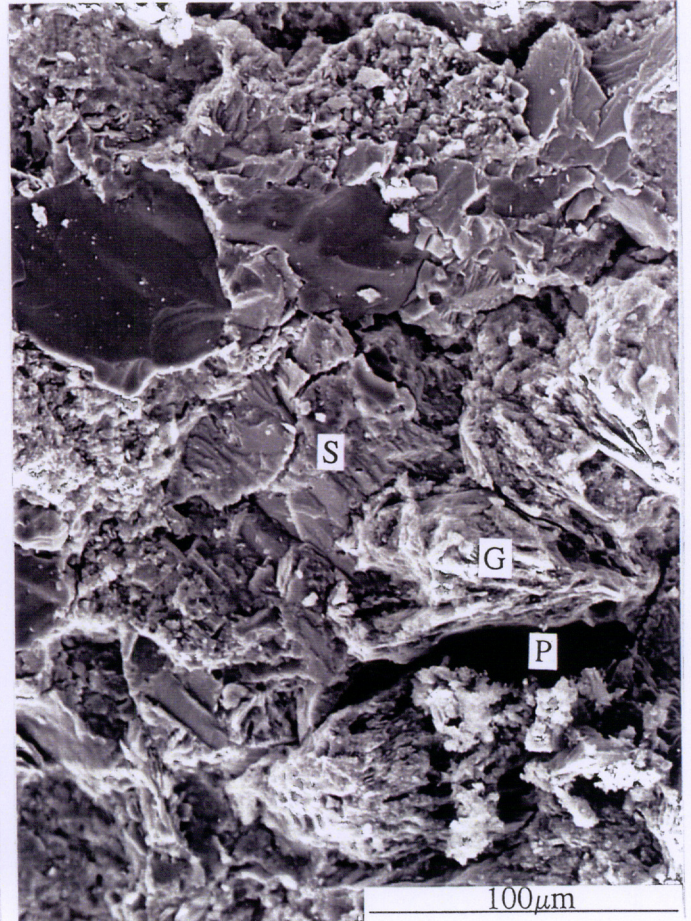
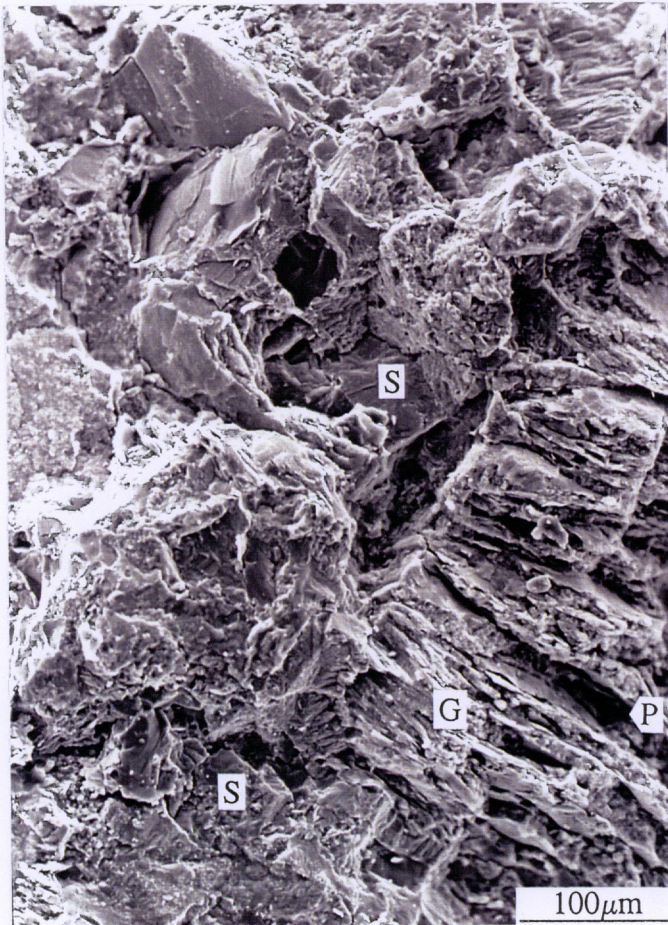


PLATE 6**S21 768.79m Zone 3****FIGURE 1** Plane polarised light**FIGURE 2** Crossed polarisers

This sandstone contains little intergranular porosity due to extensive pore filling by detrital clay (C) and associated fine pyrite (Py). Biotite has altered to glauconite (G).

FIGURE 3

Highly microporous sandstone in which most intergranular areas are occupied by detrital clay matrix (C).

FIGURE 4

Detail of detrital clay matrix (C) and associated microporosity (MP) occurring between quartz grains (Q). The clay appears to have recrystallised to kaolinite (K) in some places.

PLATE 6

907961 076

FIGURE 1

FIGURE 2

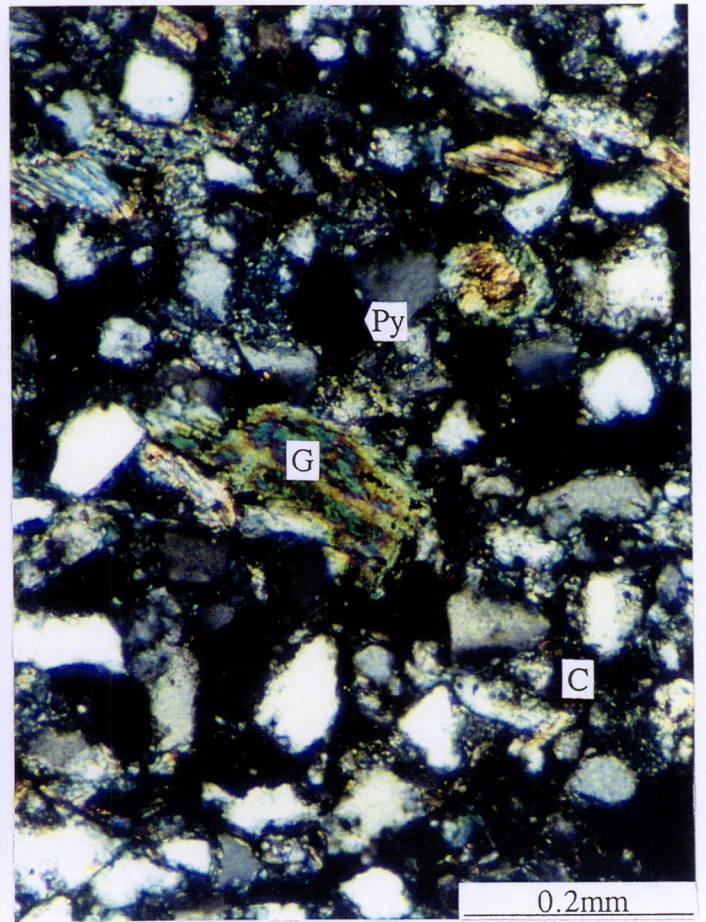
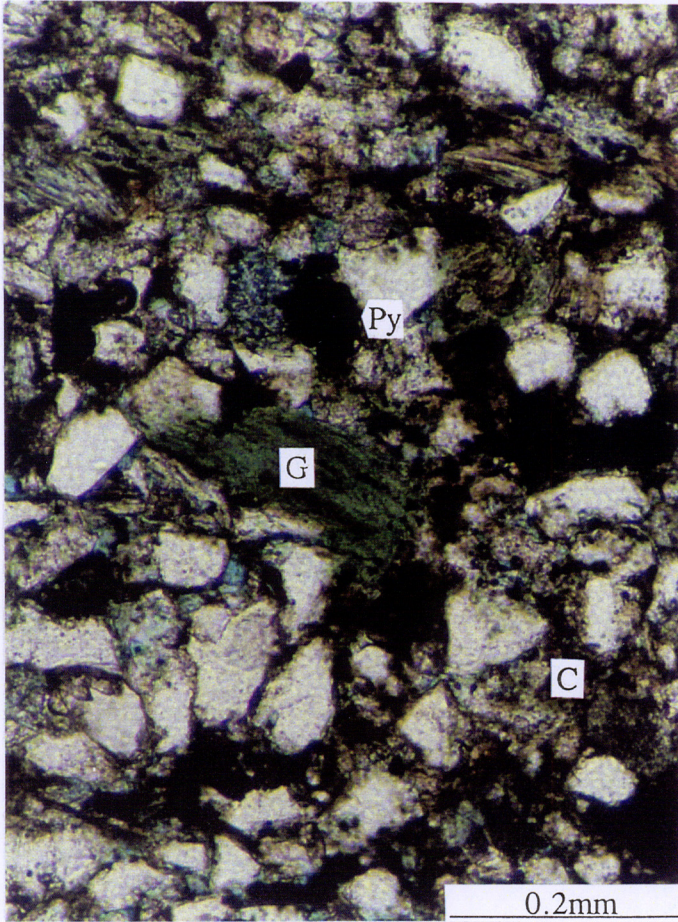


FIGURE 3

FIGURE 4

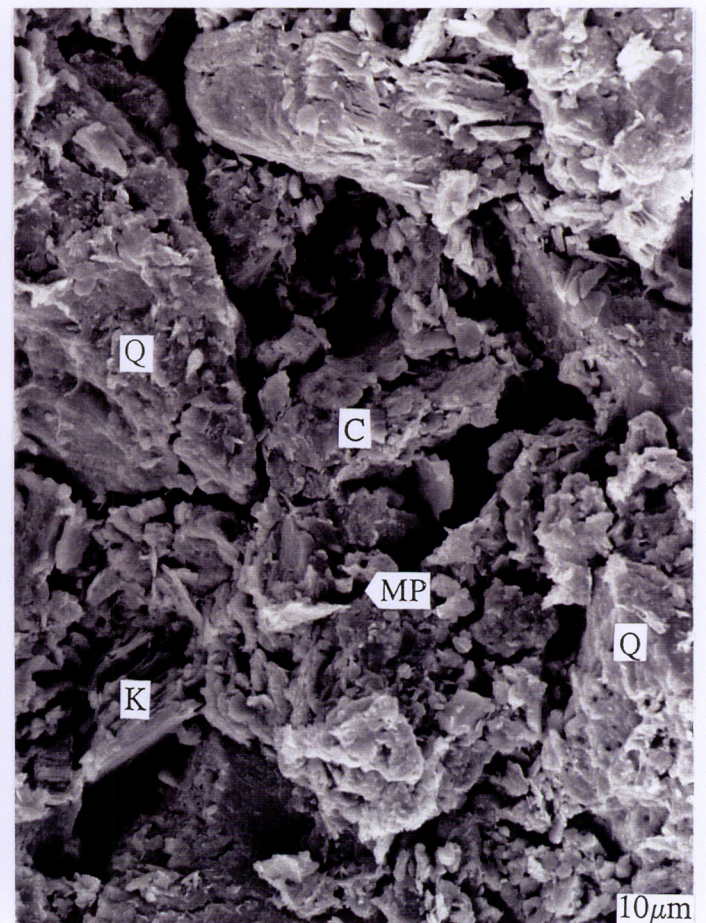


PLATE 7**S22 770.05m Zone 3****FIGURE 1** Plane polarised light**FIGURE 2** Crossed polarisers

Like in the previous sample, most intergranular areas in this sand are occupied by detrital clay (C). Muscovite (M) and biotite (B) are common grain constituents.

FIGURES 3 & 4

SEM micrographs showing representative areas in which macroporosity is lacking due to widespread pore filling by detrital clay matrix (C). A mica grain (M) is also marked in Figure 3.

PLATE 7

907961 078

FIGURE 1

FIGURE 2

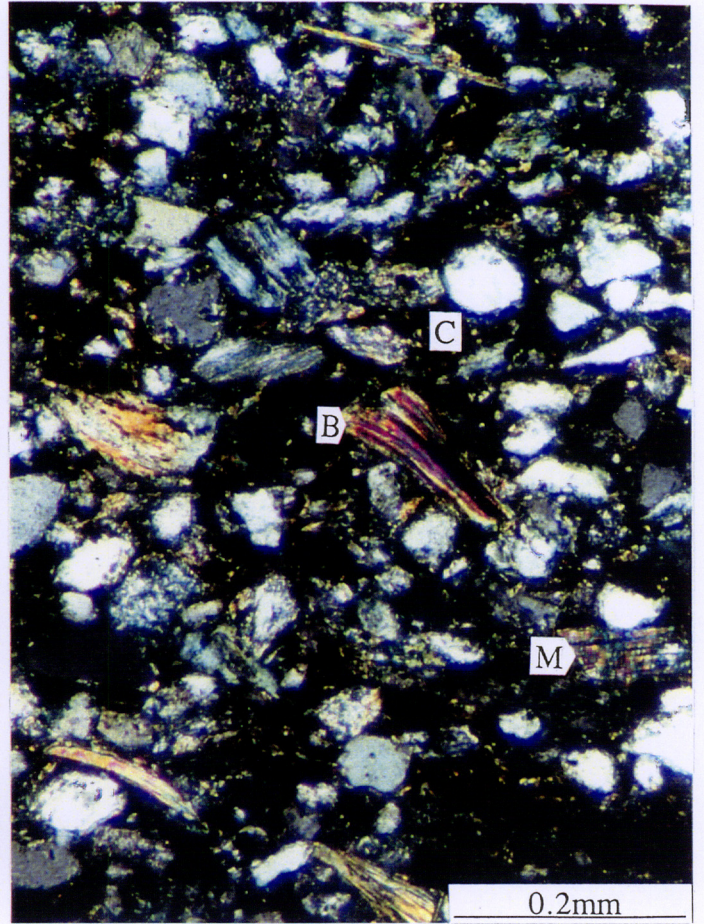
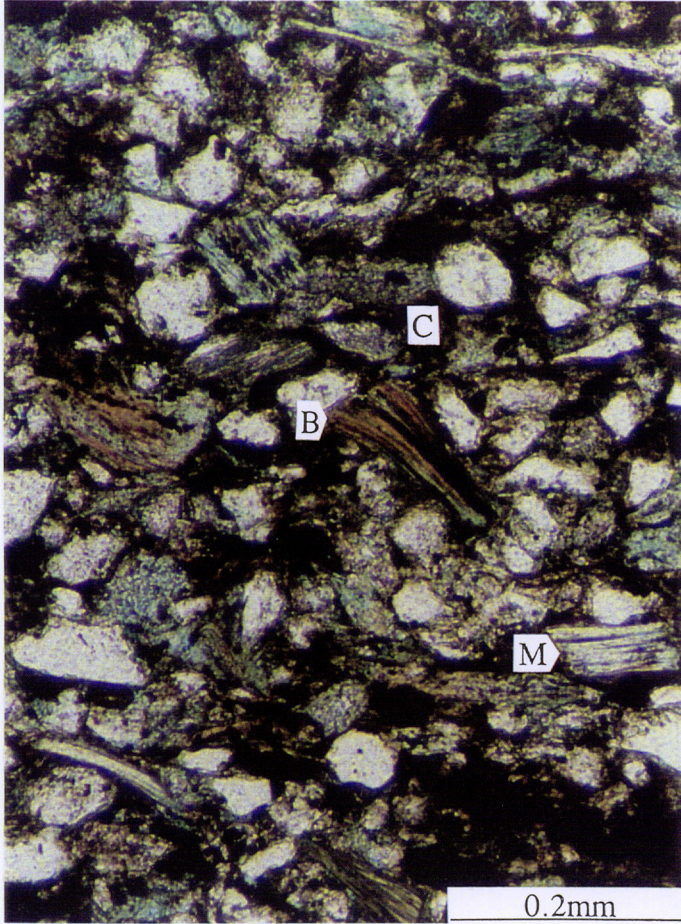


FIGURE 3

FIGURE 4

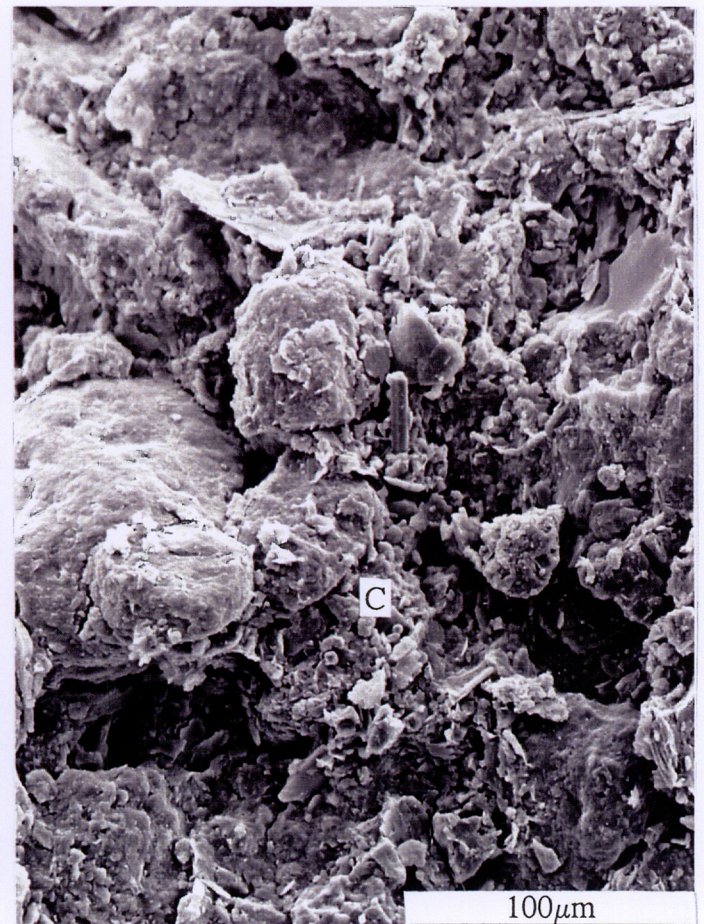


PLATE 8

70 771.60m Zone 4

FIGURE 1 Plane polarised light

FIGURE 2 Crossed polarisers

Clay matrix in this originally argillaceous, very fine grained sandstone has been largely replaced by siderite (S), the presence of which results in the rock having negligible permeability. Glauconite (G) and fine biotite (B) grains that are tightly cemented by siderite are uncompacted, indicating that siderite formed prior to compaction. The lower marked glauconite grain is a peloid, whereas the upper marked glauconite grain has formed by alteration of a biotite flake.

FIGURE 3

Most intergranular areas in this sandstone are tightly filled with siderite (S).

FIGURE 4

Detail of typical siderite (S) that largely fills an intergranular space. The siderite encloses and thus postdates framboidal pyrite (Py) that most likely formed in a shallow sulphate reduction zone. The other authigenic mineral in the field of view is kaolinite (K) that has formed by alteration of micaceous grains or detrital clay matrix. EDS analysis of siderite in the field of view revealed that the siderite is enriched in calcium and magnesium, which is consistent with siderite formation from a marine porewater.

PLATE 8

907961 080

FIGURE 1

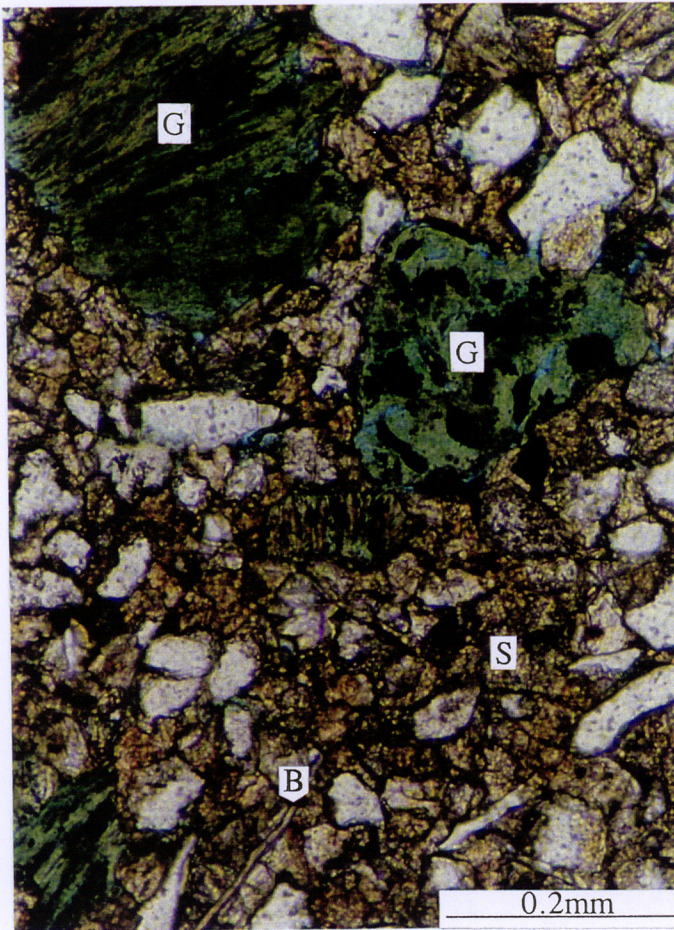


FIGURE 2

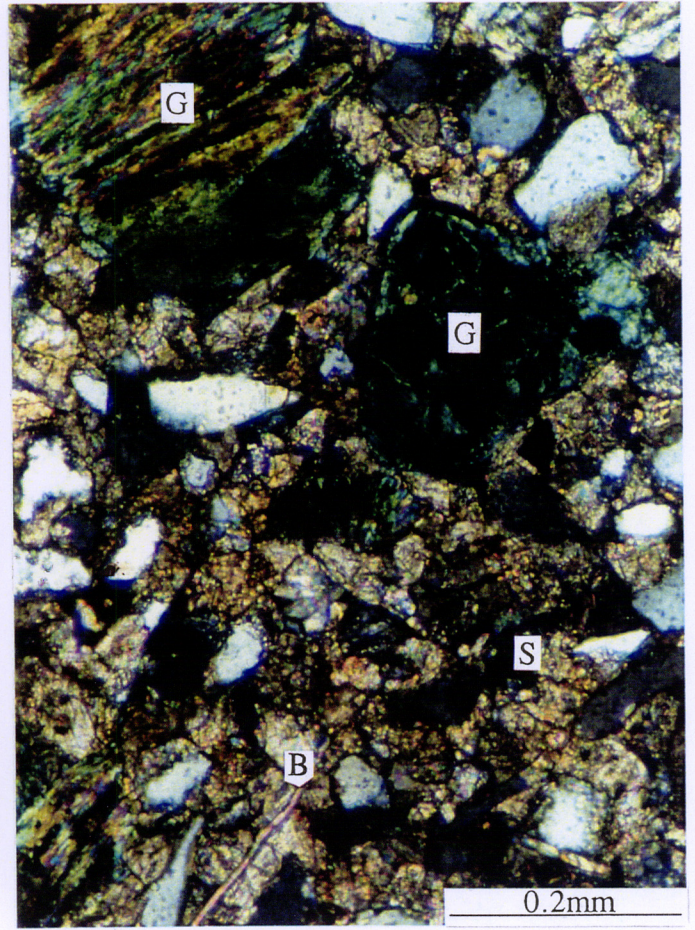


FIGURE 3

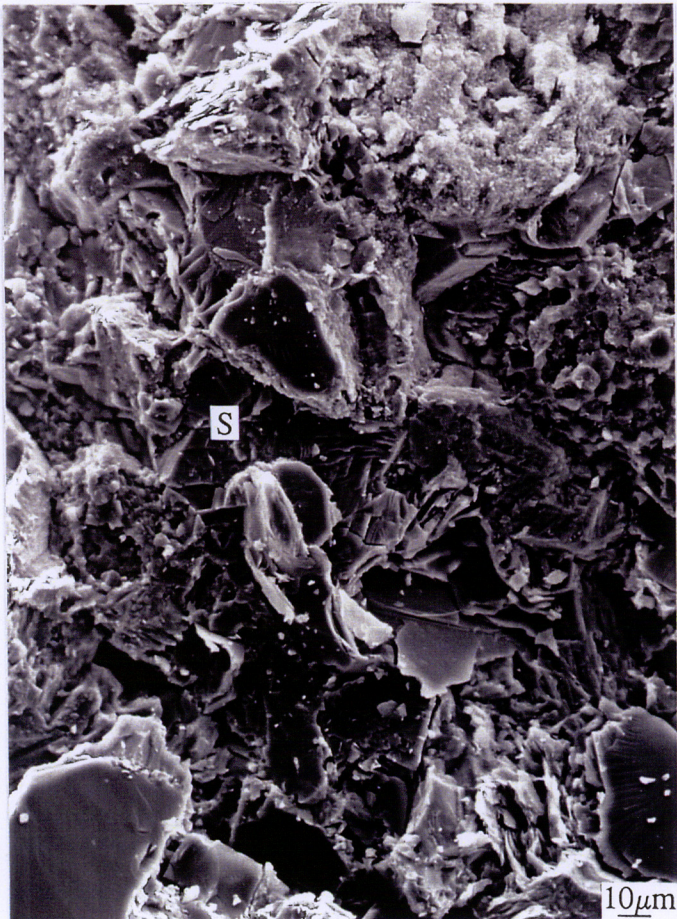


FIGURE 4

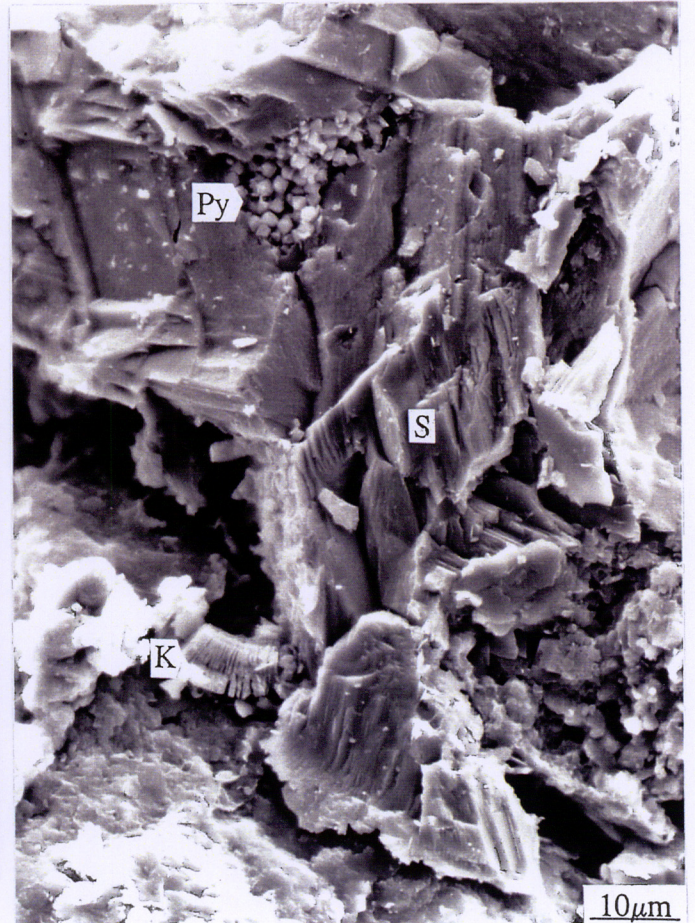


PLATE 9**S24 771.81m Zone 4****FIGURE 1** Plane polarised light**FIGURE 2** Crossed polarisers

Throughout most of this sandstone, intergranular spaces are filled by detrital clay (C) and associated fine siderite (S). Small, localised areas that are largely free of clay and siderite are macroporous (P). Glauconite (G) is the product of biotite alteration.

FIGURE 3

Only small, scattered intergranular macropores (P) remain in this sandstone due to extensive pore filling by detrital clay (C). Being scattered, the macropores are poorly interconnected.

FIGURE 4

Primary intergranular pores (PP) are preserved between loosely packed framework grains, and an adjacent intergranular area is filled by detrital clay (C) that has partly recrystallised to kaolinite (K).

PLATE 9

907961 082

FIGURE 1

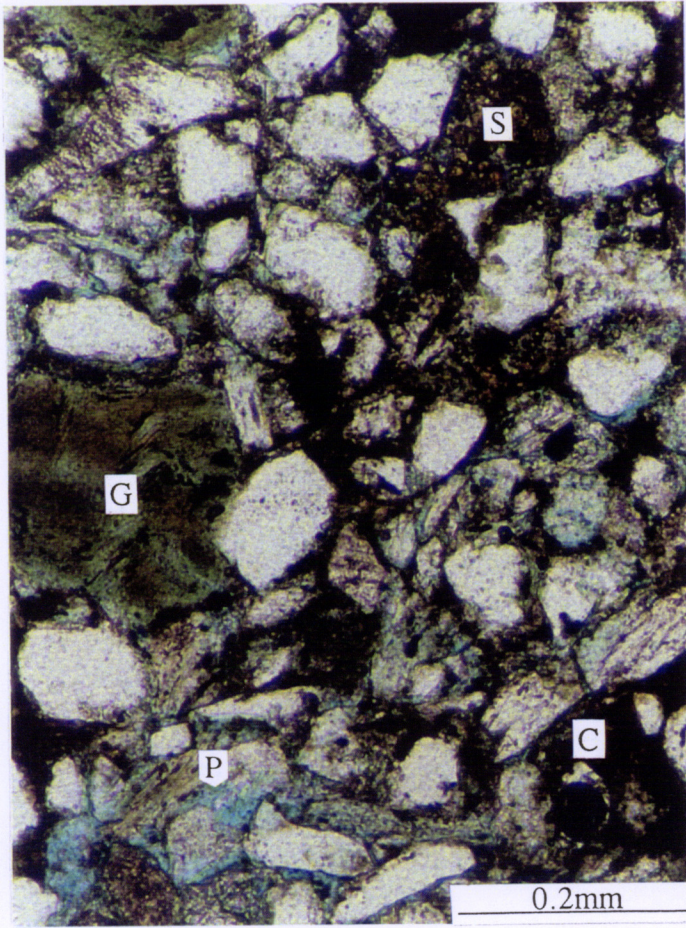


FIGURE 2

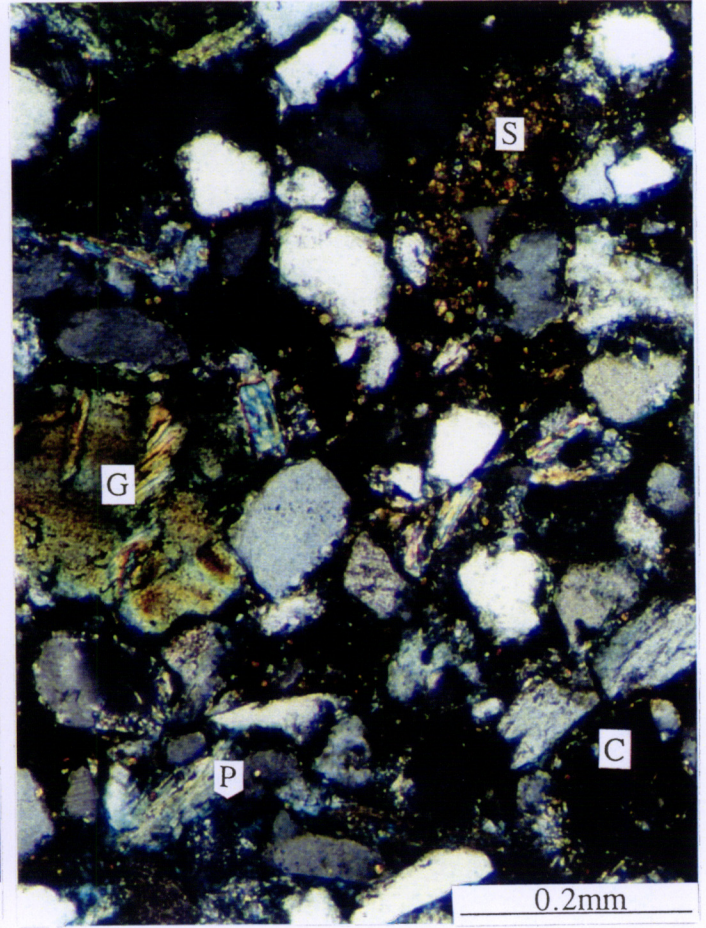


FIGURE 3



FIGURE 4

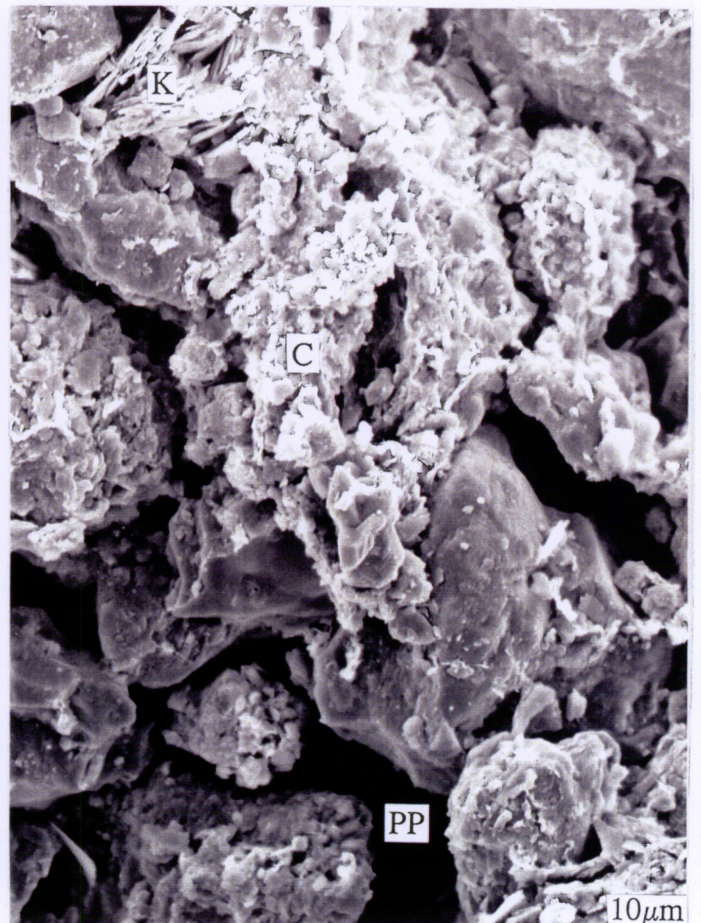


PLATE 10S26 773.79m Zone 4**FIGURE 1** Plane polarised light**FIGURE 2** Crossed polarisers

Porosity reduction in this glauconitic, very fine grained sandstone is due to pore filling by detrital clay (C) and compacted glauconite (G). Clean areas dominated by clastic grains contain abundant primary intergranular porosity (PP). Biotite (B) and a bitumen-rimmed monazite grain (arrow) are also marked.

FIGURE 3

This area is largely free of detrital clay matrix, but there has been some porosity loss by compactional deformation of glauconite (G) and altered micaceous grains. Primary intergranular pores (PP) occur mainly between adjacent rigid grains (quartz, K-feldspar).

FIGURE 4

Detail of upper right part of previous micrograph showing clean primary intergranular pores (PP) preserved where loosely compacted rigid grains are juxtaposed. Intergranular porosity has been eliminated in an adjacent area (far right side of micrograph) by compaction of juxtaposed glauconite grains (G). Glauconite compaction is a significant cause of porosity loss in cleaner parts of the sample.

FIGURE 1

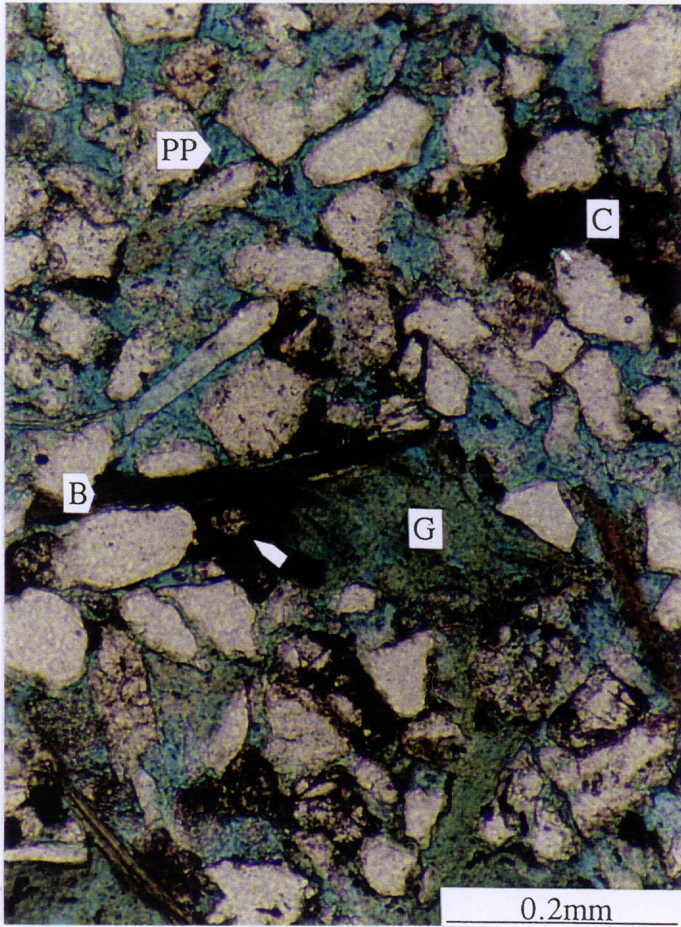


FIGURE 2

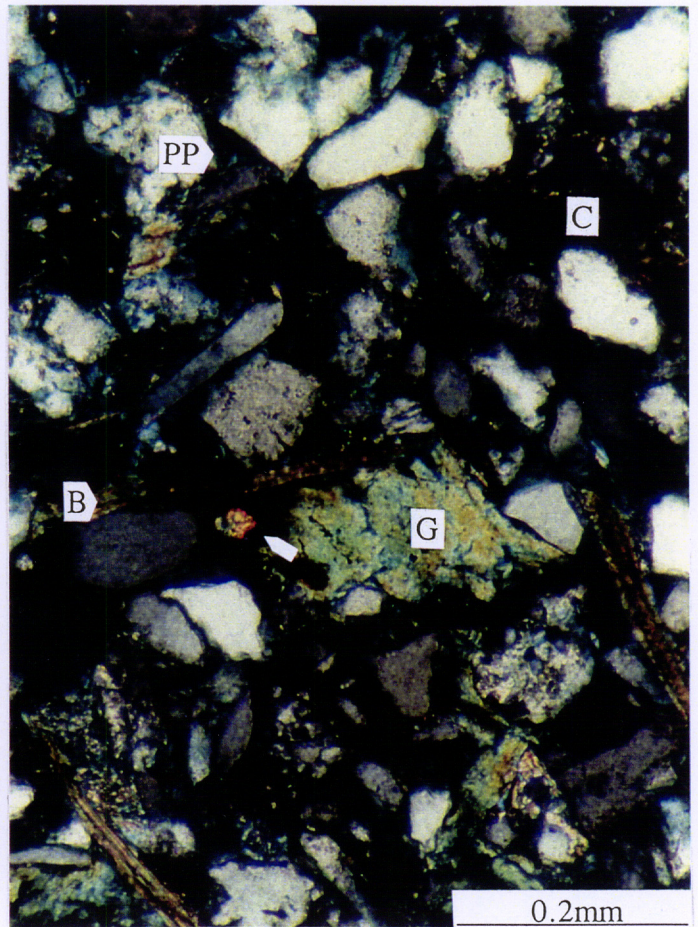


FIGURE 3



FIGURE 4

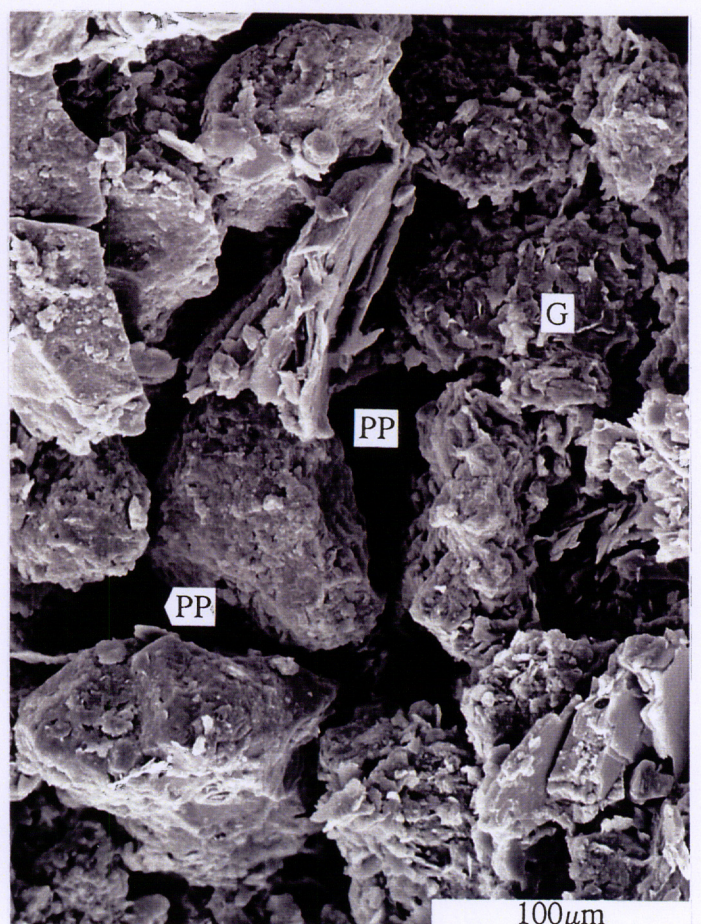


PLATE 11

S28 775.82m Zone 5

FIGURE 1 Plane polarised light

FIGURE 2 Crossed polarisers

Low magnification micrograph showing the patchy distribution of detrital clay matrix (C). Much of the sample lacks detrital clay and is consequently highly macroporous (P).

FIGURE 3 Plane polarised light

FIGURE 4 Crossed polarisers

In an area where detrital clay matrix is lacking, abundant primary intergranular porosity (PP) is preserved between loosely packed grains of quartz, K-feldspar (KF) and glauconite (G). The marked glauconite grain has undergone slight compaction between adjacent rigid grains.

PLATE 11

907961 086

FIGURE 1

FIGURE 2

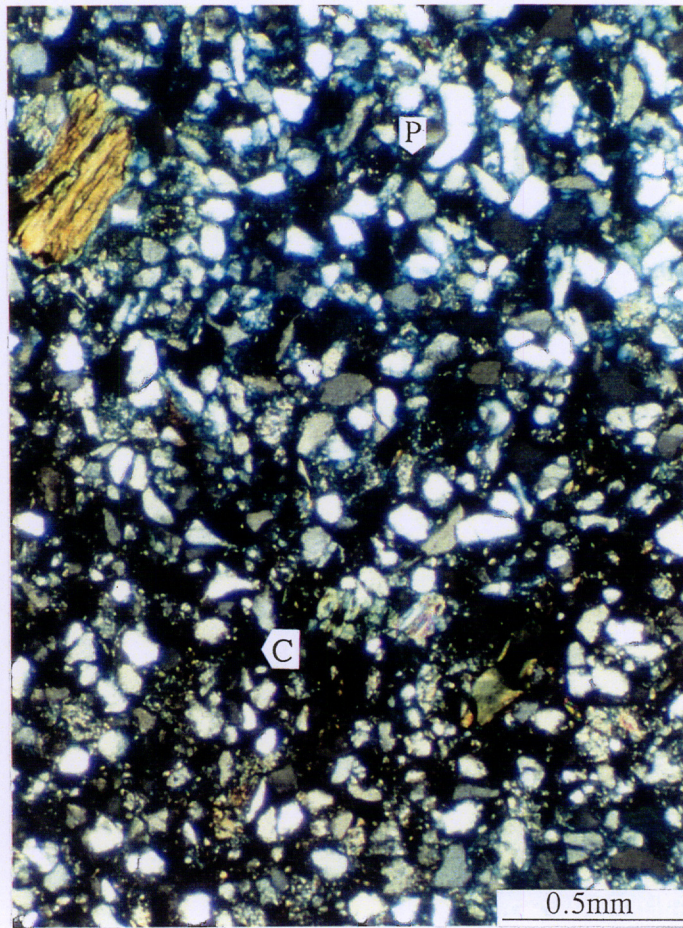
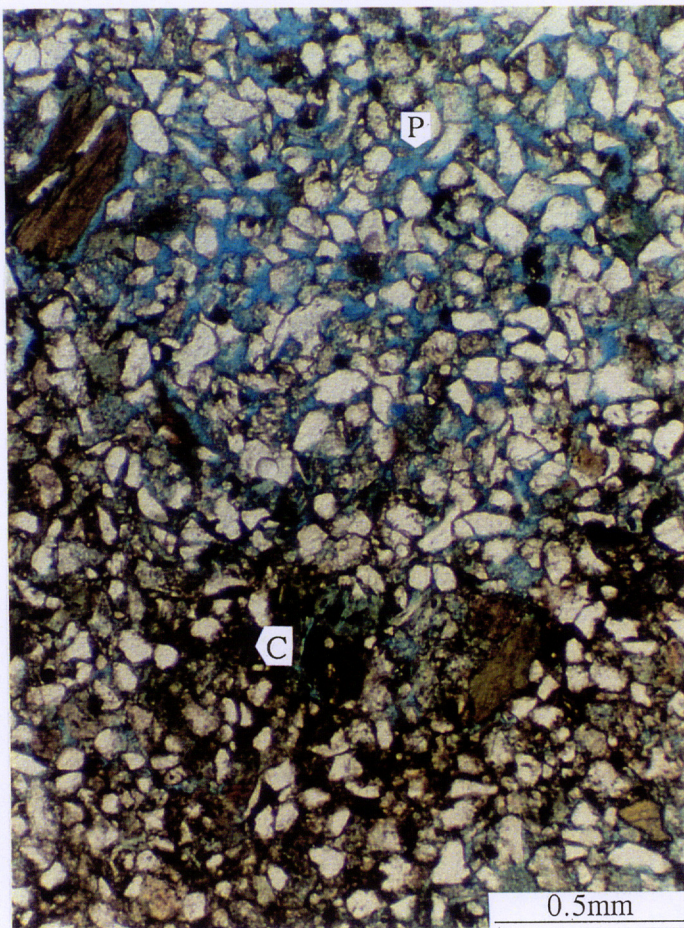


FIGURE 3

FIGURE 4

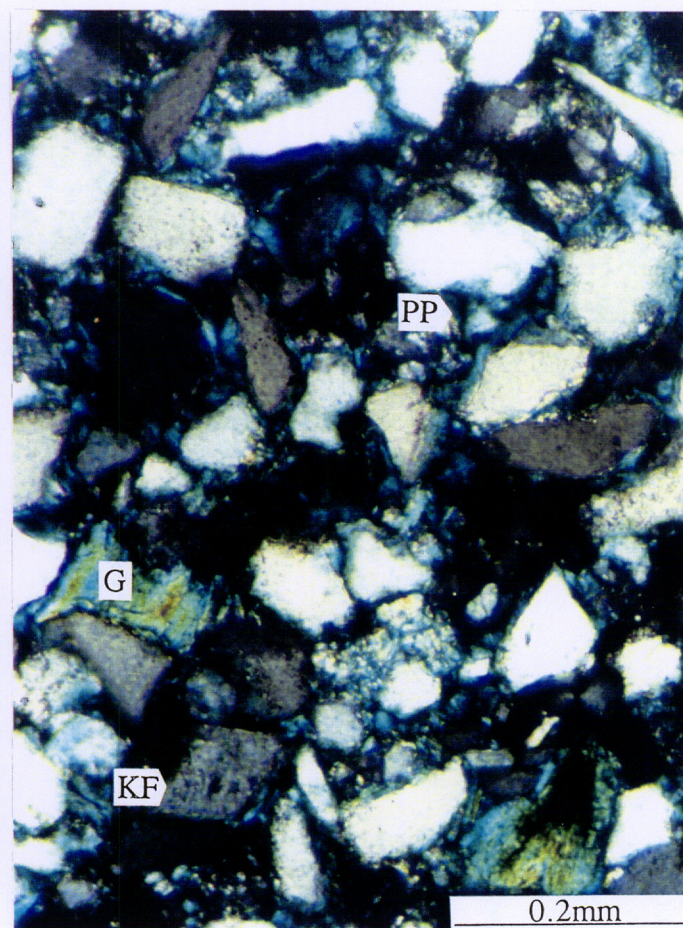
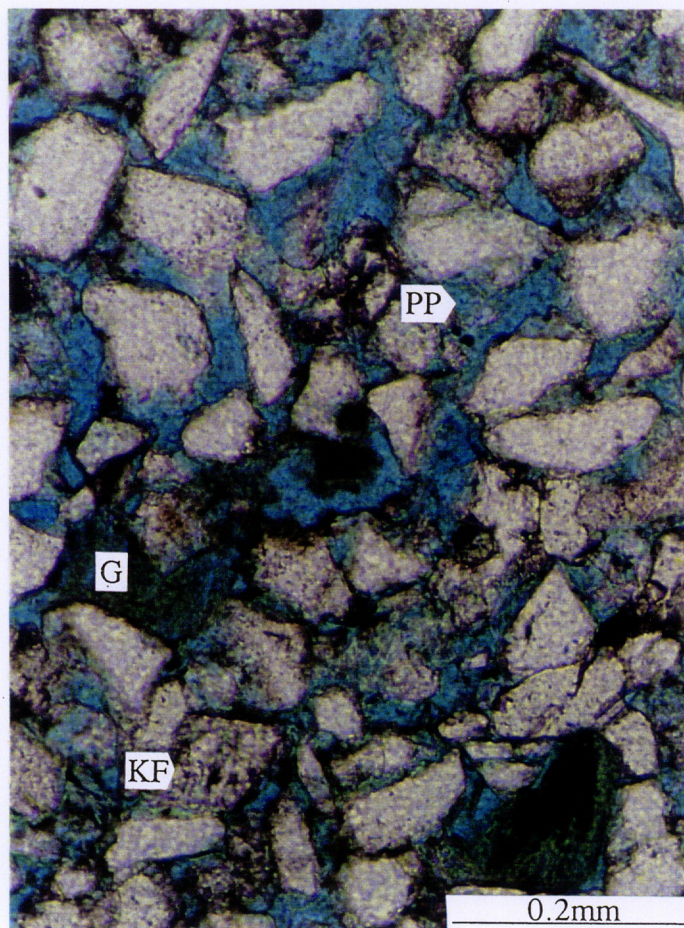


PLATE 12**S28 775.82m Zone 5 cont.****FIGURE 1**

Clean sandstone in which abundant primary intergranular porosity (PP) is preserved between loosely packed framework grains, although some intergranular spaces are occupied by compacted glauconite (G). Clay-free pore throats (arrow) are around 10-20µm in length.

FIGURE 2

Detail of loosely packed quartz (Q) and K-feldspar (KF) grains and a compacted glauconite grain (G).

S30 777.80m Zone 5

FIGURE 3 Plane polarised light

FIGURE 4 Crossed polarisers

This low magnification micrograph shows the patchy distribution of detrital clay matrix (C) and the highly macroporous (P) nature of parts of the sandstone that contain little or no detrital clay.

PLATE 12

FIGURE 1

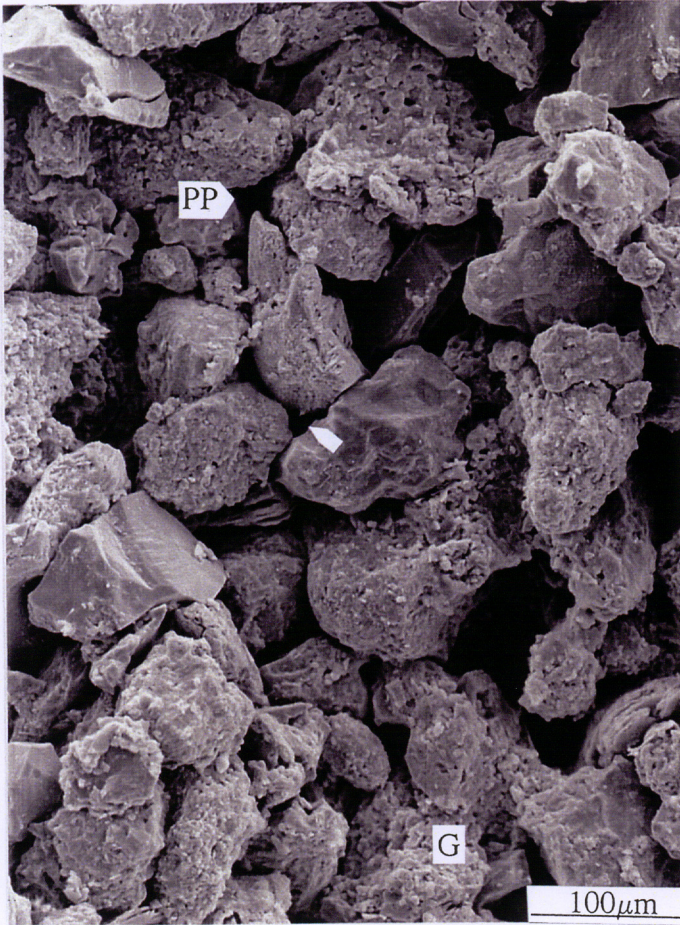


FIGURE 2

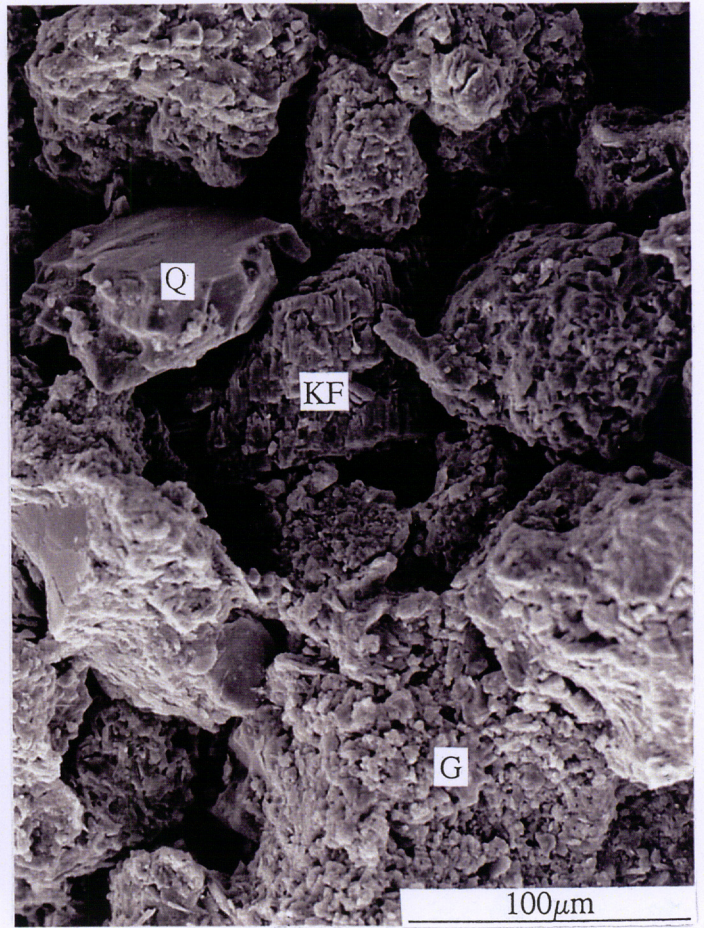


FIGURE 3

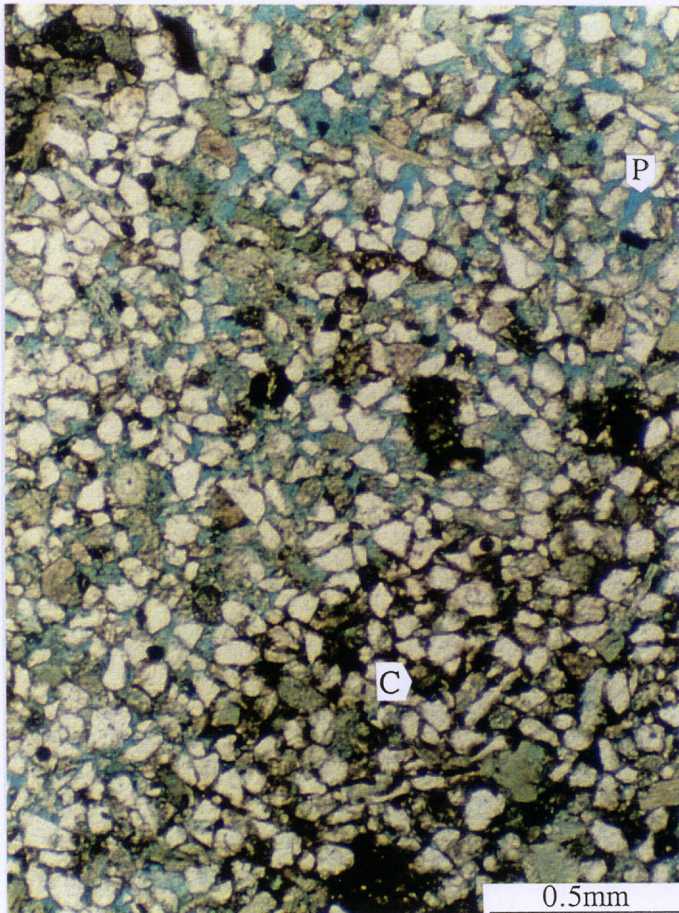


FIGURE 4

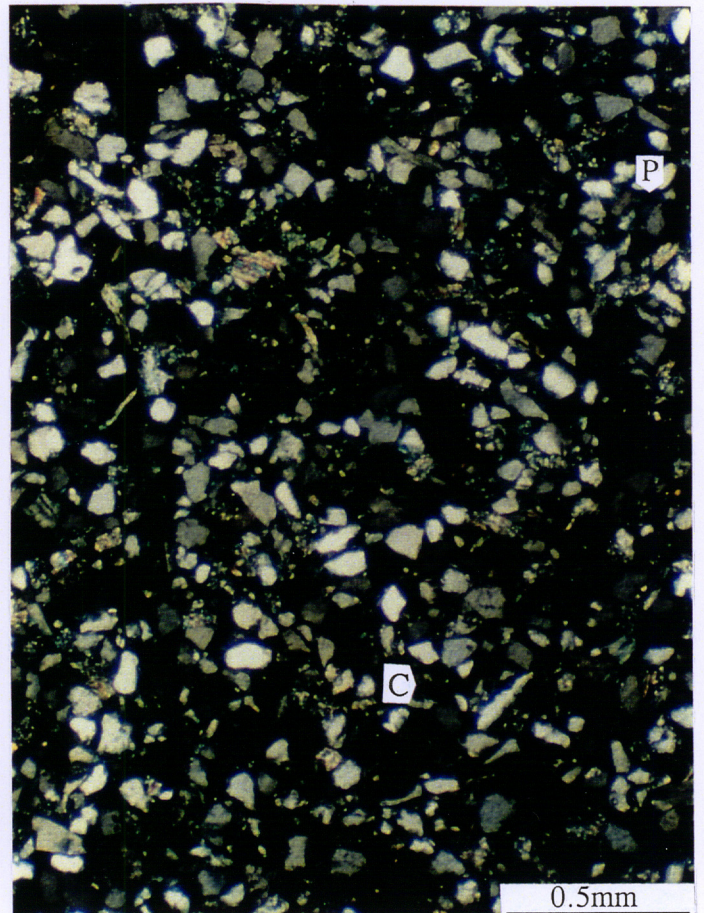


PLATE 13

S30 777.80m Zone 5 cont.

FIGURE 1 Plane polarised light

FIGURE 2 Crossed polarisers

Abundant primary intergranular porosity (PP) is preserved between poorly compacted framework grains, except where intergranular spaces are completely filled by patchy detrital clay (C).

FIGURE 3

This sandstone contains abundant primary intergranular porosity (PP), except in localised areas where intergranular spaces are filled by detrital clay (C).

FIGURE 4

Preservation of abundant intergranular porosity (PP) in clean areas of the sandstone reflects the fact that framework grains are uncemented and generally poorly compacted. Authigenic kaolinite (K) is associated with an altered micaceous grain.

FIGURE 1

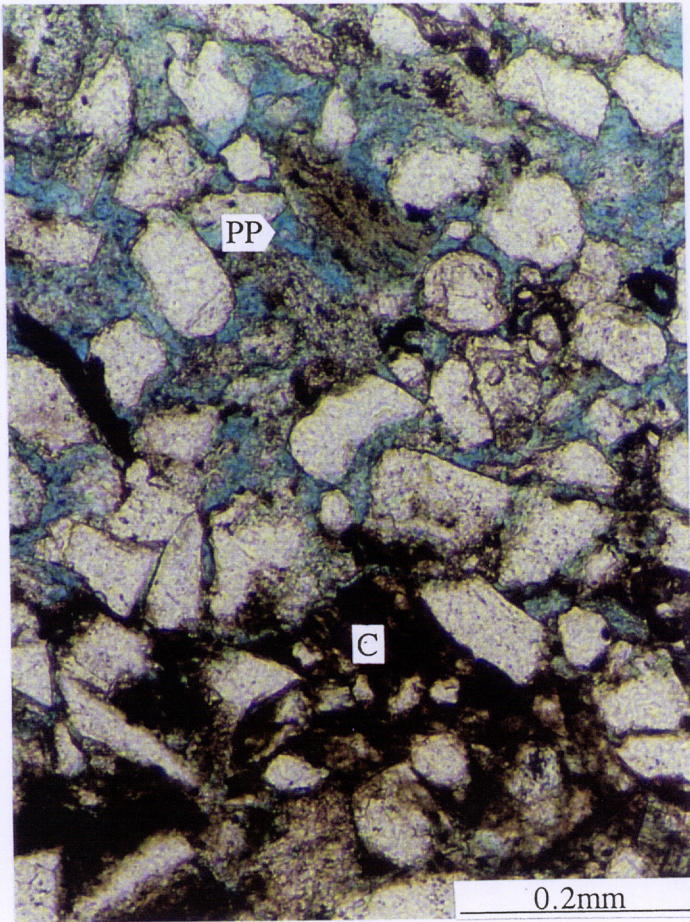


FIGURE 2

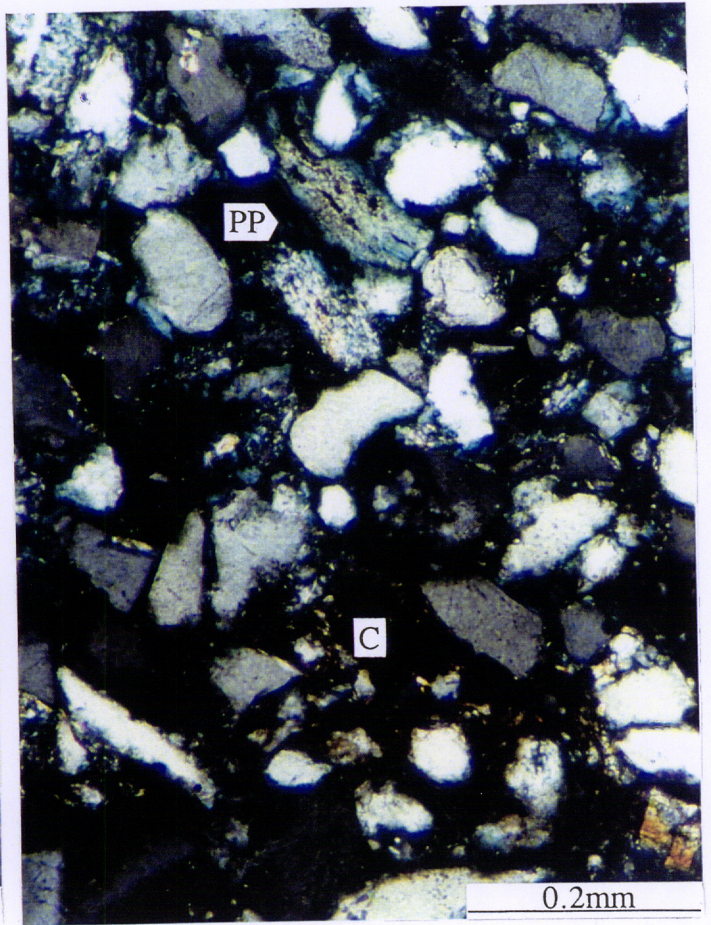
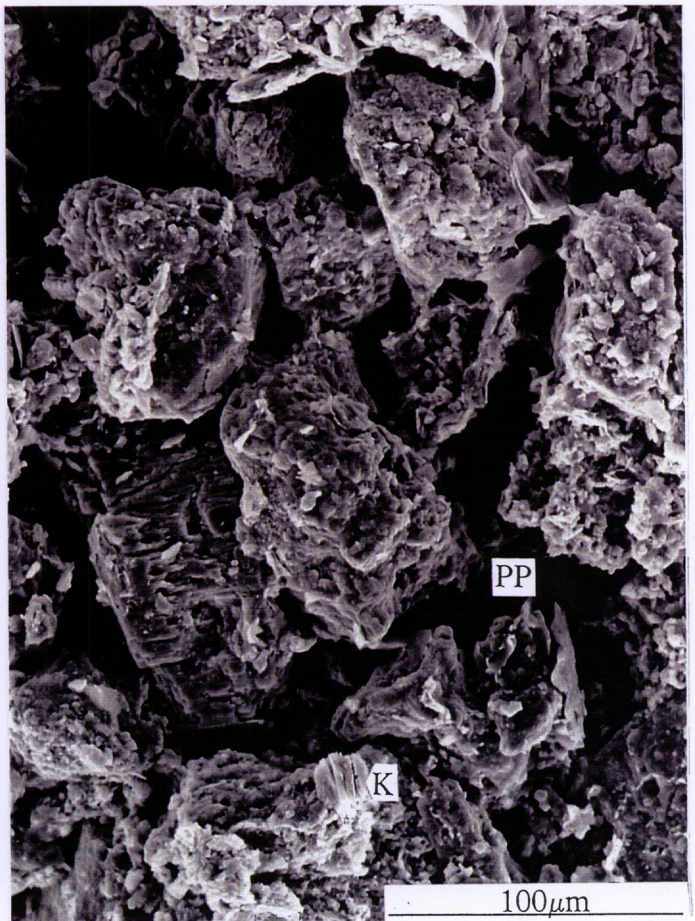


FIGURE 3



FIGURE 4



907961 031

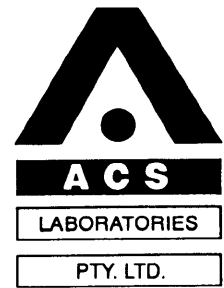
907961 092

APPENDIX 15

BALEEN-2

**CORE LITHOLOGICAL
DESCRIPTION AND
SEDIMENTOLOGICAL
INTERPRETATION REPORT
-ACS LABORATORIES-**

907861 093



**DETAILED CORE DESCRIPTION AND
SEDIMENTOLOGICAL INTERPRETATION
of**

BALEEN-2

for

BASIN OIL NL

by

ACS LABORATORIES PTY LTD

907961 094

18 January 2000



Basin Oil NL
Level 29
44 St Georges Tce
PERTH WA 6000


Attention: Mark Adamson

FINAL REPORT: 0424-01

CLIENT REFERENCE:

MATERIAL: Conventional Core
LOCALITY: Baleen-2, VIC/RL5 Gippsland Basin
WORK REQUIRED: Detailed Core Description and Sedimentological Interpretation

Please direct technical enquiries regarding this work to the signatory below under whose supervision the work was carried out.



PETER CROZIER
Operations Manager

ACS Laboratories Pty Ltd shall not be liable or responsible for any loss, cost, damages or expenses incurred by the client, or any other person or company, resulting from any information or interpretation given in this report. In no case shall ACS Laboratories Pty Ltd be responsible for consequential damages including, but not limited to, lost profits, damages for failure to meet deadlines and lost production arising from this report.

Brisbane
Laboratory:

P.O. Box 396, Chermside South Qld 4032, Australia
☎: 61 7 3350 1222 Facsimile: 3359 0666
E-mail: acs.bris@acslabs.com.au

ACS Laboratories Pty Ltd
ACN: 008 273 005

**DETAILED CORE DESCRIPTION
AND
SEDIMENTOLOGICAL INTERPRETATION**

of

BALEEN-2

A final report prepared

for

BASIN OIL NL

by

**PETER A. ARDITTO
SEDSTRAT Pty Ltd
ACN: 090 328 247**

January 2000

CONTENTS

1.	SUMMARY	1
2.	INTRODUCTION	1
3.	BALEEN-2, CORES 1 AND 2	
	3.1 Lithological Description	1
	3.2 Environmental Interpretation	2
4.	REFERENCES	4
5.	SUMMARY OF ICHNOFAUNA TERMINOLOGY	4

APPENDICES

I FIGURES

1:25 A4 Core description and interpretation sheets

1:200 A4 Core gamma ray log and wireline gamma ray log with plug permeability

1:280 A4 portions of selected wireline logs with depth-corrected position of cores

II PLATES

Selected 30 cm A4 colour core photographs

1. SUMMARY

Two 4 inch (10 cm) diameter conventional cores were recovered from Baleen-2; core #1 recovered over the interval 746.00m - 762.20m log depth, and core #2 recovered over the interval 763.70m - 779.50m log depth. These were taken from very fine to fine grained burrowed to bioturbated glauconitic silty or muddy sandstones of the Gurnard Formation, uppermost Latrobe Group, within the offshore Gippsland Basin of Victoria. A detailed lithological description and environmental interpretation of these two cores is given in sections 3.1 and 3.2 of this report.

2. INTRODUCTION

Baleen-2 was an appraisal well following the success of the discovery well, Baleen-1, in VIC/RL5, offshore Gippsland Basin. Peter Arditto, of SEDSTRAT Pty Ltd, was subcontracted by ACS Laboratories Pty Ltd on behalf of the client, Basin Oil NL, to undertake a detailed lithological description and environmental interpretation of the conventional core recovered from Baleen-2. This study was undertaken by the author over the period 10th and 11th January at the offices of ACS Laboratories Pty Ltd, 30 Boothby Street, Kedron, Queensland. During this time lithological descriptions were recorded on A4 1:25 scale graphic core logs and these form the basis of this report. Lithological descriptions and environmental interpretations are followed by the drafted A4 1:25 graphic core logs, an A4 1:200 core gamma ray log with a superimposed wireline gamma ray log and A4 reduced portions (1:280) of a selection of the 1:200 with the position of cores #1 and #2 shown. A selection of A4 colour photographs of 30 cm sections of core are included to show examples of some of the ichnofauna and depositional textures mentioned on the graphic core logs and in section 3.2 of the text.

3. BALEEN-2, CORES #1 AND #2.

3.1 Lithological Description

The interval 747.25m - 746.00m (top core #1) is muddy sandstone, very fine grained and very poorly sorted, micromicaceous (trace) and glauconitic (5%) with dispersed fine grained glauconite pellets. The base of the interval contains ferroan dolomite nodules, up to 15cm thick. Internally the interval is intensely burrowed to bioturbated by *Thalassinoides*. Sporadic *Ophiomorpha* burrows occur near the top of the core. Overall the sandstone has fair visual porosity. The interval 750.83m - 747.25m is sandstone, as below, with a gradational top. The interval 756.52m - 751.16m is silty sandstone, very fine to fine grained and moderately sorted, micromicaceous (trace) and glauconitic (5%) with dispersed fine grained glauconite pellets. Internally the interval is homogeneous to moderately burrowed by *Thalassinoides*. Sporadic *Ophiomorpha* burrows occur towards the base. Overall the sandstone has good visual porosity.

The interval 758.52m - 756.77m is muddy sandstone, very fine grained and poorly sorted, micromicaceous (trace) and glauconitic (5%) with dispersed fine grained glauconite pellets. Internally intensely churned by abundant *Thalassinoides* burrows.

Overall the sandstone has good visual porosity. The interval 762.20m (base core #1) - 760.42m and 760.22m - 758.50m is silty sandstone, very fine grained and moderately sorted, micromicaceous (trace) and glauconitic (5%) with dispersed fine grained glauconite pellets. Internally the interval is homogeneous to moderately burrowed by *Thalassinoides* with rare isolated *Skolithos* burrows. The top of the interval is gradational. The basal 0.65m is core rubble. Overall the sandstone has good visual porosity.

The interval 764.35m - 763.70m (top core #2) is silty sandstone, very fine to fine grained and moderately sorted, micromicaceous (trace) and glauconitic (5%) with dispersed fine grained glauconite pellets. Internally the interval is homogeneous to sparsely burrowed by *Ophiomorpha*. The upper half of the interval is replaced by a ferroan dolomite nodule. The interval 768.30m - 764.35m is silty sandstone, very fine to fine grained and moderately sorted, micromicaceous (trace) and glauconitic (5%) with dispersed fine grained glauconite pellets, upward coarsening to fine grained, less silty, and moderately sorted sandstone. Internally the lower half is bioturbated and contains sporadic *Ophiomorpha* burrows, while the upper half is homogeneous to moderately burrowed by *Thalassinoides*. The top is gradational into the overlying interval. Overall the sandstone has very good visual porosity.

The interval 771.53m - 769.83m and 769.66m - 768.30m is sandy mudstone, micromicaceous (trace) and glauconitic (5% - 7%) with dispersed fine grained glauconite pellets. Internally the interval contains faint wavy mudstone lenticular laminations which are highly disturbed by very fine grained sand-filled common *Zoophycos* burrows. The top is gradational into the overlying interval. Sporadic pyrite-replaced *Skolithos* burrows occur near the middle of the interval. Overall the sandstone has good visual porosity.

The interval 775.70m - 771.53m is muddy sandstone, very fine to fine grained and moderately to poorly sorted, micromicaceous (trace) and glauconitic (5% - 7%) with dispersed fine grained glauconite pellets. Internally the interval is intensely churned by *Thalassinoides* burrows. Sporadic pyrite nodules, 2cm - 3cm in diameter, are developed around some burrows. Sporadic ferroan dolomite nodules occur towards the middle and the interval is capped by a 30cm diameter nodule. The top of the interval is gradational into the overlying interval. Overall the sandstone retains good visual porosity. The interval 778.80m - 776.87m and 776.63m - 775.70m is silty sandstone, very fine to fine grained and moderately sorted, micromicaceous (trace) and glauconitic (5%) with dispersed fine grained glauconite pellets. Internally the interval is churned by common *Ophiomorpha* and *Thalassinoides* burrows. Overall the sandstone has very good visual porosity. The interval 779.50m (base core #2) - 778.80m is core rubble and loose sand, sandstone as above, with sporadic pyrite nodules.

3.2 Environmental Interpretation

Environmental interpretations made by the author are based on lithological associations, primary sedimentary structures, ichnofauna and associated wireline logs over and adjacent to the cored intervals.

The entire interval recovered in cores #1 and #2 is glauconitic and very fine to fine grained silty to muddy sandstone which has been moderately to intensely burrowed to bioturbated and is interpreted as a succession of offshore marine to ?distal transitional lower shoreface parasequence sets. A parasequence is a relatively conformable succession of genetically related progradational beds or bed sets bounded by marine-flooding surfaces or their correlative surfaces (Van Wagoner, *et al*, 1990). The associated ichnofauna is typical of deposition in a middle to outer shelfal marine setting and the presence of glauconite pellets, minor pyrite and ferroan dolomite indicate reducing conditions. No evidence of storm wave-influence was recognised in any part of the cored interval so deposition is considered to be just below storm wave base, updip storm-induced turbiditic and suspension deposition being the main mechanisms inferred for sediment transport to the well location (with subsequent biological modification). The wireline log character indicates that the cored interval is part of an overall transgressive systems tract at the top of the Latrobe Group where the fluvio-deltaic to nearshore marine siliciclastics of that group are progressively drowned (Gurnard Formation) and give way to the essentially open marine overlying carbonate succession of the Seaspray Group. Several parasequences (punctuated aggradational cycles of Goodwin and Anderson, 1985), some capped by ferroan dolomite nodules, are recognised within the Gurnard Formation and are detailed below.

The interval 747.25m - 746.00m (top core #1) is a very fine grained muddy and intensely burrowed (*Thalassinoides*, minor *Ophiomorpha*) glauconitic sandstone, with common large ferroan dolomite nodules, interpreted as a basal parasequence deposited in an offshore setting. The interval 758.50m - 747.25m is an upward coarsening succession (complete shelfal marine parasequence) of very fine to fine grained muddy to silty glauconitic sandstone, moderately to intensely burrowed by *Thalassinoides* and sporadic *Ophiomorpha*. The interval 762.20m (base core #1) - 758.50m is silty glauconitic sandstone, homogeneous to moderately burrowed by *Thalassinoides* (rare isolated *Skolithos*), interpreted as an incomplete upper shelfal marine parasequence.

The interval 764.35m - 763.70m (top core #2) is glauconitic silty sandstone with *Ophiomorpha* and a large ferroan dolomite nodule, interpreted as the basal portion of the shelfal marine parasequence in the base of core #1. The interval 771.53m - 764.35m is an upward coarsening succession (complete parasequence) of glauconitic sandy mudstone, with common *Zoophycos* burrows, to very fine grained glauconitic silty sandstone, homogeneous to moderately burrowed by *Thalassinoides* and rare *Ophiomorpha*. The base contains a large syndepositional ferroan dolomite nodule, indicative of sediment starvation.

The interval 779.50m (base core #2) - 771.53m is glauconitic silty to muddy sandstone with common *Ophiomorpha* and/or *Thalassinoides* burrows, displaying a progressive upward muddying (drowning) character. This is interpreted as an upper shelfal marine parasequence.

4. REFERENCES

GOODWIN, P.W., & ANDERSON, E.J., 1985: Punctuated aggradational cycles: a general hypothesis of episodic stratigraphic accumulation. *Journal of Geology* 93, 515-533.

PEMBERTON, S.G., (ED), 1992: Applications of Ichnology to Petroleum Exploration; A Core Workshop. SEPM Core Workshop No. 17, Calgary, June 21, 1992. ISBN #0-918985-97-8.

VAN WAGONER, J.C., MITCHUM, R.M., CAMPION, K.M., & RAHMANIAN, V.D., 1990: Siliciclastic Sequence Stratigraphy in Well Logs, Cores, and Outcrop. AAPG Methods in Exploration Series, No.7.

5. SUMMARY OF ICHNOFAUNA TERMINOLOGY

OPHIOMORPHA

Description:

Simple to complex burrow systems distinctly lined with agglutinated pelletoidal muddy sediment. Burrow lining is smooth on the interior and densely to strongly mammalated or nodose on the exterior. Individual pellets or pellet masses may be discoid, ovoid, conical, mastoid, bilobate or irregular in shape. Branching is irregular and, where present, Y-shaped. At bifurcations, burrows become swollen.

Interpretation:

Based mainly on the character of the pelletal burrow lining, four ichnospecies are recognised. In well burrowed offshore sediments, wall linings are thin and poorly developed and the species of the ichnogenus is somewhat gradational with *Thalassinoides*. Ophiomorpha represents the dwelling burrows of decapod crustaceans, including numerous species of thalassinidean shrimp.

Trophic Classification:

Dwelling burrow of suspension-feeding shrimp.

Environmental Considerations:

Ophiomorpha is commonly associated with the *Skolithos* ichnofacies and can be found in prolific numbers in marine shoreface environments. It is also found in brackish water, sandy substrates including estuaries and tidal shoals.

SKOLITHOS

Description:

Single entrance, cylindrical to subcylindrical, straight to curved, vertical to subvertical, unbranched burrows that do not cross over or interpenetrate.

The shafts are either lined or unlined with generally smooth walls, but may be annulated. The infill is typically structureless.

Interpretation:

Ethologically, *Skolithos* represents the dwelling burrows of suspension-feeding organisms or passive carnivores. A multitude of probable originators have been postulated, including: the polychaetes *Sabellaria*, *Arenicola* and *Onuphis*, the phoronid *Phoronopsis* and insect larvae.

Trophic Classification:

Dwelling burrow of suspension-feeding vermiform organism.

Environmental Considerations:

Lined specimens of *Skolithos* are generally associated with marine or brackish environments. It is an element of the *Skolithos* ichnofacies, but because *Skolithos* can be constructed by many different kinds of organisms it is found in virtually every type of environment from marine to non-marine.

THALASSINOIDES

Description:

Relatively large burrow systems consisting of smooth-walled, cylindrical components. Branches are Y to T-shaped and are enlarged at points of bifurcation. Burrow dimensions may vary within a given system and cross sections range from cylindrical, half-moon shaped, to elliptical. Most systems are essentially horizontal with some irregularly inclined.

Interpretation:

Very thinly-lined to essentially unlined burrow systems are characteristic of fine-grained coherent substrates, in which wall reinforcement is unnecessary. Structureless to parallel-laminated or graded burrow fills represent passive (gravity-induced) sedimentation, whereas meniscate or chevron-laminated sediments represent active backfilling by the tracemaker. *Thalassinoides* is generally regarded as a dwelling and/or feeding burrow of a decapod crustacean (thalassinid shrimp). Enlarged junction points are often used as turning points for the organism, or as breeding chambers.

Trophic Classification:

Dwelling/feeding burrows of a deposit-feeding crustacean.

Environmental Considerations:

Thalassinoides is associated with the *Cruziana* ichnofacies in lower shoreface to offshore environments and may also be found in low diversity, brackish-water suites.

ZOOPHYCOS**Description:**

Zoophycos is basically a circular to lobate sheet-like spreite, either flat, curved, inclined or wound in screw fashion around a central vertical axis. The spreite is a horizontal or subhorizontal web of closely juxtaposed parallel burrow tunnels. Each tunnel in the burrow system presumably represents the path of its feeding apparatus during a single probing of the sediment. Successive probings side-by-side in the same plane produce a horizontal spreite.

Interpretation:

An interpretation is that *Zoophycos* is a feeding, or grazing, structure produced by a vermiform organism with a fully extensible-retractable body (as in the phylum Sipunculida). Other interpretations suggest that the tracemaker was an annelid.

Trophic Classification:

Grazing trace of a deposit-feeding organism.

Environmental Consideration:

Associated with the distal *Cruziana* and *Zoophycos* ichnofacies in fully marine, offshore shelf environments.

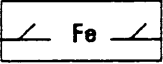


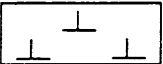

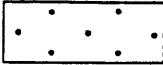
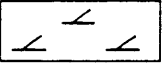



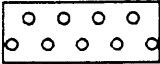

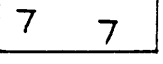
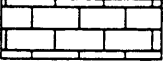
APPENDIX I

FIGURES



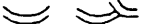










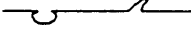





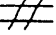

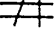






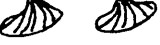

1:25 A4 Core Description and interpretation sheets

LEGEND

LITHOLOGY

 <p>siderite cement</p>	 <p>carbonaceous</p>	 <p>shale</p>
 <p>calcite cement</p>	 <p>coal</p>	 <p>sandstone</p>
 <p>dolomite cement</p>	 <p>pyrite</p>	 <p>muddy sandstone</p>
 <p>glaucanite</p>	 <p>pebble lag /conglomerate</p>	 <p>siltstone</p>
 <p>micaceous</p>		 <p>limestone</p>

SEDIMENTARY STRUCTURES

 <p>homogenous</p>	 <p><i>Ophiomorpha</i></p>
 <p>trough cross bedding</p>	 <p>gastropod</p>
 <p>hummocky cross stratification</p>	 <p>shell debris</p>
 <p>wave oscillation ripple</p>	 <p>brachiopod</p>
 <p>current ripple lamination</p>	 <p>bivalve</p>
 <p>flaser bedding</p>	 <p>cephalopod</p>
 <p>lenticular bedding</p>	 <p>load and flame structure</p>
 <p>dewatering feature</p>	 <p>microfoundering feature</p>
 <p>rip up clasts</p>	 <p>load casts</p>
 <p>scour surface</p>	 <p>mud crack</p>
 <p>stylolite</p>	 <p>fracture</p>
 <p>wavy inclined</p>	 <p>plant stems</p>
 <p><i>Skolithos</i></p>	 <p>rootlets</p>
 <p>bioturbation</p>	 <p>concretions</p>
 <p><i>Zoophycos</i></p>	
 <p><i>Thalassinoides</i></p>	

CORE DESCRIPTION

BALEEN-2

PERMIT: VIC/RL5

DATE: 10/01/2000

CORE NO.: 1

Page: 2 of 7

AUTHOR: P.A. ARDITTO

INTERVAL: 746.00m - 762.20m

RIG: SEDCO 702

CUT:

K.B.: 26.00m

W.D.: 55.00m

CORE BARREL & MUD TYPE:

DEPTH (m)	LITHOLOGY	Depositional Environment	GRAIN SIZE						SEDIMENTARY STRUCTURE	LITHOLOGICAL DESCRIPTION
			SILT	V.FINE	FINE	MEDIUM	COARSE	V.COARSE		
752	S -	MIDDLE SHELF PARASEQUENCE							S H	756.52 - 751.16m, Silty Sandstone, very fine to fine grained and moderately, micromicaceous (trace) and glauconitic with fine grained glauconite pellets. Internally it is homogeneous to moderately burrowed <i>Thalassinoides</i> . Sporadic <i>Ophiomorpha</i> burrows occur towards the base. Very good visual porosity.
	- 7 S							H S		
	S -								S H	
	- 7 S								H S	
	S -								S H	
	- 7 S								S H	
	S -								H S	
	- 7 S								S H	
	S -								H S	
	- 7 S								S H	
753	S -							H S		
	- 7 S							S H		
	S -							H S		
	- 7 S							S H		
	S -							H S		
	- 7 S							S H		
	S -							H S		
	- 7 S							S H		
	S -							H S		
	- 7 S							S H		
754	S -							H S		
	- 7 S							S H		
	S -							H S		
	- 7 S							S H		
	S -							H S		
	- 7 S							S H		
	S -							H S		
	- 7 S							S H		
	S -							H S		
	- 7 S							S H		
755	S -							H S		
	- 7 S							S H		
	S -							H S		
	- 7 S							S H		
	S -							H S		
	- 7 S							S H		
	S -							H S		
	- 7 S							S H		
	S -							H S		
	- 7 S							S H		
756	S -							H S		
	- 7 S							S H		
	S -							H S		
	- 7 S							S H		
	S -							H S		
	- 7 S							S H		
	S -							H S		
	- 7 S							S H		
	S -							H S		
	- 7 S							S H		
757	S -							H S	Sealed Sample 756.77m - 756.52m.	
	- 7 S							S H		

CORE DESCRIPTION						BALEEN-2				
PERMIT: VIC/RL5				DATE: 10/01/2000	CORE NO.: 1	Page: 3 of 7				
AUTHOR: P.A. ARDITTO				INTERVAL: 746.00m - 762.20m						
RIG: SEDCO 702				CUT:						
K.B.: 26.00m			W.D.: 55.00m			CORE BARREL & MUD TYPE:				
DEPTH (m)	LITHOLOGY	Depositional Environment	GRAIN SIZE						SEDIMENTARY STRUCTURE	LITHOLOGICAL DESCRIPTION
			SILT	V.FINE	FINE	MEDIUM	COARSE	V.COARSE		
757	— 7 — S	OUTER TO							S S	758.50 - 756.77m Muddy Sandstone, very fine grained and poorly sorted, micromicaceous (trace) and glauconitic (5%) with dispersed fine grained glauconite pellets. Internally it is churned by abundant <i>Thalassinoides</i> burrows. Good visual porosity.
758	— 7 — S								S S	
	— 7 — S								S S	
	— 7 — S								S S	
	— 7 — S								S S	
	— 7 — S								S S	
	— 7 — S								S S	
	— 7 — S								S S	
	— 7 — S								S S	
	— 7 — S								S S	
759	— 7 — S								H S	762.22 - 760.42m and 760.22 - 758.50m Silty Sandstone, very fine to fine grained and moderately sorted, micromicaceous (trace) and glauconitic (5%) with dispersed fine grained glauconite pellets. Internally it is homogeneous to moderately burrowed by <i>Thalassinoides</i> . Rare isolated <i>Skolithos</i> burrow in lower half. Top gradational into overlying interval. Good visual porosity.
	— 7 — S								S H	
	— 7 — S								H S	
	— 7 — S								S H	
760	— 7 — S								S H	
	— 7 — S									Sealed Sample 760.42 - 760.22m.
761	— 7 — S	PARASEQUENCE							H S	762.20 - 761.55m Core Rubble
	— 7 — S								S H	
	— 7 — S								H S	
	— 7 — S								S H	
762	— 7 — S								? ?	
	— 7 — S									BASE CORE 1

CORE DESCRIPTION						BALEEN-2			
PERMIT: VIC/RL5					DATE: 10/01/2000	CORE NO.: 2	Page: 4 of 7		
AUTHOR: P.A. ARDITTO					INTERVAL: 763.70m - 779.50m				
RIG: SEDCO 702					CUT:				
K.B.: 26.00m			W.D.: 55.00m			CORE BARREL & MUD TYPE:			
DEPTH (m)	LITHOLOGY	Depositional Environment	GRAIN SIZE					SEDIMENTARY STRUCTURE	LITHOLOGICAL DESCRIPTION
			SILT	V.FINE	FINE	MEDIUM	COARSE		
763		MIDDLE SHELF							TOP CORE2
764		MIDDLE SHELF						<p>764.35 - 763.70m, Silty Sandstone, very fine to fine grained and moderately sorted, micromicaceous (trace) and glauconitic (5%) with dispersed fine grained glauconite pellets. Internally it is homogeneous to sparsely burrowed by <i>Ophiomorpha</i>. The upper half of the interval is replaced by a large ferroan dolomite nodule.</p>	
765		MIDDLE SHELF PARASEQUENCE						<p>768.30 - 764.35m, Silty Sandstone, very fine to fine grained and moderately sorted, micromicaceous (trace) and glauconitic (5%) with dispersed fine grained glauconite pellets, upward coarsening to fine grained, less silty, sandstone. Internally the lower half is bioturbated And contains sporadic <i>Ophiomorpha</i> burrows, and the upper half is homogeneous to moderately burrowed by <i>Thalassinoides</i>. Top gradational into overlying interval. Very good visual porosity.</p>	
766		MIDDLE SHELF PARASEQUENCE							
767		MIDDLE SHELF PARASEQUENCE							
768		MIDDLE SHELF PARASEQUENCE							

CORE DESCRIPTION

BALEEN-2

PERMIT: VIC/RL5

DATE: 11/01/2000

CORE NO.: 2

Page: 5 of 7

AUTHOR: P.A. ARDITTO

INTERVAL: 763.70m - 779.50m

RIG: SEDCO 702

CUT:

K.B.: 26.00m

W.D.: 55.00m

CORE BARREL & MUD TYPE:

DEPTH (m)	LITHOLOGY	Depositional Environment	GRAIN SIZE						SEDIMENTARY STRUCTURE	LITHOLOGICAL DESCRIPTION
			SILT	V.FINE	FINE	MEDIUM	COARSE	V.COARSE		
768		SHELF TO PROXIMAL								771.53 - 769.83m and 769.66 - 768.30m, Sandy Mudstone, micromicaceous (trace) and glauconitic (5% - 7%) with dispersed fine grained glauconite pellets. Internally it has common faint lenticular wavy mudstone laminations which are highly disturbed by very fine grained glauconitic sand-filled common <i>Zoophycos</i> burrows. Sporadic pyrite-replaced ? <i>Skolithos</i> burrows in the middle of the interval. Top gradational into overlying interval. Good visual porosity.
769										
Sealed Sample 769.83 - 769.66m.										
770		DISTAL OUTER								775.70 - 771.53m, Muddy Sandstone, very fine to fine grained and moderately to poorly sorted, micromicaceous (trace) and glauconitic (5% - 7%) with dispersed fine grained glauconite pellets. Internally it is intensely churned by <i>Thalassinoides</i> burrows. Sporadic pyrite nodules, 2cm - 3cm diameter, are developed around burrows. Sporadic ferroan dolomite nodules occur towards the middle and the interval is capped by a 30cm diameter nodule. Top is gradational into overlying interval. Good visual porosity.
771										
772										
773										

CORE DESCRIPTION					BALEEN-2						
PERMIT: VIC/RL5			DATE: 11/01/2000		CORE NO.: 2	Page: 6 of 7					
AUTHOR: P.A. ARDITTO			INTERVAL: 763.70m - 779.50m								
RIG: SEDCO 702			CUT:								
K.B.: 26.00m		W.D.: 55.00m		CORE BARREL & MUD TYPE:							
DEPTH (m)	LITHOLOGY	Depositional Environment	GRAIN SIZE					SEDIMENTARY STRUCTURE	LITHOLOGICAL DESCRIPTION		
			SILT V.FINE	FINE	MEDIUM	COARSE	V.COARSE				
774		PARASEQUENCE							<p>778.80 - 776.87m and 776.63 - 775.70m, Silty Sandstone, very fine to fine grained and moderately sorted, micromicaceous (trace) and glauconitic (5%) with dispersed fine grained glauconite pellets. Internally it is churned by common <i>Ophiomorpha</i> and <i>Thalassinoides</i> burrows. Gradational Top. Very good visual porosity.</p>		
775											
776											
Sealed Sample 776.87 - 776.63m.											
777			MIDDLE SHELF								
778											
779											
779.00 - 778.80m, Core rubble.											

APPENDIX I

FIGURES

**1:200 A4 Core gamma ray log and wireline gamma ray log
with plug permeability**

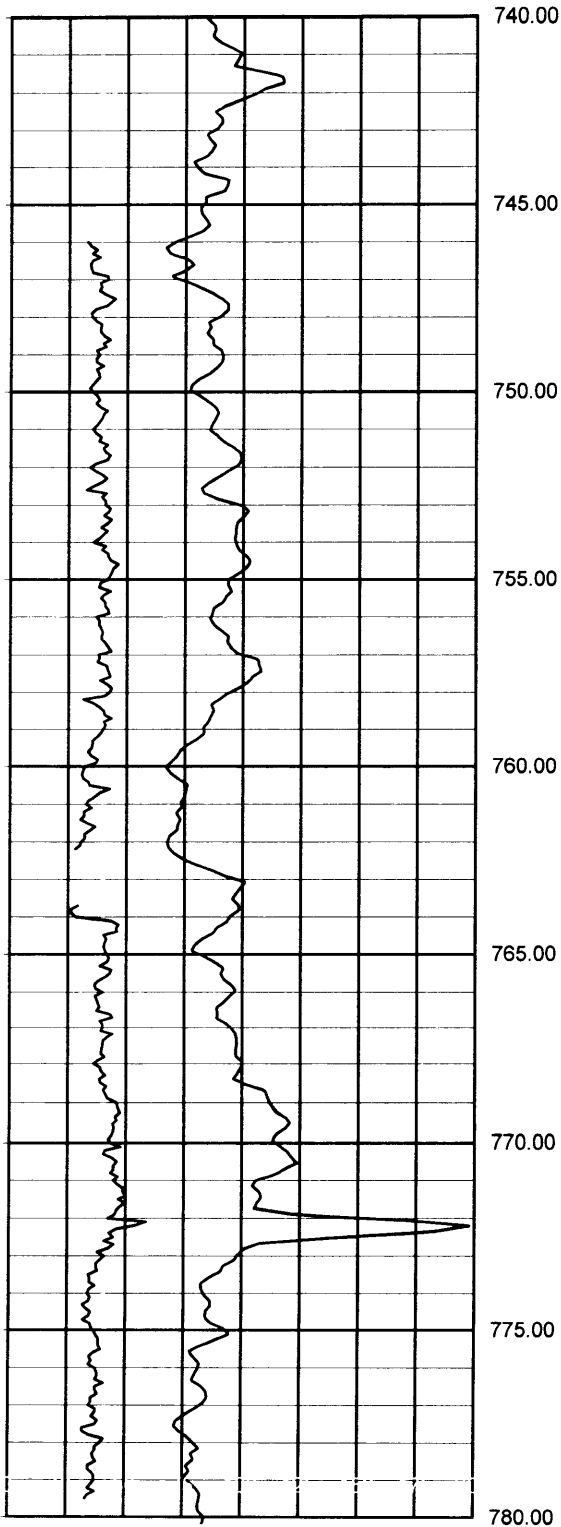
CORE PLOT

Scale 200:1

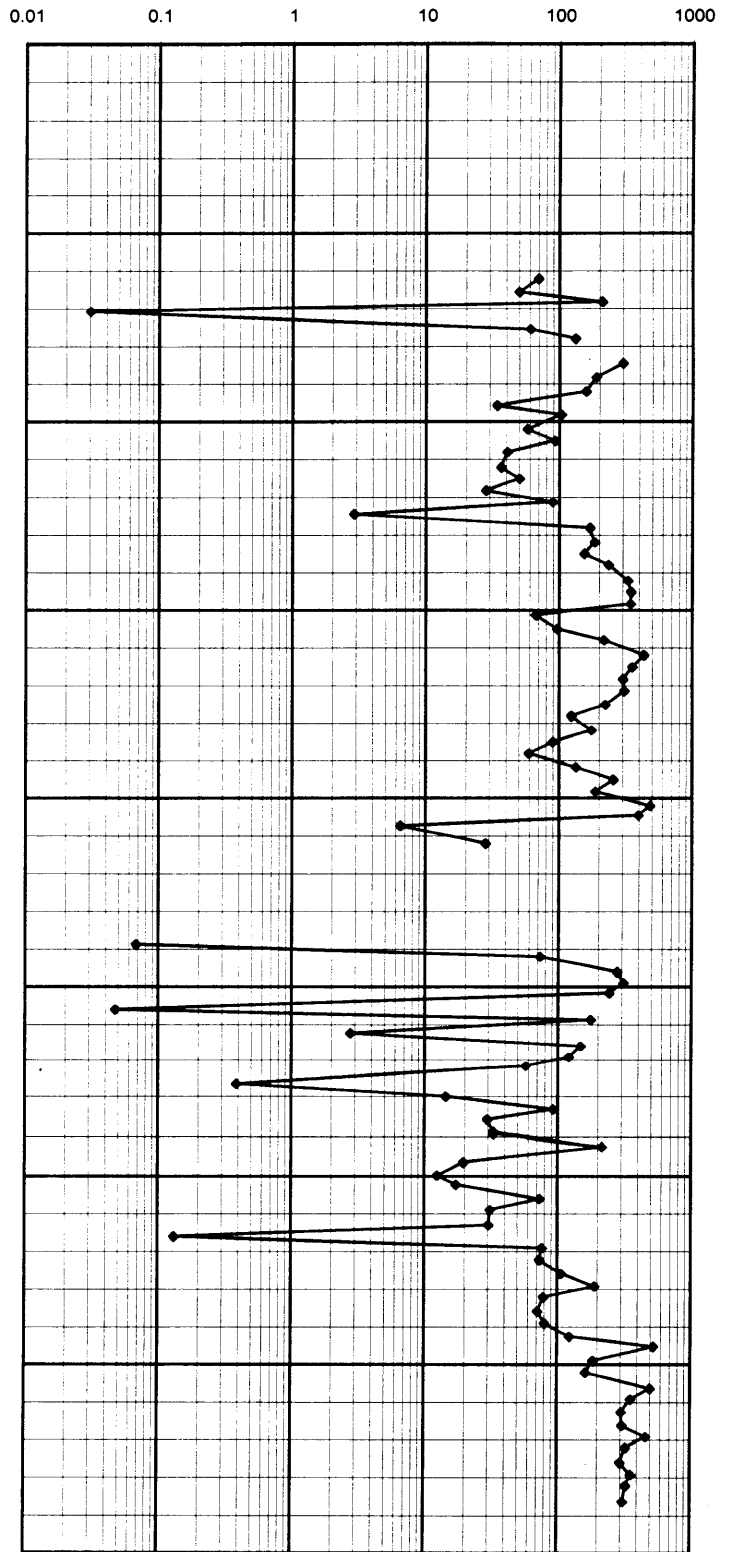


Client: Basin Oil NL
Well: Baleen-2

CORE GAMMA



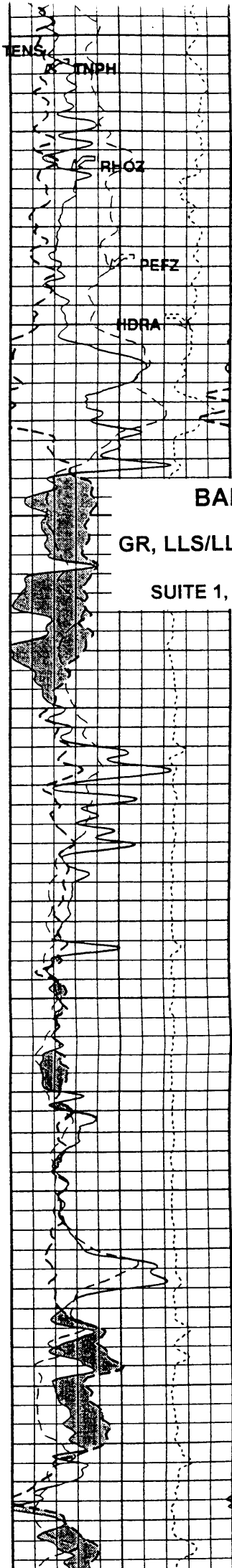
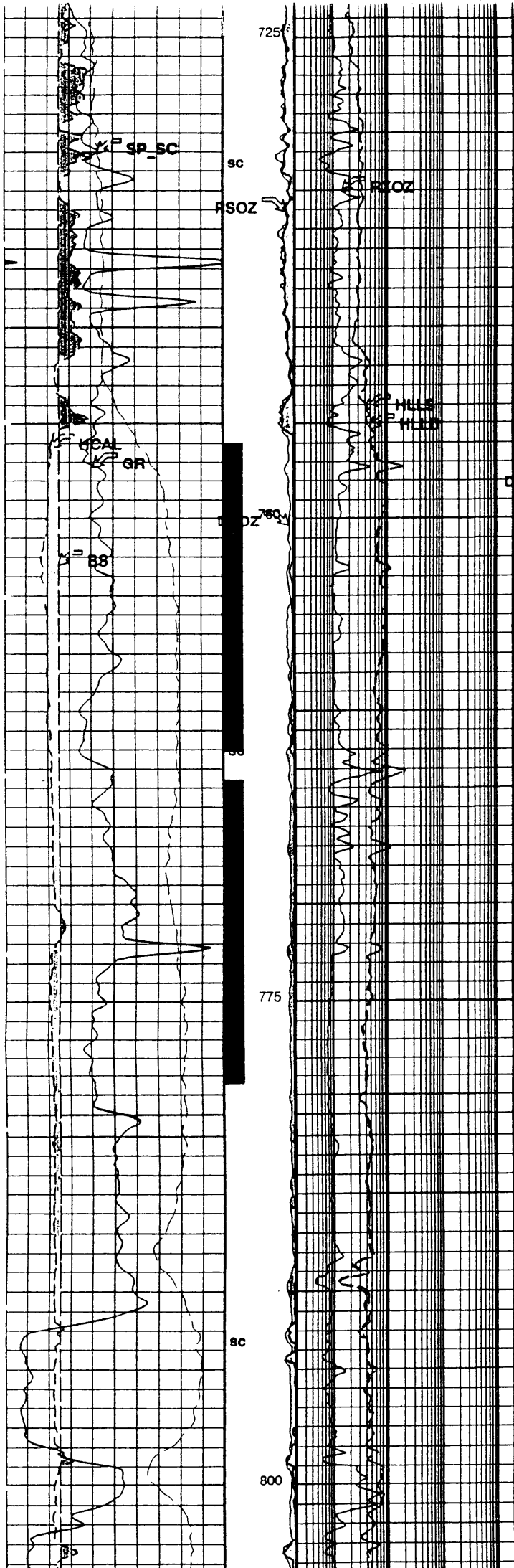
PERMEABILITY



APPENDIX I

FIGURES

**1:280 A4 portions of selected wireline logs
with depth-corrected position of cores**



BALEEN-2

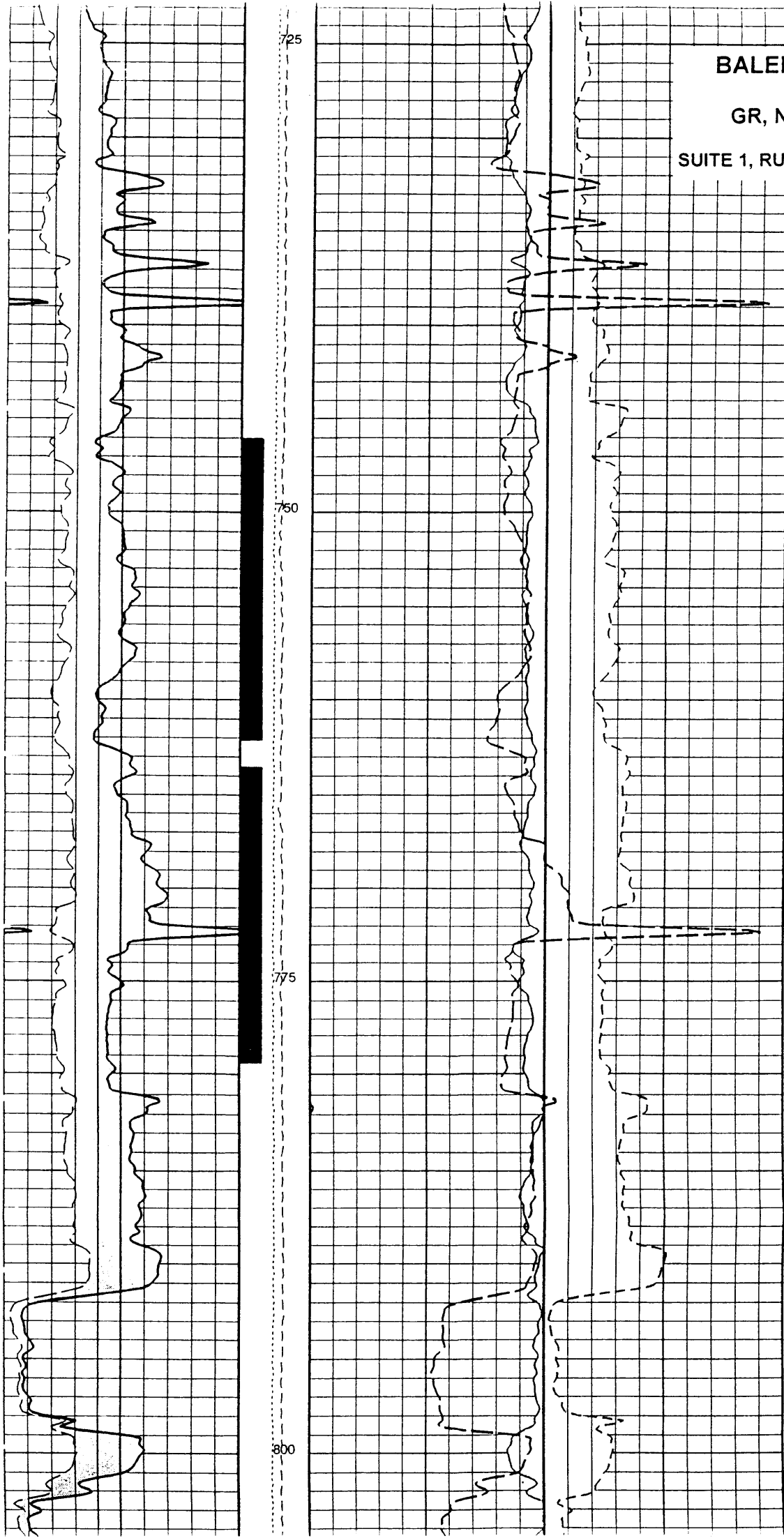
GR, LLS/LLD, NPHI/RHOB

SUITE 1, RUN 1 1:280

BALEEN-2

GR, NGS

SUITE 1, RUN 1 1:280



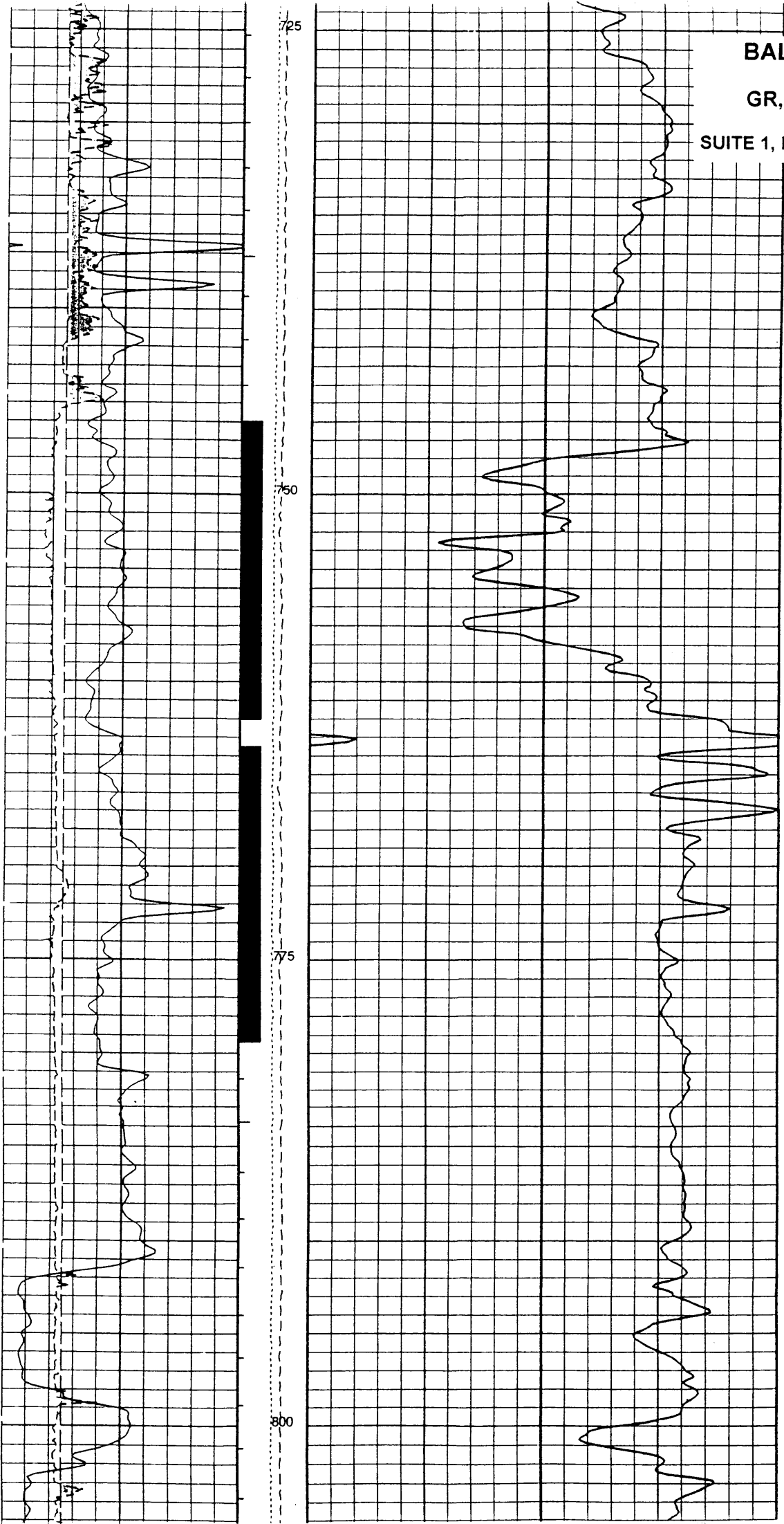
907961 116

BALEEN-2

GR, SONIC

SUITE 1, RUN 1 1:280

907961 117



907961 118

APPENDIX 11

PLATES

Selected 30 cm A4 colour core photographs

907961 119

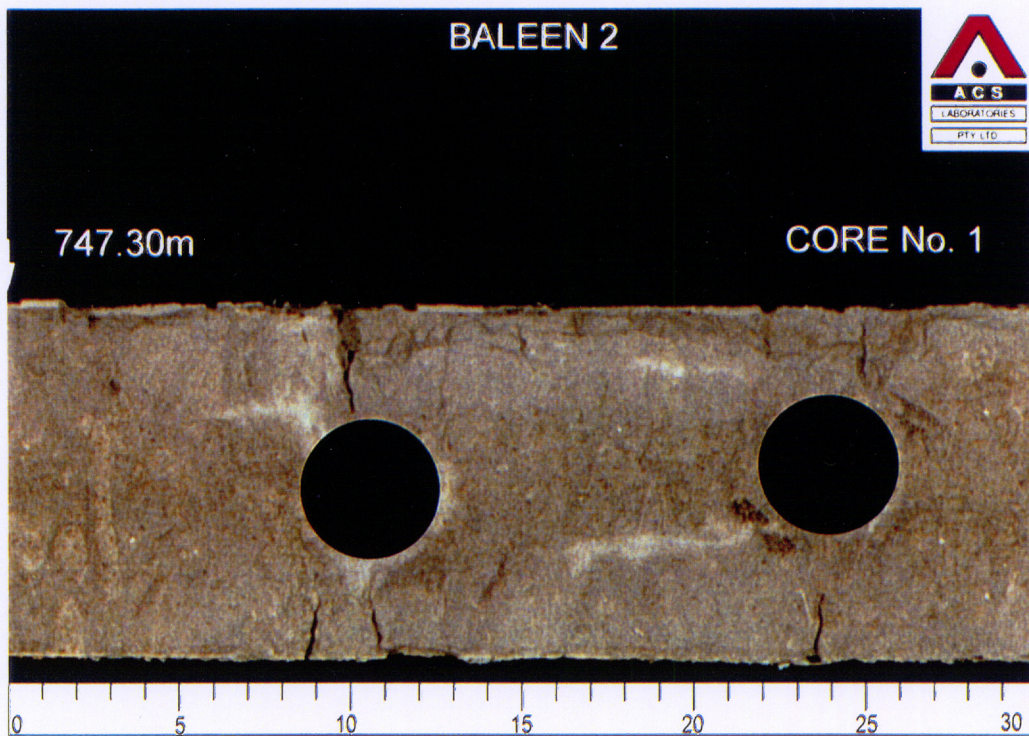


Plate 1: Core Photograph 747.30 m - 747.60 m. Uppermost part of a mid shelfal marine parasequence of a very fine to fine grained glauconitic silty sandstone with common sub-horizontal branching *Thalassinoides* burrows. The top 5 cm of the photograph shows the development of nodular ferroan siderite capping the top of the parasequence, indicating a sediment-starved surface.

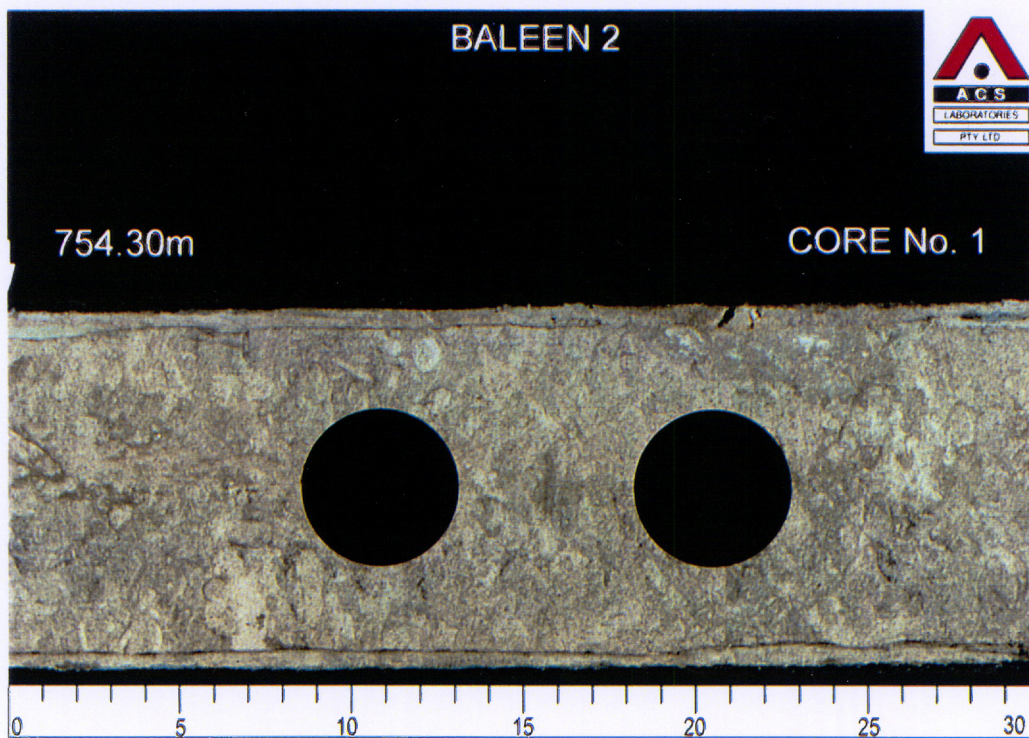


Plate 2: Core Photograph 754.30 m - 754.60 m. Very fine to fine grained glauconitic silty to muddy sandstone moderately burrowed by sub-horizontal branching *Thalassinoides* burrows and sporadic mud-walled sub-vertical *Ophiomorpha* burrows (example of *Ophiomorpha* burrow at 754.30 m).

907961 120

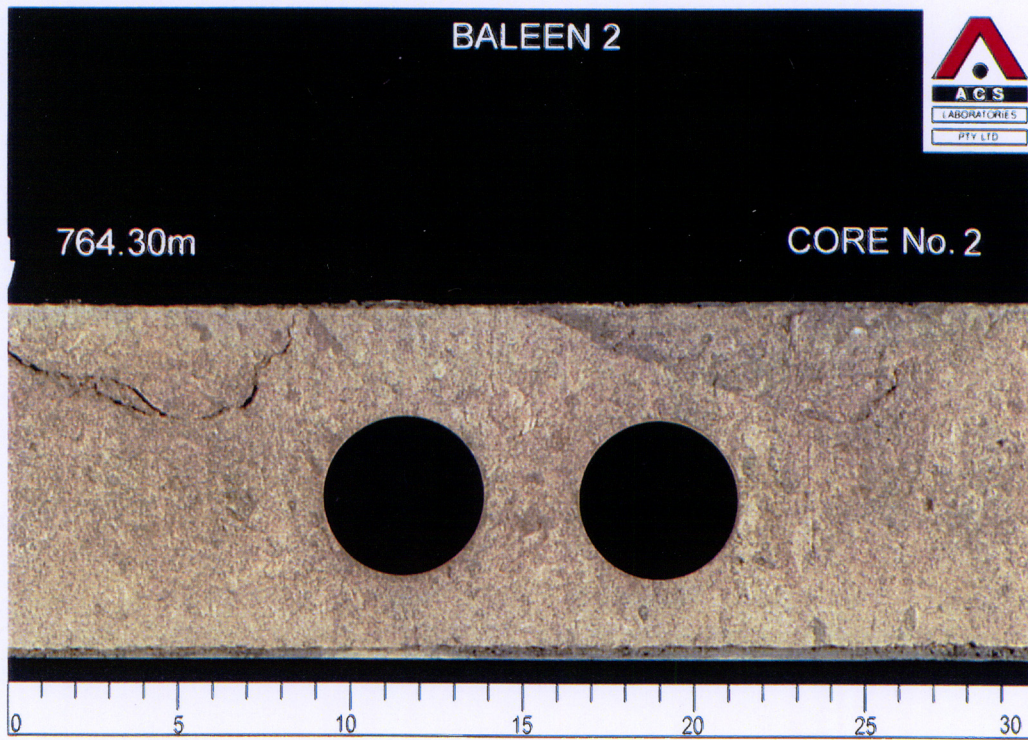


Plate 3: Core Photograph 764.70m - 765.00 m. Uppermost part of mid shelfal marine parasequence of fine grained glauconitic silty sandstone. It is homogeneous to moderately burrowed by branching *Thalassinoides*.

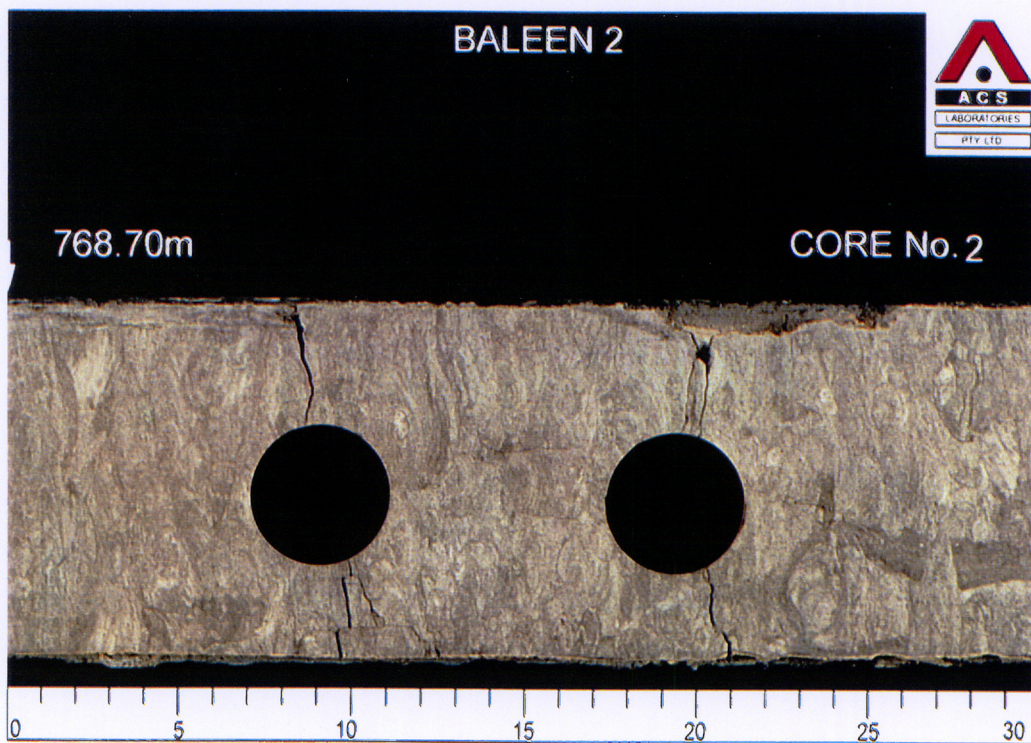


Plate 4: Core photograph 768.70 m - 769.00 m. Glauconitic sandy mudstone laminations disturbed by common *Zoophycos* burrows. Lower part of parasequence in Plate 3.

907961 121

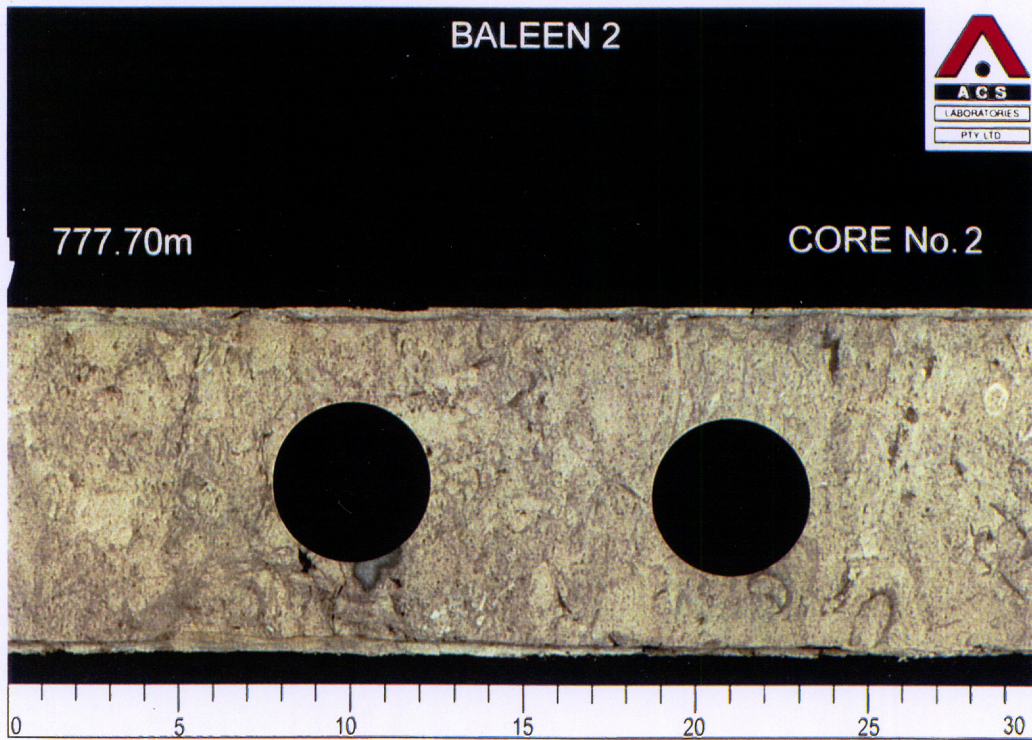


Plate 5: Core Photograph 777.70 m - 778.00 m. Lowermost mid shelfal parasequence, within the lower part of Core #2, of very fine to fine grained glauconitic silty sandstone disturbed by common *Thalassinoides* and *Ophiomorpha* burrows. Good mud-walled *Ophiomorpha* burrow at 777.95 m.

907961 122

907961 123

APPENDIX 16

BALEEN-2

**SINGLE AND MULTIPLE FAILURE
TRIAXIAL TESTS ON BALEEN-2
SANDS REPORT**
-CSIRO-



CSIRO Petroleum Confidential Report No. 00-013
March 2000

Single and Multiple Failure State Triaxial Tests on Baleen-2 Sands

B. Wu, C.P. Tan and L. Connelly

For further information contact:

Dr B. Wu
CSIRO Petroleum
PO Box 3000, Glen Waverley, Victoria Australia 3150
Telephone (03) 9259 6800, Facsimilie: (03) 9259 6900

THIS IS A CONFIDENTIAL REPORT FOR
INTERNAL DISTRIBUTION ONLY

Copies to: B. Wu
C.P. Tan
W. Boon, Schlumberger IPM
J. Hann, OMV
M. Adamson, OMV
Confidential Archive (2)

CONTENTS

NOTATION	<i>i</i>
EXECUTIVE SUMMARY	<i>ii</i>
1 INTRODUCTION	<i>1</i>
2 TEST EQUIPMENT	<i>1</i>
3 TEST SAMPLES	<i>2</i>
4 TEST PROCEDURES	<i>2</i>
5 TEST CONDITIONS	<i>4</i>
6 RESULTS AND ANALYSES	<i>4</i>
6.1 Experimental Results and Observations	<i>4</i>
6.2 Elastic Parameters	<i>5</i>
6.3 Strength Parameters	<i>6</i>
6.4 Discussion - comparison between single and multiple stage triaxial test results	<i>6</i>
7 SUMMARY AND CONCLUSIONS	<i>8</i>
8 ACKNOWLEDGEMENTS	<i>8</i>
9 REFERENCES	<i>9</i>
APPENDIX 1 - Shell Process Oil P784 Data Sheet	
APPENDIX 2 - Experimental Results	
APPENDIX 3 - Photos of Tested Samples	

NOTATION

E_o	Young's modulus
ν_o	Poisson's ratio
A, B	Regression constants
l_o, d_o	Sample length and diameter
$\Delta l_1, \Delta l_2$	Axial displacements
$\Delta d_1, \Delta d_2$	Radial displacements
$\varepsilon_a, \varepsilon_r$	Average axial and radial strains
P	Deviator axial load
σ_1, σ_1'	Total and effective axial stress
σ_3, σ_3'	Total and effective confining pressure
c'	Effective cohesion
ϕ'	Effective angle of internal friction

EXECUTIVE SUMMARY

CSIRO Petroleum has been requested by Schlumberger IPM to conduct an experimental study on core samples obtained from Baleen-2 well of Patricia reservoir. The prime objective of the study is to conduct rock mechanics laboratory tests to measure the strength of sand core plugs. The compressive strength and elastic parameters are required for sand production evaluation for the reservoir.

Five core sections were obtained from different depths in Baleen-2 well of Patricia reservoir. Two conventional (single stage) and one multiple failure state (multiple stage) triaxial tests were conducted on core samples for each core section. The materials tested were poorly/weakly consolidated sands. The single stage triaxial tests were conducted at effective confining pressures of 6 and 9 MPa, and the multiple stage tests at effective confining pressure of 1, 2, 5, 9 and 12 MPa. Elastic and strength properties were determined for the materials.

The elastic parameters were found to be dependent on effective confining pressure. The Young's modulus increases and Poisson's ratio decreases with increase in effective confining pressure. Relationships between elastic parameters (Young's modulus and Poisson's ratio) and effective confining pressure were established for the multiple stage tests of all core sections.

It was observed that the deformation behaviour of the sands depended on the applied effective confining pressure. The sands showed brittle deformation behaviour when the effective confining pressure was less than 6 MPa and either ductile deformation behaviour or transitional behaviour between brittle and ductile when the effective confining pressure was greater than 9 MPa (except for Core Section 5). The strength parameters were derived for the Mohr-Coulomb strength criterion. To exclude the effect of ductile deformation on the derived strength parameters, the strength parameters were derived in two effective confining pressure ranges: 0 to 6 MPa and 0 to 9 MPa.

**SINGLE AND MULTIPLE FAILURE STATE TRIAXIAL TESTS ON BALEEN –
2 SANDS**

B. Wu, C. P. Tan, L. T. Connelly

1 INTRODUCTION

CSIRO Petroleum (CSIRO) has been requested by Schlumberger IPM to conduct an experimental study on core samples obtained from Baleen-2 well of Patricia reservoir. The prime objective of the study is to conduct rock mechanics laboratory tests to measure the strength of sand core plugs. The compressive strength and elastic parameters are required for sand production evaluation for the reservoir.

Sand core plugs were obtained from five core sections at different reservoir depths. Three plugs were tested from each core section. Two of them were for conventional triaxial tests (single stage) and the other for multiple failure state triaxial test (multiple stages). The tests were conducted at stress conditions covering the *in situ* effective stress range as specified by Schlumberger-Holditch Reservoir Technologies (Fuller, 2000).

This report describes the test equipment, test procedures and conditions, and results and their analyses. Strength and elastic parameters were derived from the test results.

2 TEST EQUIPMENT

A 45 MPa capacity triaxial cell was used for the tests, with provision for measurements of sample deformations, axial load, and cell and pore pressures.

The instruments used to measure the behaviour of the test sample were as follows:

- (a) two diametrically-opposed LVDTs (Linear Variable Differential Transformers) mounted between the sample end platens to measure axial deformation of the sample;
- (b) four cantilever (orthogonal) radial gauges mounted at mid-height of the sample to measure radial deformation;
- (c) a load cell located on top of the top steel platen to measure axial deviatoric load;
- (d) a pressure transducer to measure cell (confining) pressure; and
- (e) two pressure transducers to measure pore pressures at both ends of the sample.

A schematic of the sample stack assembly is illustrated in Figure 1. As shown, the bottom pore pressure transducer is built inside the bolster directly underneath the bottom platen which provides an independent measurement of the sample pore pressure. A computer-controlled system was used to control the axial deviatoric stress or displacement, and cell and pore pressures, and to perform data acquisition.

3 TEST SAMPLES

A total of 20 sand plugs were cored from five core sections at different depths at Amdel Core Services Ltd under a frozen state by using liquid nitrogen as coring fluid. They were cored in vertical direction along the core axis. Four plugs were obtained from each core section and three of them were tested, with one plug as a contingency plug. All the plugs were kept in a frozen state by packing them in dry ice during transportation to CSIRO. They were then stored in a deep freezer until required for testing. The plugs had a nominal diameter of 41 mm and a length ranging from 70 to 100 mm. Both ends of the plugs were unfinished when delivered to CSIRO.

The reservoir sand plugs were poorly/weakly consolidated and extremely friable in an unfrozen state. Due to the friable nature of the materials, sample end surfaces were prepared/lapped manually in a frozen state under the protection of a thick metal jacket. The perpendicularity of the end surfaces to circumferential surface and flatness of the end surfaces of the finished sample were in general accordance with the specifications recommended by ISRM (Brown, 1981). The sample dimensions and weight (before test in frozen state and after test), sample depth and test type are summarised in *Table 1*.

All but two of the finished samples had a length to diameter ratio of approximately 2.0, which is within the range of 2 to 3 suggested by ISRM. The other two samples had a ratio of length to diameter between 1.7 and 1.8, slightly lower than that suggested by ISRM. However, previous research showed that a ratio of between 1.5 and 2 has little effect on Young's modulus, although it may increase peak strength slightly, in comparison with the strength measured on a sample with a length to diameter ratio of between 2 and 3 (Brady and Brown, 1985).

4 TEST PROCEDURES

The frozen sample was jacketed with a flexible rubber membrane (0.5 mm thick Viton) and installed between the top and bottom steel platens. Prior to the installation, the temperature of the platens was cooled down using dry ice to delay the thawing of the sample. The transducers for measuring the sample axial and radial displacements, and the deviatoric load were then mounted. Finally, the triaxial cell was closed and filled with hydraulic oil. The sample was then subjected to the following testing procedures.

Test procedure for single stage triaxial test

- *Saturation.* Apply confining pressure and back pore pressure at a constant rate of 0.5 MPa/min. to 6 and 5 MPa respectively. The back pore pressure was applied from the top end of the sample while the other (bottom) end of the sample was undrained (built-in pore pressure transducer). A thin mineral oil (Shell process oil P874, Appendix 1) was used as the pore fluid. The cell and back pore pressures were maintained constant until the pore pressure measured at the bottom end of the sample reached 5 MPa. The sample was then assumed to be fully saturated.
- *Pressurization.* This was conducted undrained (i.e., the top pore pressure line was closed, and the pore fluid was not allowed to flow from the sample). Apply confining pressure at a rate of 0.5 MPa/min. until the required confining pressure level was established.

- *Consolidation.* After the pore pressure inside the sample stabilised, open the back pore pressure line and control the pressure at 5 MPa to allow the excess pore pressure to dissipate (consolidation). The consolidation was assumed to be completed when the pore pressure measured at the bottom end of the sample was equal to the back pore pressure.
- *Axial loading.* Apply axial stress at a constant average axial strain rate under computer control until either a residual strength was observed or average axial strain was more than 5% in the case of strain hardening material behaviour, while the confining and pore pressures were maintained constant.

The axial loading rate selected was 1%/hour for all the tests. It was sufficiently slow to allow an essentially uniform pore pressure distribution inside the sample for the tests with an effective confining pressure equal or below 6 MPa. It was observed, however, an excess pore pressure of approximately 0.4 MPa (or 8% of the back pore pressure) was developed towards the end of the test with an effective confining pressure of 9 MPa (Sample PAT_1C, see Appendix 2). Consequently, a special sidedrain was installed on the sample surface for tests with an effective confining pressure equal or higher than 9 MPa to expedite the dissipation of the excess pore pressure during axial loading. The sidedrain, comprising of stainless steel mesh and filter paper, was developed at CSIRO for testing low permeability shales (Wu & Tan, 1997). Figure 2 shows the configuration of the sidedrain. Some of the advantages of the sidedrain include significantly shorter pore fluid flow path, independent pore pressure measurement and highly effective when subjected to a high effective confining pressure. With the thickness of the sidedrain material in the order of micrometre, it has ignorable effect on the sample strength and deformation.

Test procedure for multiple stage triaxial test

The test procedure for multiple stage failure triaxial tests suggested by ISRM (Kovari et al., 1983) was slightly modified in the aspects of axial loading rate, indicator for imminent failure and stress path, as described below.

After the required cell and pore pressures were established, the axial deviatoric stress was increased at a constant axial strain rate of 1%/hour (instead of ISRM suggested 3600%/hour to 3.6%/hour). The axial deviatoric force vs average axial displacement curve and its instant slope were displayed on the computer screen in real time as the test progressed. Prior to failure of the sample, a curved response of the axial deviatoric force vs. average axial displacement was observed and the instant slope of the curve decreased gradually, indicating an imminent failure. Where the instant slope decreased to approximately 2 kN/mm (or 0.1 GPa for a typical sample size), the axial deviatoric force was quickly reduced to close to zero and the confining pressure was increased to the next required level of effective confining pressure. After the pore pressure was stabilised and equal to the back pore pressure, the axial deviatoric load was increased again at a constant axial strain rate. This procedure was repeated at each required effective confining pressure. At the last stage (effective confining pressure of 12 MPa), the axial loading was allowed to proceed until either a residual strength was observed or the average axial strain was more than 5%.

The advantages of the modified test procedure over the original version suggested by ISRM are:

- A much slower loading ratio ensured an essentially uniform pore pressure distribution inside the sample during loading;
- An indicator for imminent failure based on the instant slope of the deviatoric force vs average axial strain curve ensured consistency of the strength obtained; and
- The stress path adopted (starting the axial deviatoric loading at hydrostatic stress for each stage) allowed elastic parameters to be measured at different effective confining pressures. The specimen is allowed to recover part of the deformation and is in equilibrium at the end of each stage (hydrostatic stress state). A schematic of the adopted stress path is shown in Figure 3 and compared with the stress path suggested by ISRM.

5 TEST CONDITIONS

Two single stage and one multiple stage triaxial tests were conducted for each core section. The ranges of the effective confining pressure were specified by Schlumberger-Holditch Reservoir Technologies (Fuller, 2000). The cell and pore pressure conditions prior to axial loading are summarised in *Table 2* for all the tests.

6 RESULTS AND ANALYSES

6.1 Experimental Results and Observations

The axial and radial strains ($\varepsilon_a, \varepsilon_r$) are calculated from Equations (1) and (2) respectively:

$$\varepsilon_a = \frac{\Delta l_1 + \Delta l_2}{2 \times l_0} \quad (1)$$

$$\varepsilon_r = \frac{\Delta d_1 + \Delta d_2}{2 \times d_0} \quad (2)$$

where Δl_1 and Δl_2 are axial displacements measured at two diametrically opposed positions; Δd_1 and Δd_2 are radial displacements measured in two orthogonal directions; and l_0 and d_0 are sample length and diameter respectively. Note that extension radial strain is defined as positive and compression axial strain as positive. The deviatoric axial stress ($\sigma_1 - \sigma_3$) is calculated from Equation (3):

$$\sigma_1 - \sigma_3 = \frac{4P}{\pi[d_0 + (\Delta d_1 + \Delta d_2)/2]^2} \quad (3)$$

where P is the deviatoric load measured by the load cell. The change in sample diameter during axial loading is taken into account in the calculation of deviatoric axial stress. The effective axial stress is the sum of the deviatoric axial stress and confining pressure less pore pressure.

The experimental results are presented as curves of axial deviatoric stress vs average axial strain and average radial strain vs average axial strain, as shown in Figures 4 to 23. The other plots for all individual tests are included in Appendix 2.

Observations on all the post-test samples indicated no shear failure along a single shear plane, as would be for more competent rocks such as sandstones. The photos for each tested sample are included in Appendix 3. Some of the tested samples broke in the plane perpendicular to the sample axis after being removed from the membrane.

6.2 Elastic Parameters

The Young's modulus (E) and Poisson's ratio (ν) are determined as the tangential slope of the curve of deviator axial stress vs average axial strain, and the tangential slope of the curve of average radial strain vs average axial strain at approximately 50% of the maximum deviatoric stress respectively. This is one of the methods recommended by ISRM for elastic parameter determination (Brown, 1981). The derived Young's modulus and Poisson's ratio are summarised in *Table 3* and presented in Figures 24 to 28 as a function of effective confining pressure for each core section.

Both Young's modulus and Poisson's ratio appear to be dependent on effective confining pressure. The Young's modulus increases with effective confining pressure. The Poisson's ratio decreases with increase in effective confining pressure in the low effective confining pressure range, but slightly increases with effective confining pressure for effective confining pressures greater than 9 MPa. The dependence of Young's modulus and Poisson's ratio on effective confining pressure is more significant in the low effective confining pressure range. The influence of effective confining pressure on Young's modulus and Poisson's ratio may be represented by relationships such as those proposed by Santarelli (1987):

$$E = E_0(1 + \sigma_3')^A \quad (4)$$

and

$$\nu = \frac{\nu_0}{(1 + \sigma_3')^B} \quad (5)$$

where E_0 and ν_0 are Young's modulus and Poisson's ratio respectively at zero effective confining pressure; A and B are material constants; and σ_3' is effective confining pressure.

Equations 4 and 5 were applied to the data of Young's modulus and Poisson's ratio of the multiple stage tests of each core section by linear regression analyses. The data from single stage tests were not included in the analyses and the reason will be discussed in Section 6.4. The fitted curves are presented in Figures 24 to 28. These relationships generally described adequately the influence of effective confining pressure on Young's modulus and Poisson's ratio. The regression constants for each core section are summarised in *Table 4*.

6.3 Strength Parameters

As shown in Figures 4 to 23, the mechanical behaviour of the samples is dependent on the applied effective confining pressure. The material showed ductile behaviour when the effective confining pressure was equal or greater than 9 MPa (with exception for the single stage triaxial test of Core Section 5 at 9 MPa effective confining pressure) and either brittle or transitional behaviour when the effective confining pressure was equal or less than 6 MPa. The peak strength is simply taken as the maximum deviatoric stress on a deviatoric stress vs average axial strain curve, and the residual strength is taken as the deviatoric stress when the curve becomes almost constant for samples with either brittle or transitional mechanical behaviour. For ductile mechanical behaviour, a unique peak or residual strength does not exist, rather the deviatoric stress increases with axial deformation. Various methods exist to determine the yield strength for ductile mechanical behaviour. In this study, the strength with ductile mechanical behaviour was taken as the deviatoric stress when the deviatoric stress vs average axial strain curve became almost a straight line, as illustrated in Figure 4. However, the mixed mechanical behaviour makes the comparison of the strength between brittle and ductile mechanical behaviours difficult. *Table 3* summarises all the strength data obtained from the single and multiple stage triaxial tests.

The Mohr-Coulomb failure criterion is applied to the peak strength data. In terms of principal effective stresses, the criterion can be expressed as (Goodman, 1989):

$$\sigma_1 = 2c' \tan\left(45^\circ + \frac{\phi'}{2}\right) + \sigma_3' \tan^2\left(45^\circ + \frac{\phi'}{2}\right) \quad (6)$$

where c' and ϕ' are effective cohesion and effective angle of internal friction respectively.

Equation (6) is fitted by regression analyses to the strength data. To exclude the effect of ductile deformation on the derived strength parameters, the regression analyses are conducted for two effective confining pressure ranges, i.e., between 0 to 9 MPa and between 0 to 6 MPa. The derived strength parameters of the Mohr-Coulomb strength criterion are given in *Table 5*. Note that the strength parameters for Core Section 5 were derived only based on the multiple stage test. The reason will be discussed in Section 6.4. No regression analyses were performed on the residual strength data due to insufficient number of data points.

Figures 29 to 33 show the Mohr circles and the derived strength envelopes for the five test materials.

6.4 Discussion – Comparison between Single and Multiple Stage Triaxial Test Results

Material homogeneity

For the comparison between the single stage and multiple stage triaxial test results to be meaningful, it is necessary to clarify the effect of material homogeneity on the test results of each core section. In the absence of other physical parameters (such as porosity), the bulk densities for each sample before and after test (based on the initial sample dimensions) may be used as an indicator of the material homogeneity for the core section. Figure 34 shows the bulk density for all the samples. Whilst the samples obtained from Core Sections 1, 2 and 4 were quite homogeneous in terms of bulk density, the variations are quite considerable among the samples from the other sections. This is particularly true for Core

Section 5, where the bulk densities for Samples PAT_5A and PAT_5C are considerably smaller than that of Sample PAT_5B before test (1.68g/cm^3 vs. 1.80g/cm^3). This may indicate that the samples obtained from Core Section 5 may be of two material types. Hence, the strength data for the single stage and multiple stage triaxial tests of Core Section 5 were analysed separately in Section 6.3. Furthermore, the sample bulk density after tests generally increased for all the core sections, indicating that the samples were not fully saturated before the tests. Whilst the increase was quite small for Core Sections 1 and 4, it was quite significant for the other core sections. The change in sample density before and after test may be an indication of the sample porosity, i.e. the larger the change, the higher was the porosity.

Strength parameters

The use of several samples to define a failure envelope is the preferred method. However, the multiple stage test enables the failure envelope to be determined from one sample. This is particularly beneficial where there is not enough material for the required number of samples. Studies by others on well-consolidated sandstones showed that the strength obtained using the multiple stage test method is approximately 5% less than that determined with single stage tests (Cain et al. 1987 and Holt & Fjaer 1991).

As can be seen from Figures 29b , 30b and 32b for effective confining pressure less than 6 MPa, the peak strengths obtained from the single and multiple stage tests are consistent for Core Sections 1, 2 and 4. However, for Core Section 3, the strength obtained from the single stage tests is lower than that obtained from the multiple stage test. This could be due to core damage during coring or transportation, rather than intrinsic inhomogeneity of the material, as the three samples were cored side by side (at the same depth). However, no observations could be made visually on core damage before the tests as the samples were in a frozen state. The two samples for the single stage tests were 70 mm and 74 mm in length, and were shorter than the one for the multiple stage test (83 mm). This may indicate occurrence of core damage because of the difficulties in obtaining longer samples. In addition, the strength obtained from the single stage test at an effective confining pressure of 6 MPa for Core Section 5 is inconsistent (much higher) with the multiple stage test results. However, this could be due to different material type as discussed earlier.

For an effective confining pressure of 9 MPa, the strength obtained from the multiple stage tests are considerably lower than that obtained from the single stage tests, with the exception for Core Section 3. This may be caused by the different strain states prior to the axial deviatoric loading for the single and multiple stage triaxial tests. Figures 35 to 39 show the axial and radial strains as a function of effective confining pressure for all the single stage triaxial tests during hydrostatic pressurization and consolidation. The strains were defined as zero at an effective confining pressure of 1 MPa so as to enable a direct comparison with the strain states for multiple stage triaxial tests (Figures 7, 11, 15, 19 and 23). *Table 6* compares the strain states between the single and multiple stage triaxial tests at effective confining pressures of 5 MPa and 9 MPa for all the core sections. It can be seen that the shear strain of the single stage triaxial tests is, in general, lower than that of the multiple stage tests. With the strength of the material governed by shear failure, a higher initial shear strain would result in a low shear strength, assuming an intrinsically homogeneous material.

Elastic parameters

As shown in Figures 24 to 28, the Poisson's ratio is, in general, consistent between the single and multiple stage tests. However, the Young's moduli obtained from the single stage tests are generally lower than those obtained from the multiple stage tests. This could be as a result of different strain states of the two types of test, in addition to the intrinsic material inhomogeneity. As shown in *Table 6* the axial strain of multiple stage triaxial tests is, in general, greater than that of single stage triaxial tests whilst the radial strain of the former is less than that of the latter. A higher axial strain would indicate a higher degree of compaction in the axial direction, hence a higher stiffness of the sample in that direction, provided the material is intrinsically homogeneous. Due to the different initial strain states at the beginning of the axial deviatoric loading, the Young's moduli obtained from the single stage triaxial tests were not used together with that obtained from the multiple stage tests in the regression analysis.

7 SUMMARY AND CONCLUSIONS

Five core sections were obtained from different depths in Baleen-2 well of Patricia reservoir. Two conventional (single stage) and one multiple failure state (multiple stage) triaxial tests were conducted on core samples for each core section. The materials tested were poorly/weakly consolidated sands. The single stage triaxial tests were conducted at effective confining pressures of 6 and 9 MPa, and the multiple stage tests at effective confining pressure of 1, 2, 5, 9 and 12 MPa. Elastic and strength properties were determined for the materials.

The elastic parameters were found to be dependent on effective confining pressure. The Young's modulus increases and Poisson's ratio decreases with increase in effective confining pressure. Relationships between elastic parameters (Young's modulus and Poisson's ratio) and effective confining pressure were established for the multiple stage tests of all core sections.

It was observed that the deformation behaviour of the sands depended on the applied effective confining pressure. The sands showed brittle deformation behaviour when the effective confining pressure was less than 6 MPa and either ductile deformation behaviour or transitional behaviour between brittle and ductile when the effective confining pressure was greater than 9 MPa (except for Core Section 5). The strength parameters were derived for the Mohr-Coulomb strength criterion. To exclude the effect of ductile deformation on the derived strength parameters, the strength parameters were derived in two effective confining pressure ranges: 0 to 6 MPa and 0 to 9 MPa.

8 ACKNOWLEDGEMENT

The authors wish to express their sincere thanks to the following people who assisted in the study: Willem Boon (Schlumberger IPM), John Fuller and Laura Murphy (Schlumberger-Holditch Reservoir Technologies), Peter Crozier and Keith Window (Amdel Core Services), and Don Willoughby (CSIRO Petroleum).

9 REFERENCES

- Brady, B. H. G. and Brown, E. T. (1985). *Rock Mechanics for Underground Mining*. George Allen & Unwin, London, U.K.
- Brown, E. T. (1981). *Rock Characterisation, Testing and Monitoring, ISRM Suggested Methods*. Pergamon Press, Oxford, U.K.
- Cain, P., Yuen, M. K., Le Bell, G. R., Crawford, A. M. and Lau, D. H. C. (1987). Triaxial testing of brittle sandstone using a multiple failure state method. *Geotechnical Testing Journal*, Vol. 10, No. 4, pp. 213-217.
- Fuller, J (2000). Personal Communications. Schlumberger-Holditch Reservoir Technologies, Gatwick, England.
- Goodman, R. E. (1989). *Introduction to Rock Mechanics*. John Wiley & Sons, 2nd Edition, New York, U.S.A.
- Holt, R. M. and Fjaer, E. (1991). Validity of multiple failure state triaxial tests in sandstones. *Proc. 7th Int. Cong. Rock Mech., ISRM*, Ed. W. Wittke, Aachen, pp. 509-511.
- Kavari, K., Tisa, A., Einsteirn, H. H. & Franklin, J. J. (1983). Suggested methods for determining the strength of rock materials in triaxial compression: revised version. *Int. J. Rock Mech. Min. Sci. & Geomech. Abstr.* Vol.20, pp. 283-290.
- Santarelli, F. J. and Brown, E. T. (1987). Performance of Deep Wellbores in Rocks with a Confining-Pressure Dependent Elastic Modulus. *Proc. 6th Int. Cong. Rock Mechanics*, Montreal, Canada, pp. 1217-1222.
- Wu, B., Tan, C. P., and Aoki, T. (1997). Specially designed techniques for conducting consolidated undrained triaxial tests on low permeability shales. In: K. Kim (editor), *NYRocks '97: 36th U.S. Rock Mechanics Symposium*, Columbia University, New York. pp.458.

Table 1: Summary of Sample Details

Core Section No.	Core depth (m)	Sample Reference No.	Diameter (mm)	Length (mm)	Weight (g)		Bulk Density (g/cm ³)		Test type
					Before test	After test	Before test	After test	
1	750.82-751.17	PAT_1B	41.00	81.72	215.80	219.30	2.000	2.033	Single stage
1	750.82-751.17	PAT_1C	40.63	82.05	210.56	212.96	1.979	2.002	Single stage
1	750.82-751.17	PAT_1D	41.00	82.45	214.68	216.89	1.972	1.992	Multiple stage
2	756.52-756.77	PAT_2A	40.90	82.35	193.96	205.09	1.793	1.896	Single stage
2	756.52-756.77	PAT_2B	40.93	82.23	193.70	204.70	1.790	1.892	Single stage
2	756.52-756.77	PAT_2C	40.47	80.58	185.91	196.47	1.794	1.895	Multiple stage
3	760.23-760.41	PAT_3D	41.00	74.05	191.65	197.39	1.960	2.019	Single stage
3	760.23-760.41	PAT_3C	41.54	70.34	181.24	185.45	1.901	1.945	Single stage
3	760.23-760.41	PAT_3B	40.93	82.95	198.38	210.42	1.818	1.928	Multiple stage
4	769.67-769.85	PAT_4B	41.16	83.00	214.91	218.91	1.946	1.982	Single stage
4	769.67-769.85	PAT_4D	40.96	82.74	216.91	218.29	1.990	2.002	Single stage
4	769.67-769.85	PAT_4C	41.26	81.33	216.03	219.80	1.987	2.021	Multiple stage
5	776.66-777.40	PAT_5A	40.82	80.57	177.90	200.33	1.687	1.900	Single stage
5	776.66-777.40	PAT_5C	40.53	83.13	179.70	200.87	1.676	1.873	Single stage
5	776.66-777.40	PAT_5B	40.93	81.97	193.82	202.51	1.797	1.878	Multiple stage

Table 2: Summary of Test Conditions

<i>Sample Ref. No.</i>	<i>Axial Stress (MPa)</i>	<i>Cell Pressure (MPa)</i>	<i>Pore Pressure (MPa)</i>	<i>Test type</i>
PAT_1B	11	11	5.0	Single stage
PAT_1C	14	14	5.0	Single stage
PAT_1D	1, 2, 5, 9 & 12	1, 2, 5, 9 & 12	5.0	Multiple stage
PAT_2A	11	11	5.0	Single stage
PAT_2B	14	14	5.0	Single stage
PAT_2C	1, 2, 5, 9 & 12	1, 2, 5, 9 & 12	5.0	Multiple stage
PAT_3D	11	11	5.0	Single stage
PAT_3C	14	14	5.0	Single stage
PAT_3B	1, 2, 5, 9 & 12	1, 2, 5, 9 & 12	5.0	Multiple stage
PAT_4B	11	11	5.0	Single stage
PAT_4D	14	14	5.0	Single stage
PAT_4C	1, 2, 5, 9 & 12	1, 2, 5, 9 & 12	5.0	Multiple stage
PAT_5A	11	11	5.0	Single stage
PAT_5C	14	14	5.0	Single stage
PAT_5B	1, 2, 5, 9 & 12	1, 2, 5, 9 & 12	5.0	Multiple stage

Table 3: Summary of Test Results

Sample Ref. No.	Elastic Properties		Eff. Conf. Press. σ_3' (MPa)	Peak Strength $\sigma_1' - \sigma_3'$ (MPa)	Residual Strength $\sigma_1' - \sigma_3'$ (MPa)
	E (GPa)	ν			
PAT_1B	1.046	0.258	6	12.206	11.31
PAT_1C	1.167	0.182	9	13.36	-
PAT_1D (Stage 1)	0.391	0.486	1	4.312	-
PAT_1D (Stage 2)	0.739	0.412	2	6.540	-
PAT_1D (Stage 3)	1.146	0.271	5	9.709	-
PAT_1D (Stage 4)	1.595	0.233	9	11.740	-
PAT_1D (Stage 5)	2.025	0.246	12	12.745	-
PAT_2A	1.213	0.176	6	10.53	10.57
PAT_2B	1.590	0.182	9	11.61	-
PAT_2C (Stage 1)	0.779	0.475	1	5.023	-
PAT_2C (Stage 2)	1.280	0.362	2	6.629	-
PAT_2C (Stage 3)	1.667	0.219	5	9.099	-
PAT_2C (Stage 4)	2.034	0.184	9	10.400	-
PAT_2C (Stage 5)	2.500	0.190	12	10.770	-
PAT_3D	1.022	0.207	6	7.9	-
PAT_3C	1.304	0.188	9	8.95	-
PAT_3B (Stage 1)	0.763	0.474	1	5.280	-
PAT_3B (Stage 2)	1.357	0.395	2	7.244	-
PAT_3B (Stage 3)	1.800	0.255	5	9.620	-
PAT_3B (Stage 4)	2.308	0.215	9	10.748	-
PAT_3B (Stage 5)	2.600	0.227	12	10.860	-

Table 3: Summary of Test Results - continued

Sample Ref. No.	Elastic Properties		Eff. Conf. Press. σ_3' (MPa)	Peak Strength $\sigma_1' - \sigma_3'$ (MPa)	Residual Strength $\sigma_1' - \sigma_3'$ (MPa)
	E (GPa)	ν			
PAT_4B	0.652	0.183	6	11.96	11.25
PAT_4D	1.243	0.239	9	11.52	-
PAT_4C (Stage 1)	0.235	0.455	1	2.460	-
PAT_4C (Stage 2)	0.592	0.313	2	4.246	-
PAT_4C (Stage 3)	0.792	0.209	5	10.335	-
PAT_4C (Stage 4)	1.174	0.213	9	10.335	-
PAT_4C (Stage 5)	1.029	0.239	12	12.850	-
PAT_5A	1.000	0.274	6	12.063	11.24
PAT_5C	1.800	0.244	9	15.323	15.11
PAT_5B (Stage 1)	0.263	0.385	1	2.447	-
PAT_5B (Stage 2)	0.662	0.284	2	4.213	-
PAT_5B (Stage 3)	0.943	0.193	5	6.979	-
PAT_5B (Stage 4)	1.364	0.176	9	8.337	-
PAT_5B (Stage 5)	1.800	0.215	12	8.997	-

Table 4: Regressional Constants for Young's Modulus and Poisson's Ratio

Core Section No.	E_o (GPa)	A	ν_o	B
1	0.256	0.815	0.624	0.404
2	0.597	0.558	0.640	0.521
3	0.588	0.600	0.620	0.434
4	0.190	0.743	0.497	0.355
5	0.179	0.912	0.436	0.352

Table 5: Parameter for Mohr-Coulomb Strength Criterion

Core Section No.	Excluding ($\sigma_3'=12$ MPa)		Excluding ($\sigma_3'=9$ & 12 MPa)	
	c' (MPa)	ϕ' (deg.)	c' (MPa)	ϕ' (deg.)
1	1.56	19.26	1.00	24.75
2	1.94	15.22	1.48	19.84
3	2.37	11.07	2.15	13.25
4	1.02	20.1	0.14	29.45
5	0.95*	15.10*	0.57*	20.6*

*: Derived from multiple stage triaxial test results only.

Table 6: Strain States of Single and Multiple Stage Triaxial Tests at Hydrostatic Stresses of 5 MPa and 9 MPa

Core Section No.	Test Type	5 MPa			9 MPa		
		Axial Strain* (mstr)	RadialStrain* (mstr)	Shear Strain (mstr)	Axial Strain* (mstr)	Radial Strain* (mstr)	Shear Strain (mstr)
1	Single Stage	5.748	-7.446	-1.698	9.224	-10.760	-1.535
	Multiple Stage	10.633	-0.977	9.656	16.863	-3.072	13.790
2	Single Stage	3.523	-4.452	-0.928	5.164	-5.977	-0.813
	Multiple Stage	7.152	-2.536	4.617	11.400	-4.993	6.407
3	Single Stage	5.754	-4.635	1.119	8.609	-6.776	1.832
	Multiple Stage	6.213	-2.188	4.026	10.099	-4.443	5.656
4	Single Stage	6.341	-9.247	-2.906	11.568	-16.455	-4.887
	Multiple Stage	12.178	-1.172	11.006	21.109	-3.873	17.236
5	Single Stage	5.325	-7.758	-2.433	7.812	-12.758	-4.945
	Multiple Stage	10.785	-1.407	9.379	18.826	-3.138	15.688

*: Compressive strain is defined as positive for axial strain and negative for radial strain.

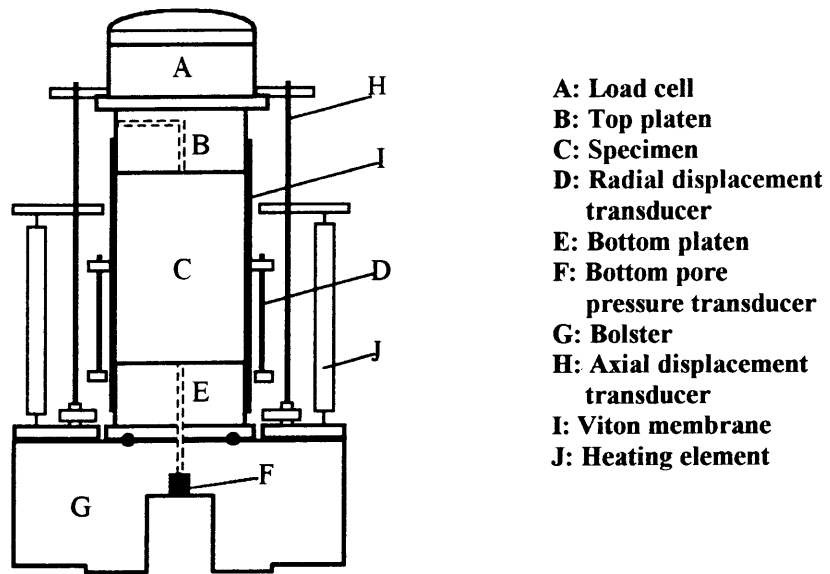


Figure 1 A schematic of the sample stack assembly.

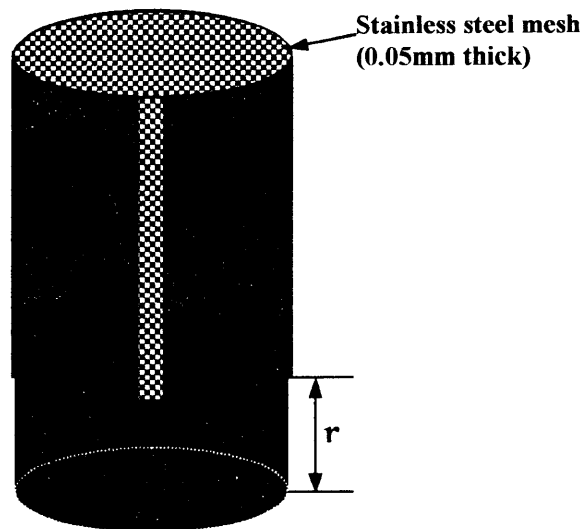


Figure 2 Configuration of sidedrain.

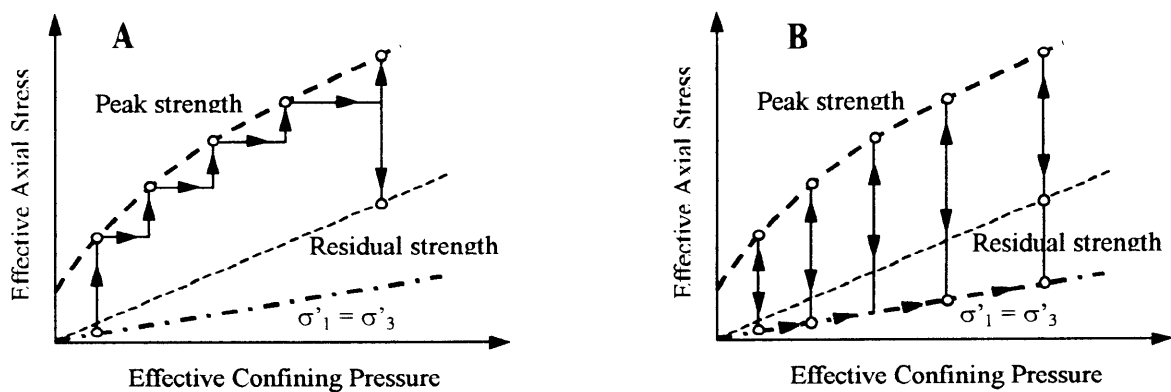


Figure 3. ISRM suggested stress path (A) and modified stress path (B).

PATRICIA BALEEN - 2 SAND CORE SECTION 1
(Single Stage Triaxial Test)

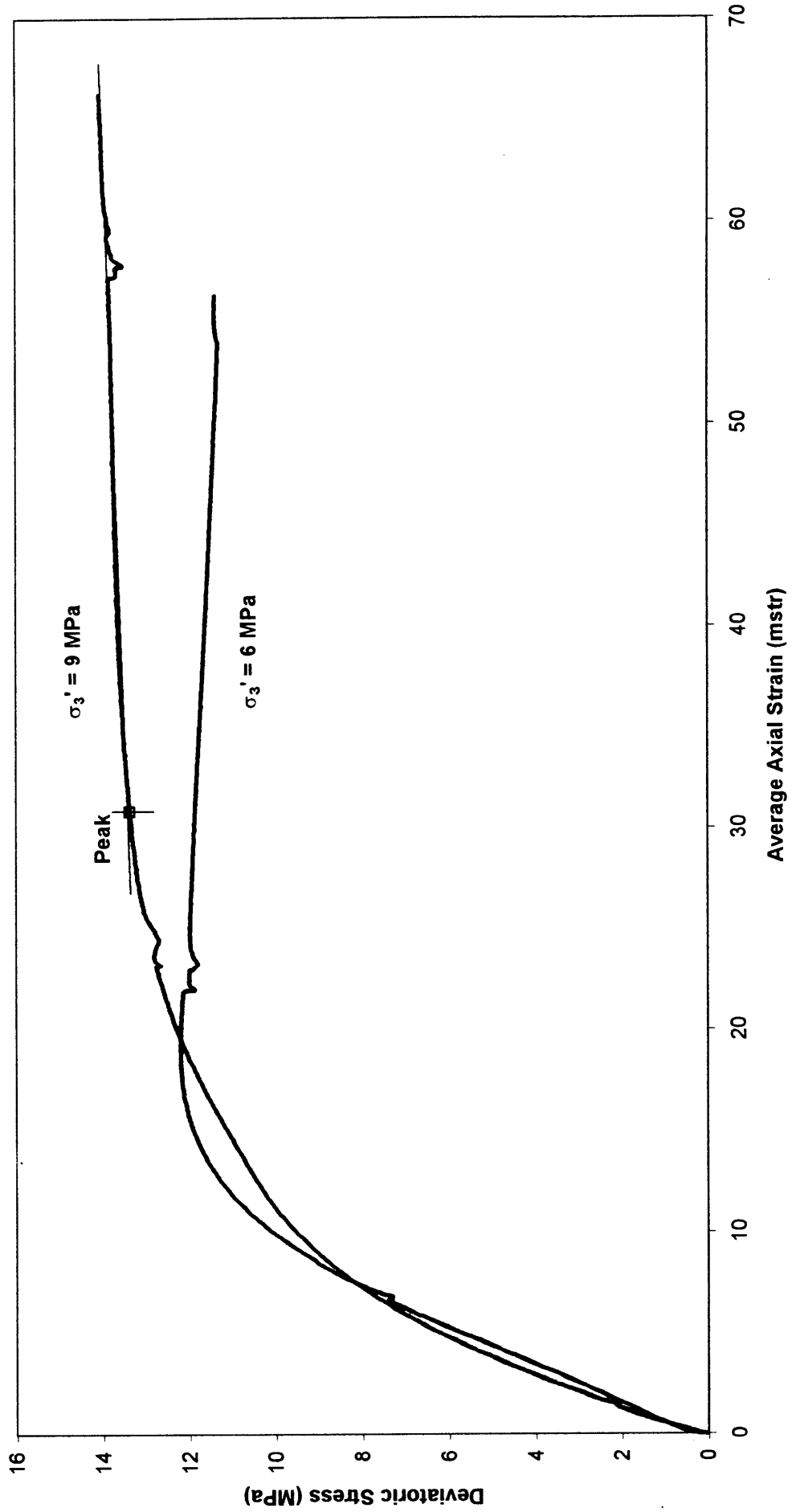


Figure 4 Deviatoric stress vs average axial strain behaviour for single stage triaxial tests on Core Section 1.

PATRICIA BALEEN - 2 SAND CORE SECTION 1
 (Single Stage Triaxial Test)

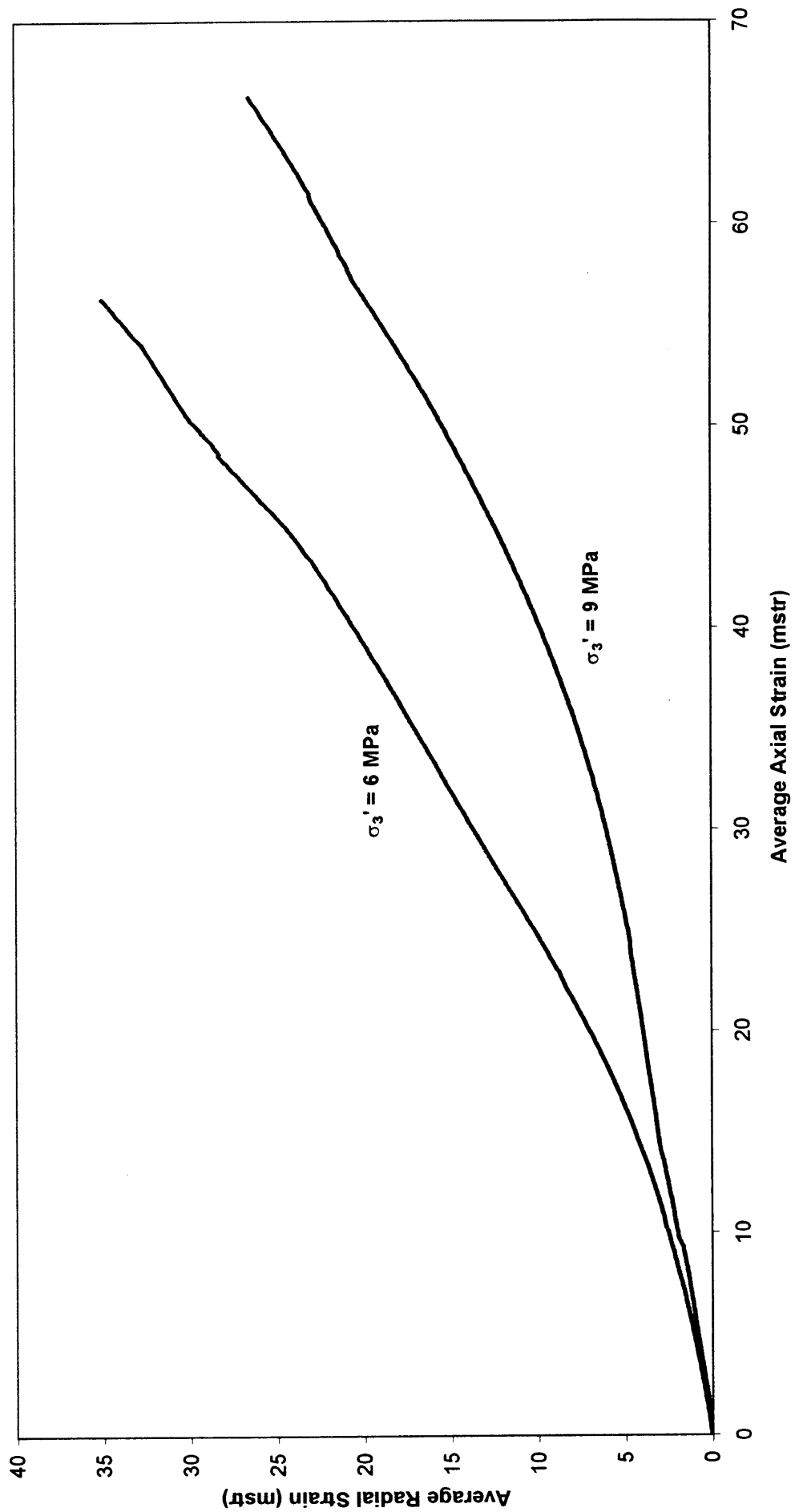


Figure 5 Average radial strain vs average axial strain behaviour for single stage triaxial tests on Core Section 1.

PATRICIA BALEEN - 2 SAND CORE SECTION 1
(Multiple Stage Test)

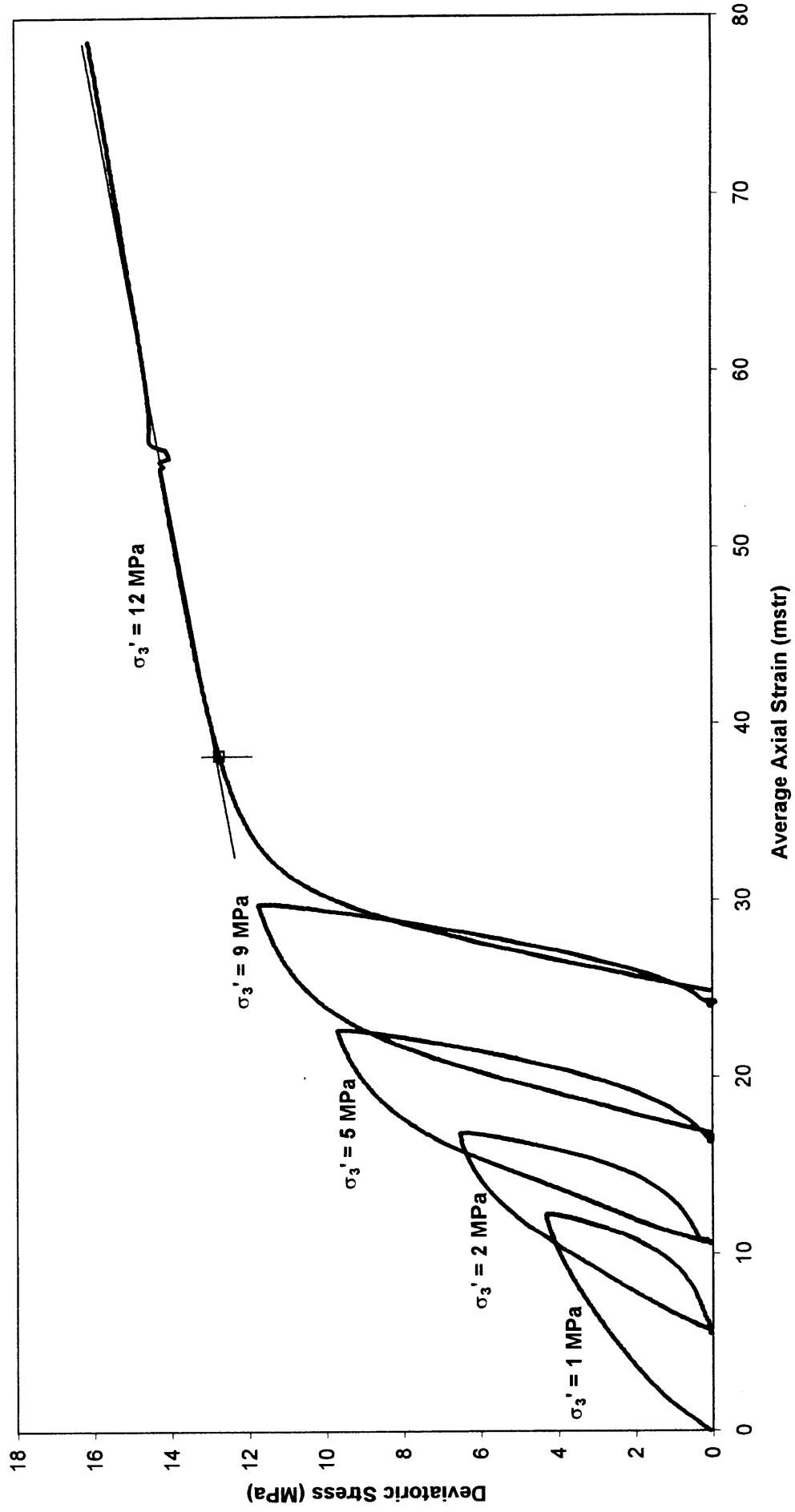


Figure 6 Deviatoric stress vs average axial strain behaviour for multiple stage triaxial tests on Core Section 1.

PATRICIA BALEEN - 2 SAND CORE SECTION 1
(Multiple Stage Test)

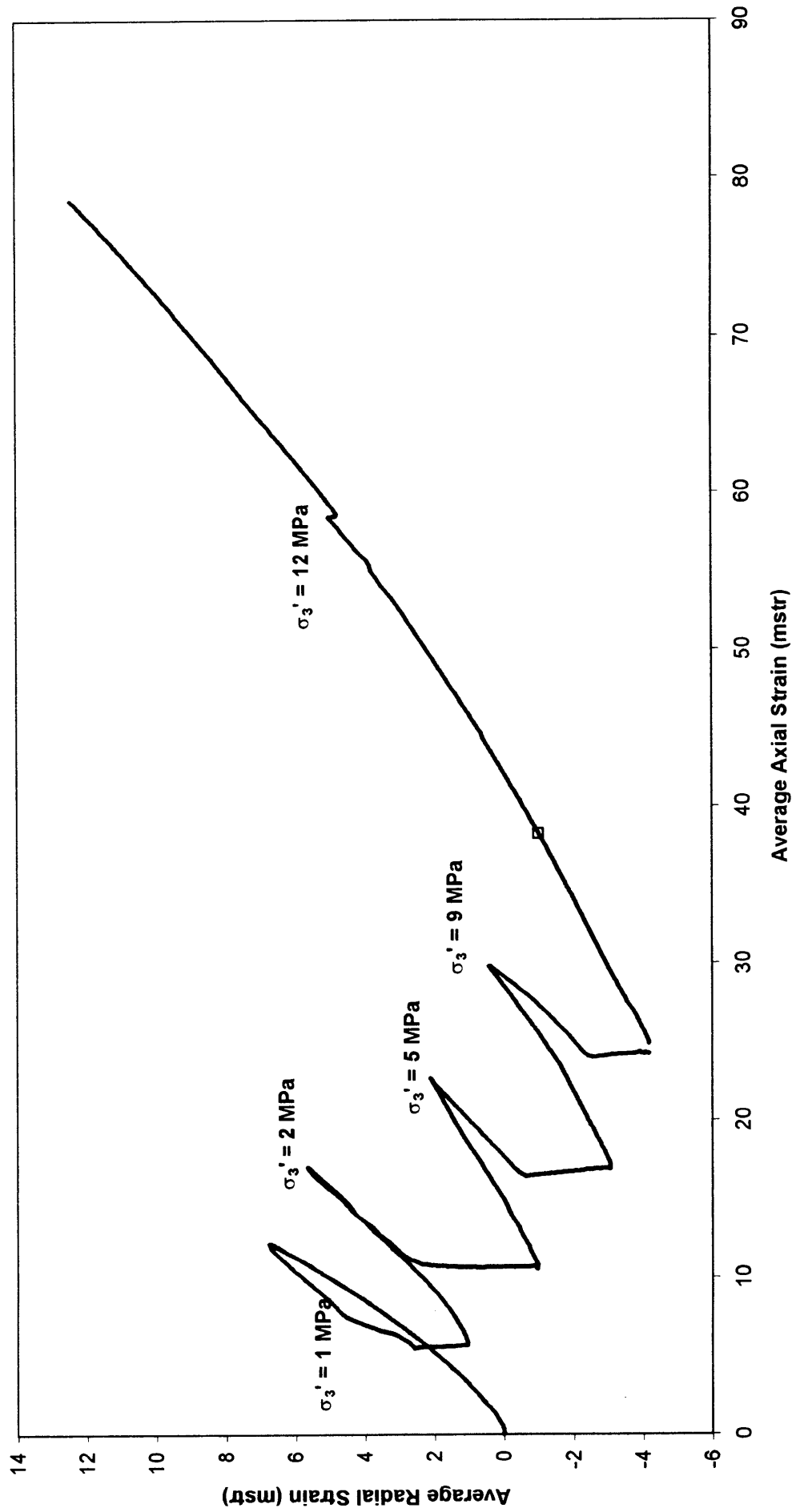


Figure 7 Average radial strain vs average axial strain behaviour for multiple failure state triaxial tests on Core Section 1.

PATRICIA BALEEN - 2 SAND CORE SECTION 2
(Single Stage Triaxial Test)

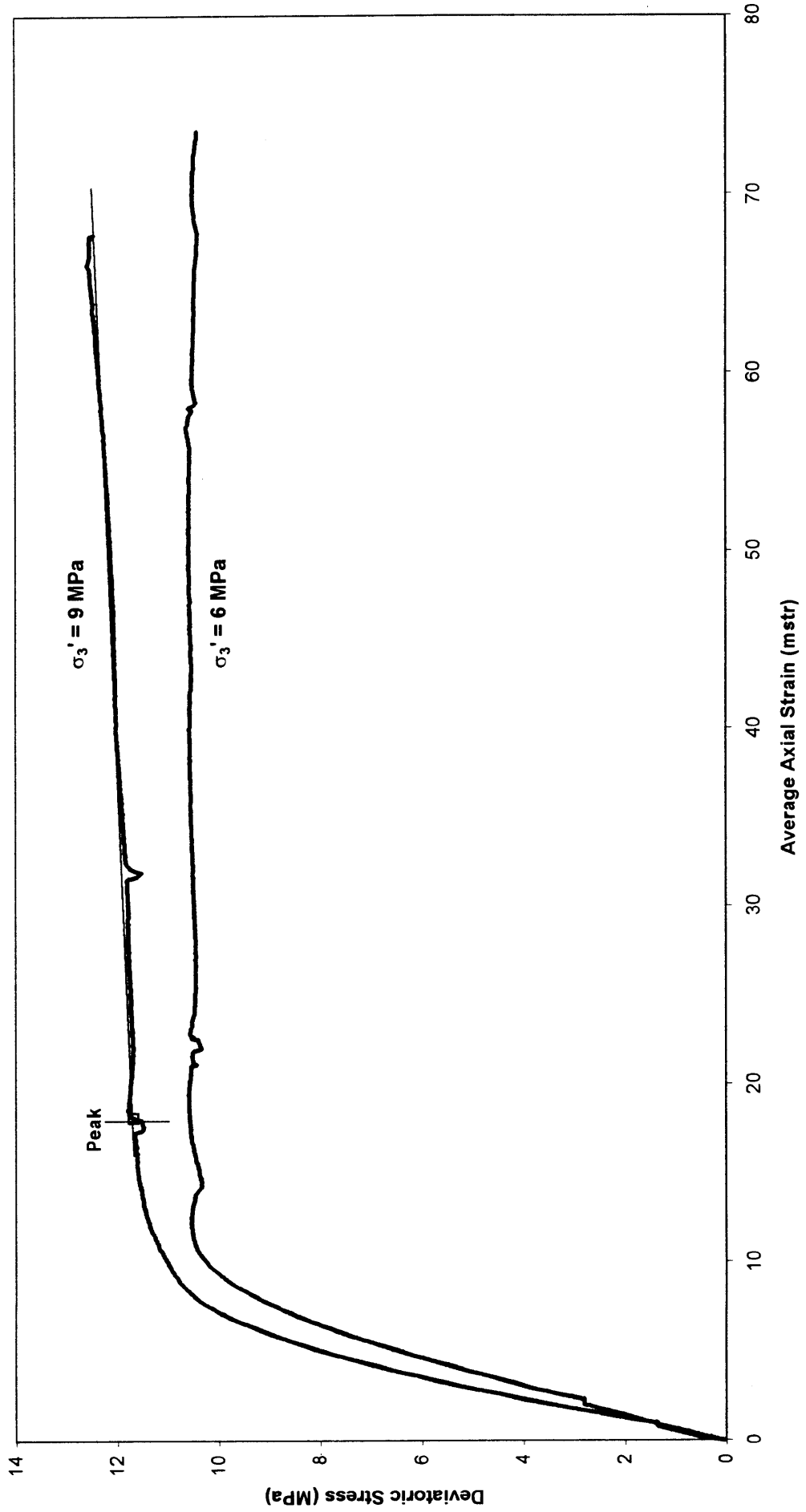


Figure 8 Deviatoric stress vs average axial strain behaviour for single stage triaxial tests on Core Section 2.

PATRICIA BALEEN - 2 SAND CORE SECTION 2
(Single Stage Triaxial Test)

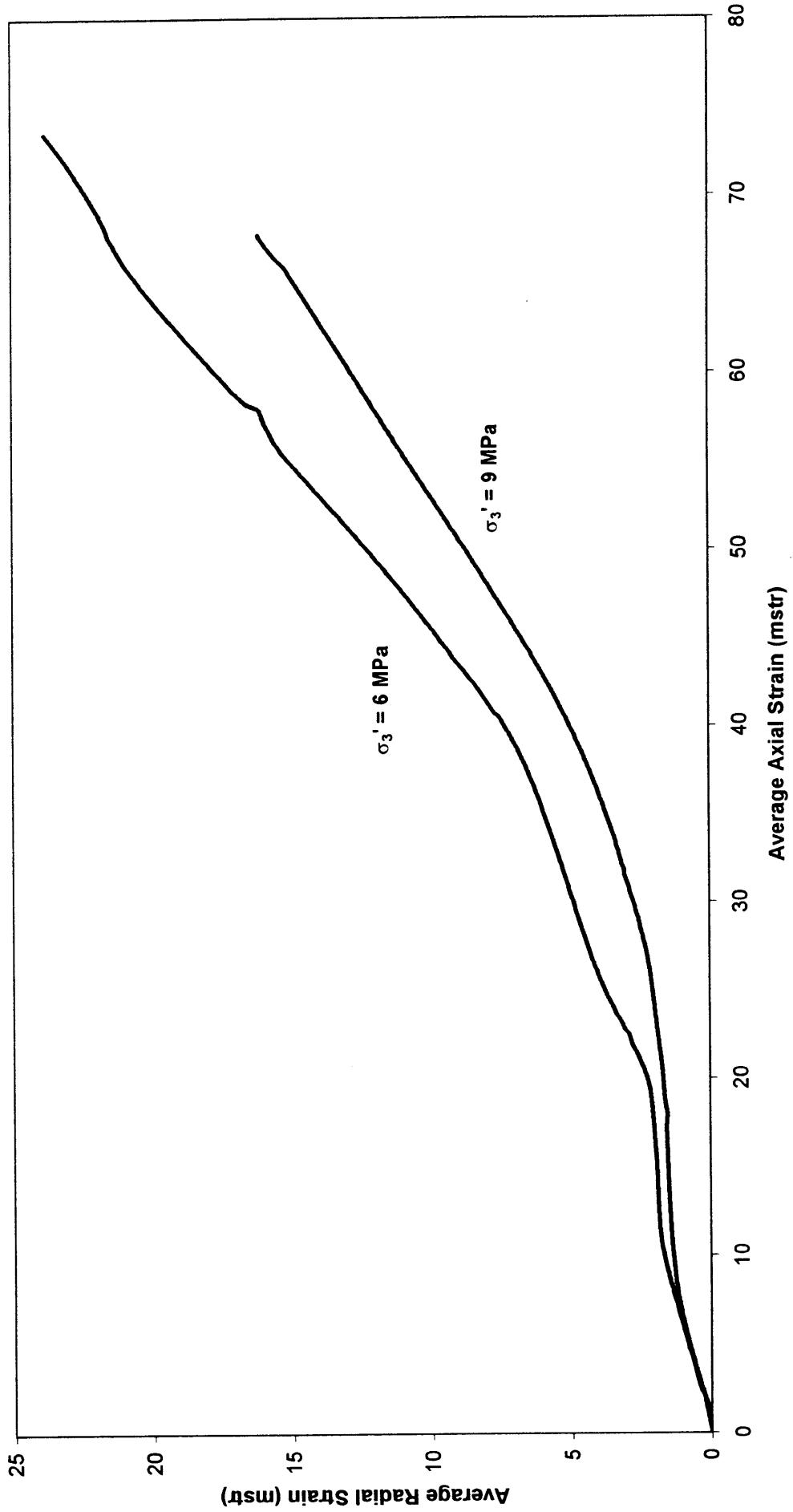


Figure 9 Average radial strain vs average axial strain behaviour for single stage triaxial tests Core Section 2.

PATRICIA BALEEN - 2 SAND CORE SECTION 2
(Multiple Stage Test)

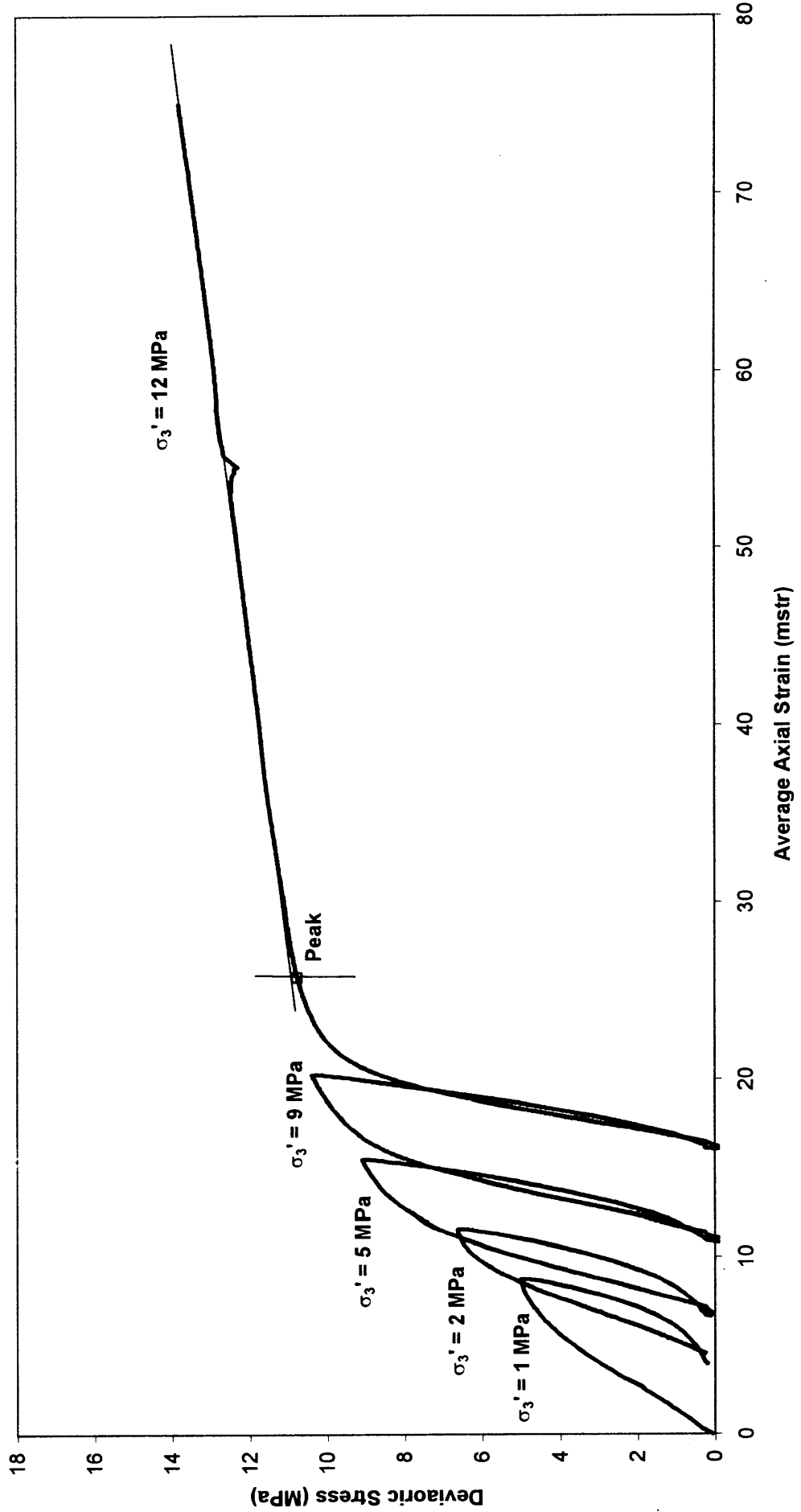


Figure 10 Deviatoric stress vs average axial strain behaviour for multiple stage triaxial tests on Core Section 2.

PATRICIA BALEEN - 2 SAND CORE SECTION 2
(Multiple Stage Test)

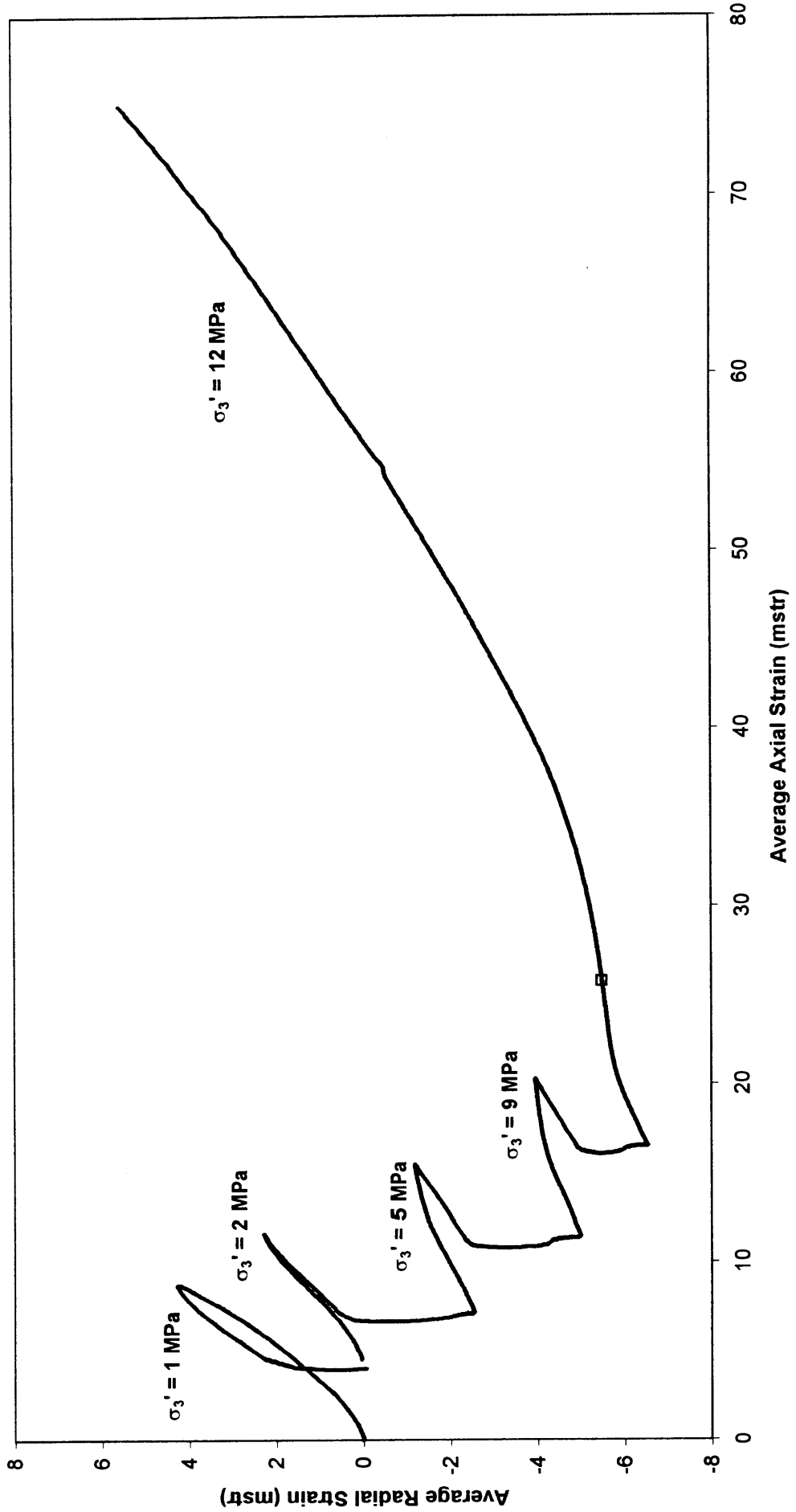


Figure 11 Average radial strain vs average axial strain behaviour for multiple stage triaxial tests on Core Section 2.

PATRICIA BALEEN - 2 SAND CORE SECTION 3
(Single Stage Triaxial Test)

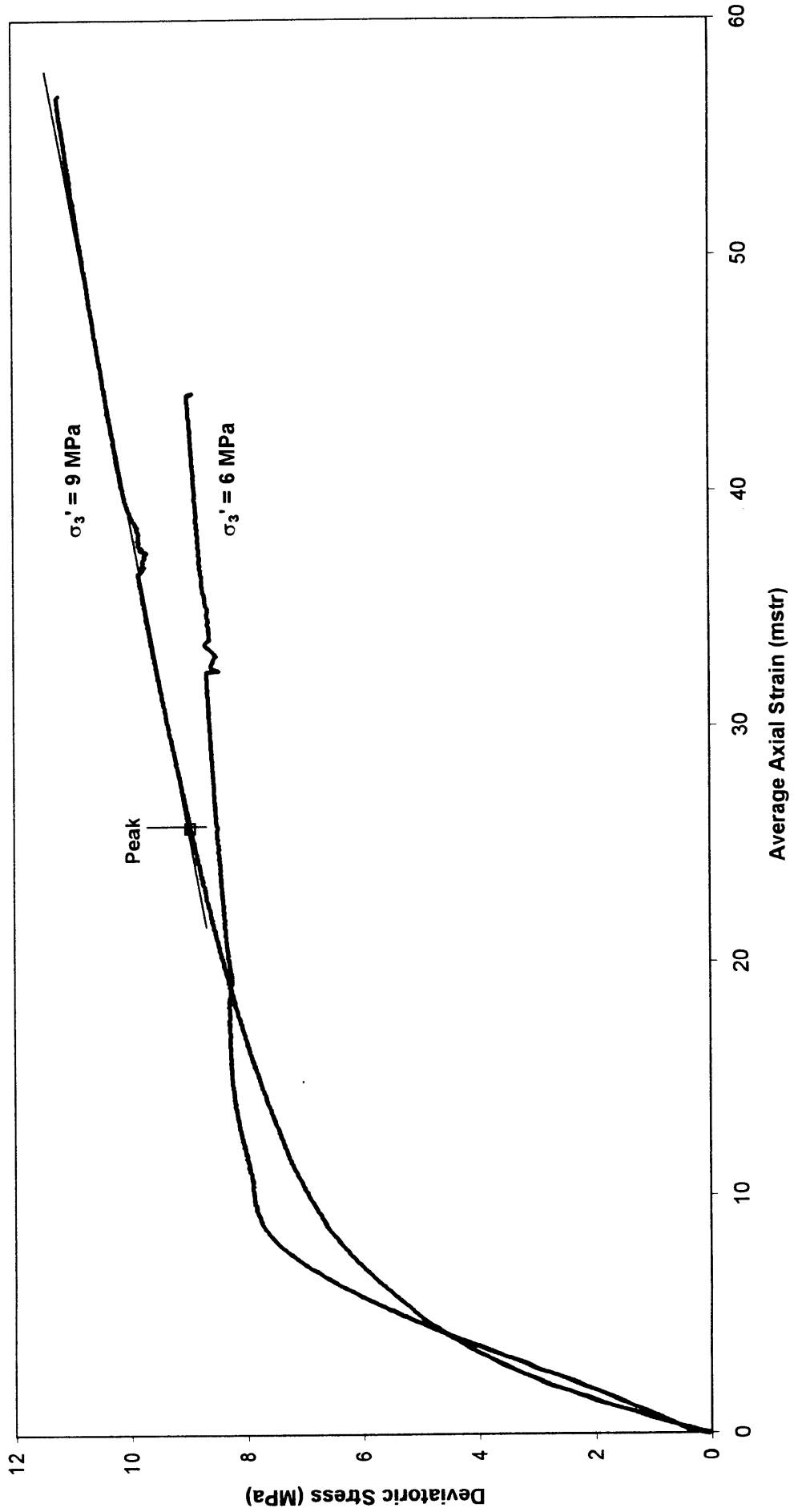


Figure 12 Deviatoric stress vs average axial strain behaviour for single stage triaxial tests on Core Section 3.

PATRICIA BALEEN - 2 SAND CORE SECTION 3
(Single Stage Triaxial Test)

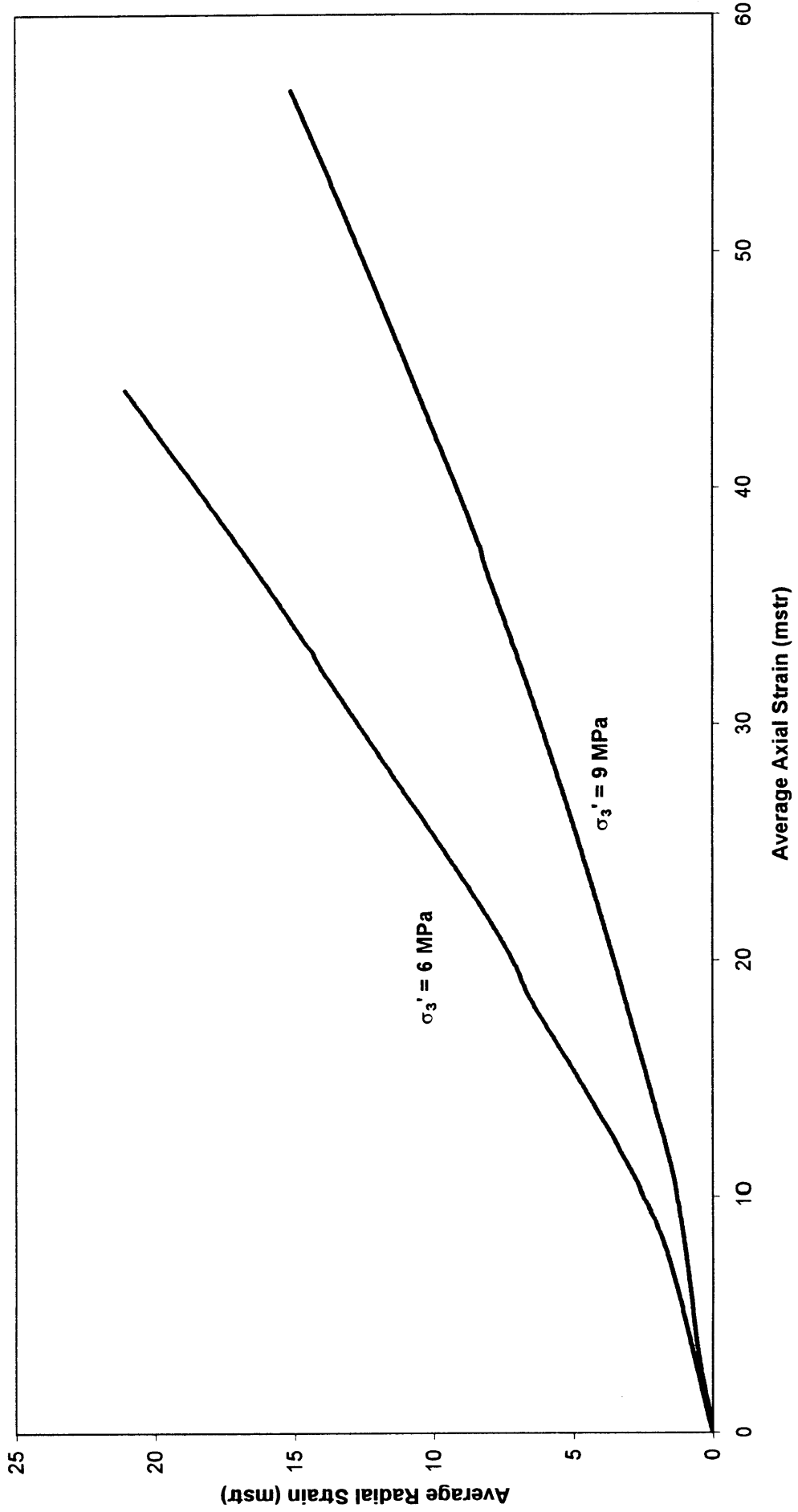


Figure 13 Average radial strain vs average axial strain behaviour for single stage triaxial tests on Core Section 3.

PATRICIA BALEEN - 2 SAND CORE SECTION 3
 (Multiple Stage Test)

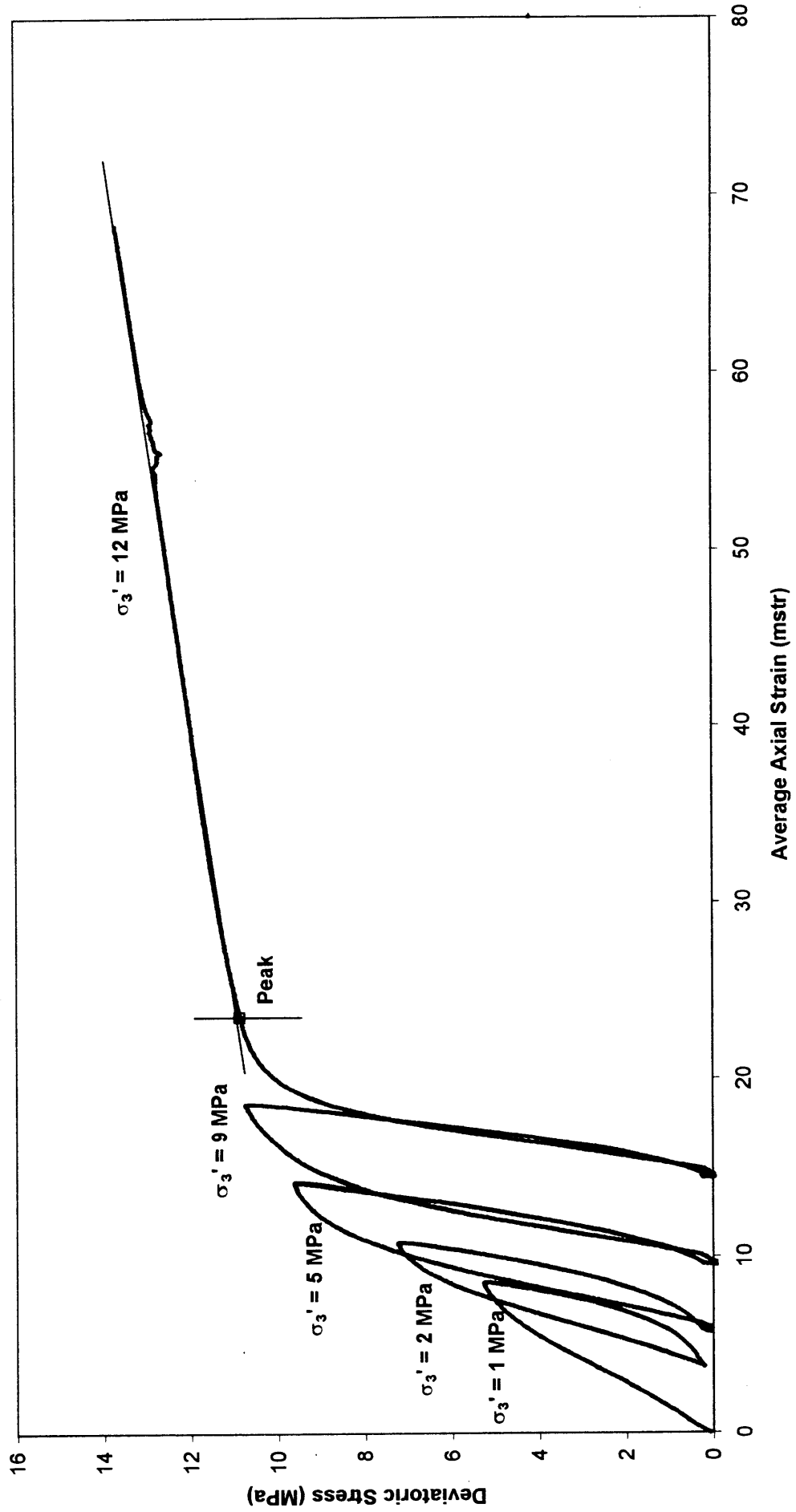


Figure 14 Deviatoric stress vs average axial strain behaviour for multiple stage triaxial tests on Core Section 3.

PATRICIA BALEEN - 2 SAND CORE SECTION 3
(Multiple Stage Test)

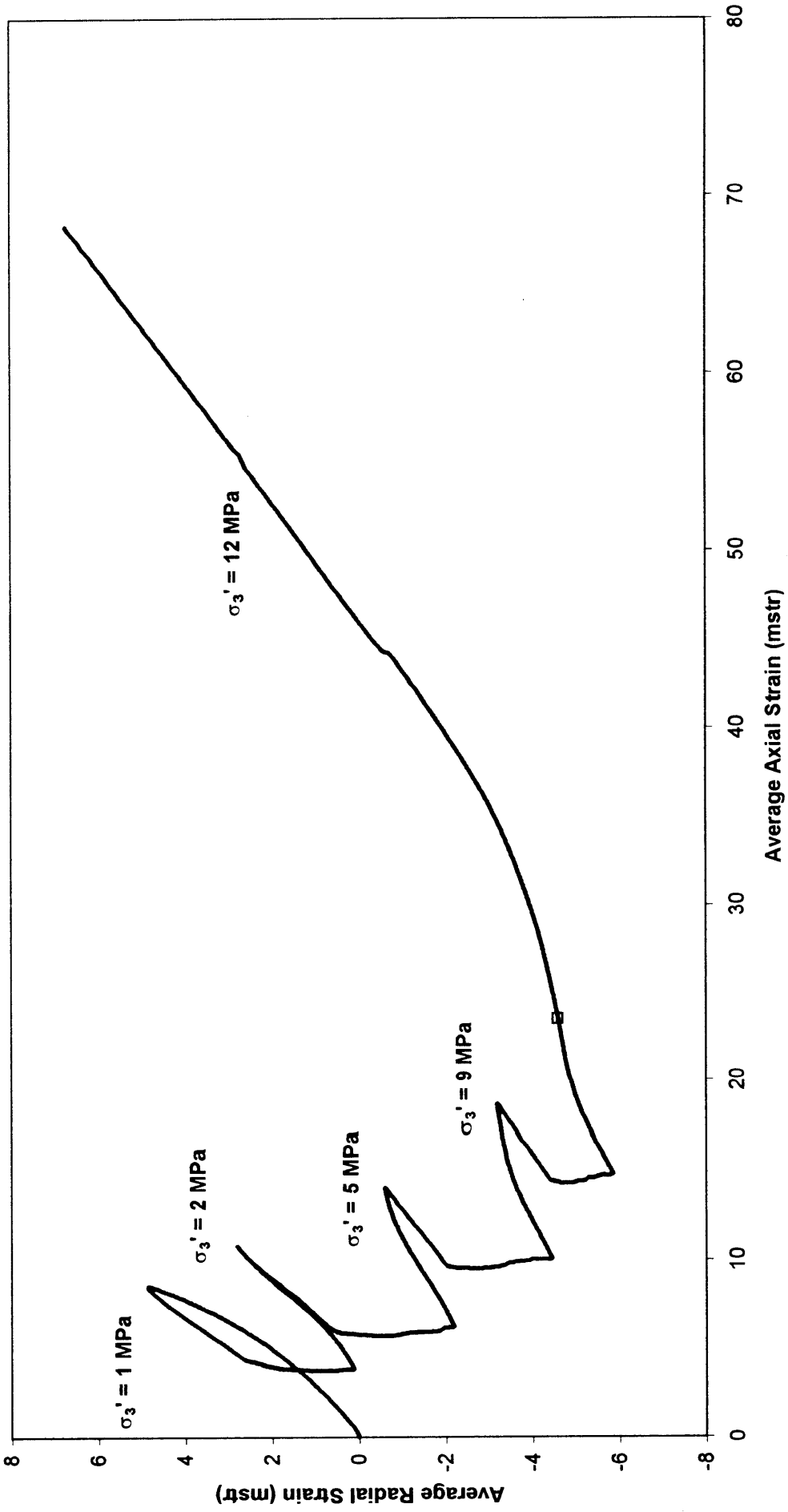


Figure 15 Average radial strain vs average axial strain behaviour for multiple failure state triaxial tests on Core Section 3.

PATRICIA BALEEN - 2 SAND CORE SECTION 4
(Single Stage Triaxial Test)

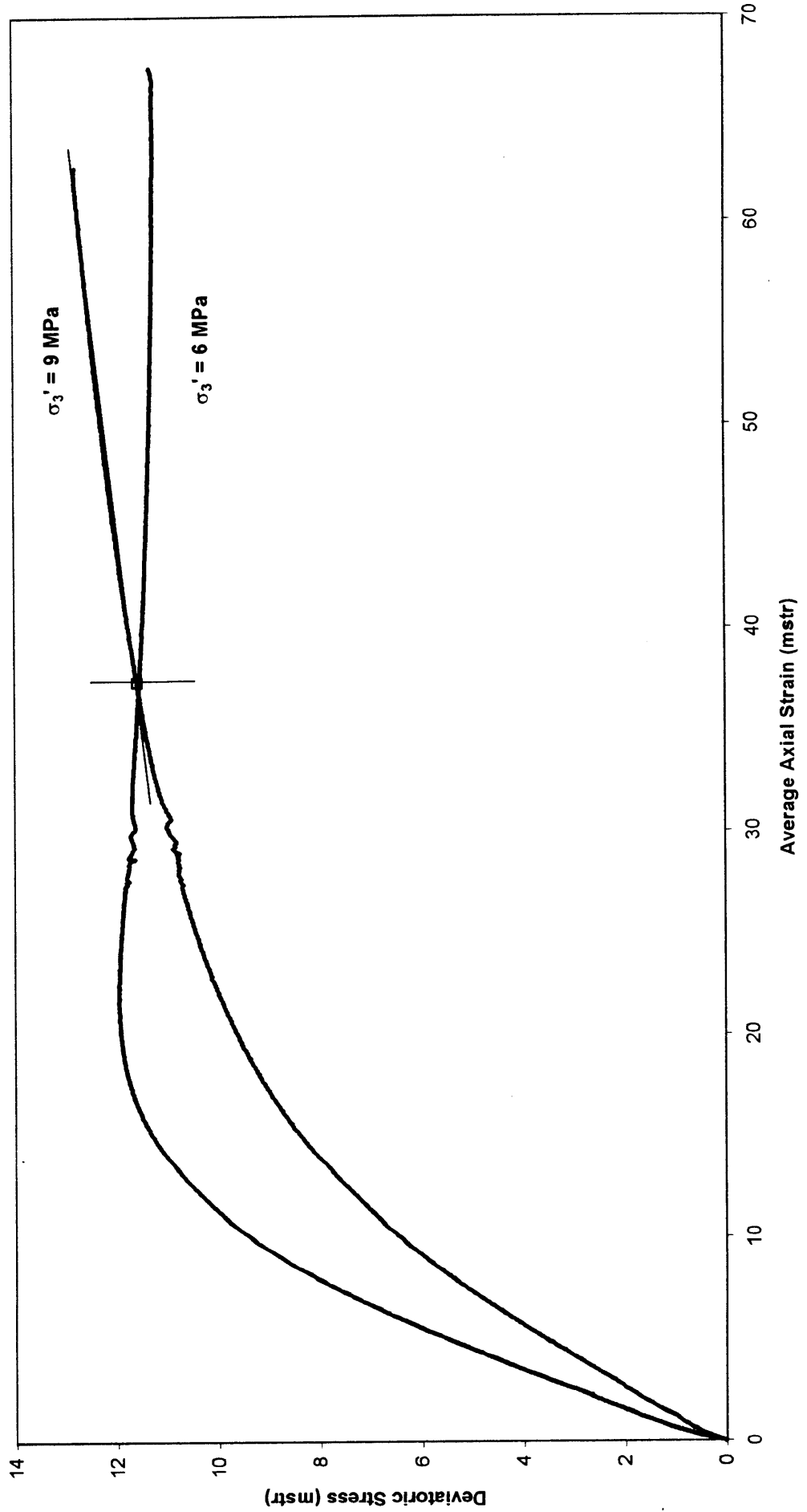


Figure 16 Deviatoric stress vs average axial strain behaviour for single stage triaxial tests on Core Section 4.

PATRICIA BALEEN - 2 SAND CORE SECTION 4
(Single Stage Triaxial Test)

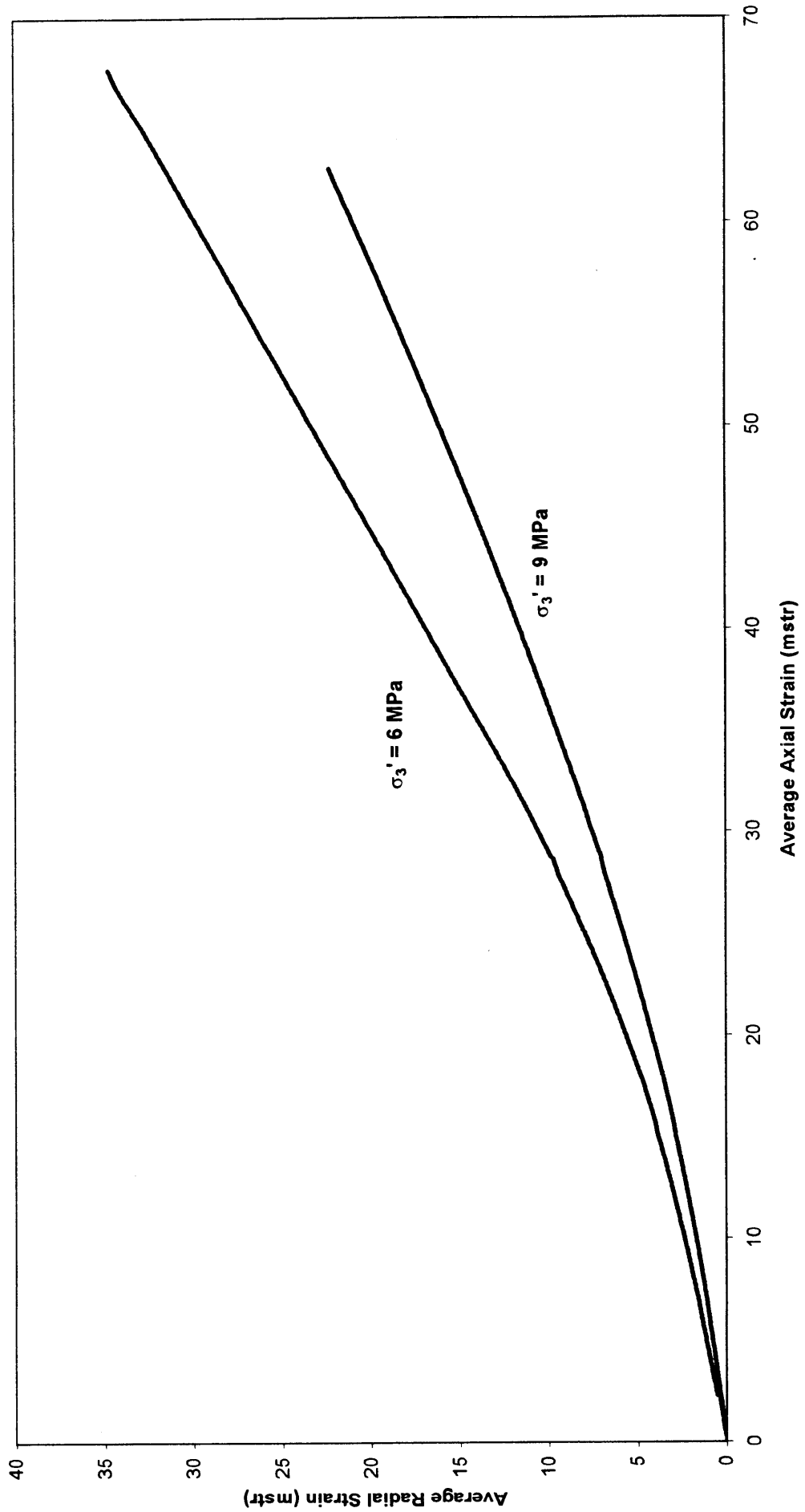


Figure 17 Average radial strain vs average axial strain behaviour for single stage triaxial tests on Core Section 4.

PATRICIA BALEEN - 2 SAND CORE SECTION 4
 (Multiple Stage Test)

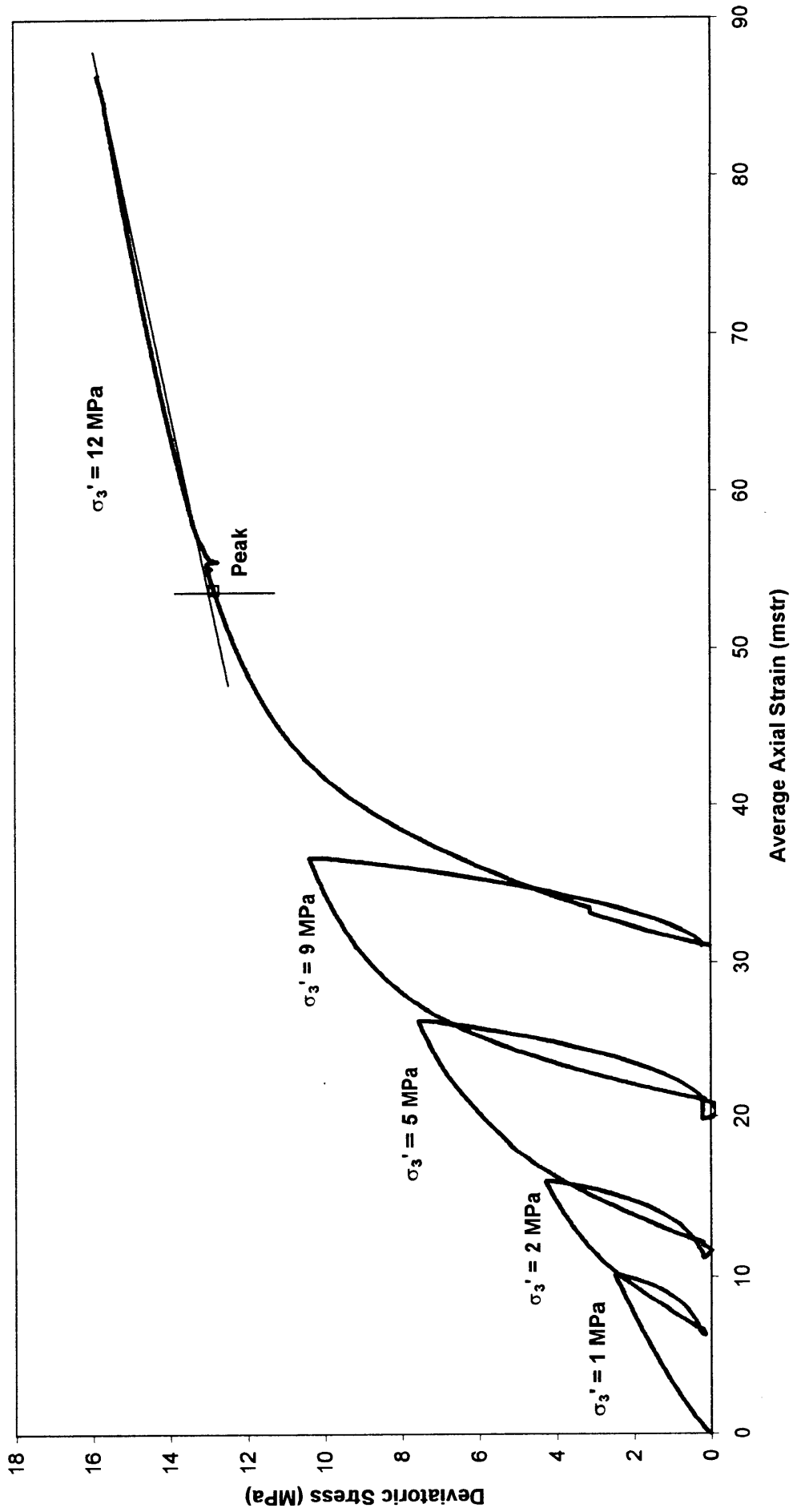


Figure 18 Deviatoric stress vs average axial strain behaviour for multiple stage triaxial tests on Core Section 4.

PATRICIA BALEEN - 2 SAND CORE SECTION 4
(Multiple Stage Test)

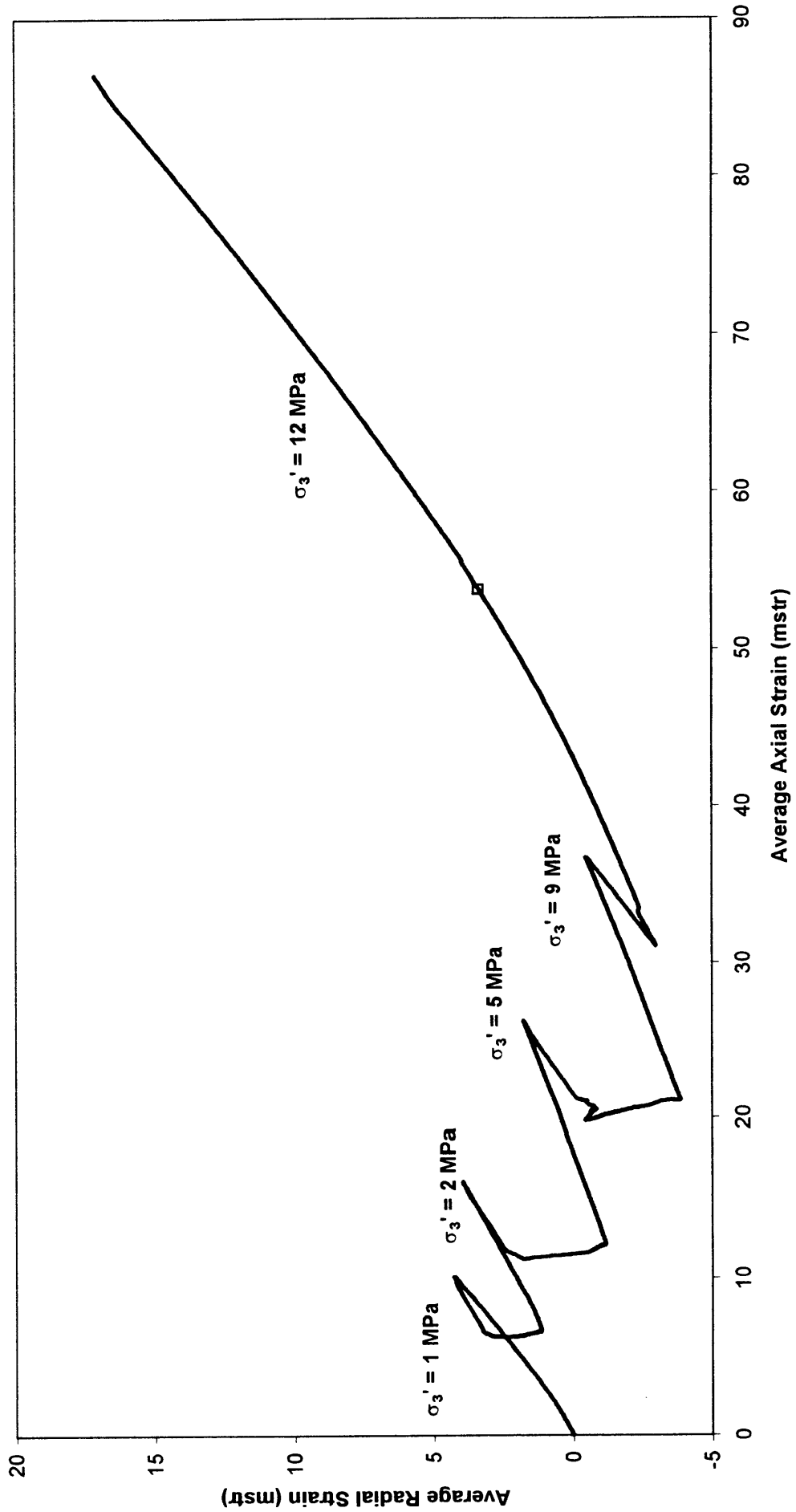


Figure 19 Average radial strain vs average axial strain behaviour for multiple stage triaxial tests on Core Section 4.

PATRICIA BALEEN - 2 SAND CORE SECTION 5
(Single Stage Triaxial Test)

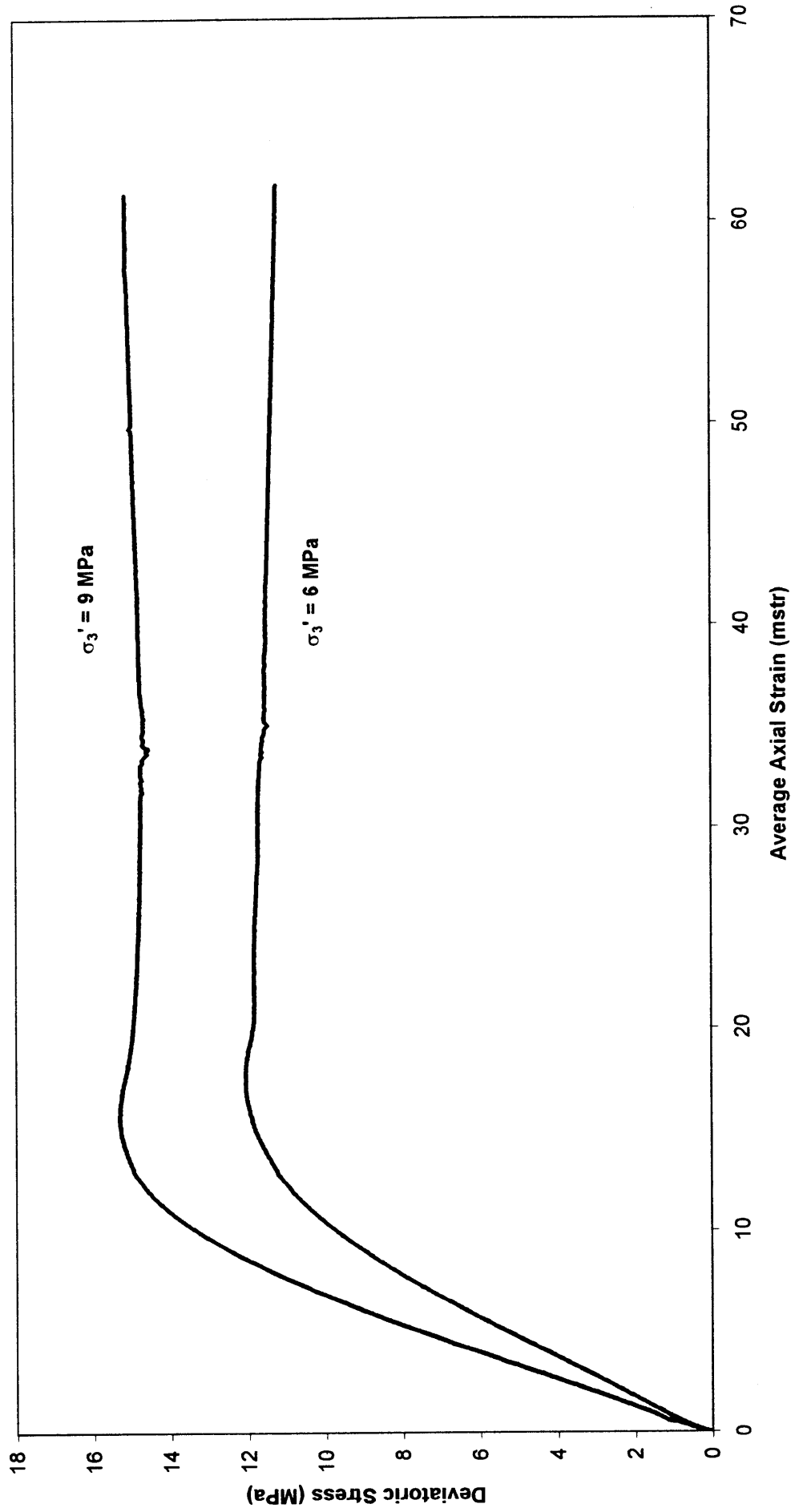


Figure 20 Deviatoric stress vs average axial strain behaviour for single stage triaxial tests on Core Section 5.

PATRICIA BALEEN - 2 SAND CORE SECTION 5
(Single Stage Triaxial Test)

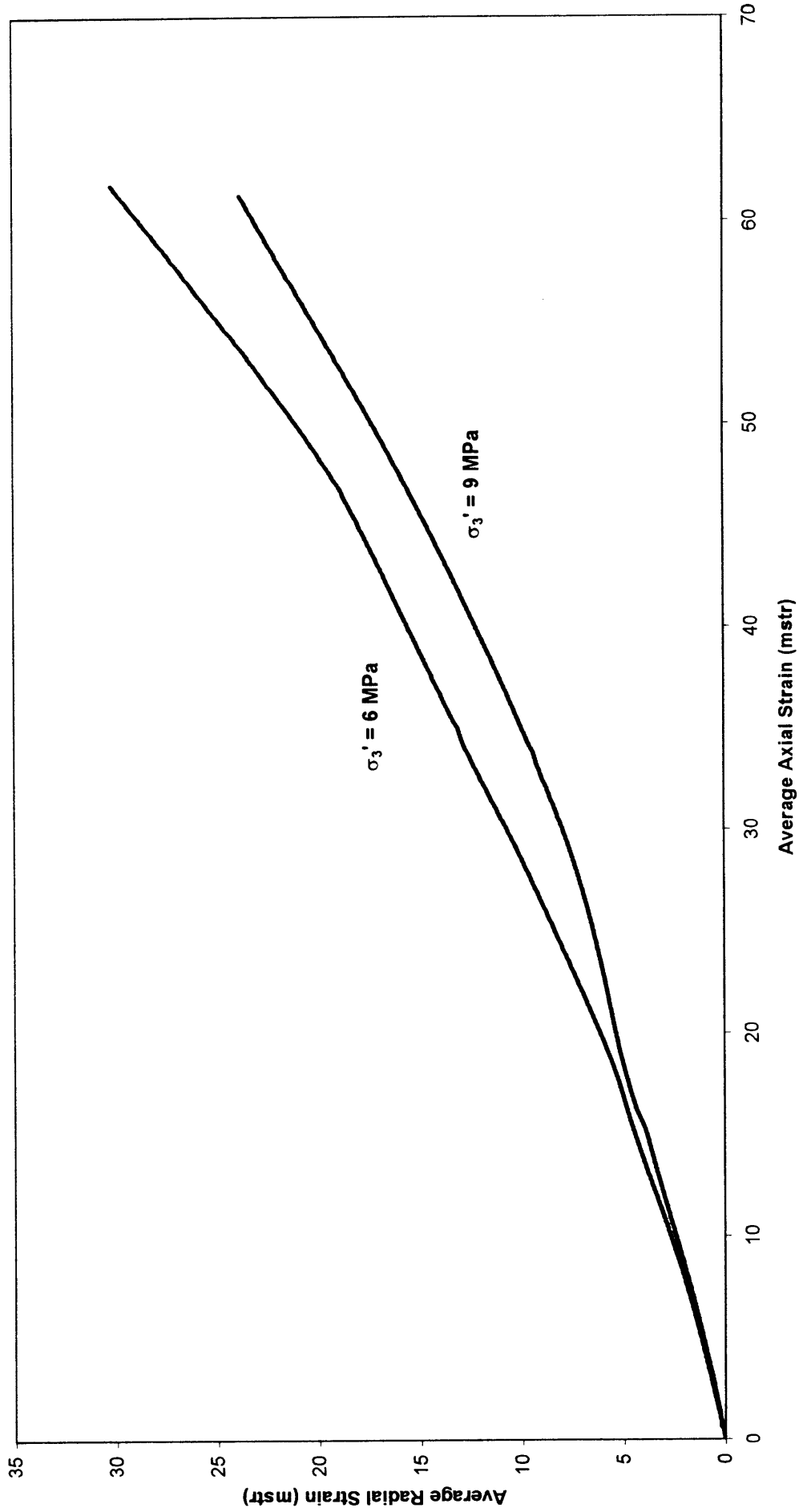


Figure 21 Average radial strain vs average axial strain behaviour for single stage triaxial tests on Core Section 5.

PATRICIA BALEEN - 2 SAND CORE SECTION 5
(Multiple Stage Test)

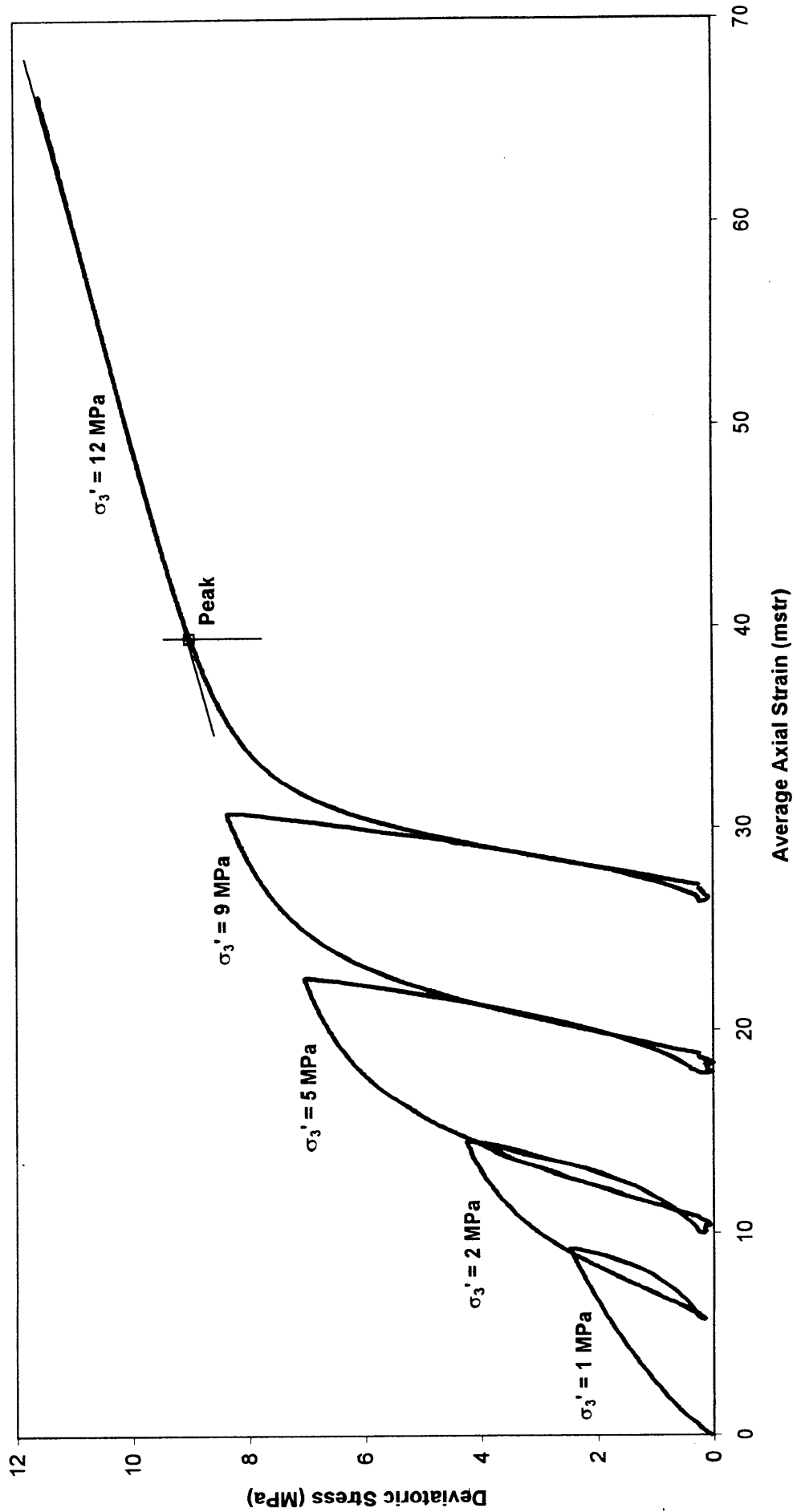


Figure 22 Deviatoric stress vs average axial strain behaviour for multiple stage triaxial tests on Core Section 5.

PATRICIA BALEEN - 2 SAND CORE SECTION 5
(Multiple Stage Test)

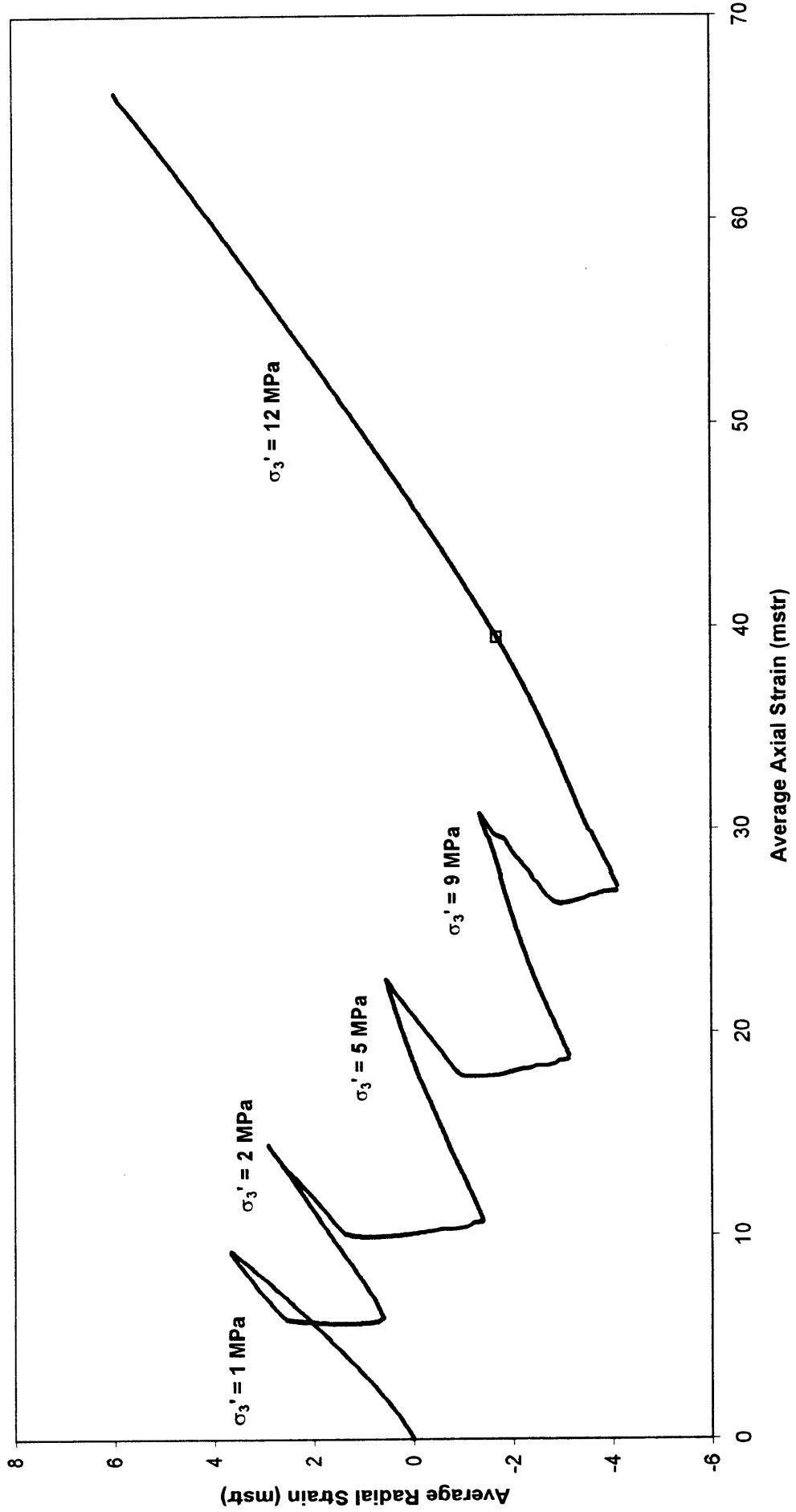


Figure 23 Average radial strain vs average axial strain behaviour for multiple stage triaxial tests on Core Section 5.

Elastic Parameters - Core Section 1

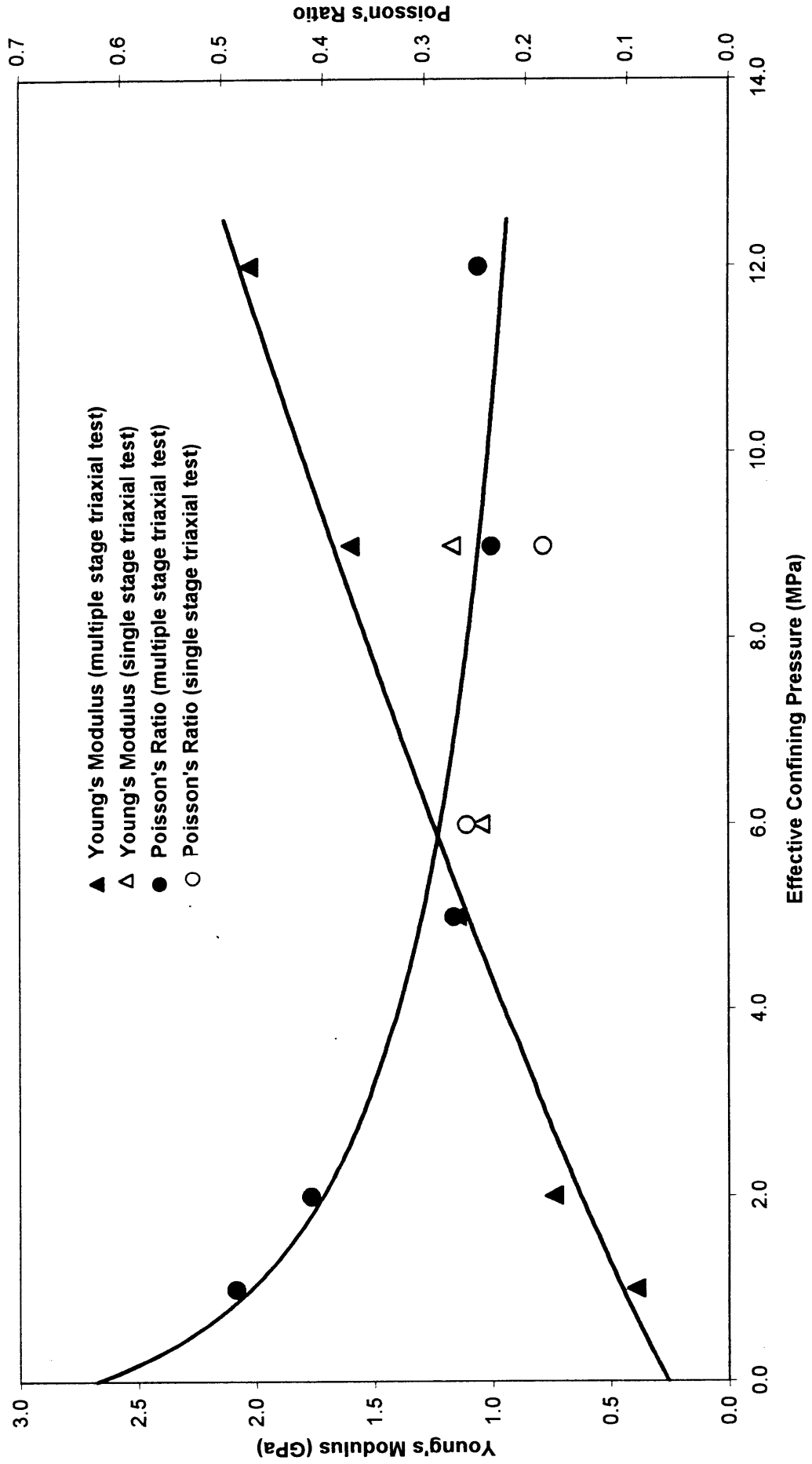


Figure 24 Correlations between Young's modulus and Poisson's ratio, and effective confining pressure for Core Section 1.

Elastic Parameters - Core Section 2

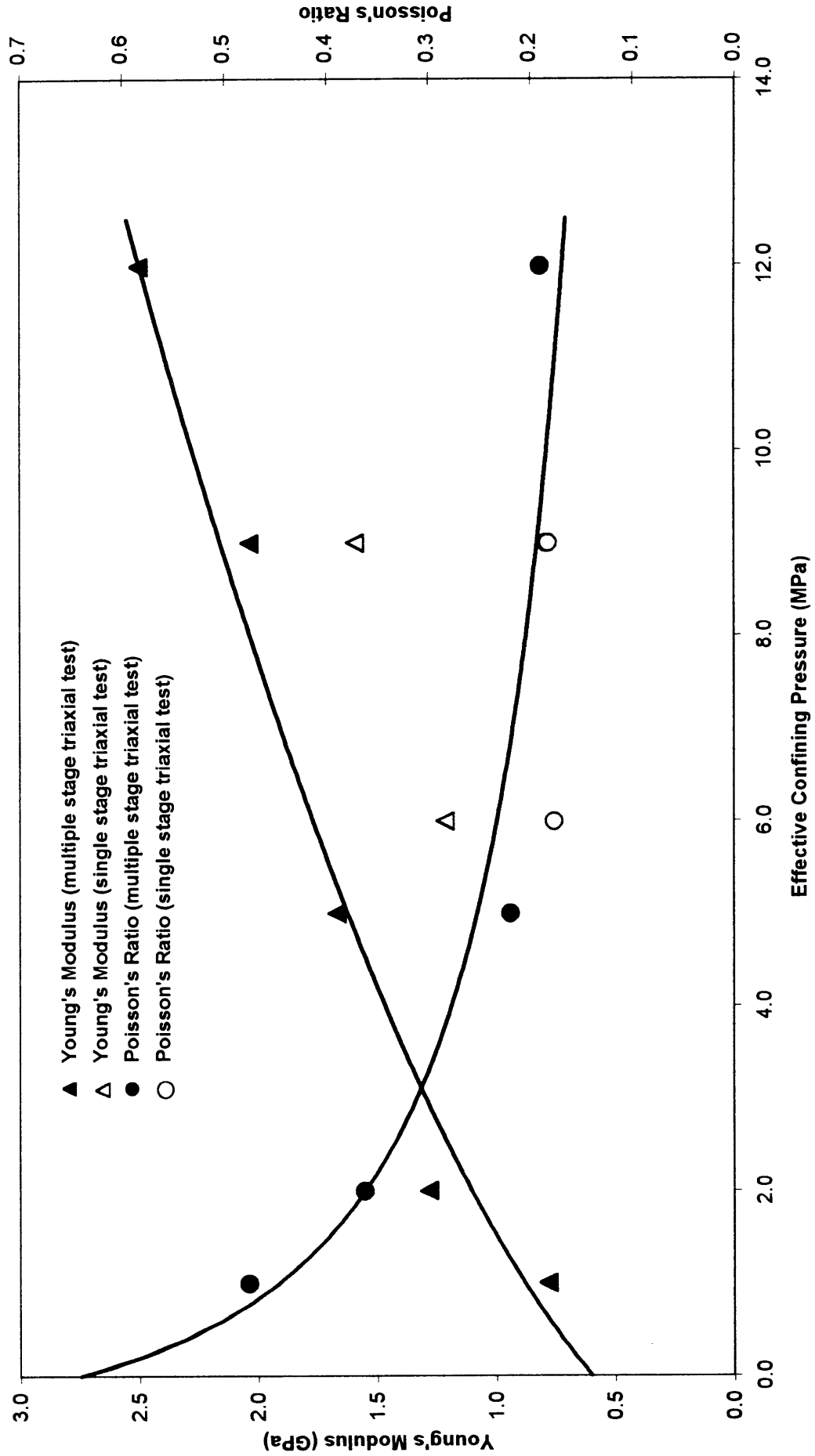


Figure 25 Correlations between Young's modulus and Poisson's ratio, and effective confining pressure for Core Section 2.

Elastic Parameters - Core Section 3

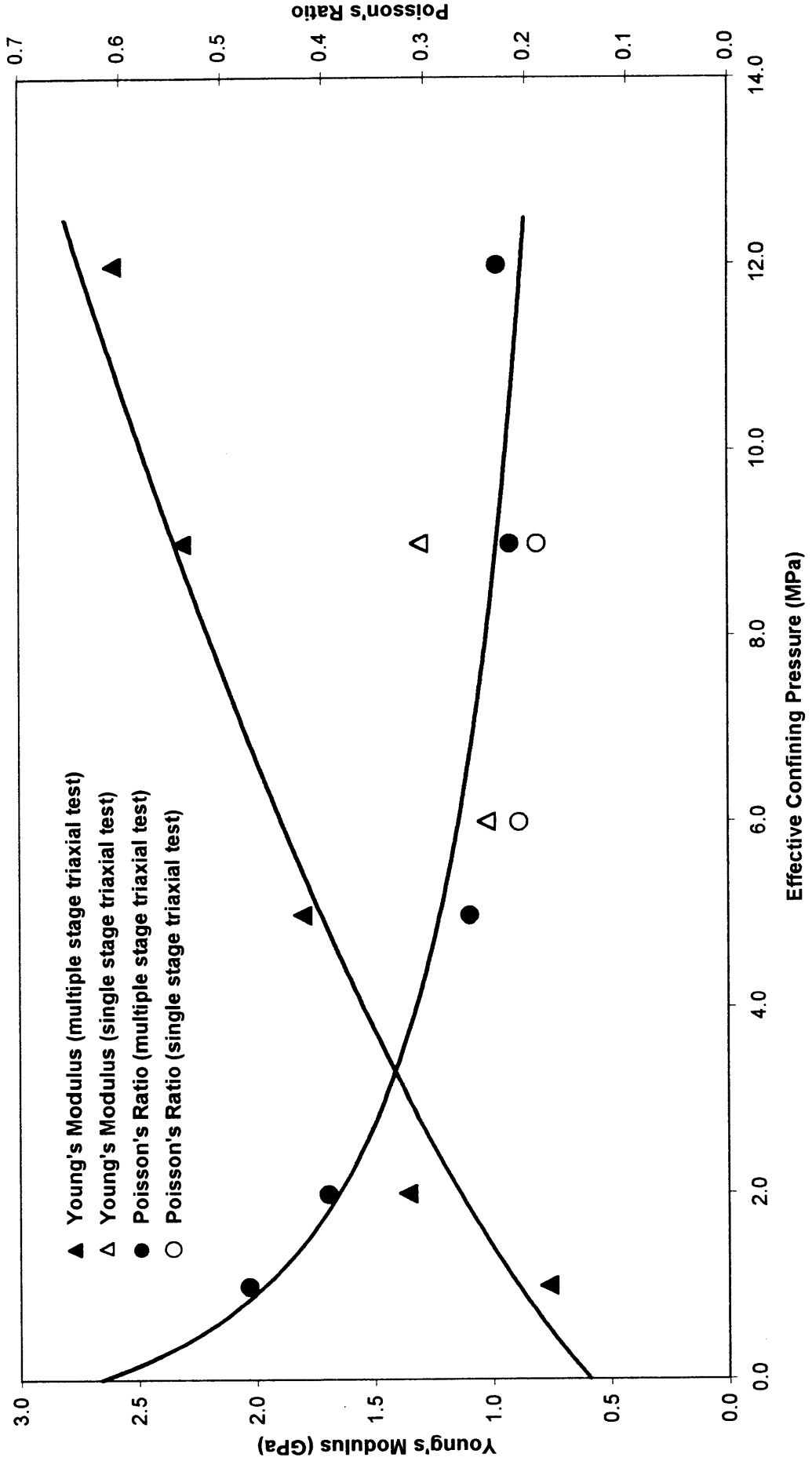


Figure 26 Correlations between Young's modulus and Poisson's ratio, and effective confining pressure for Core Section 3.

Elastic Parameters - Core Section 4

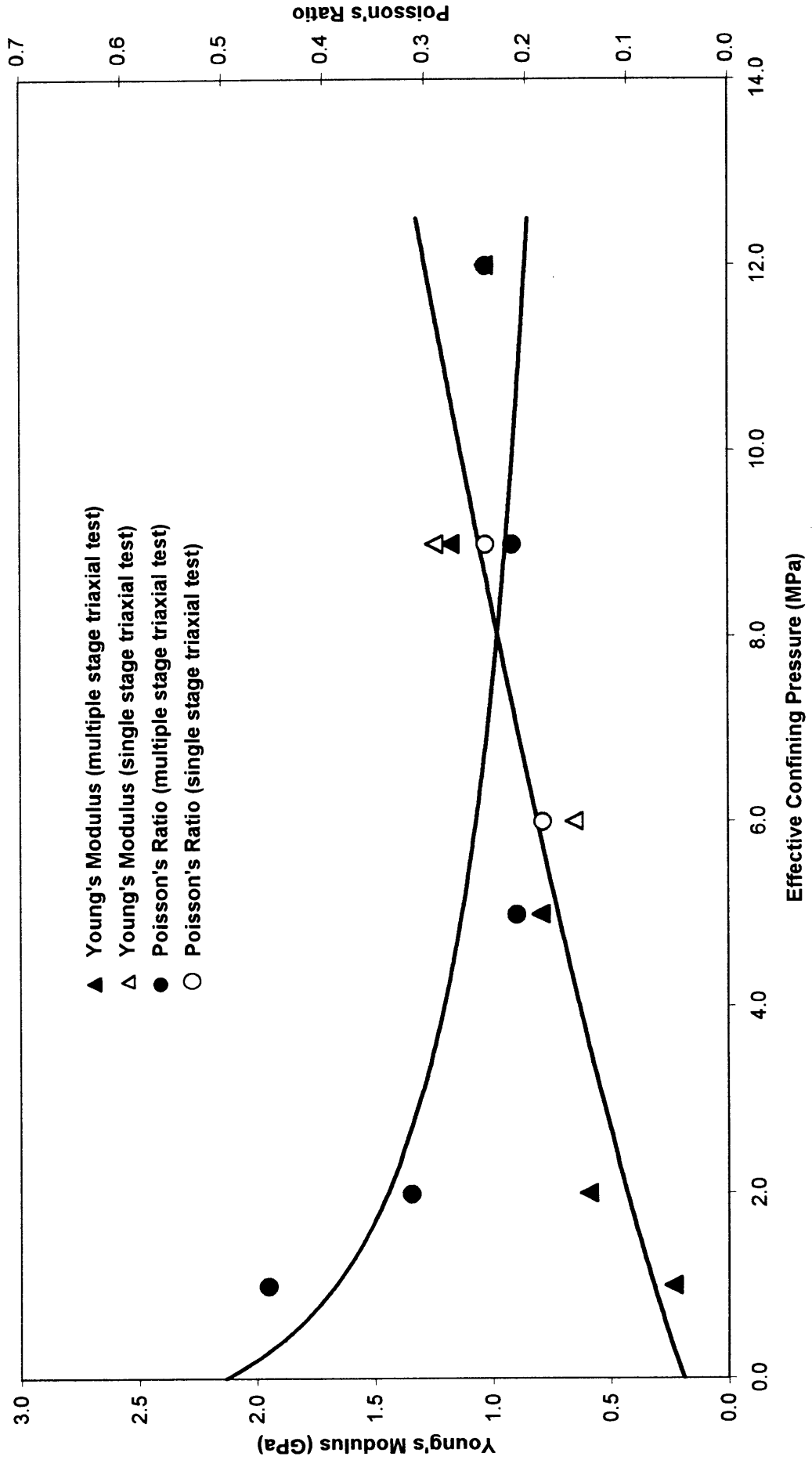


Figure 27 Correlations between Young's modulus and Poisson's ratio, and effective confining pressure for Core Section 4.

Elastic Parameters - Core Section 5

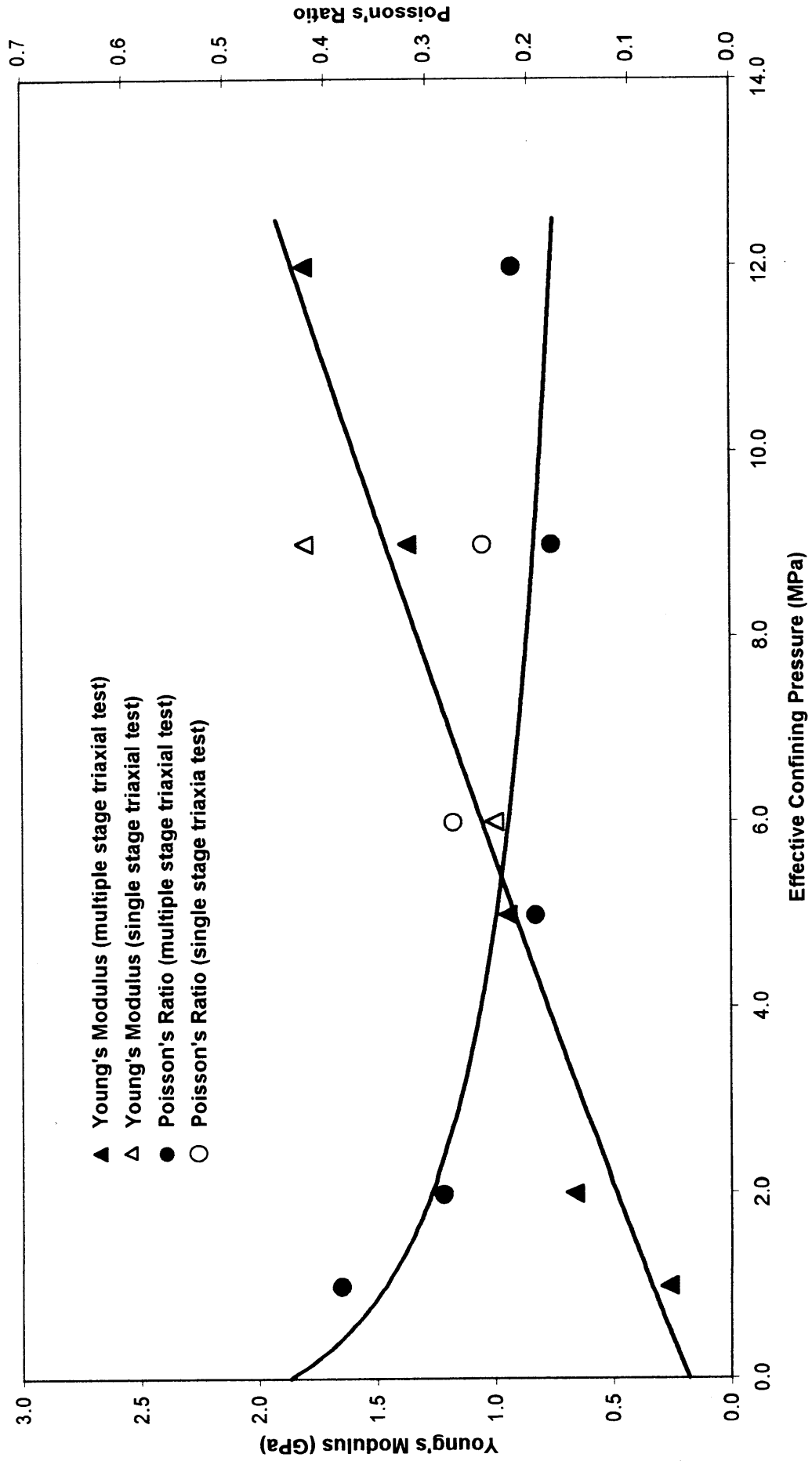


Figure 28 Correlations between Young's modulus and Poisson's ratio, and effective confining pressure for Core Section 5.

Peak Strength - Core Section 1
(Excluding effective confining pressure of 12 MPa data point)

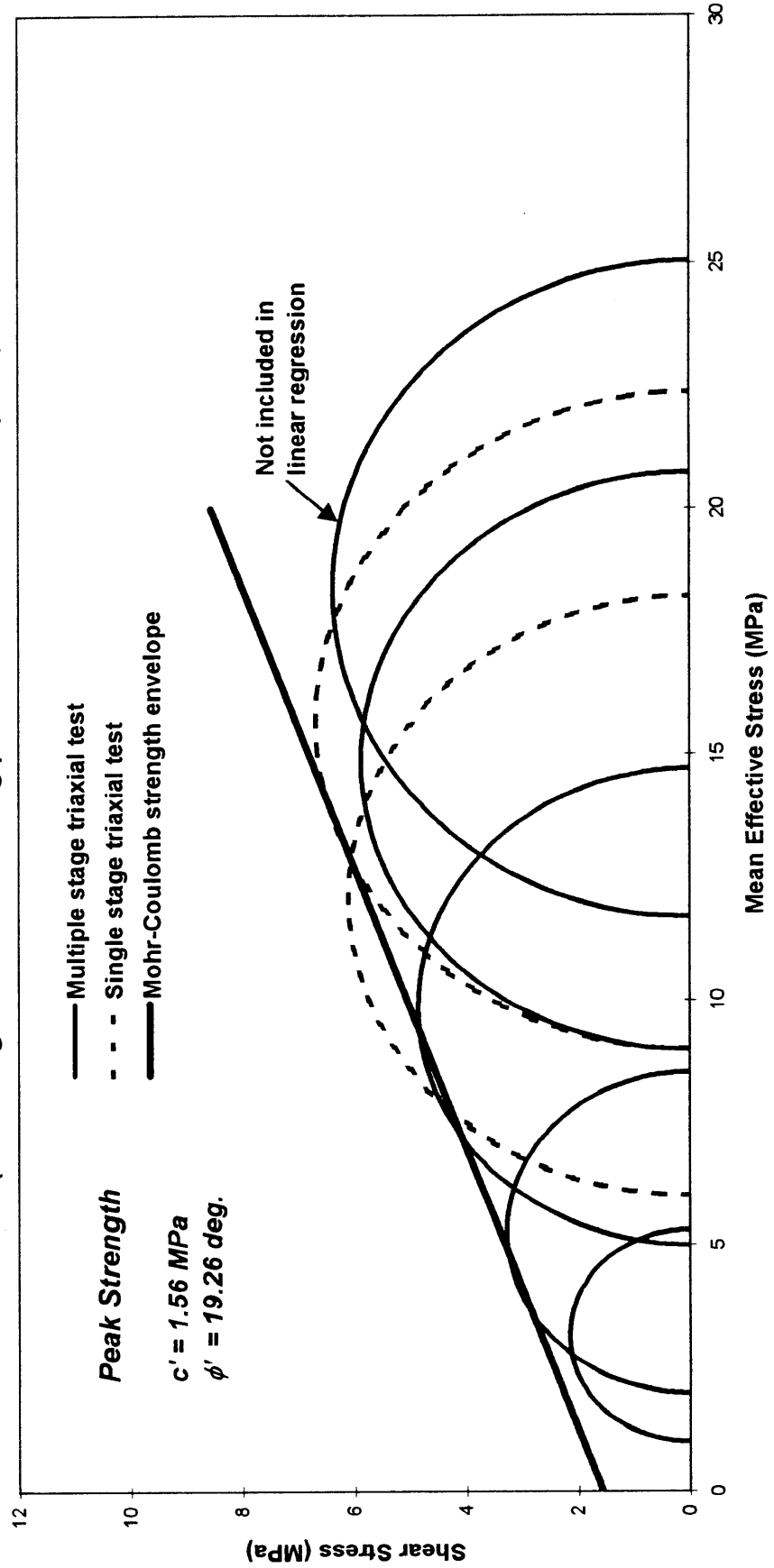


Figure 29a Peak strength Mohr circles and Mohr-Coulomb strength envelope for Core Section 1 (excluding data with an effective confining pressure of 12 MPa).

Peak Strength - Core Section 1
(Excluding effective confining pressure of 9 & 12 MPa data points)

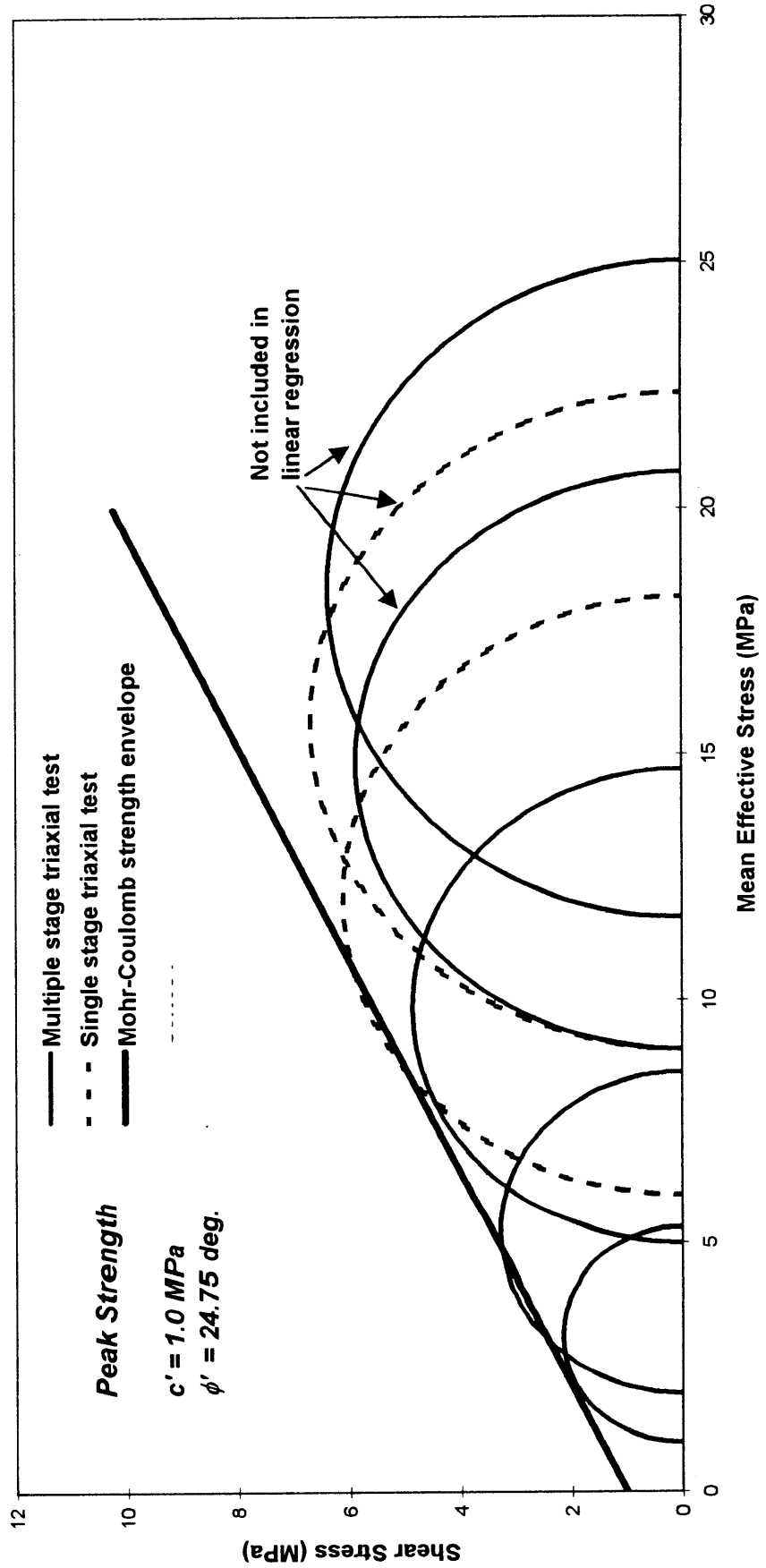


Figure 29b Peak strength Mohr circles and Mohr-Coulomb strength envelope for Core Section 1 (excluding data with effective confining pressures of 9 and 12 MPa).

Peak Strength - Core Section 2
(Excluding effective confining pressure of 12 MPa data point)

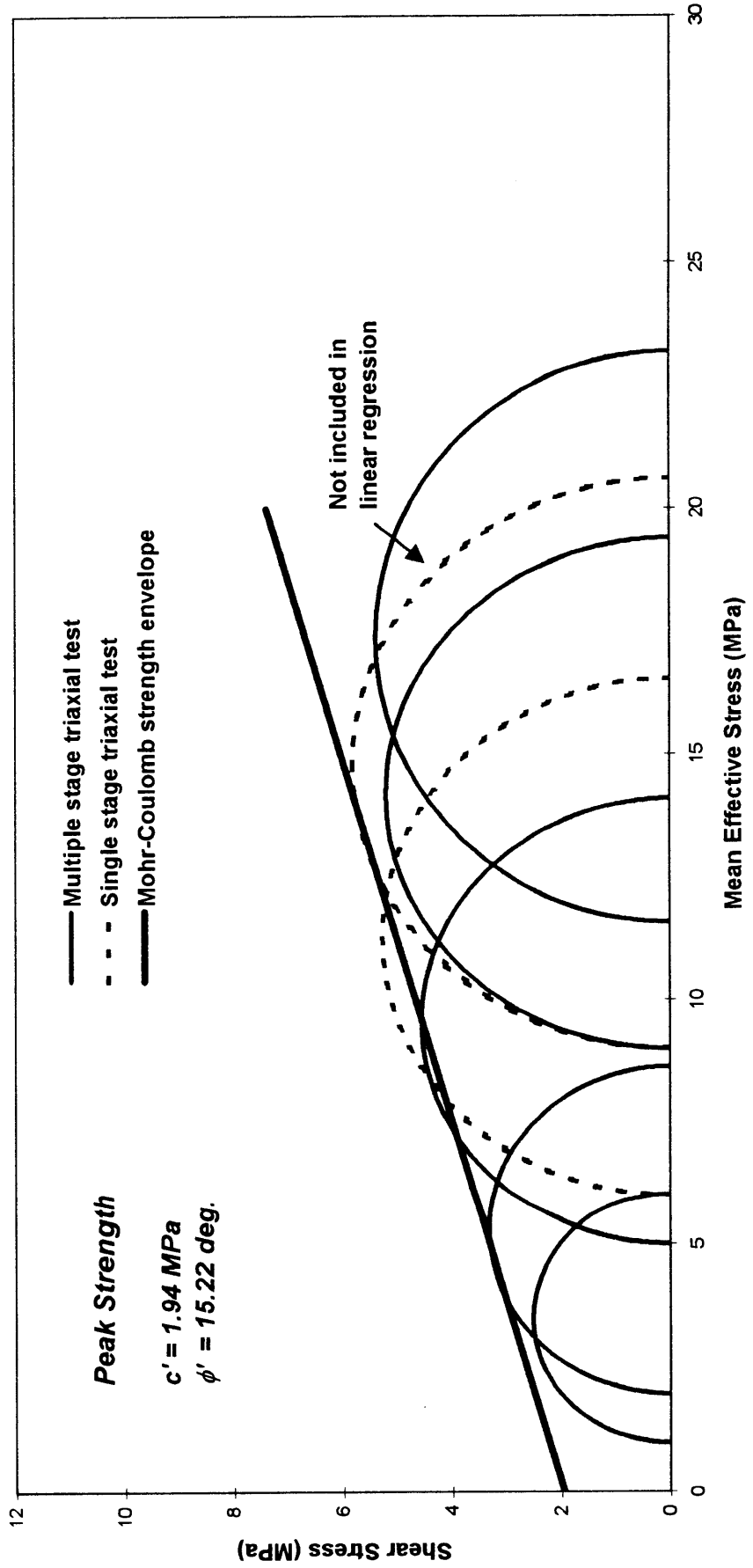


Figure 30a Peak strength Mohr circles and Mohr-Coulomb strength envelope for Core Section 2 (excluding data with an effective confining pressure of 12 MPa).

Peak Strength - Core Section 2
(Excluding effective confining pressure of 9 & 12 MPa data points)

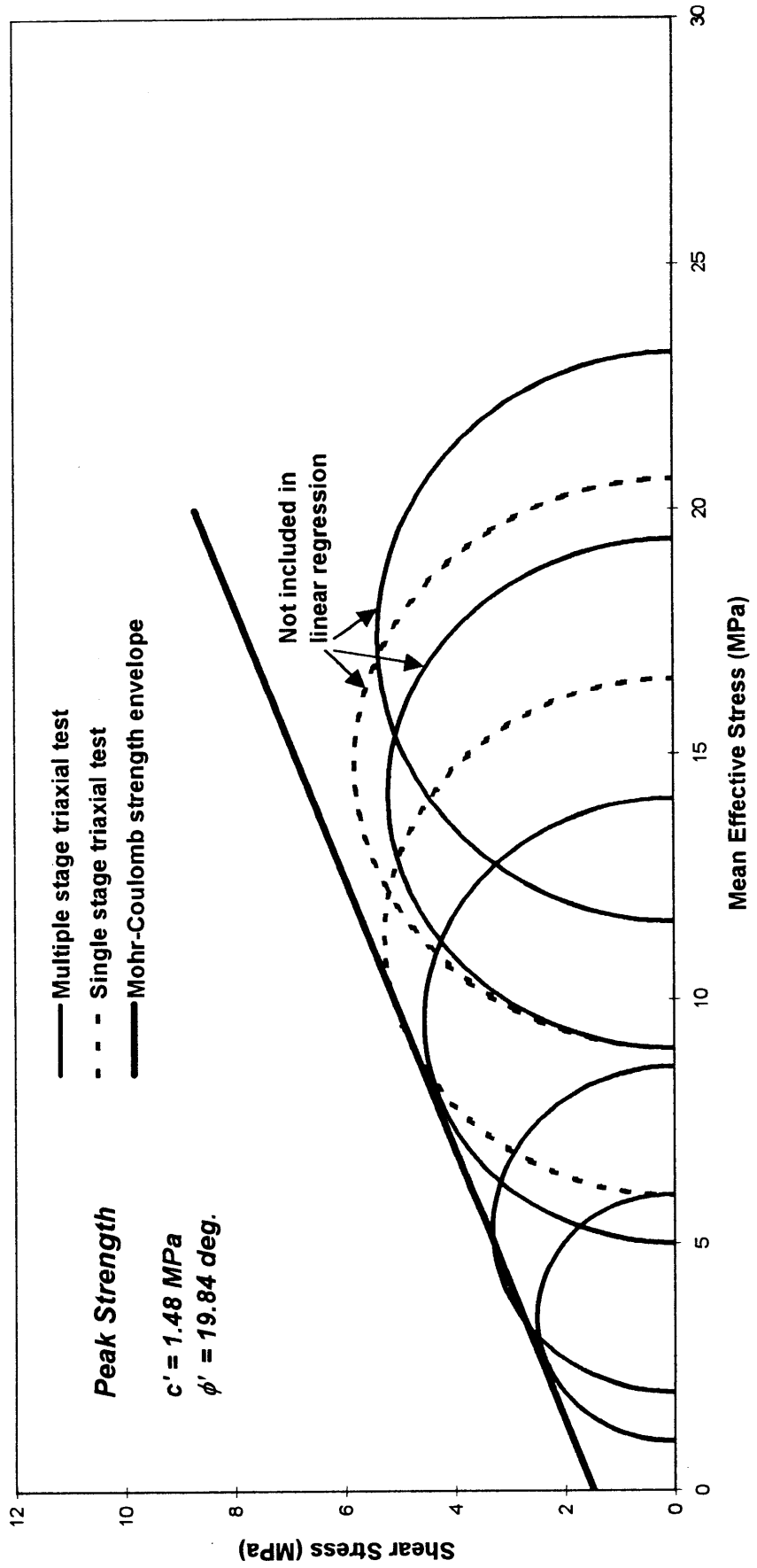


Figure 30b Peak strength Mohr circles and Mohr-Coulomb strength envelope for Core Section 2 (excluding data with effective confining pressures of 9 and 12 MPa).

**Peak Strength - Core Section 3
(Excluding effective confining pressure of 12 MPa data point)**

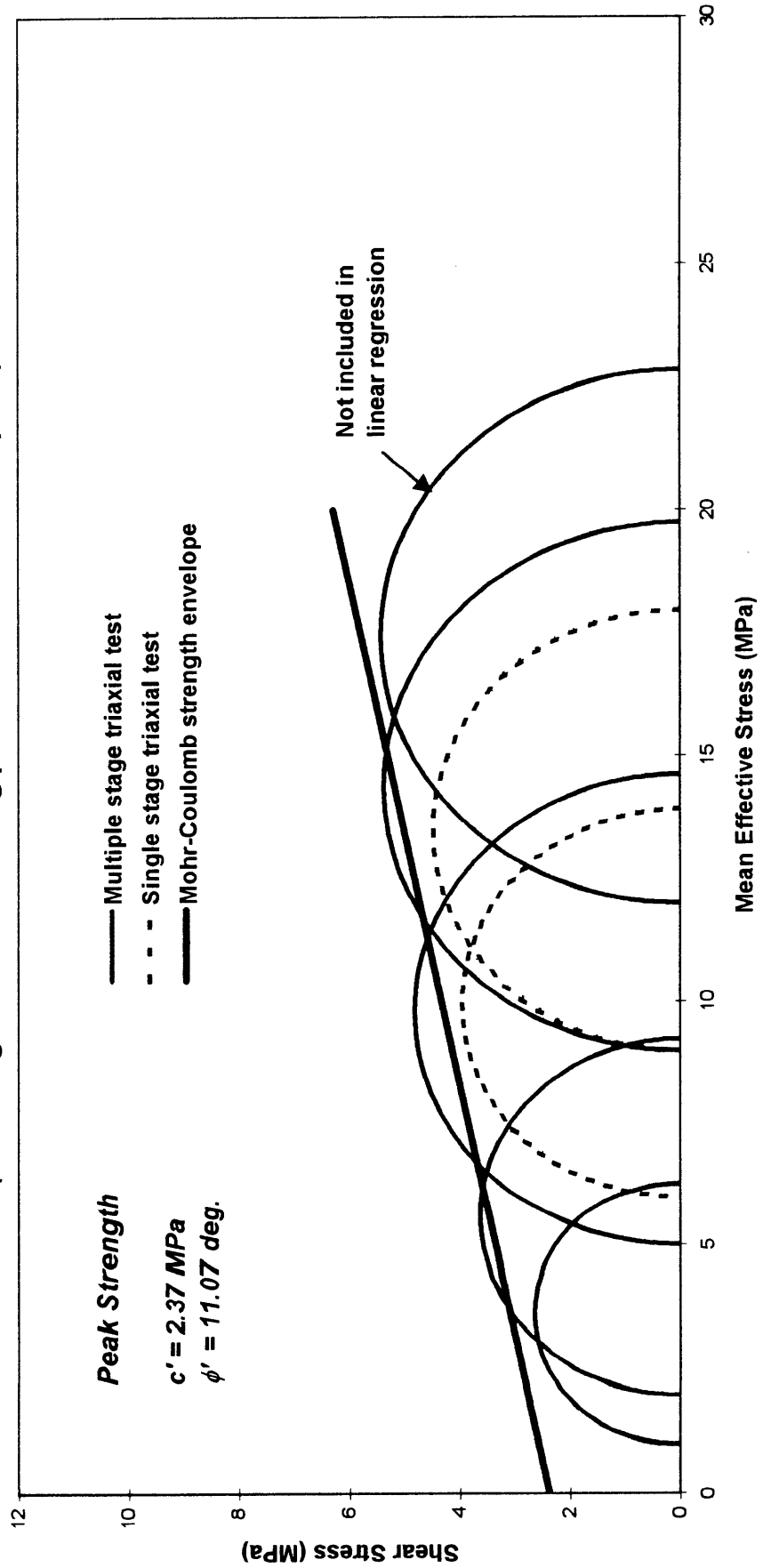


Figure 31a Peak strength Mohr circles and Mohr-Coulomb strength envelope for Core Section 3 (excluding data with an effective confining pressure of 12 MPa).

Peak Strength - Core Section 3
(Excluding effective confining pressure of 9 & 12 MPa data points)

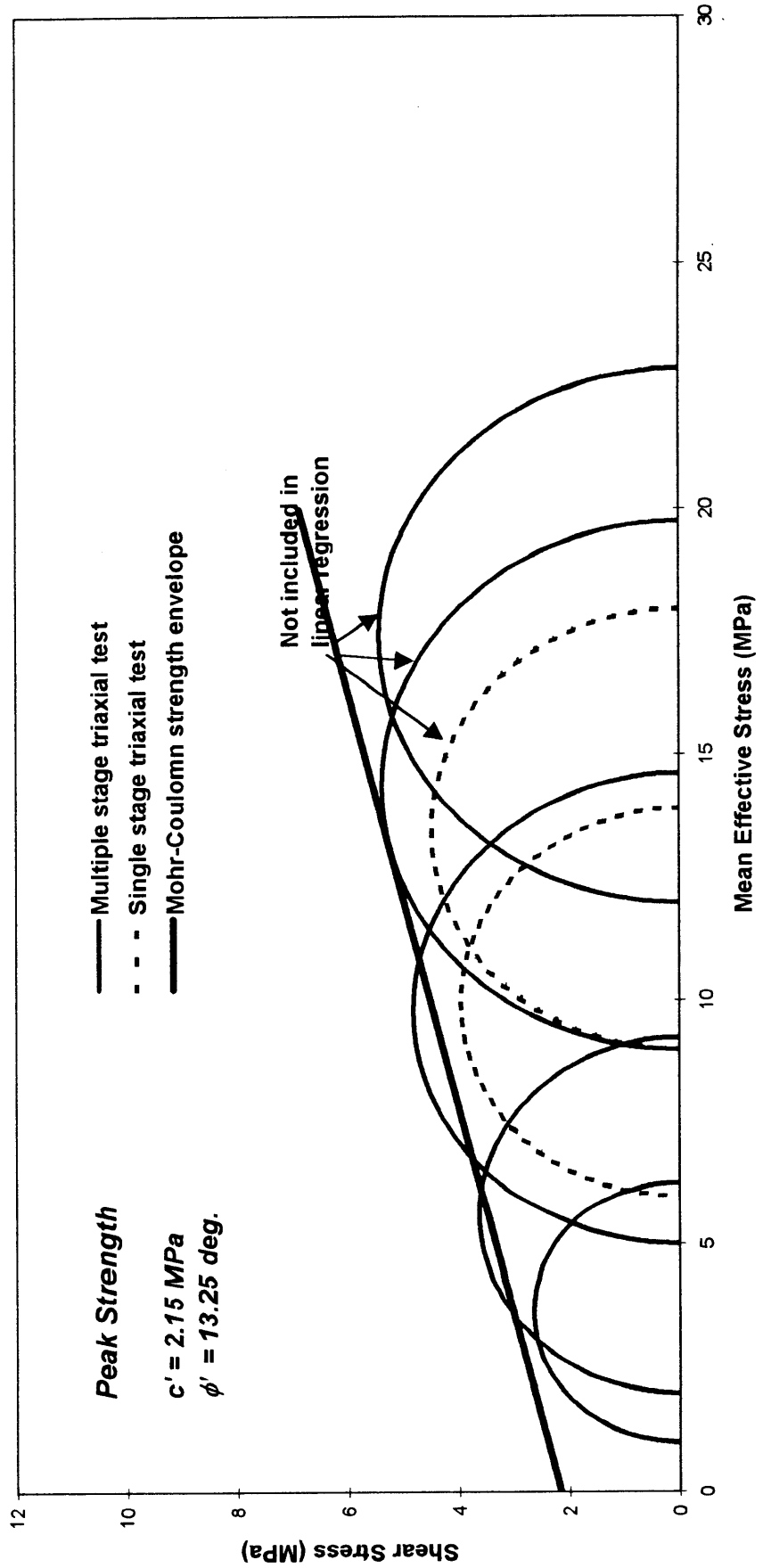
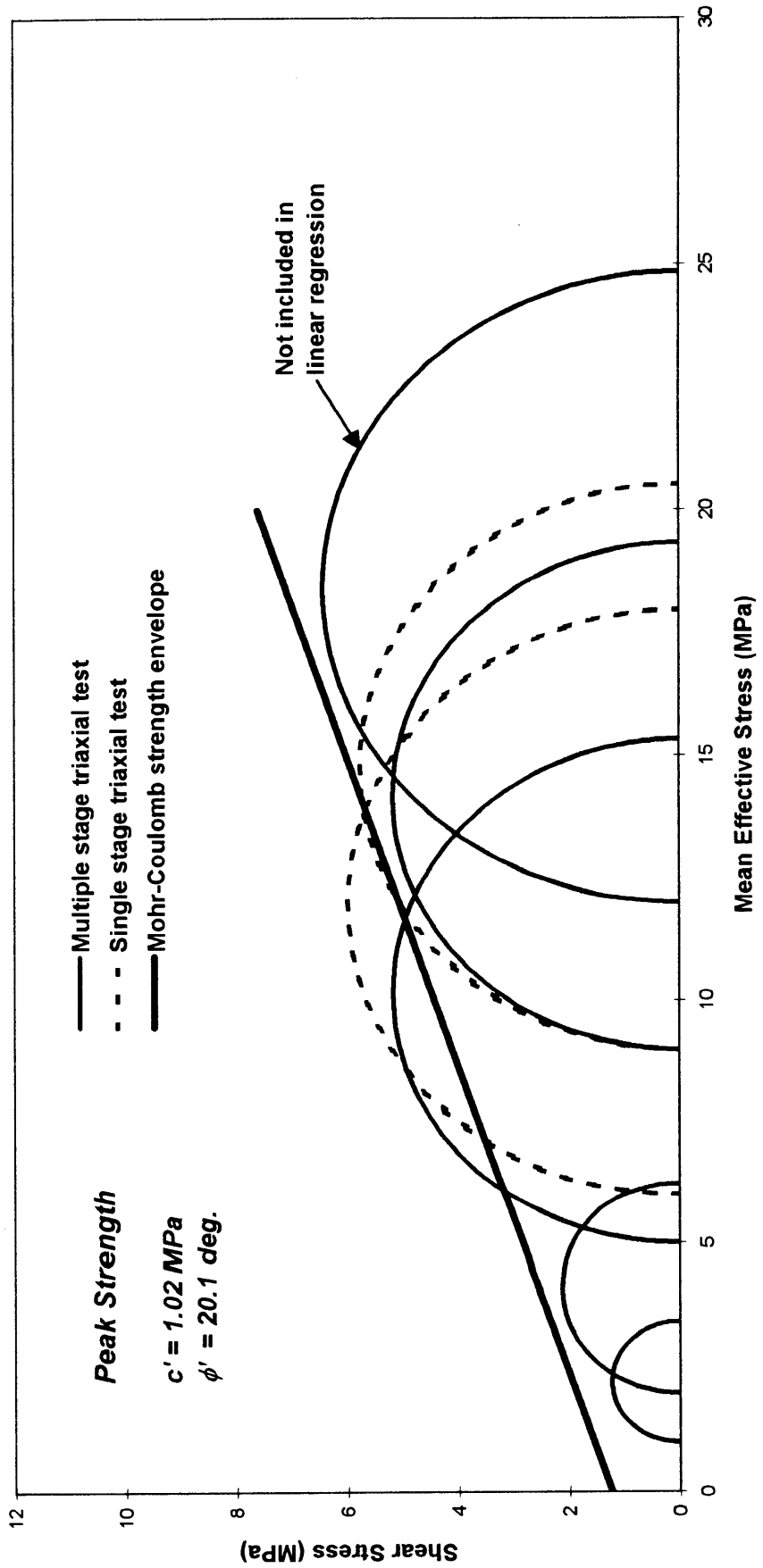


Figure 31b Peak strength Mohr circles and Mohr-Coulomb strength envelope for Core Section 3 (excluding data with effective confining pressure of 9 & 12 MPa).

Peak Strength - Core Section 4
(Excluding effective confining pressure of 12 MPa data point)



Peak Strength - Core Section 4
 (Excluding effective confining pressure of 9 & 12 MPa data points)

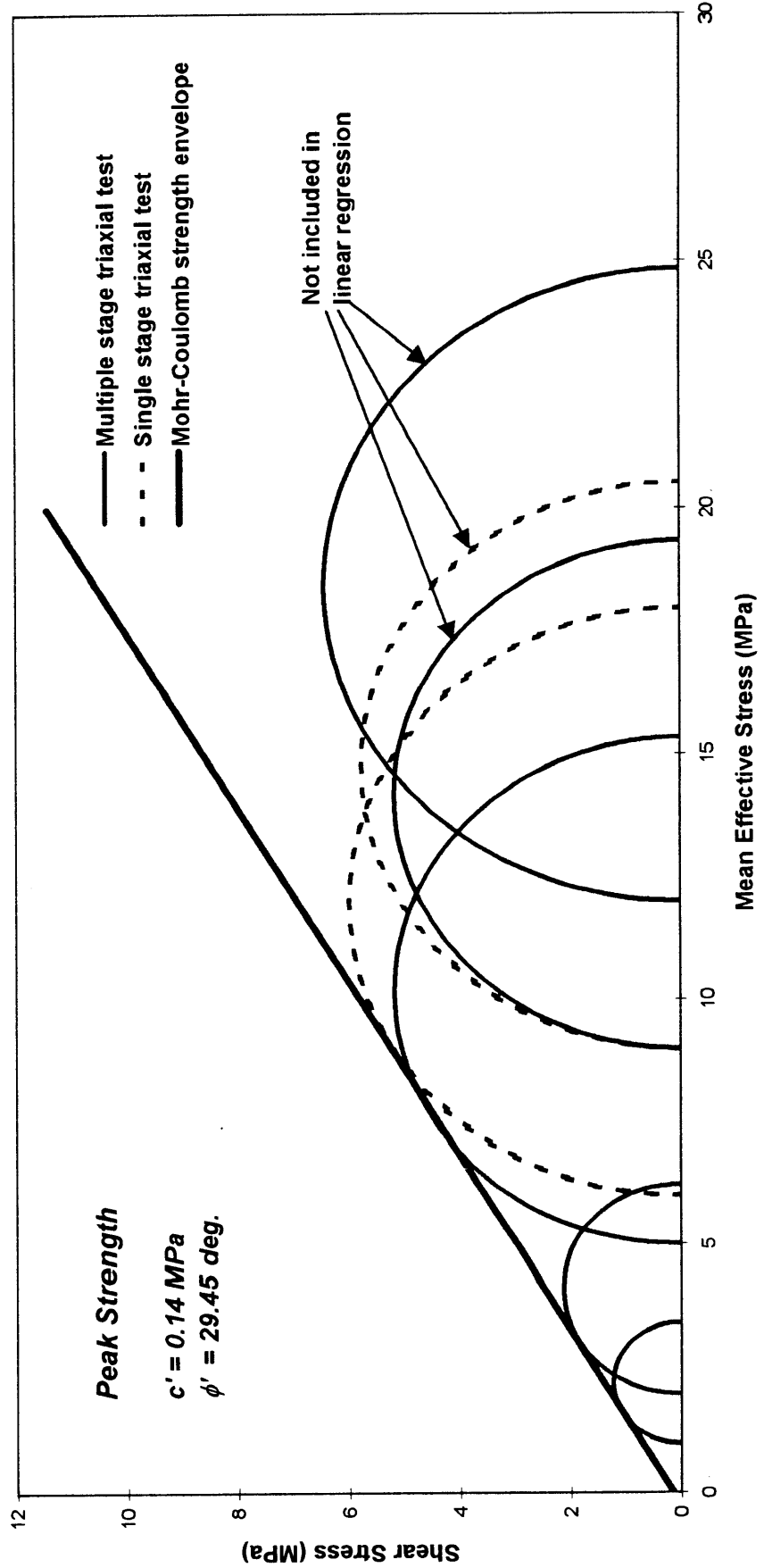


Figure 32b Peak strength Mohr circles and Mohr-Coulomb strength envelope for Core Section 4 (excluding data with effective confining pressures of 9 and 12 MPa).

**Peak Strength - Core Section 5
(Excluding effective confining pressure of 12 MPa data point)**

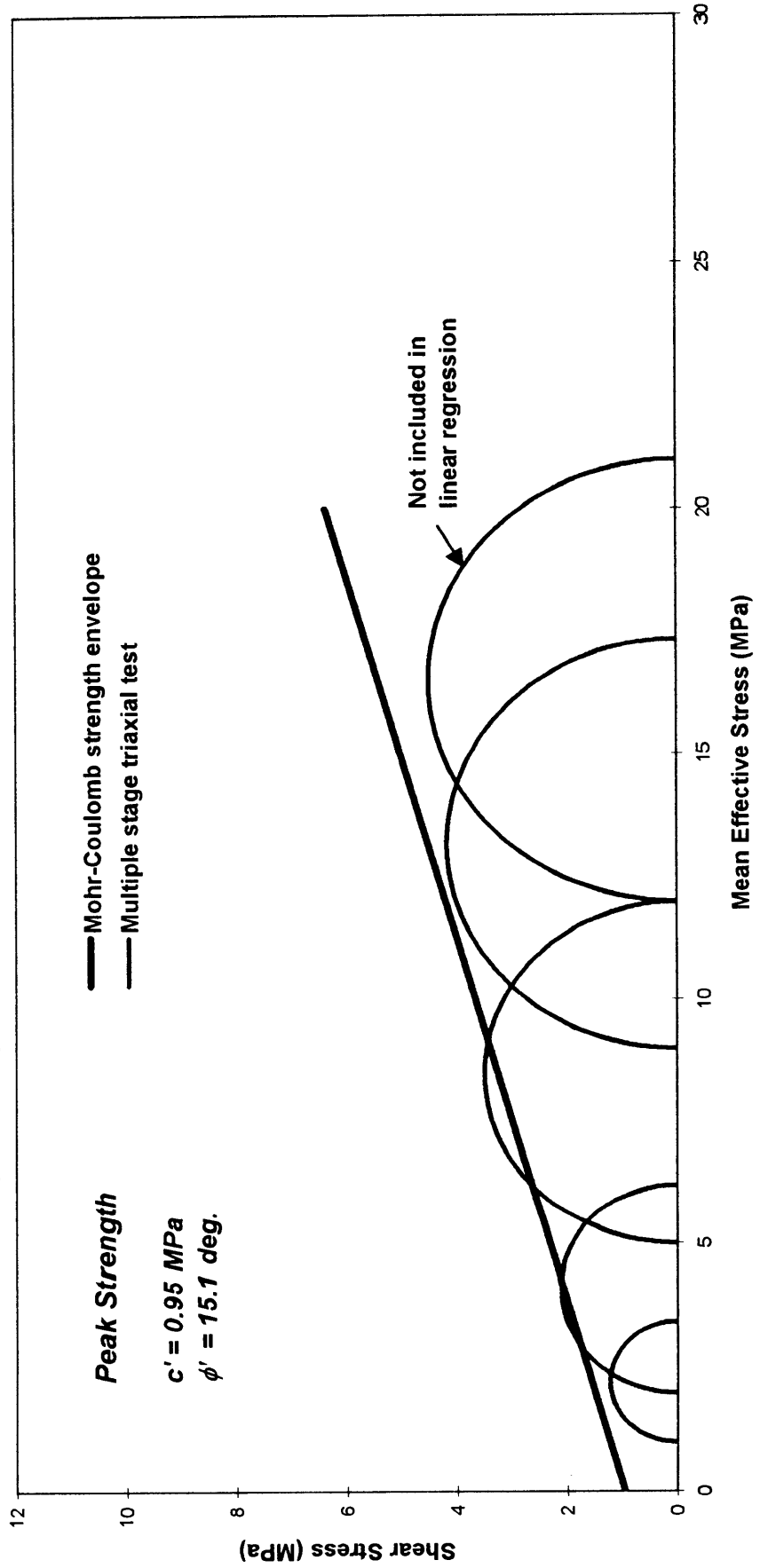


Figure 33a Peak strength Mohr circles and Mohr-Coulomb strength envelope for Core Section 5 (multiple stage data only, excluding data with an effective confining pressure of 12 MPa).

Peak Strength - Core Section 5
(Excluding effective confining pressure of 9 & 12 MPa data points)

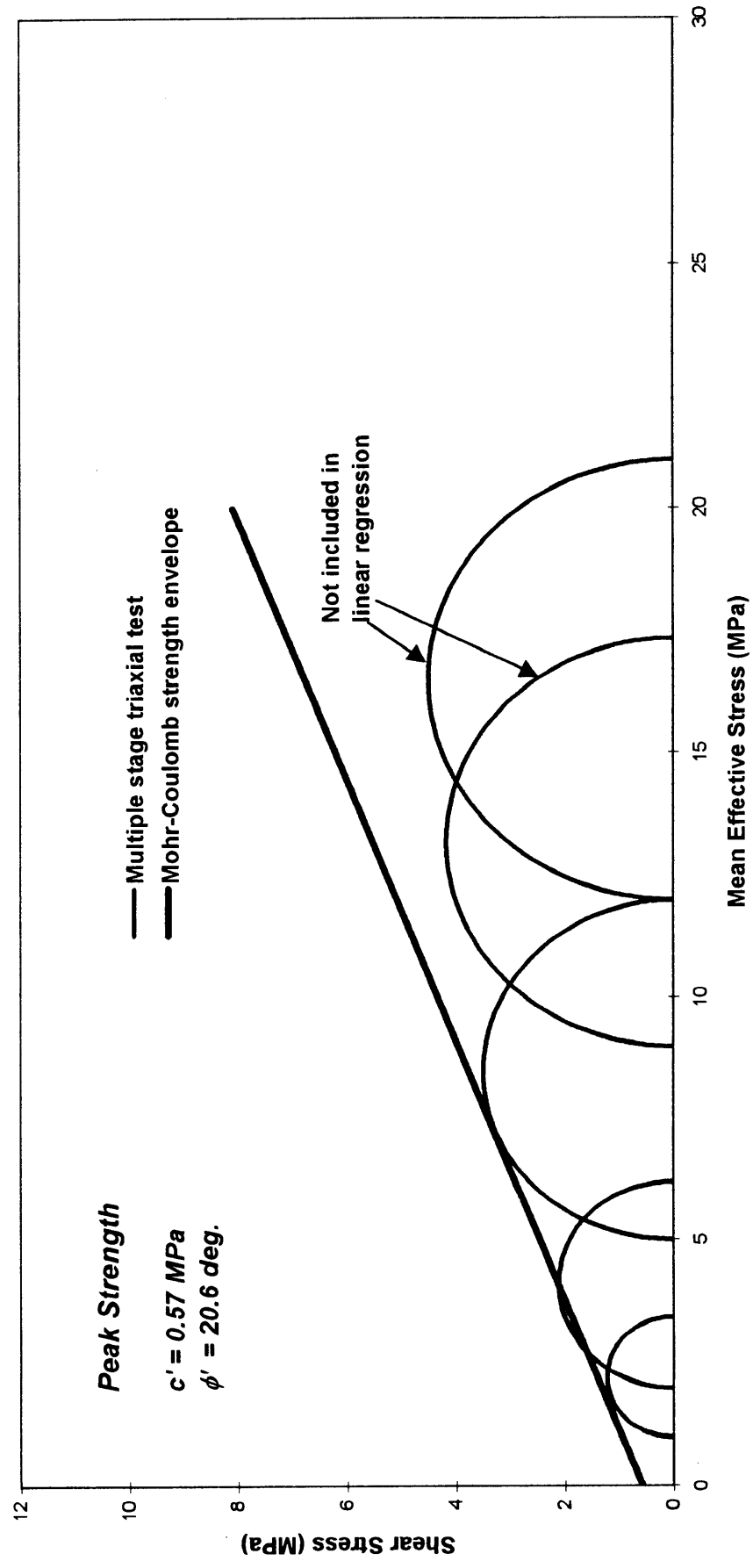


Figure 33b Peak strength Mohr circles and Mohr-Coulomb strength envelope for Core Section 5 (multiple stage data only, excluding data with effective confining pressures of 9 and 12 MPa).

**Peak Strength - Core Section 5
(Single Stage Test only)**

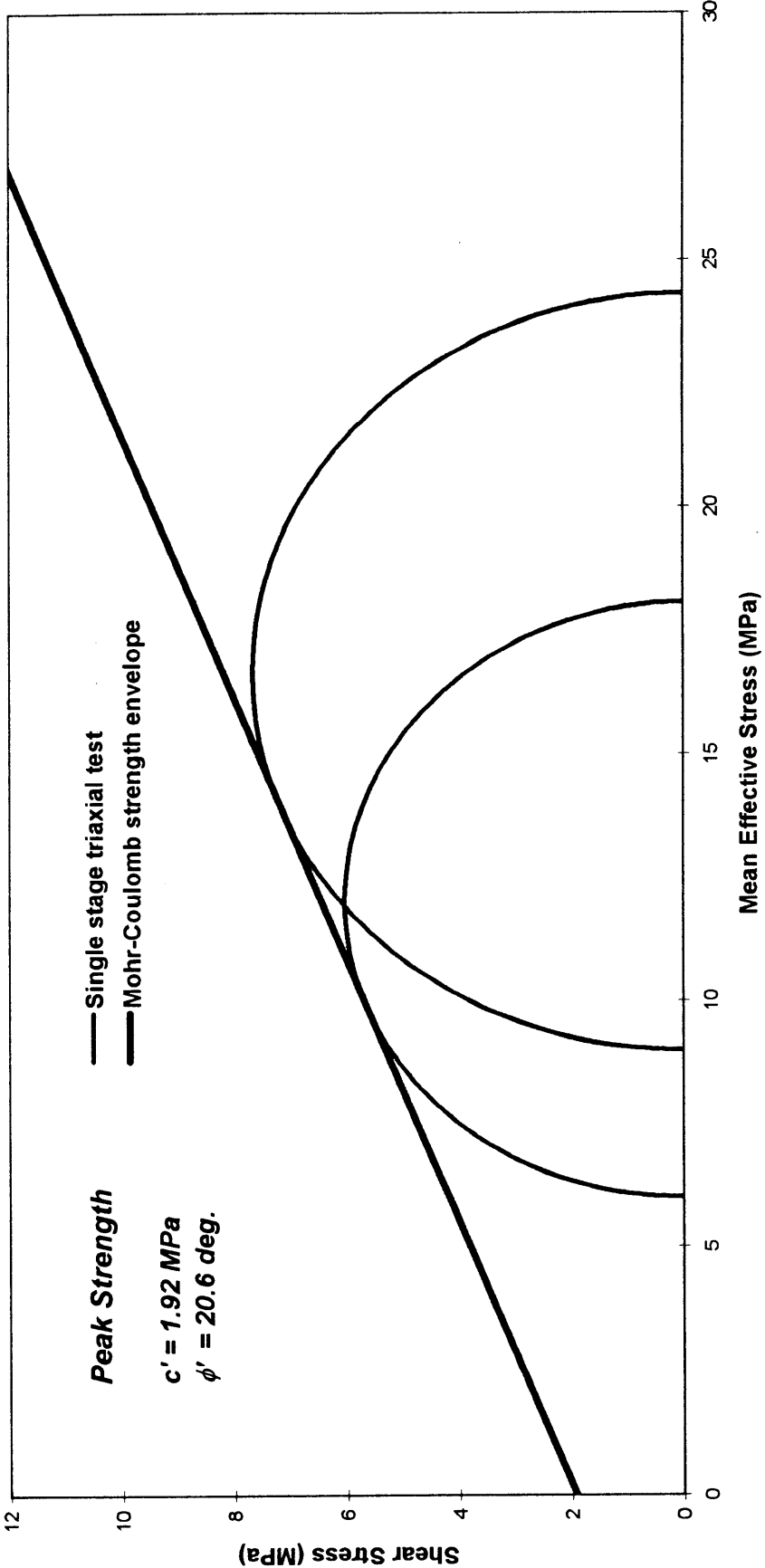


Figure 33c Peak strength Mohr circles and Mohr-Coulomb strength envelope for Core Section 5 (single stage test data only).

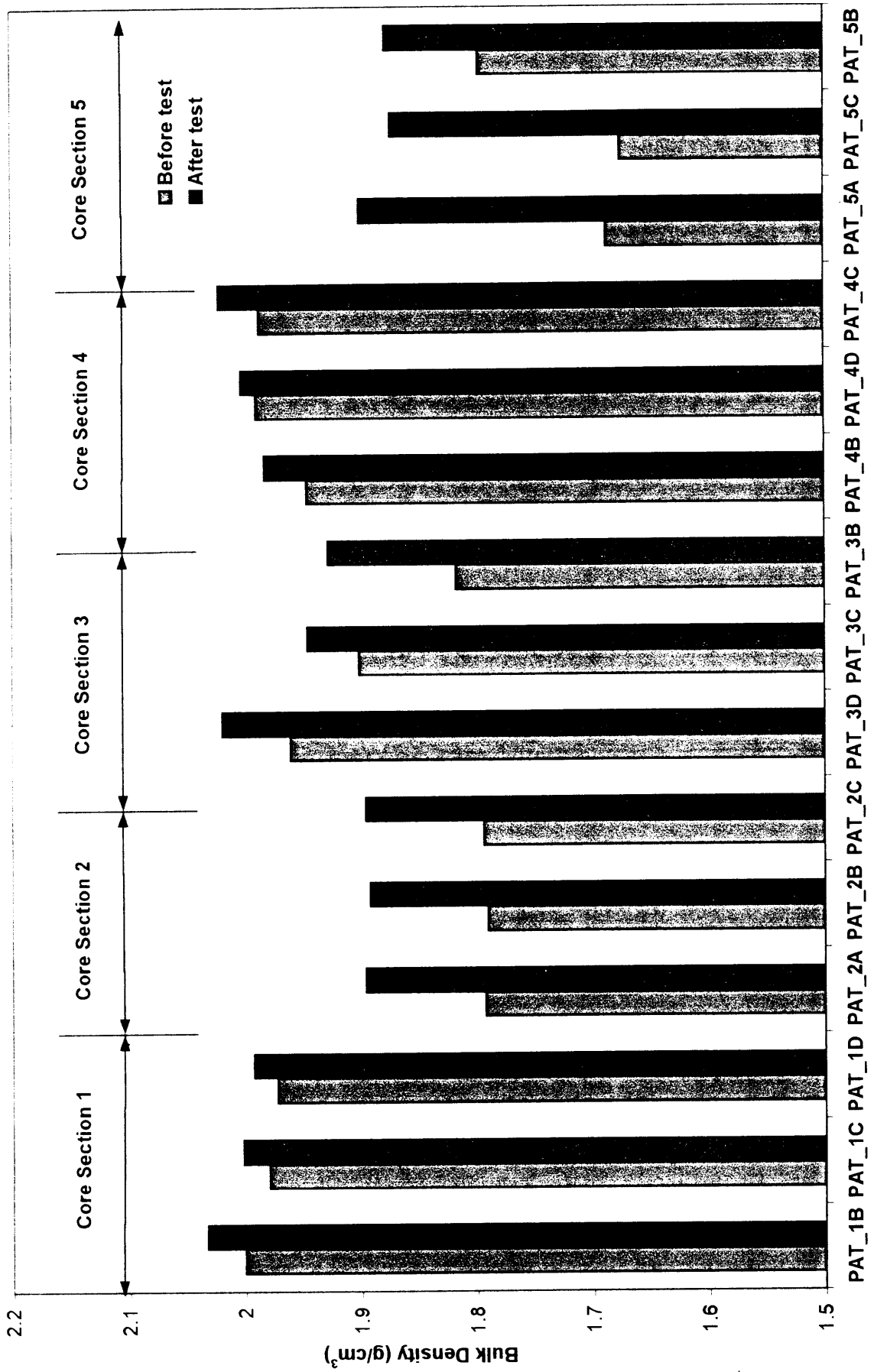


Figure 34 Bulk densities for each sample before and after test.

PATRICIA BALEEN - 2 SAND CORE SECTION 1
(Strain During Pressurization & Consolidation, Single Stage Triaxial Test)

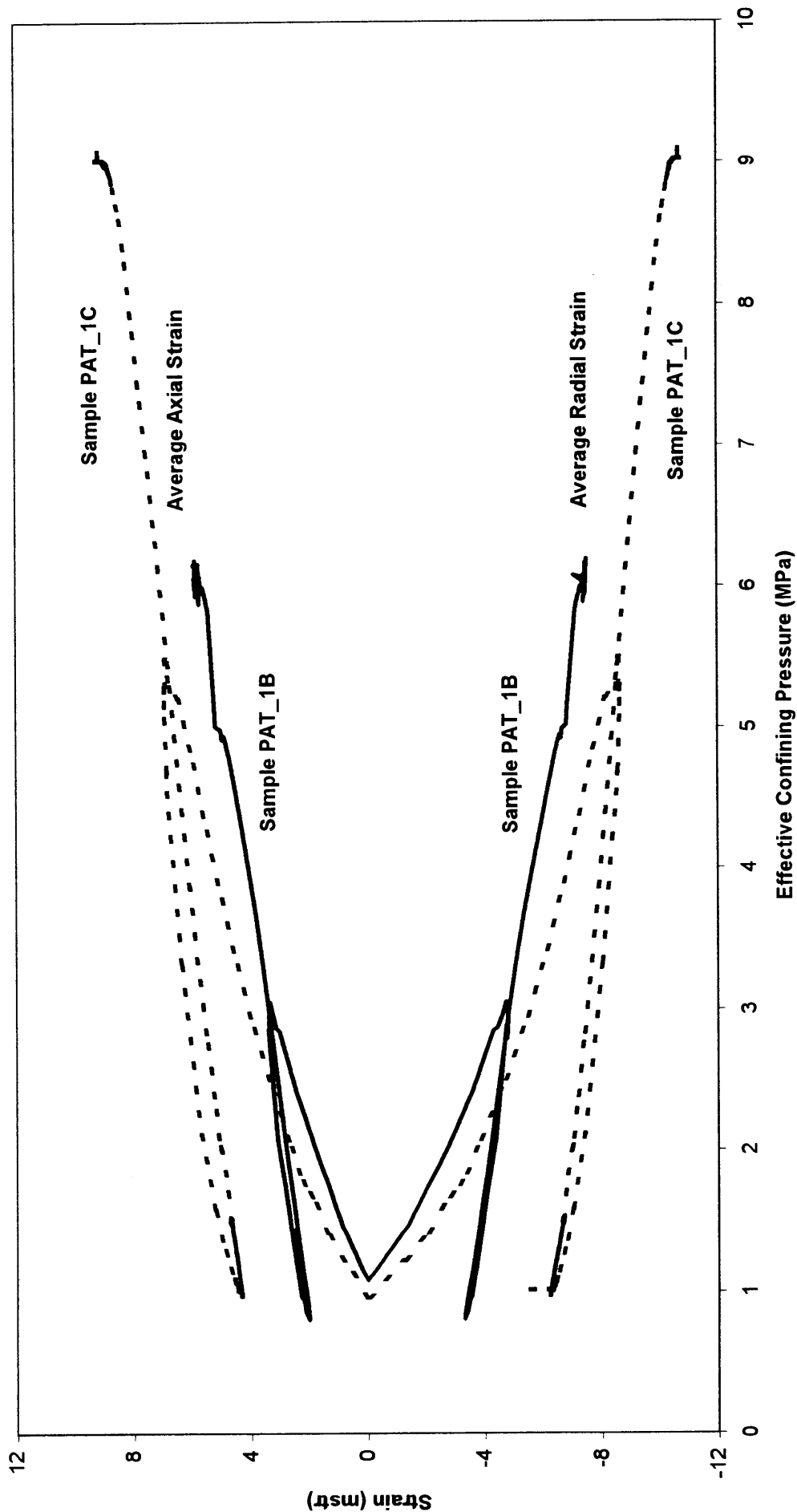


Figure 35 Average axial and radial strains as a function of effective confining pressure for single stage triaxial tests during pressurization and consolidation on Core Section 1.

PATRICIA BALEEN - 2 SAND CORE SECTION 2
(Strain During Pressurization & Consolidation, Single Stage Triaxial Test)

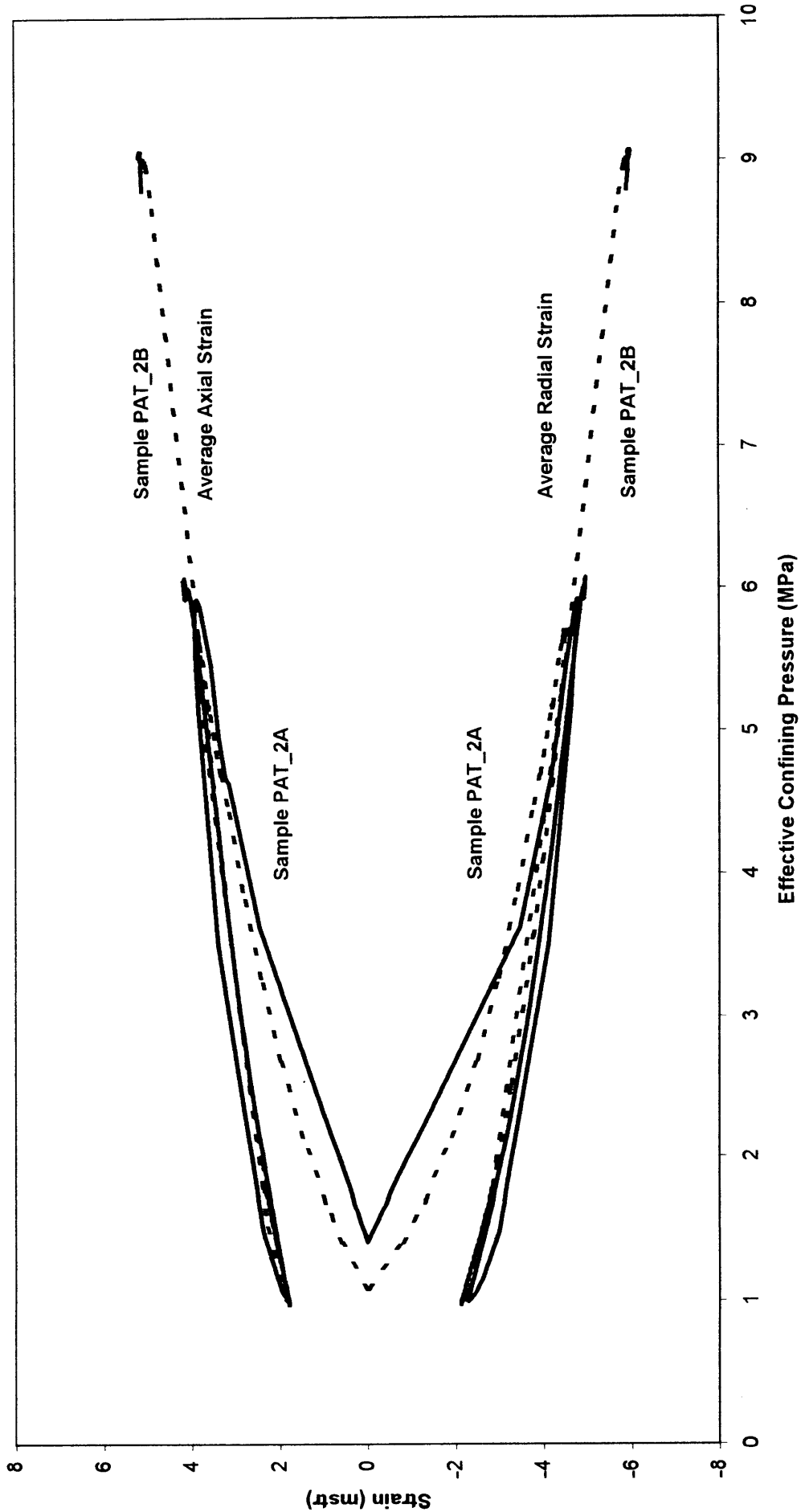


Figure 36 Average axial and radial strains as a function of effective confining pressure for single stage triaxial tests during pressurization and consolidation on Core Section 2.

PATRICIA BALEEN - 2 SAND CORE SECTION 3
(Strain During Pressurization & Consolidation, Single Stage Triaxial Test)

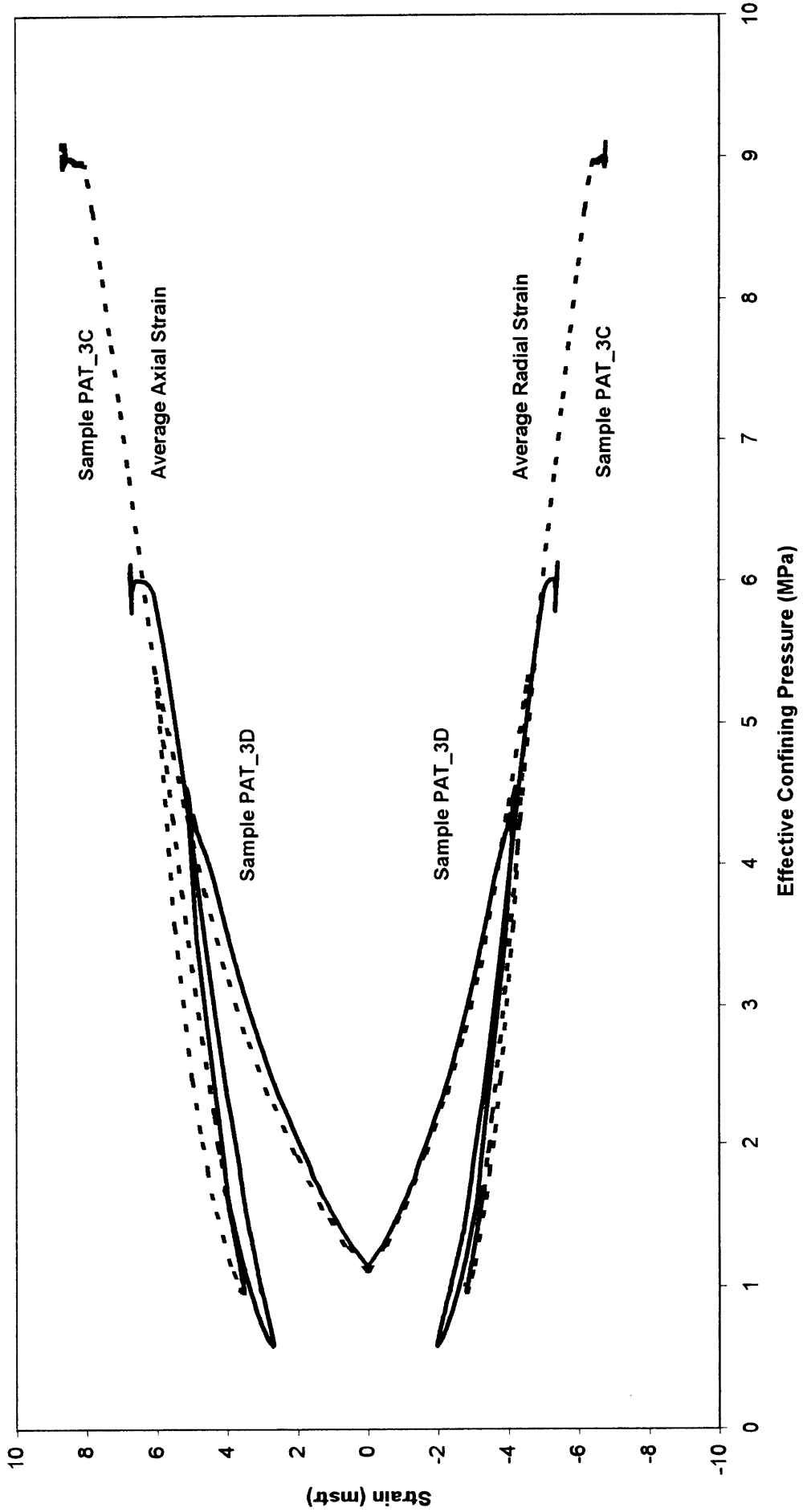


Figure 37 Average axial and radial strains as a function of effective confining pressure for single stage triaxial tests during pressurization and consolidation on Core Section 3.

PATRICIA BALEEN - 2 SAND CORE SECTION 4
(Strain During Pressurization & Consolidation, Single Stage Triaxial Test)

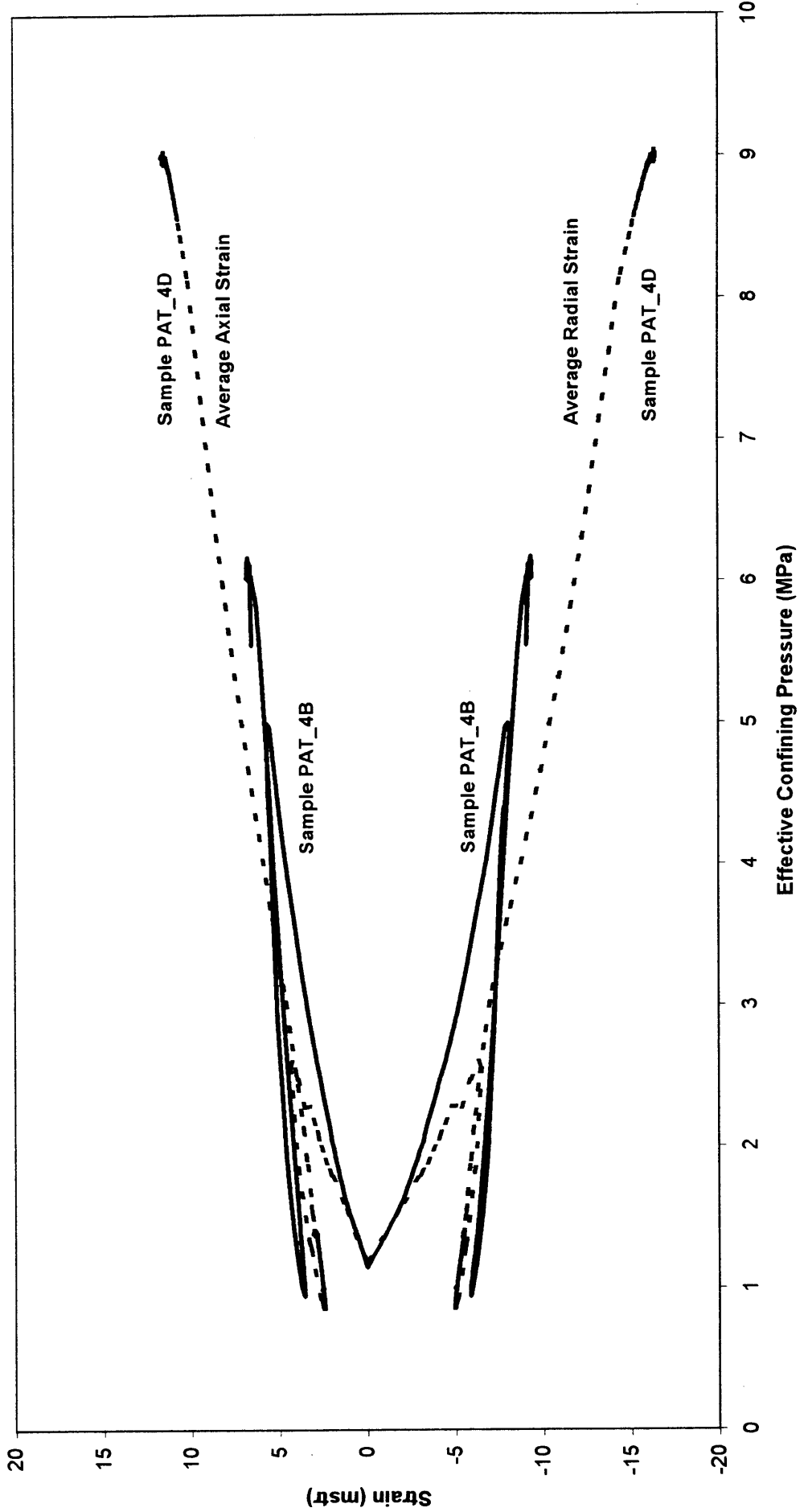


Figure 38 Average axial and radial strains as a function of effective confining pressure for single stage triaxial tests during pressurization and consolidation on Core Section 4.

PATRICIA BALEEN - 2 SAND CORE SECTION 5
(Strain During Pressurization & Consolidation, Single Stage Triaxial Test)

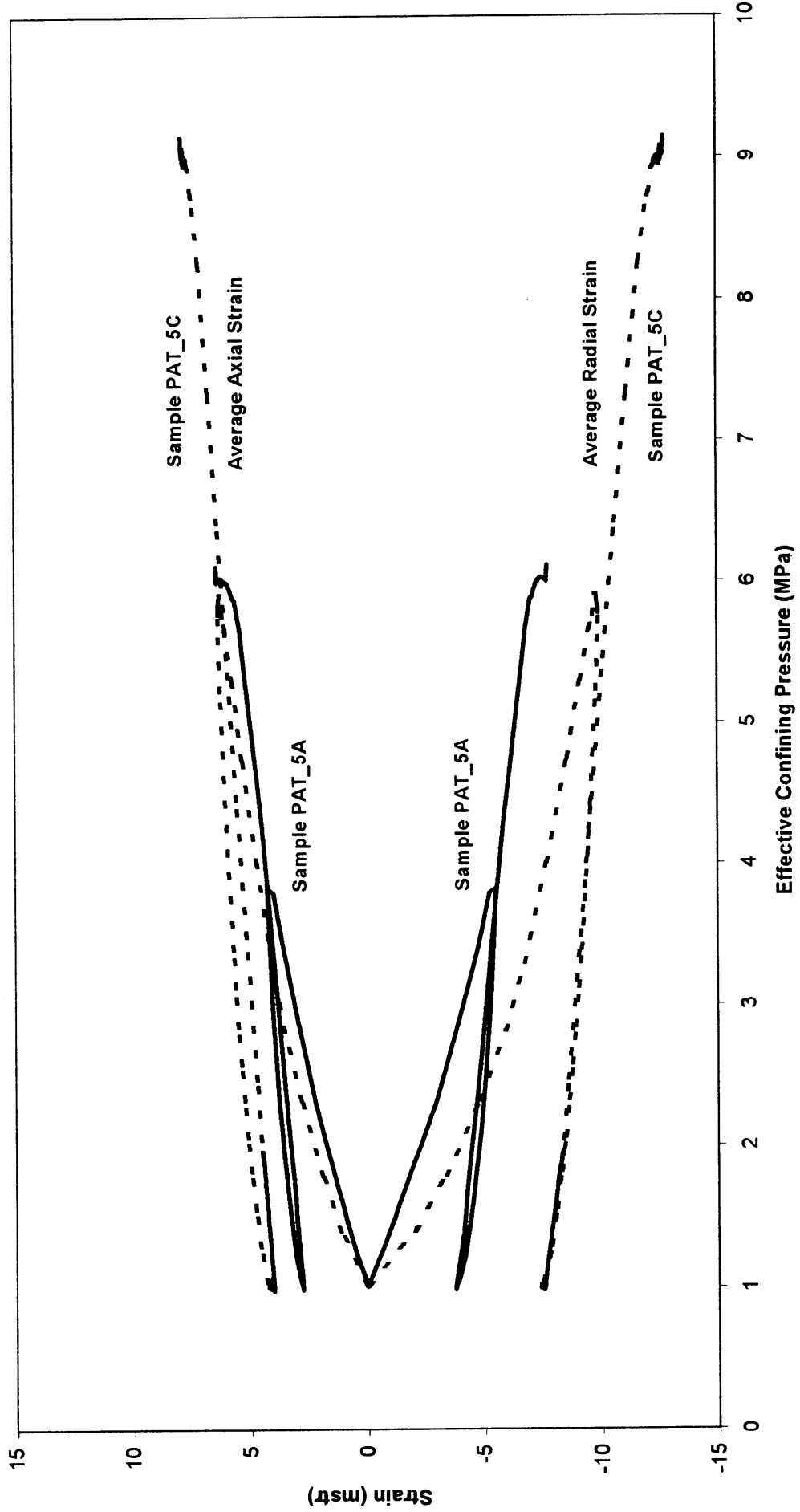


Figure 39 Average axial and radial strains as a function of effective confining pressure for single stage triaxial tests during pressurization and consolidation on Core Section 5.

907961 186

Appendix1

Shell Process Oil p874 Data Sheet



Shell Oils

Product Data Sheet

PDS No.

PROCESS OIL P874

MANUFACTURING SPECIFICATION

DESCRIPTION	METHOD	SPECIFICATION
APPEARANCE	VISUAL	CLEAR & BRIGHT
DENSITY @ 15°C (KG/L)	ASTM D1298	0.796 - 0.805
VISCOSITY @ 40°C (cSt)	ASTM D445	3.90 - 4.30
FLASH POINT P.M.C.C. (°C)	ASTM D93	135 min.
DISTILLATION (°C)	ASTM D86	
IBP		270 min.
FBP		330 max.
COLOUR (Saybolt)	ASTM D156	+16 min.

Signed:

Position:

Date:

The Shell Companies of Australia Limited
 2000000-000000

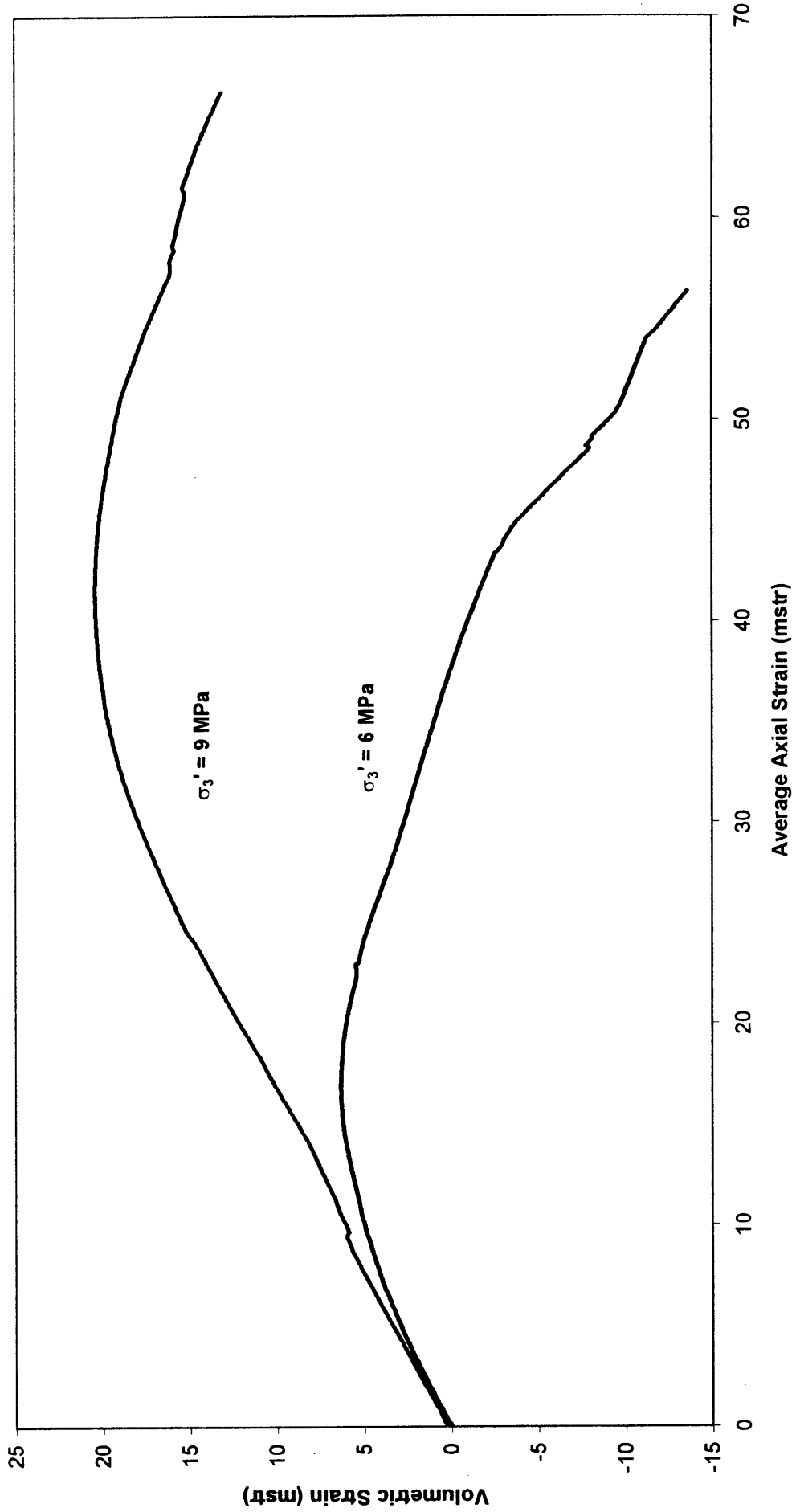
This information contains product information current at the time of printing. Because product characteristics and applications may change over time, users should check product information immediately prior to use.

907961 188

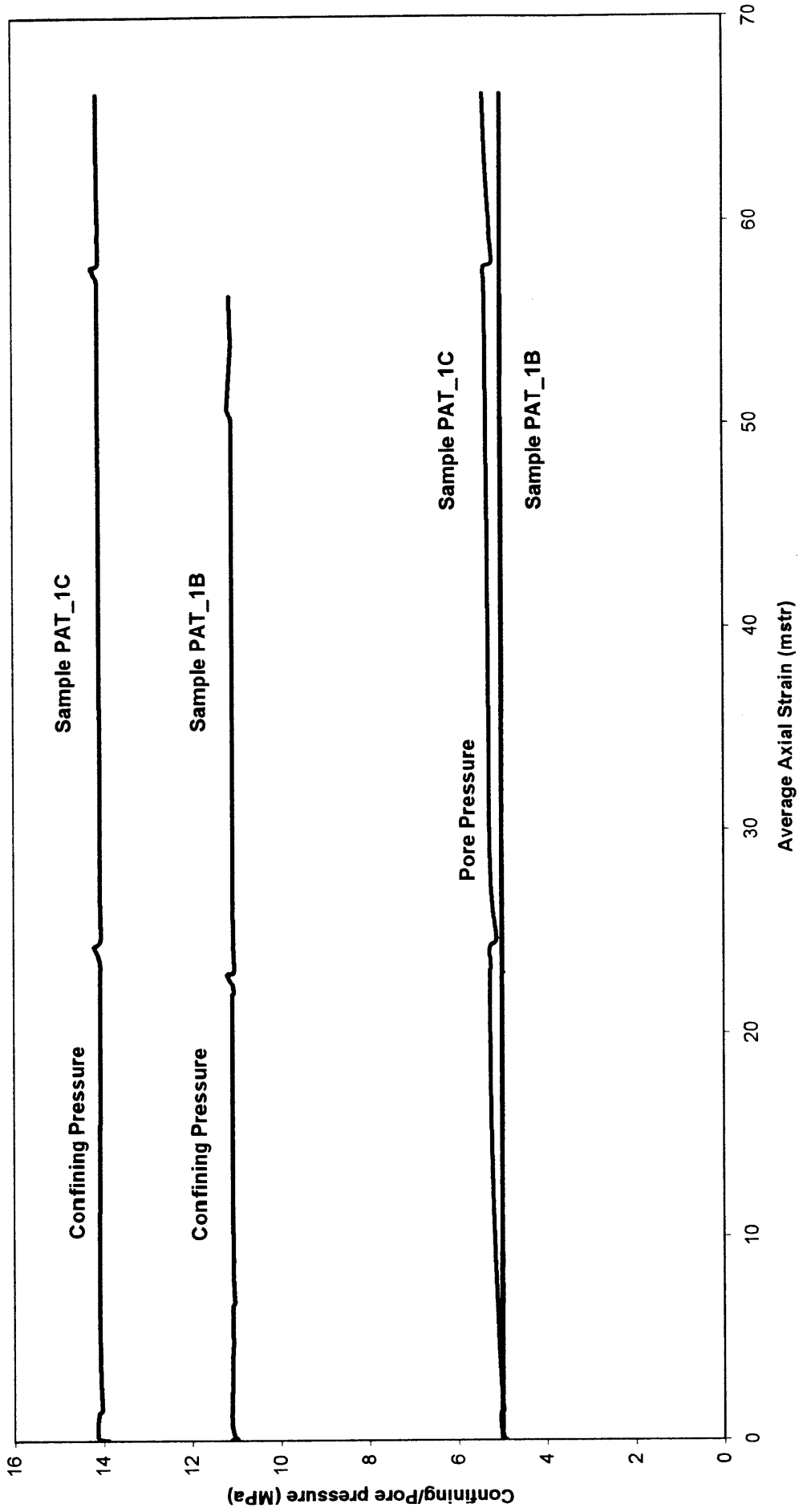
Appendix 2

Experimental Results

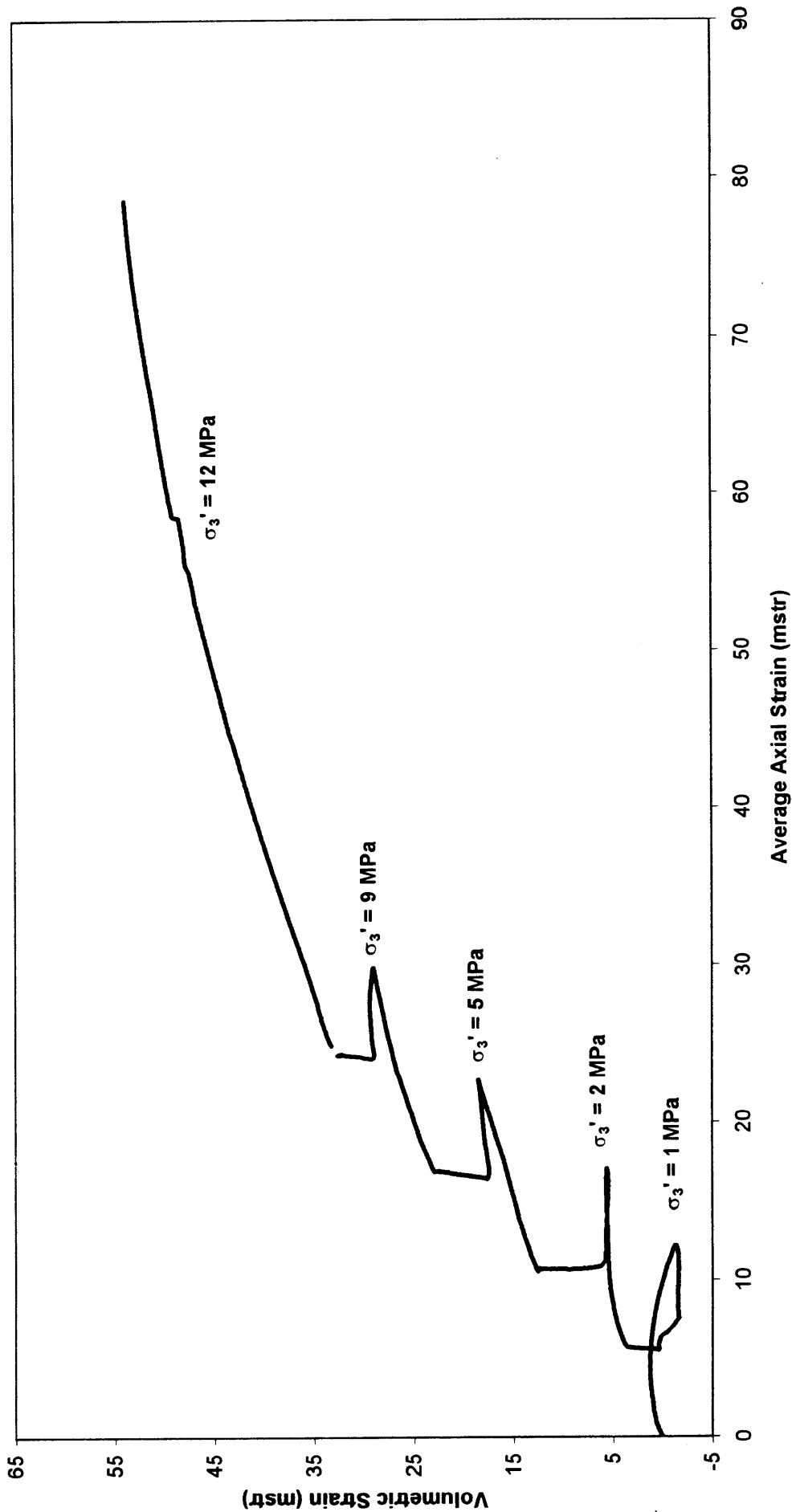
PATRICIA BALEEN - 2 SAND CORE SECTION 1
(Single Stage Triaxial Test)



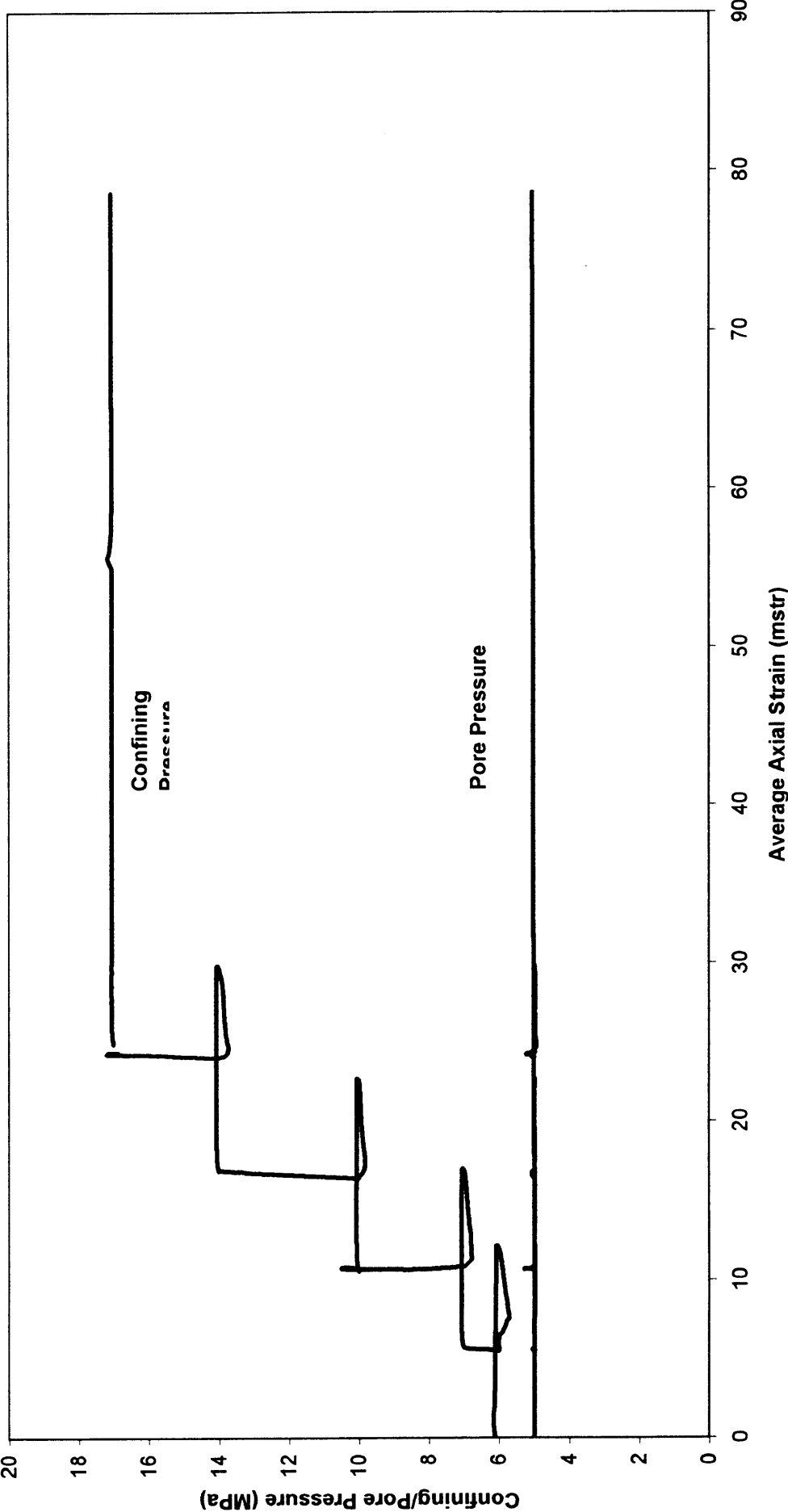
PATRICIA BALEEN - 2 SAND CORE SECTION 1
(Single Stage Triaxial Test)



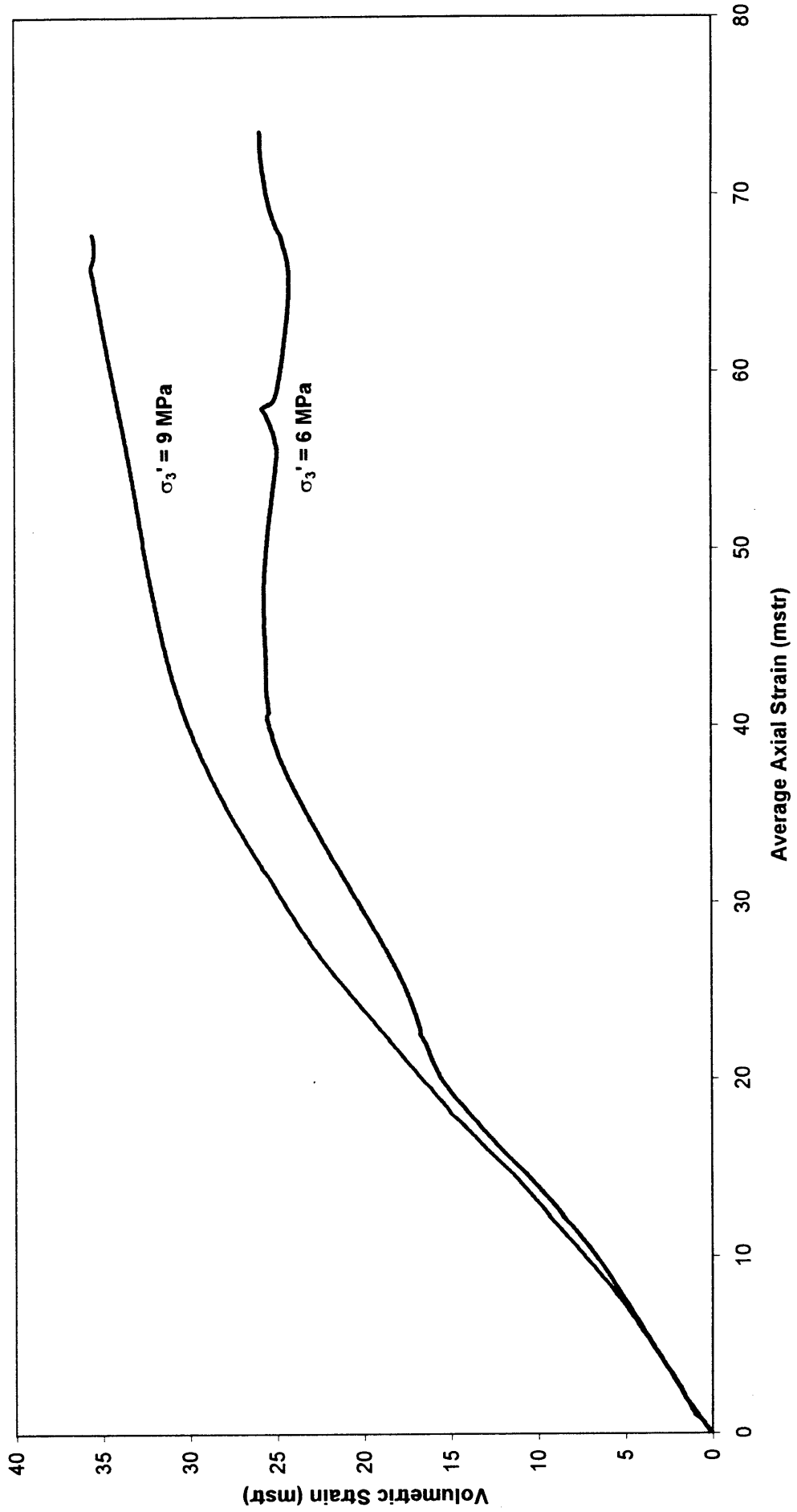
PATRICIA BALEEN - 2 SAND CORE SECTION 1
(Multiple Stage Test)



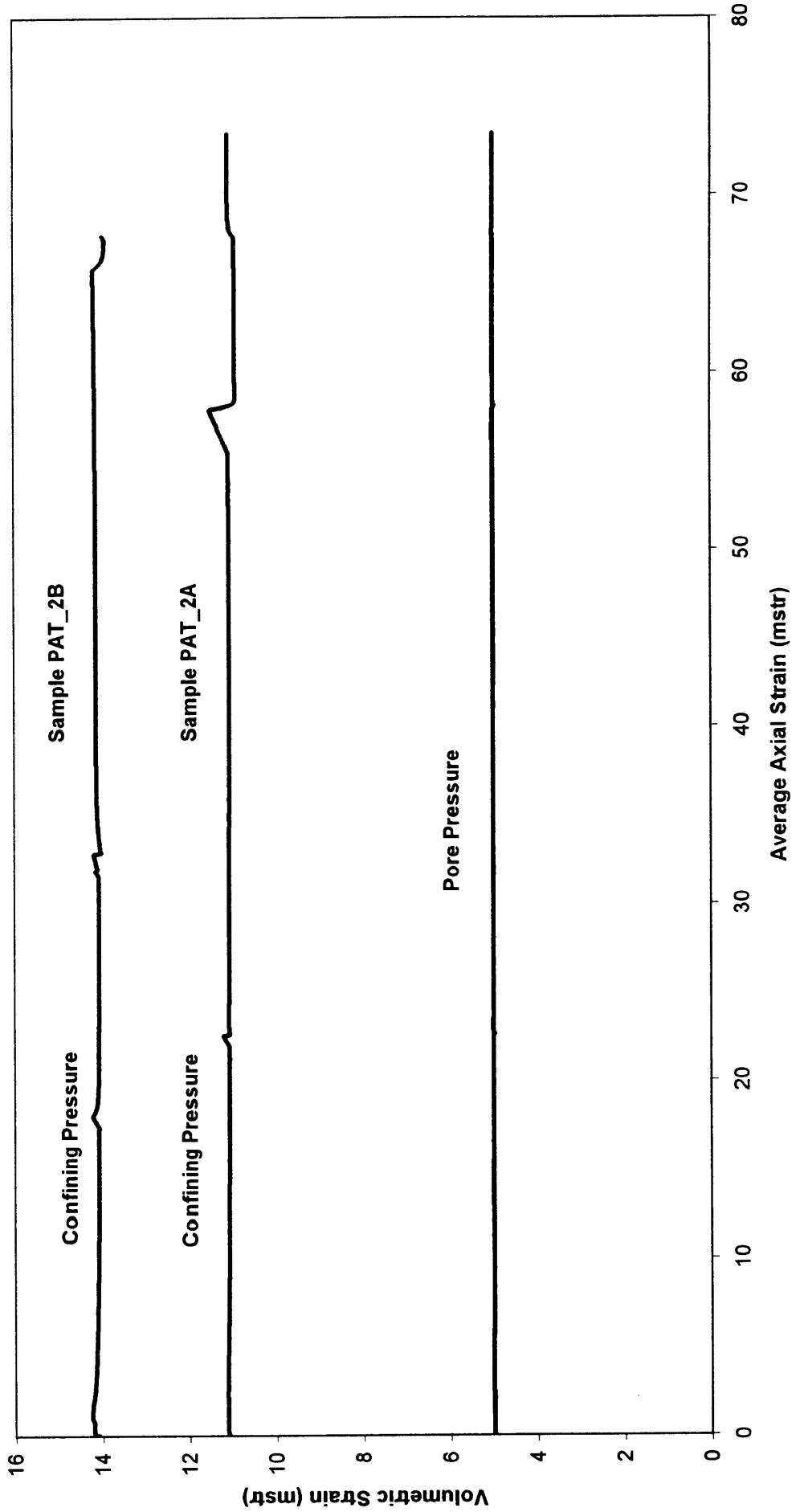
PATRICIA BALEEN - 2 SAND CORE SECTION 1
(Multiple Stage Test)



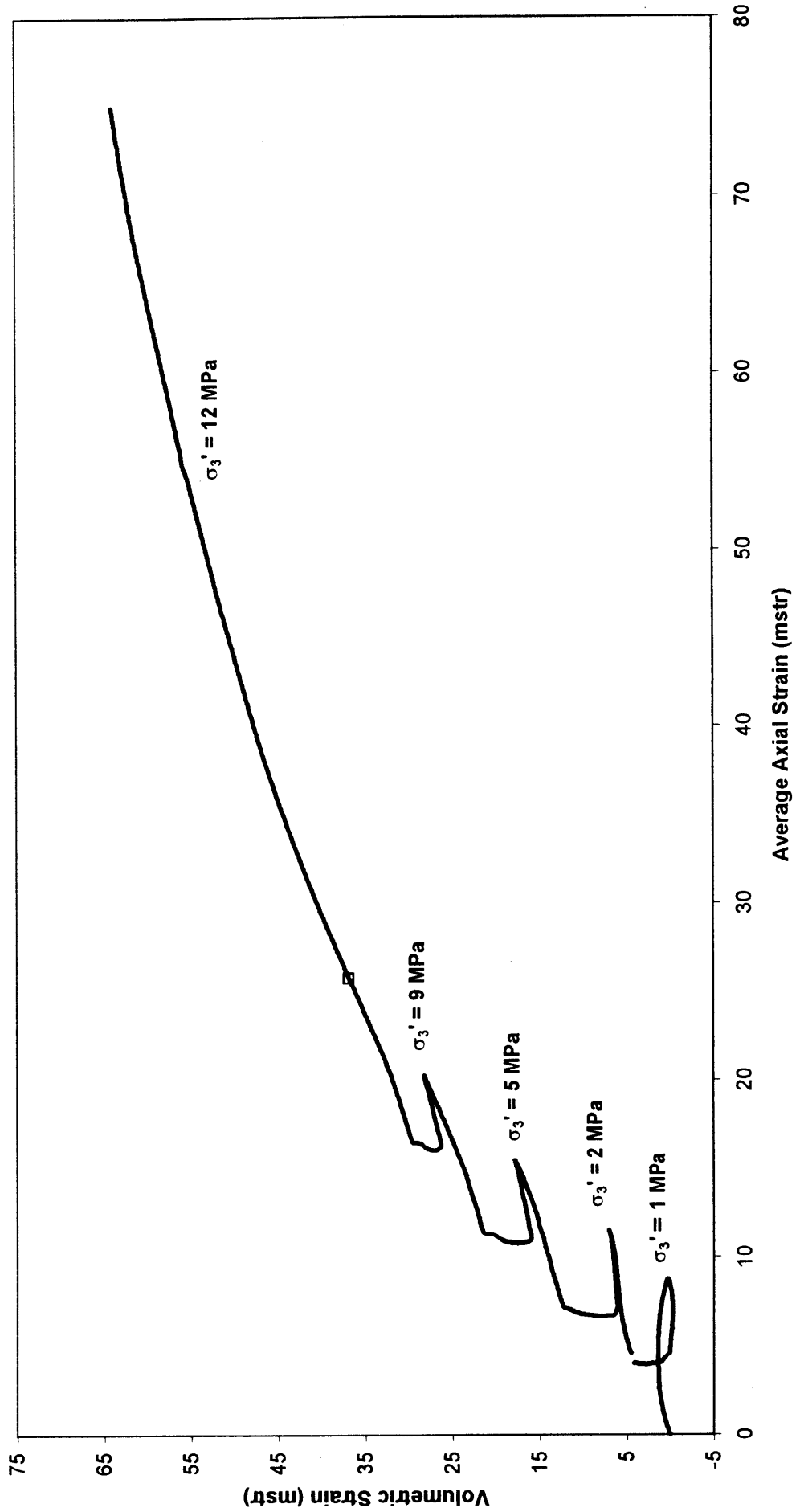
PATRICIA BALEEN - 2 SAND CORE SECTION 2
(Single Stage Triaxial Test)



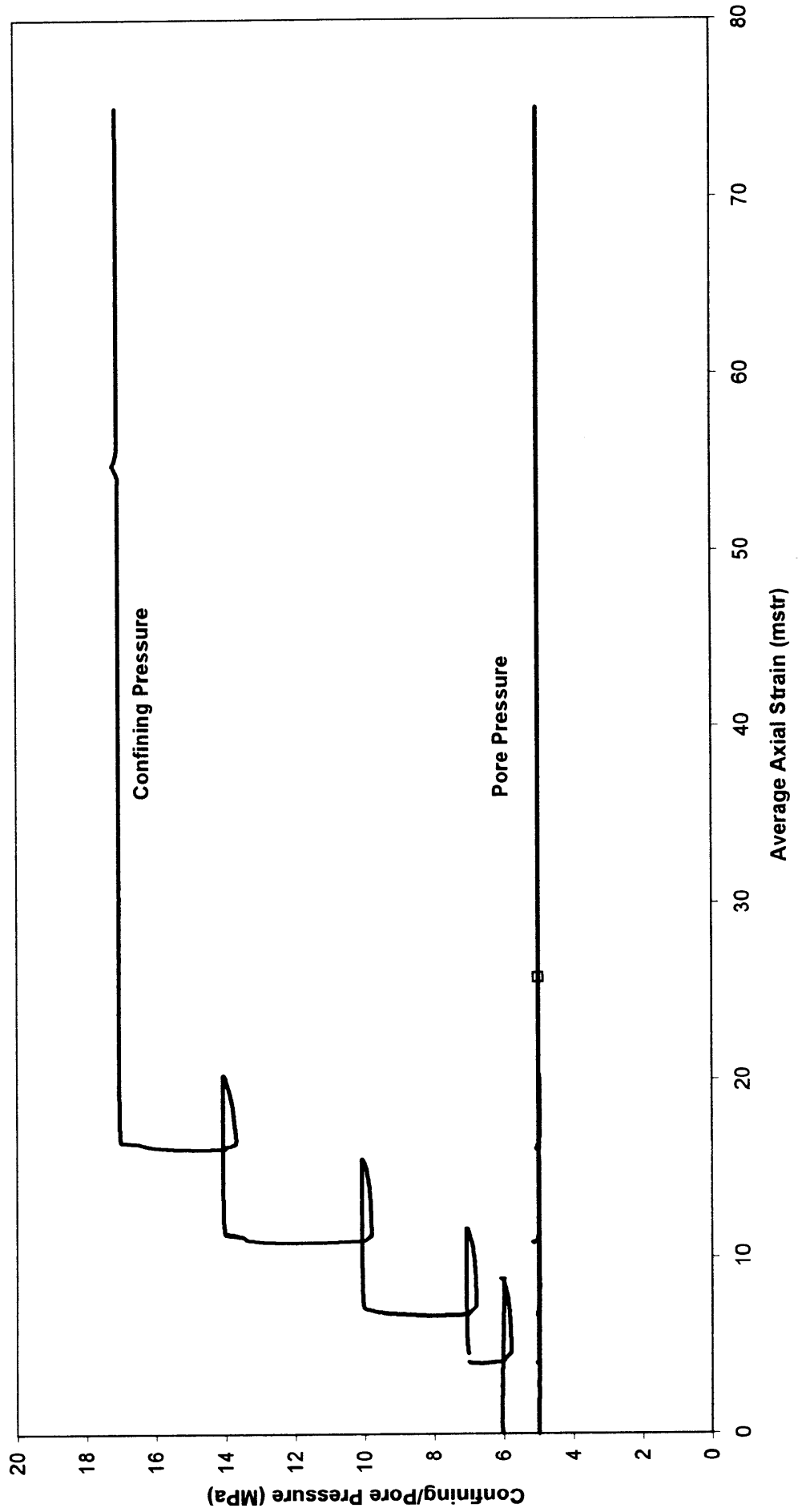
PATRICIA BALEEN - 2 SAND CORE SECTION 2
(Single Stage Triaxial Test)



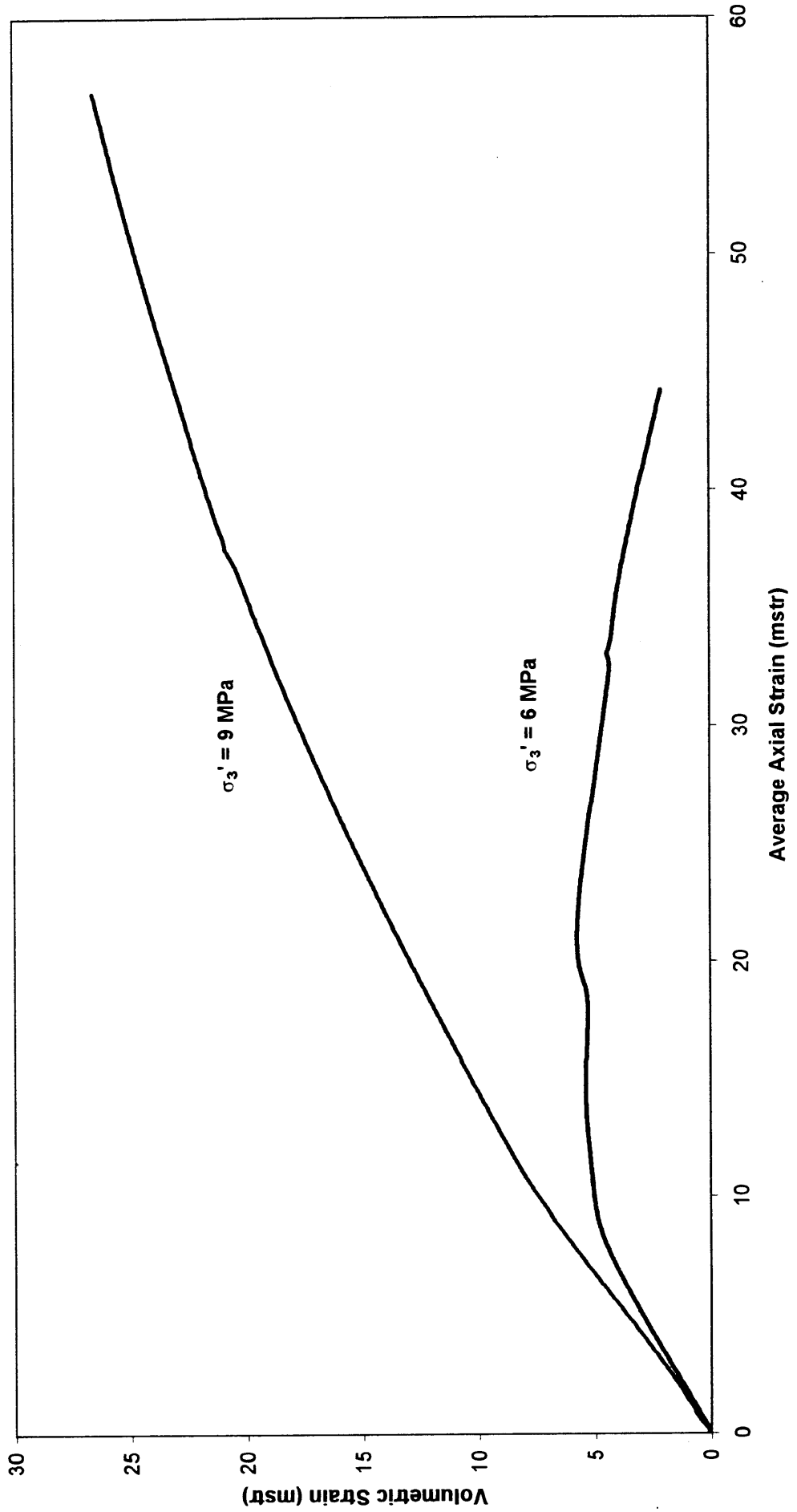
PATRICIA BALEEN - 2 SAND CORE SECTION 2
 (Multiple Stage Test)



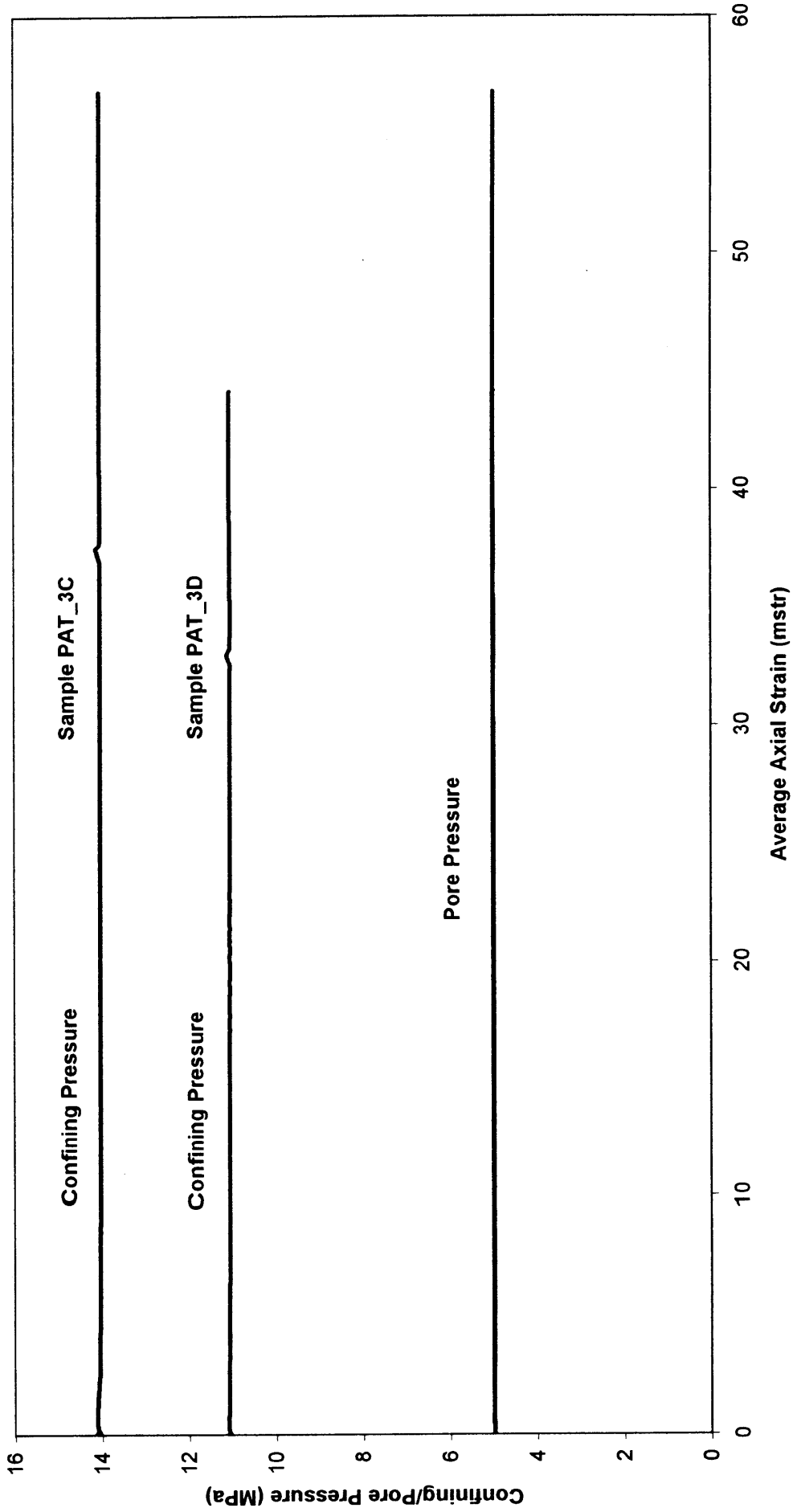
PATRICIA BALEEN - 2 SAND CORE SECTION 2
(Multiple Stage Test)



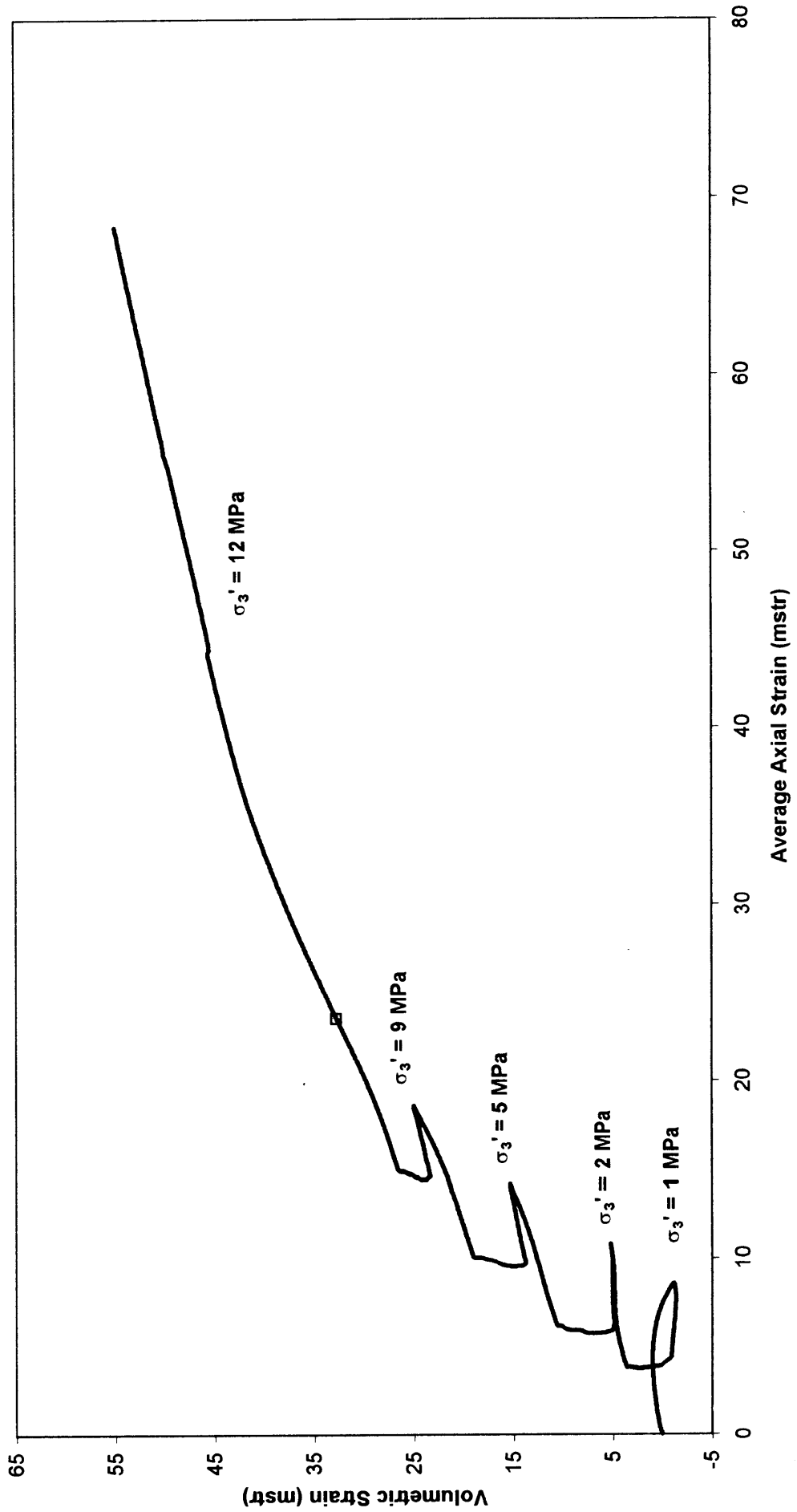
PATRICIA BALEEN - 2 SAND CORE SECTION 3
(Single Stage Triaxial Test)



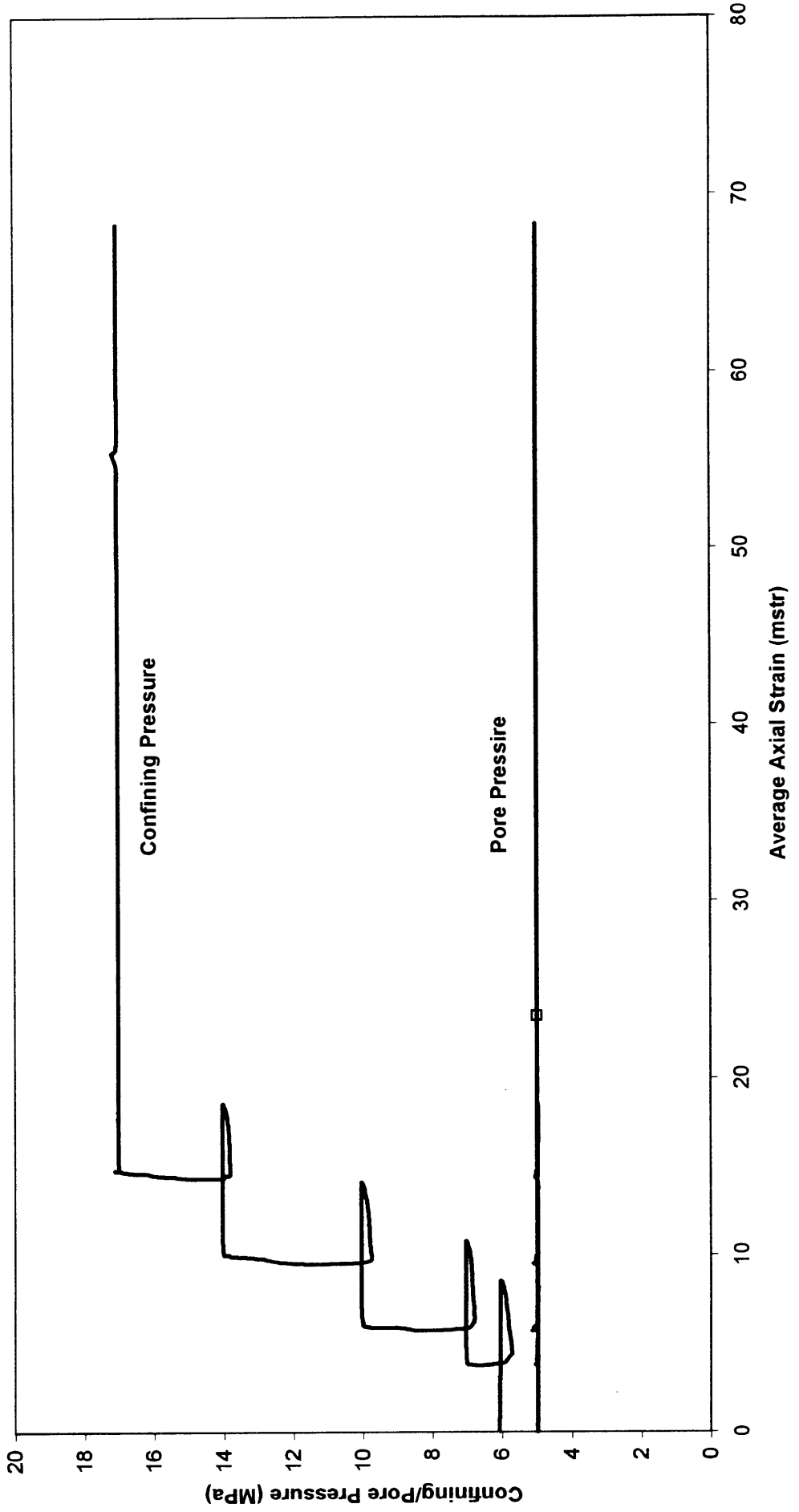
PATRICIA BALEEN - 2 SAND CORE SECTION 3
(Single Stage Triaxial Test)



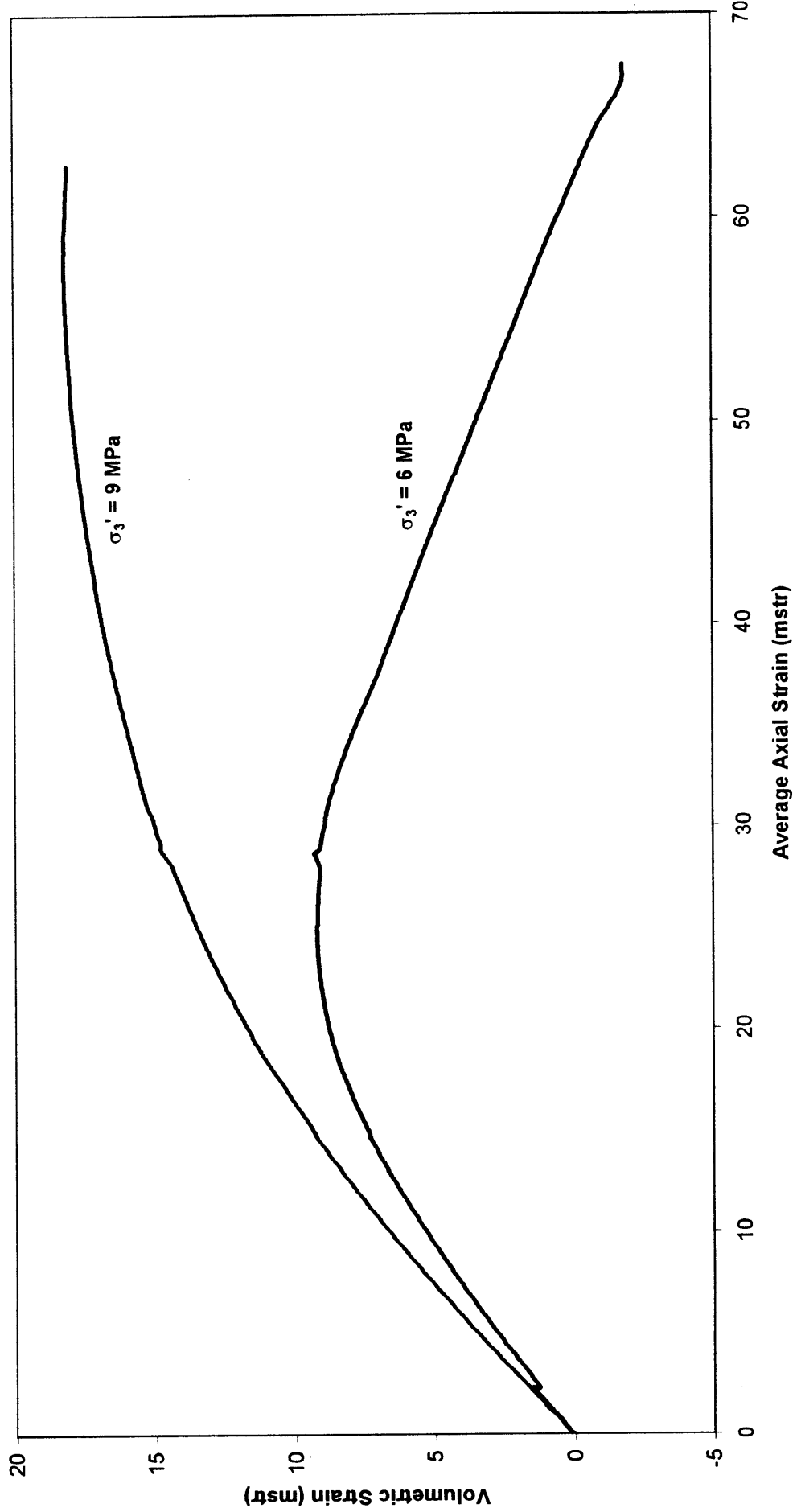
PATRICIA BALEEN - 2 SAND CORE SECTION 3
 (Multiple Stage Test)



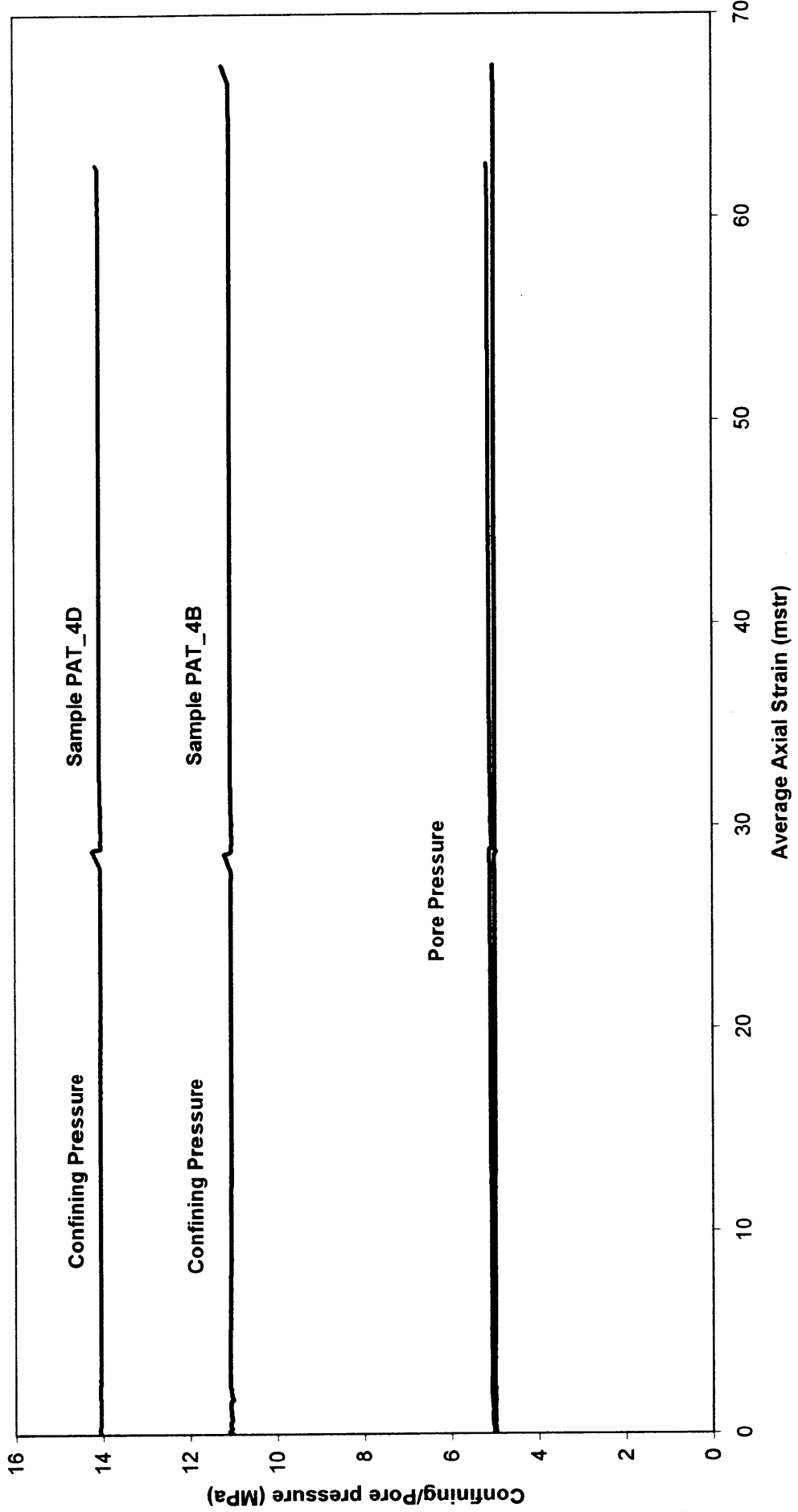
PATRICIA BALEEN - 2 SAND CORE SECTION 3
(Multiple Stage Test)



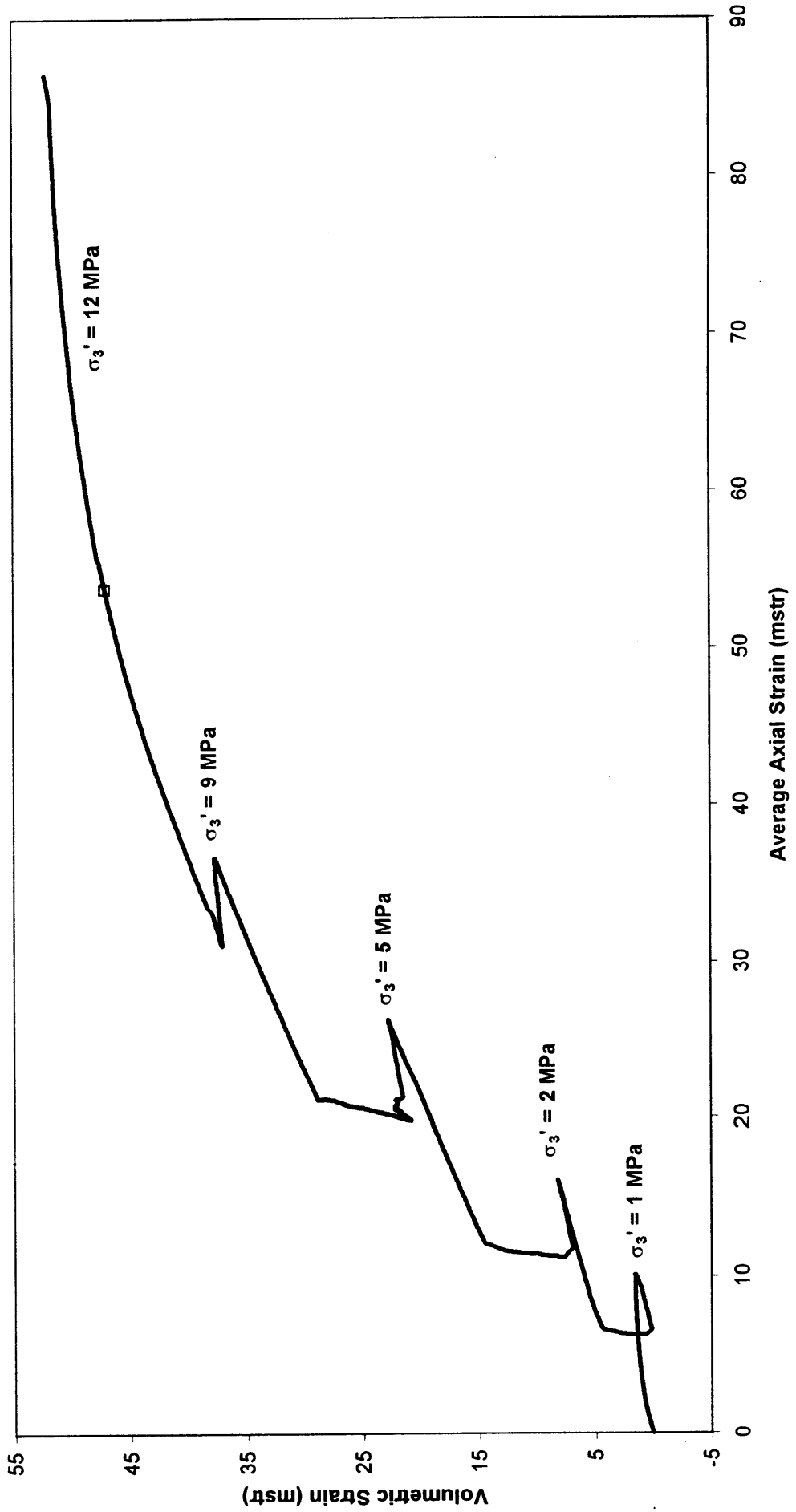
PATRICIA BALEEN - 2 SAND CORE SECTION 4
(Single Stage Triaxial Test)



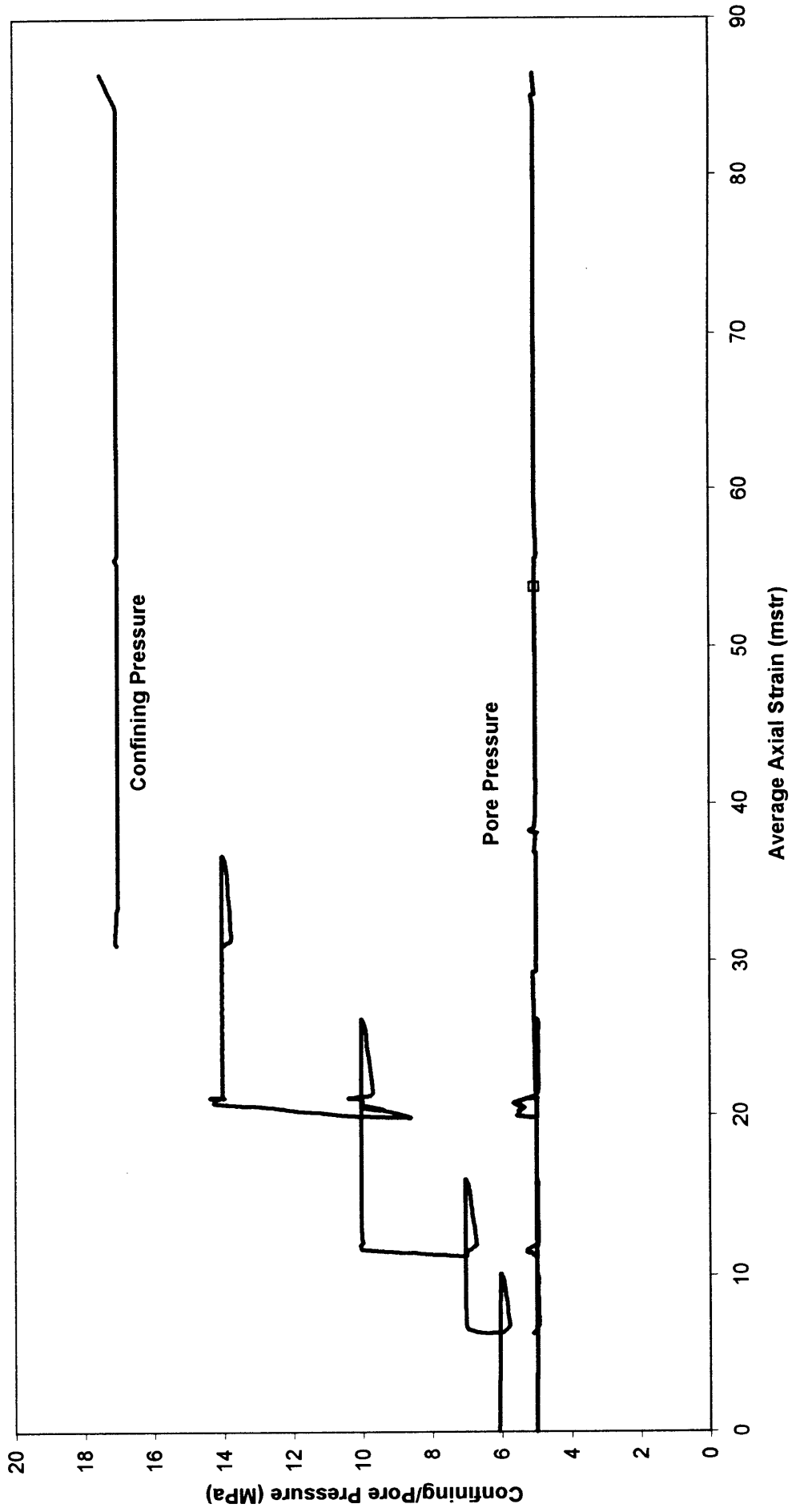
PATRICIA BALEEN - 2 SAND CORE SECTION 4
(Single Stage Triaxial Test)



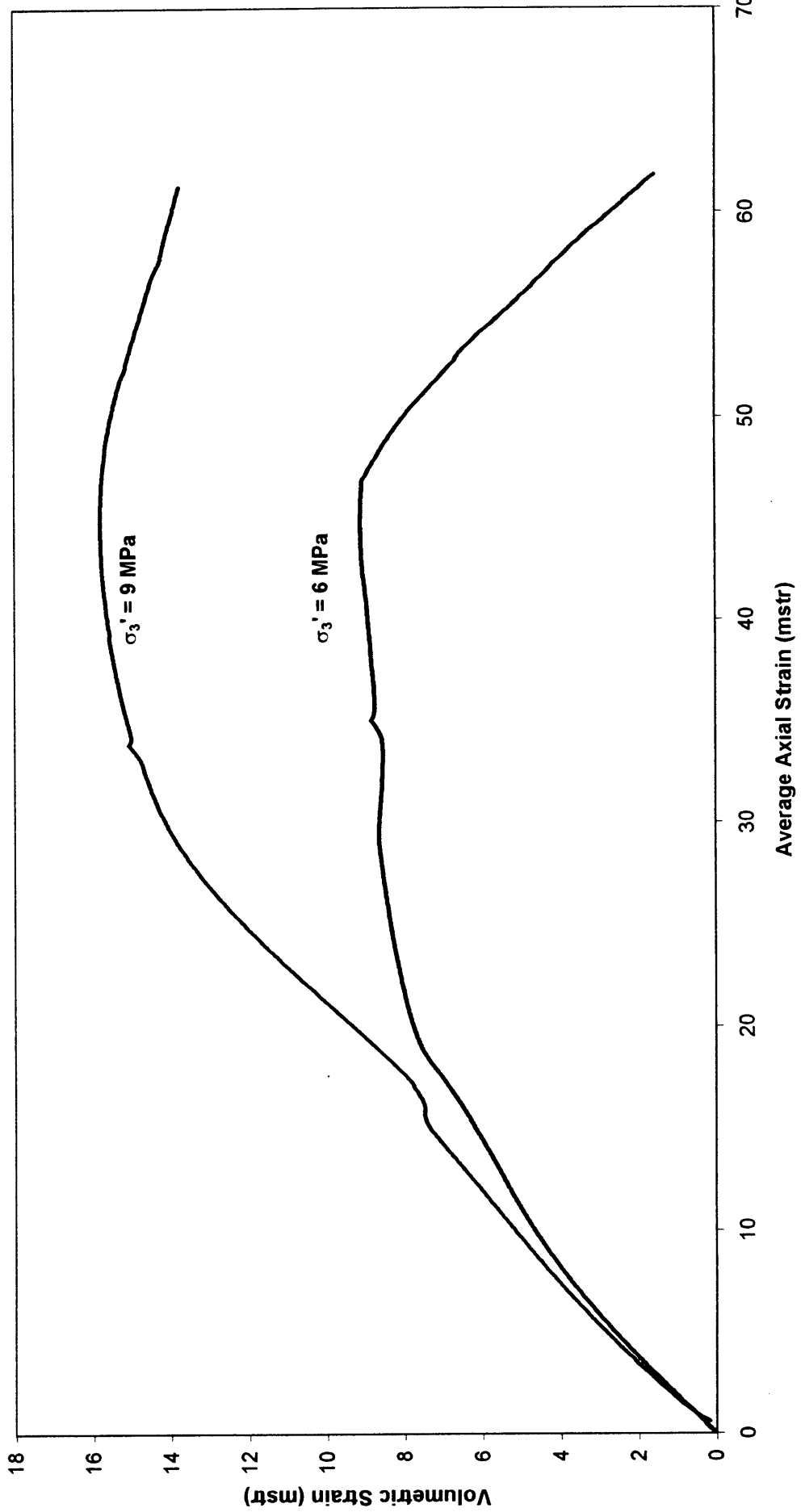
PATRICIA BALEEN - 2 SAND CORE SECTION 4
(Multiple Stage Test)



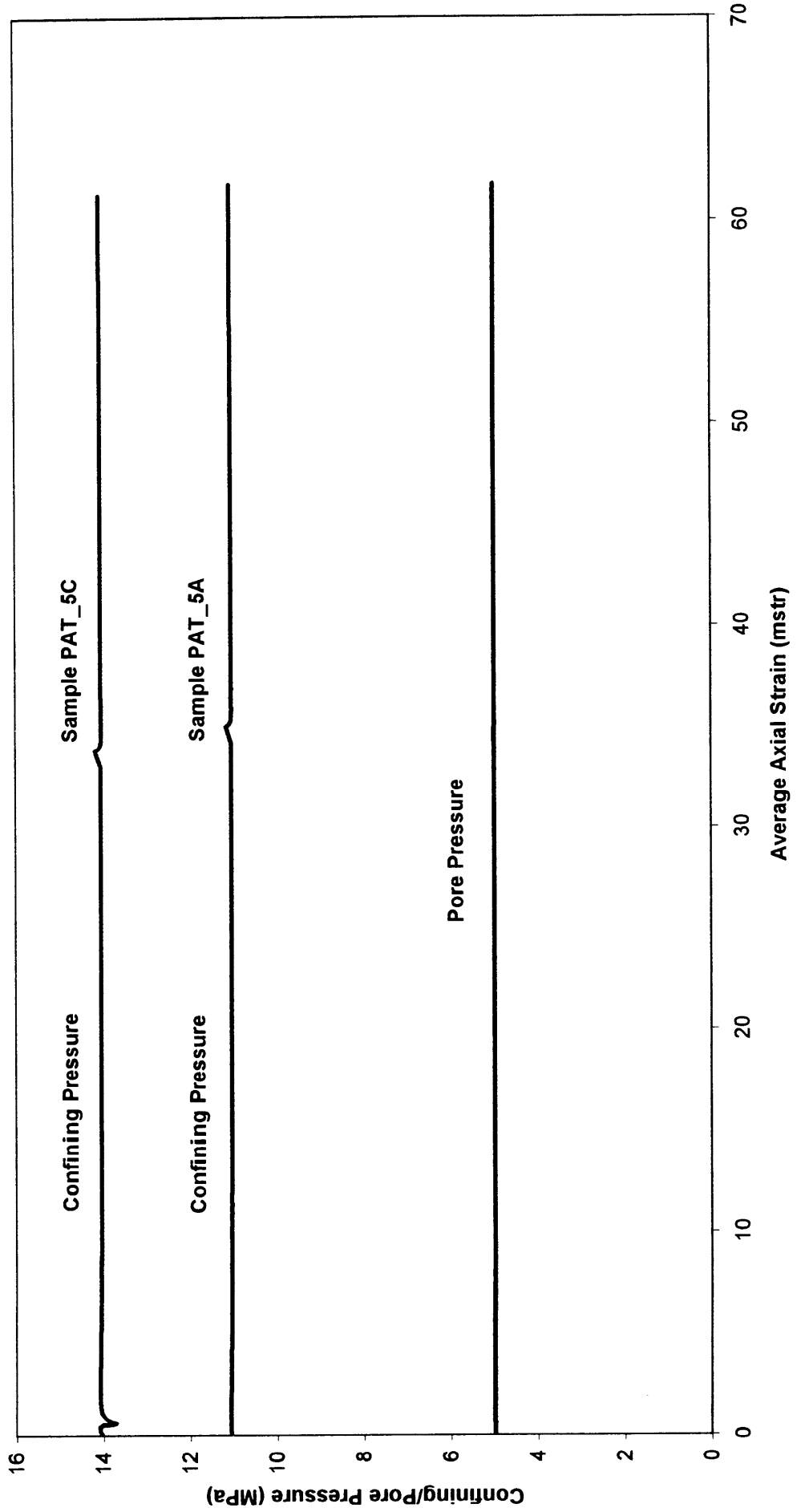
PATRICIA BALEEN - 2 SAND CORE SECTION 4
(Multiple Stage Test)



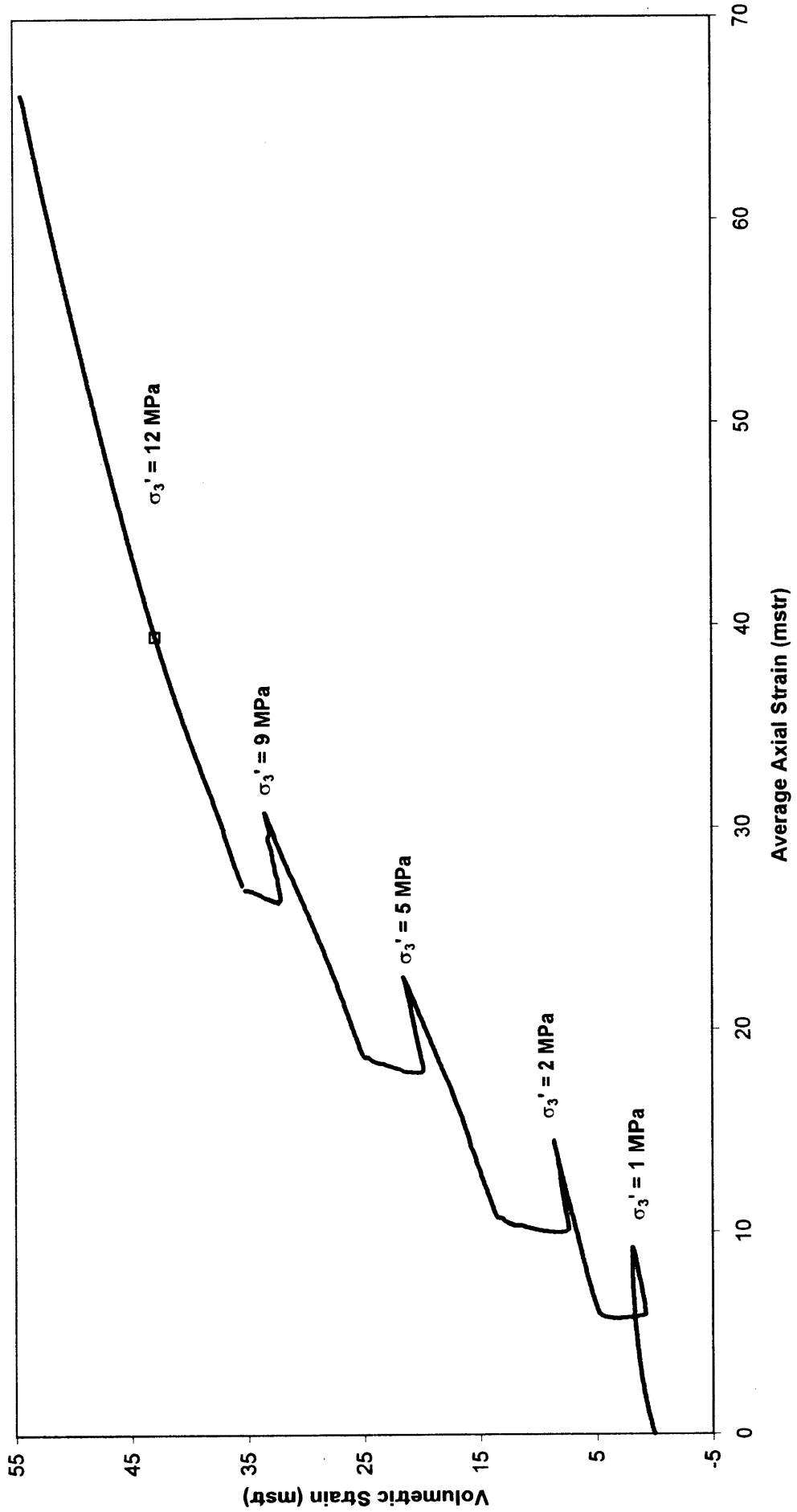
PATRICIA BALEEN - 2 SAND CORE SECTION 5
(Single Stage Triaxial Test)



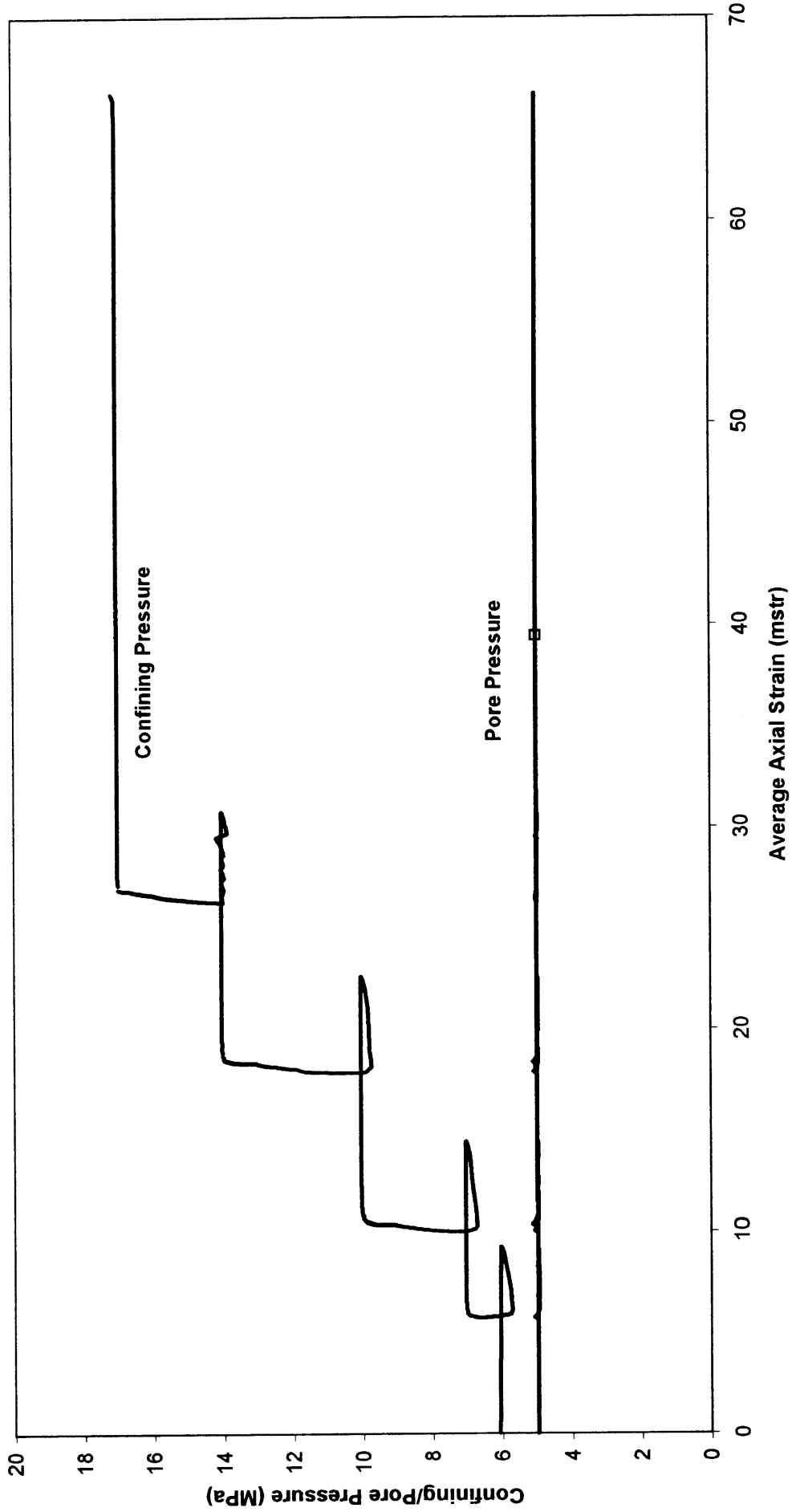
PATRICIA BALEEN - 2 SAND CORE SECTION 5
(Single Stage Triaxial Test)



PATRICIA BALEEN - 2 SAND CORE SECTION 5
(Multiple Stage Test)



PATRICIA BALEEN - 2 SAND CORE SECTION 5
(Multiple Stage Test)

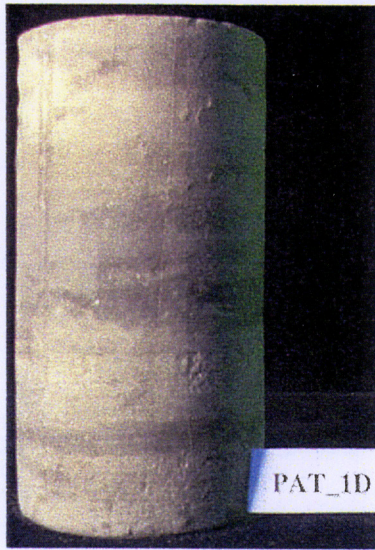


907961 209

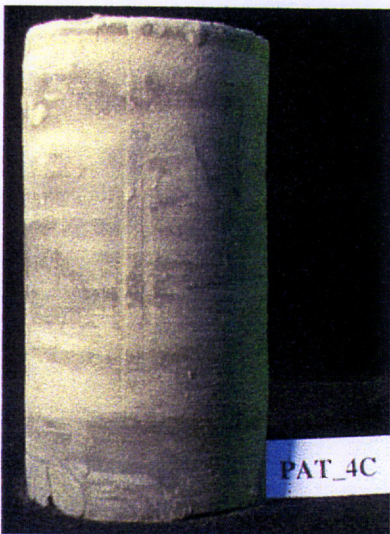
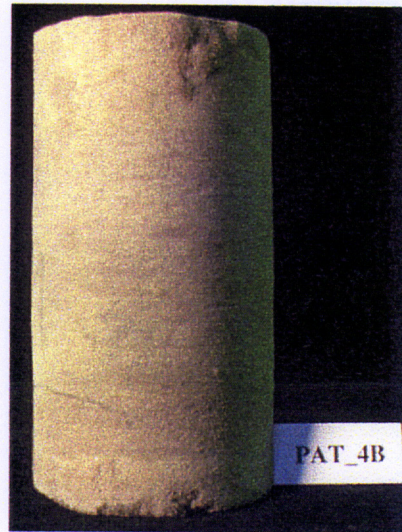
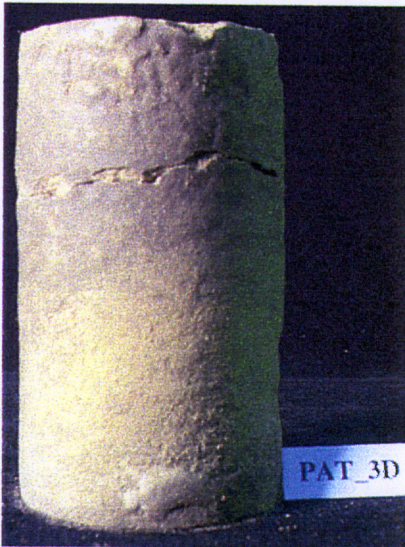
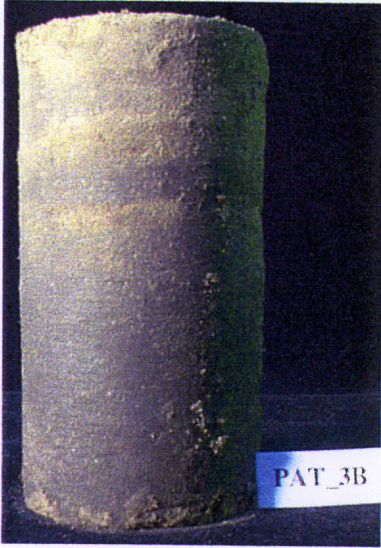
Appendix 3

Photos of Tested Samples

9073C1 210



907961 211



907961 212



907961 213

ENCLOSURES

907901 214

BALEEN-2

ENCLOSURES

PE907962

This is an enclosure indicator page.
The enclosure PE907962 is enclosed within the
container PE907961 at this location in this
document.

The enclosure PE907962 has the following characteristics:

ITEM_BARCODE = PE907962
CONTAINER_BARCODE = PE907961
 NAME = Baleen-2 Composite Playback Log
 BASIN = GIPPSLAND
 ONSHORE? = N
 DATA_TYPE = WELL
 DATA_SUB_TYPE = MONTAGE_LOG
 DESCRIPTION = Baleen-2 Merged Composite Playback
 Scale 1:200 Enclosure 1
 REMARKS =
 DATE_WRITTEN =
 DATE_PROCESSED =
 DATE_RECEIVED = 04-AUG-2000
 RECEIVED_FROM = Cultus Timor Sea Ltd
 WELL_NAME = Baleen-2
 CONTRACTOR =
 AUTHOR =
 ORIGINATOR = Cultus Timor Sea Ltd
 TOP_DEPTH =
 BOTTOM_DEPTH =
 ROW_CREATED_BY = DN07_SW

(Inserted by DNRE - Vic Govt Mines Dept)

PE907963

This is an enclosure indicator page.
The enclosure PE907963 is enclosed within the
container PE907961 at this location in this
document.

The enclosure PE907963 has the following characteristics:

ITEM_BARCODE = PE907963
CONTAINER_BARCODE = PE907961
 NAME = Baleen-2 Mud Log
 BASIN = GIPPSLAND
 ONSHORE? = N
 DATA_TYPE = WELL
 DATA_SUB_TYPE = MUD_LOG
 DESCRIPTION = Baleen-2 Formation Evaluation Log Scale
 1:500 Enclosure 2
 REMARKS =
 DATE_WRITTEN =
 DATE_PROCESSED =
 DATE_RECEIVED = 04-AUG-2000
 RECEIVED_FROM = Cultus Timor Sea Ltd
 WELL_NAME = Baleen-2
 CONTRACTOR = Geoservices
 AUTHOR =
 ORIGINATOR = Cultus Timor Sea Ltd
 TOP_DEPTH = 80
 BOTTOM_DEPTH = 920
 ROW_CREATED_BY = DN07_SW

(Inserted by DNRE - Vic Govt Mines Dept)

PE907964

This is an enclosure indicator page.
The enclosure PE907964 is enclosed within the
container PE907961 at this location in this
document.

The enclosure PE907964 has the following characteristics:

ITEM_BARCODE = PE907964
CONTAINER_BARCODE = PE907961
NAME = Baleen-2 Drilling Data Log
BASIN = GIPPSLAND
ONSHORE? = N
DATA_TYPE = WELL
DATA_SUB_TYPE = WELL_LOG
DESCRIPTION = Baleen-2 Drilling Data Log Scale 1:1000
Enclosure 3
REMARKS =
DATE_WRITTEN =
DATE_PROCESSED =
DATE_RECEIVED = 04-AUG-2000
RECEIVED_FROM = Cultus Timor Sea Ltd
WELL_NAME = Baleen-2
CONTRACTOR = Geoservices
AUTHOR =
ORIGINATOR = Cultus Timor Sea Ltd
TOP_DEPTH = 80
BOTTOM_DEPTH = 920
ROW_CREATED_BY = DN07_SW

(Inserted by DNRE - Vic Govt Mines Dept)

PE907965

This is an enclosure indicator page.
The enclosure PE907965 is enclosed within the
container PE907961 at this location in this
document.

The enclosure PE907965 has the following characteristics:

ITEM_BARCODE = PE907965
CONTAINER_BARCODE = PE907961
NAME = Baleen-2 Pressure Log
BASIN = GIPPSLAND
ONSHORE? = N
DATA_TYPE = WELL
DATA_SUB_TYPE = WELL_LOG
DESCRIPTION = Baleen-2 Pressure Log Scale 1:500
Enclosure 4
REMARKS =
DATE_WRITTEN =
DATE_PROCESSED =
DATE_RECEIVED = 04-AUG-2000
RECEIVED_FROM = Cultus Timor Sea Ltd
WELL_NAME = Baleen-2
CONTRACTOR = Geoservices
AUTHOR =
ORIGINATOR = Cultus Timor Sea Ltd
TOP_DEPTH = 80
BOTTOM_DEPTH = 920
ROW_CREATED_BY = DN07_SW

(Inserted by DNRE - Vic Govt Mines Dept)

PE907966

This is an enclosure indicator page.
The enclosure PE907966 is enclosed within the
container PE907961 at this location in this
document.

The enclosure PE907966 has the following characteristics:

ITEM_BARCODE = PE907966
CONTAINER_BARCODE = PE907961
 NAME = Baleen-2 Vertical Seismic Profile
 BASIN = GIPPSLAND
 ONSHORE? = N
 DATA_TYPE = WELL
 DATA_SUB_TYPE = VELOCITY_CHART
 DESCRIPTION = Baleen-2 Vertical Seismic Profile
 Z-Axis Processing Steps Plot #1 Z
 Median Stack Enclosure 5
 REMARKS =
 DATE_WRITTEN =
 DATE_PROCESSED =
 DATE_RECEIVED = 04-AUG-2000
 RECEIVED_FROM = Cultus Timor Sea Ltd
 WELL_NAME = Baleen-2
 CONTRACTOR = Schlumberger
 AUTHOR =
 ORIGINATOR = Cultus Timor Sea Ltd
 TOP_DEPTH =
 BOTTOM_DEPTH =
 ROW_CREATED_BY = DN07_SW

(Inserted by DNRE - Vic Govt Mines Dept)

PE907967

This is an enclosure indicator page.
The enclosure PE907967 is enclosed within the
container PE907961 at this location in this
document.

The enclosure PE907967 has the following characteristics:

ITEM_BARCODE = PE907967
CONTAINER_BARCODE = PE907961
NAME = Baleen-2 Vertical Seismic Profile
BASIN = GIPPSLAND
ONSHORE? = N
DATA_TYPE = WELL
DATA_SUB_TYPE = VELOCITY_CHART
DESCRIPTION = Baleen-2 Z-Axis Processing Steps Plot 2
Downgoing Wavefield after VELF; Plot 3
Upgoing Wavefield after VELF; Plot 4
Downgoing Wavefield after WSF; Plot 5
Upgoing Wavefield after WSF and Upgoing
Enhancement Enclosure 6
REMARKS =
DATE_WRITTEN =
DATE_PROCESSED =
DATE_RECEIVED = 04-AUG-2000
RECEIVED_FROM = Cultus Timor Sea Ltd
WELL_NAME = Baleen-2
CONTRACTOR = Schlumberger
AUTHOR =
ORIGINATOR = Cultus Timor Sea Ltd
TOP_DEPTH =
BOTTOM_DEPTH =
ROW_CREATED_BY = DN07_SW

(Inserted by DNRE - Vic Govt Mines Dept)

PE907968

This is an enclosure indicator page.
The enclosure PE907968 is enclosed within the
container PE907961 at this location in this
document.

The enclosure PE907968 has the following characteristics:

ITEM_BARCODE = PE907968
CONTAINER_BARCODE = PE907961
 NAME = Baleen-2 Vertical Seismic Profile
 BASIN = GIPPSLAND
 ONSHORE? = N
 DATA_TYPE = WELL
 DATA_SUB_TYPE = VELOCITY_CHART
 DESCRIPTION = Baleen-2 Vertical Seismic Profile
 Composite Display Normal Polarity
 Enclosure 7
 REMARKS =
 DATE_WRITTEN =
 DATE_PROCESSED =
 DATE_RECEIVED = 04-AUG-2000
 RECEIVED_FROM = Cultus Timor Sea Ltd
 WELL_NAME = Baleen-2
 CONTRACTOR = Schlumberger
 AUTHOR =
 ORIGINATOR = Cultus Timor Sea Ltd
 TOP_DEPTH =
 BOTTOM_DEPTH =
 ROW_CREATED_BY = DN07_SW

(Inserted by DNRE - Vic Govt Mines Dept)

PE907969

This is an enclosure indicator page.
The enclosure PE907969 is enclosed within the
container PE907961 at this location in this
document.

The enclosure PE907969 has the following characteristics:

ITEM_BARCODE = PE907969
CONTAINER_BARCODE = PE907961
 NAME = Baleen-2 Vertical Seismic Profile
 BASIN = GIPPSLAND
 ONSHORE? = N
 DATA_TYPE = WELL
 DATA_SUB_TYPE = VELOCITY_CHART
 DESCRIPTION = Baleen-2 Vertical Seismic Profile
 Composite Display Reversed Polarity
 Enclosure 8
 REMARKS =
 DATE_WRITTEN =
 DATE_PROCESSED =
 DATE_RECEIVED = 04-AUG-2000
 RECEIVED_FROM = Cultus Timor Sea Ltd
 WELL_NAME = Baleen-2
 CONTRACTOR = Schlumberger
 AUTHOR =
 ORIGINATOR = Cultus Timor Sea Ltd
 TOP_DEPTH =
 BOTTOM_DEPTH =
 ROW_CREATED_BY = DN07_SW

(Inserted by DNRE - Vic Govt Mines Dept)

PE907970

This is an enclosure indicator page.
The enclosure PE907970 is enclosed within the
container PE907961 at this location in this
document.

The enclosure PE907970 has the following characteristics:

ITEM_BARCODE = PE907970
CONTAINER_BARCODE = PE907961
NAME = Baleen-2 Drift Corrected Sonic
BASIN = GIPPSLAND
ONSHORE? = N
DATA_TYPE = WELL
DATA_SUB_TYPE = WELL_LOG
DESCRIPTION = Baleen-2 Drift Corrected Sonic Scale
1:500 Enclosure 9
REMARKS =
DATE_WRITTEN =
DATE_PROCESSED = 16-NOV-1999
DATE_RECEIVED = 04-AUG-2000
RECEIVED_FROM = Cultus Timor Sea Ltd
WELL_NAME = Baleen-2
CONTRACTOR = Schlumberger
AUTHOR =
ORIGINATOR = Cultus Timor Sea Ltd
TOP_DEPTH = 0
BOTTOM_DEPTH = 850
ROW_CREATED_BY = DN07_SW

(Inserted by DNRE - Vic Govt Mines Dept)

PE907971

This is an enclosure indicator page.
The enclosure PE907971 is enclosed within the
container PE907961 at this location in this
document.

The enclosure PE907971 has the following characteristics:

ITEM_BARCODE = PE907971
CONTAINER_BARCODE = PE907961
 NAME = Baleen-2 Check Shot Survey
 BASIN = GIPPSLAND
 ONSHORE? = N
 DATA_TYPE = WELL
 DATA_SUB_TYPE = VELOCITY_CHART
 DESCRIPTION = Baleen-2 Check Shot Survey Velocity
 Cross Plot Depth Scale 1:50000
 Enclosure 10
 REMARKS =
 DATE_WRITTEN =
 DATE_PROCESSED =
 DATE_RECEIVED = 04-AUG-2000
 RECEIVED_FROM = Cultus Timor Sea Ltd
 WELL_NAME = Baleen-2
 CONTRACTOR = Schlumberger
 AUTHOR =
 ORIGINATOR = Cultus Timor Sea Ltd
 TOP_DEPTH =
 BOTTOM_DEPTH =
 ROW_CREATED_BY = DN07_SW

(Inserted by DNRE - Vic Govt Mines Dept)